

AD-A239 653



**NUCLEAR MONITORING RESEARCH
AT THE CENTER FOR SEISMIC STUDIES**

by

*Jerry Carter
John Coyne
Hans Israelsson
Florence Riviere-Barbier
Vladislav Ryaboy
Anne Suteau-Henson*

Science Applications International Corporation
Center for Seismic Studies
1300 N. 17th Street, Suite 1450
Arlington, VA 22209

13 May 1991

Scientific Report No. 1



Approved for Public Release; Distribution Unlimited



Phillips Laboratory
Air Force Systems Command
Hanscom Air Force Base, Massachusetts 01731-5000

91-08325



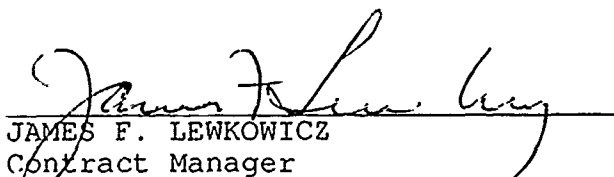
91 8 20 031

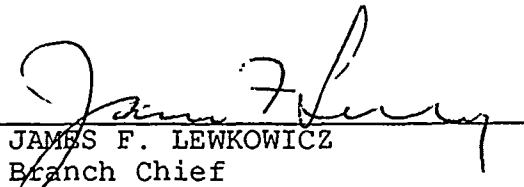
SPONSORED BY
Defense Advanced Research Projects Agency
Nuclear Monitoring Research Office
ARPA ORDER NO. 5299

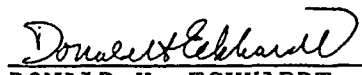
MONITORED BY
Phillips Laboratory
Contract F19628-89-C-0203

The views and conclusions contained in this document are those of the authors and should not be interpreted as representing the official policies, either expressed or implied, of the Defense Advanced Research Projects Agency or the U.S. Government.

This technical report has been reviewed and is approved for publication.


JAMES F. LEWKOWICZ
Contract Manager
Solid Earth Geophysics Branch
Earth Sciences Division


JAMES F. LEWKOWICZ
Branch Chief
Solid Earth Geophysics Branch
Earth Sciences Division


DONALD H. ECKHARDT, Director
Earth Sciences Division

This report has been reviewed by the ESD Public Affairs Office (PA) and is releasable to the National Technical Information Service (NTIS).

Qualified requestors may obtain additional copies from the Defense Technical Information Center. All others should apply to the National Technical Information Service.

If your address has changed, or if you wish to be removed from the mailing list, or if the addressee is no longer employed by your organization, please notify PL/IMA, Hanscom AFB, MA 01731-5000. This will assist us in maintaining a current mailing list.

Do not return copies of this report unless contractual obligations or notices on a specific document requires that it be returned.

REPORT DOCUMENTATION PAGE				Form Approved OMB No. 0704-0188 Exp. Date Jun 30 1986	
1a REPORT SECURITY CLASSIFICATION UNCLASSIFIED			1b RESTRICTIVE MARKINGS		
2a SECURITY CLASSIFICATION AUTHORITY			3 DISTRIBUTION/AVAILABILITY OF REPORT Approved for Public Release; Distribution Unlimited		
2b DECLASSIFICATION/DOWNGRADING SCHEDULE					
4 PERFORMING ORGANIZATION REPORT NUMBER(S) SAIC CSS Technical Report C90-04			5. MONITORING ORGANIZATION REPORT NUMBER(S) PL-TR-91-2127		
6a NAME OF PERFORMING ORGANIZATION Science Applications International Corporation		6b OFFICE SYMBOL (If applicable)	7a NAME OF MONITORING ORGANIZATION Phillips Laboratory		
6c ADDRESS (City, State, and ZIP Code) Center for Seismic Studies 1300 N. 17th Street, Suite 1450 Arlington, VA 22209		7b ADDRESS (City, State, and ZIP Code) Hanscom AFB, MA 01731-5000			
8a NAME OF FUNDING/SPONSORING ORGANIZATION Defense Advanced Research Projects Agency		8b OFFICE SYMBOL (If applicable)	9 PROCUREMENT INSTRUMENT IDENTIFICATION NUMBER F19628-89-C-0203		
8c. ADDRESS (City, State, and ZIP Code) 1400 Wilson Boulevard Arlington, VA 22209		10. SOURCE OF FUNDING NUMBERS			
		PROGRAM ELEMENT NO 62714E	PROJECT NO. 9A10	TASK NO DA	WORK UNIT ACCESSION NO BI
11 TITLE (Include Security Classification) Nuclear Monitoring Research at the Center for Seismic Studies					
12. PERSONAL AUTHOR(S) J. Carter, J. Coyne, H. Israelsson, F. Riviere-Barbier, V. Ryaboy, A. Suteau-Henson					
13a TYPE OF REPORT Scientific No. 1		13b TIME COVERED FROM 10/1/89 TO 10/1/90		14 DATE OF REPORT (Year, Month, Day) 1991 May 13	
15 PAGE COUNT 220					
16 SUPPLEMENTARY NOTATION					
17 COSATI CODES			18 SUBJECT TERMS (Continue on reverse if necessary and identify by block number) Seismology Attenuation Soviet Seismic Data Arrays Inhomogeneities Waveform Simulation 3-Component Lg		
FIELD	GROUP	SUB-GROUP			
19 ABSTRACT (Continue on reverse if necessary and identify by block number) The research presented in this report covers activity by the research staff of the Center for Seismic Studies for the period between 1 October 1989 and 1 October 1990. The report is divided into five sections covering topics relevant to underground nuclear test monitoring of the Soviet Union. Data for these studies came from the Scandinavian arrays NORESS, ARCESS, and FINESA; the IRIS stations within the Soviet Union, and hand digitized records of Soviet underground nuclear explosions recorded at stations of the Soviet Seismic Network. A brief description of the contents of the report are given below. The first section is composed of two reports by Ryaboy that review Soviet literature focused on the seismic characteristics of the crust and upper-mantle near					
20 DISTRIBUTION/AVAILABILITY OF ABSTRACT <input checked="" type="checkbox"/> UNCLASSIFIED/UNLIMITED <input type="checkbox"/> SAME AS RPT <input type="checkbox"/> DTIC USERS			21. ABSTRACT SECURITY CLASSIFICATION UNCLASSIFIED		
22a NAME OF RESPONSIBLE INDIVIDUAL James Lewkowicz			22b. TELEPHONE (Include Area Code) (617) 377-3222		22c OFFICE SYMBOL PL/LWH

the IRIS stations in the Soviet Union. The first report discusses the crust and upper mantle velocity and Q structure beneath the stations, and the second discusses lateral heterogeneity of the upper mantle inferred from refraction data. Four of the five areas studied encompass major geologic boundaries that are large lateral velocity inhomogeneities in the Earth's crust and upper mantle. These heterogeneities can significantly affect the travel time and amplitude of arrivals at these stations.

The second section is devoted to studies based on the Scandinavian Arrays. The first report in this section is a paper by Suteau-Henson on three-component phase identification using data gathered by the Intelligent Monitoring System (IMS). Using just the three-component elements of the arrays, phase identification can be made from the polarization information, but the same discriminants cannot be used at different arrays due to differences in the polarization characteristics at each array. Signal-to-noise ratio is a dominant factor in phase identification using these methods. In the second report, Ryaboy compares the Helsinki and IMS bulletins for selected events between ARCESS and FINESA. The IMS empirical travel time curve for ARCESS fit data with known origin time and location better than the Helsinki empirical travel-time curve. This comparison could only be made outside of the Helsinki network, and therefore, is not conclusive.

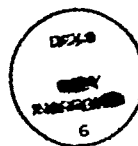
In the third section, data from the IRIS stations in the Soviet Union were analyzed. Three-component polarization characteristics were used to identify phases and to obtain estimates of backazimuth. These stations will soon be included in IMS processing and this research directly supports the useful addition of this data to the IMS. One of the most important conclusions of this work is that polarization characteristics are highly station dependent and similar studies must be made for any new station that is added to the system.

Hand digitized data of historical seismic records from Soviet stations were obtained in 1990. The fourth section gives preliminary results from an Lg-yield study conducted by Israelsson. In this study, the data quality are described and RMS Lg magnitudes are compared for a subset of the data. The stability of this measure is promising.

The last section of this report is a magnitude study of multiple event waveform simulations. Event sequences with shot delays between 0.1 and 2.0 seconds and similar magnitudes were studied. Both mb and RMS Lg measurements were made and compared to the actual shot sequence parameters. RMS Lg measurements gave the square-root of the sum of the squares of the individual measurements for all delays studied. At delays of two seconds or greater, multiple events could easily be distinguished from the P waveforms if the signal-to-noise ratio was good. For delays between 0.1 and 0.5 seconds, constructive and destructive interference of P-waves could alter the mb for narrow-band data. By examining several narrow bands, however, it was possible to obtain good estimates of the mb of the largest shot.

TABLE OF CONTENTS

List of Figures	iv
1.1 The Earth's Crust and Upper Mantle Structure and Attenuation Beneath IRIS Stations in the USSR	1-1
References	1-32
1.2 Lateral Inhomogeneities of the Upper Mantle Beneath Northern Eurasia Inferred from Pn-Wave Explosion Seismology Observations	1-38
References	1-62
2.1 Three-Component Analysis of Regional Phases at NORESS and ARCESS: Polarization and Phase Identification	2-1
References	2-31
2.2 Comparative Analysis of the Helsinki and IMS Bulletins for Selected Events along the ARCESS-FINESA Profile	2-33
References	2-45
3.1 Analysis of 3-Component Data from IRIS Stations in the USSR	3-1
References	3-38
4.1 Preliminary Results of Lg-Yield Studies from Analysis of Soviet Seismic Data	4-1
References	4-24
5.1 Multiple Event Waveform Simulations	5-1
References	5-23



Accession For	
NTIS GRA&I	<input checked="" type="checkbox"/>
DTIC TAB	<input type="checkbox"/>
Unannounced	<input type="checkbox"/>
Justification	
By	
Distribution/	
Availability Codes	
Dist	Avail and/or Special
A-1	

LIST OF FIGURES

Figure	Page
1.1-1 Geographical distribution of deep seismic studies in the USSR and neighboring countries.	1-3
1.1-2 Velocity section of the upper mantle for the Pamir-Baikal profile based on earthquake seismology data.	1-6
1.1-3 Location map of deep seismic profiles used in this study.	1-7
1.1-4 Seismic cross-section of the earth crust along the DSS profile from Klupiansk to Kineshma crossing central areas of the East-European platform.	1-8
1.1-5 Seismic velocity-section of the earth crust and upper mantle along the DSS profile crossing north-eastern areas of the East-European platform from Kineshma to Vorkuta.	1-9
1.1-6 Seismic cross-section of the earth crust along the west-east DSS profile from the eastern margin of the East-European platform to the Urals and to the West-Siberian platform.	1-11
1.1-7 Seismic cross-section of the earth crust along the south-north DSS profile crossing the Caucasus area and neighboring Scythian and East-European platform units from Nahichevan to Volgograd.	1-13
1.1-8 Seismic cross-section of the earth crust along the north-south DSS profile crossing the Himalayas, Pamirs and Tien-Shans from Srinagar (India) to Toktogul (USSR).	1-15
1.1-9 Results of study of the upper mantle velocity structure of the Tien-Shan region and neighboring areas of the Turanian platform by explosion seismology.	1-16
1.1-10 Results of studies of the earth crust and uppermost mantle of the Baikal rift zone by DSS.	1-17
1.1-11 Comparison of a velocity section of the earth crust and upper mantle with deep electromagnetic data for north-south DSS profile crossing the Siberian platform and Baikal rift zone from Dikson to Hilok.	1-18
1.1-12 Relationship between quality factor Q and velocity of P waves in the upper mantle.	1-25
1.1-13 Map of the quality factor Q in the lower subcrustal lithosphere beneath Central Asia.	1-27
1.1-14 Map of variations in the attenuation of shear waves in the upper mantle of the Tien-Shan and adjacent geological structures based on combined interpretation of Lg surface wave and its coda.	1-28

1.1-15	Seismic velocity-depth functions of the earth crust and upper mantle of major geological provinces of Northern Eurasia where the NORESS array and IRIS stations were installed.	1-29
1.2-1	The effect of lateral heterogeneities on upper mantle velocity sections.	1-40
1.2-2	A comparison of refracted wave ray paths.	1-41
1.2-3a-f	Pn wave seismic record sections constructed for long-range DSS profiles within major geological provinces of Northern Eurasia.	1-43
1.2-4	Averaged Pn wave amplitude versus distance variations for different geological provinces of Northern Eurasia.	1-49
1.2-5	Pn wave amplitude versus distance for the west-east Khanty-Mansiisk-Lena river long-range DSS profile.	1-50
1.2-6	Barnaul-Tura long-range DSS profile.	1-52
1.2-7	Results of studies of the upper mantle velocity structure beneath major geological provinces of Central Asia by explosion seismology.	1-53
1.2-8	Results of studies of the upper mantle velocity structure of Tien-Shan by explosion seismology.	1-55
1.2-9	Location map of long-range DSS profiles in Siberia.	1-56
1.2-10	Observed travel-time curves of Pn and P waves recorded along two long-range DSS profiles in Siberia.	1-57
1.2-11	A comparison of reversed Pn travel-time curves for long-range DSS profiles in Siberia.	1-59
1.2-12	Averaged travel-time curves of Pn waves for major geological provinces of Northern Eurasia.	1-60
2.1-1	Map of study area, Histograms of arrivals at NORESS and ARCESS.	2-4
2.1-2	Incidence angle plotted against 3-C SNR.	2-8
2.1-3	Incidence angle plotted against epicentral distance.	2-9
2.1-4	Azimuth residuals plotted against 3-C SNR.	2-11
2.1-5	Ratio of horizontal to vertical power plotted on a log scale versus epicentral distance.	2-14
2.1-6	The center frequency of the wide band used for polarization analysis plotted against epicentral distance.	2-15
2.1-7	Histograms of azimuth residuals.	2-18
2.1-8	Method for automated phase identification.	2-20
2.1-9	Plot of density of the discriminant scores for arrivals.	2-23

2.1-10	Histograms of the probability of membership in the P-type group.	2-24
2.1-11	Number of arrivals correctly and incorrectly identified.	2-25
2.2-1	Location map of selected events.	2-34
2.2-2	Probability density plots of differences between origin times, epicentral distances, and azimuths.	2-35
2.2-3	Pn travel-times for selected events based on POLAR DSS profile data.	2-41
2.2-4	Sn travel-times for the ARCESS-FINESA profile.	2-42
2.2-5	POLAR DSS profile.	2-43
3-1	Locations of the IRIS stations and DSS profiles used for this study.	3-4
3-2	Seismic velocity-depth curves of the earth crust and upper mantle near the IRIS stations.	3-6
3-3	Locations of the teleseismic events recorded at the IRIS stations.	3-8
3-4	Histograms of epicentral distance and backazimuth for events.	3-11
3-5	Schematic north-south cross-section of the upper crust under station GAR.	3-13
3-6	Plots of incidence angle as a function of event backazimuth for arrivals at GAR.	3-15
3-7	Discriminant plane showing the first and second discriminants separating three phase groups at GAR.	3-18
3-8	Discriminant plane plotted at ARU and KIV.	3-20
3-9	Predicted backazimuth vs. backazimuth residual for 148 teleseisms at GAR.	3-22
3-10	Locations of 27 regional events recorded at GAR.	3-24
3-11	Predicted backazimuth vs. backazimuth residual for 27 regional events at GAR.	3-25
3-12	Local magnitude as a function of distance from GAR for events reported in a local catalog.	3-26
3-13	Predicted backazimuth vs. backazimuth residual for 89 local events at GAR.	3-28
3-14	Predicted backazimuth vs. backazimuth residuals for 85 teleseisms recorded at ARU.	3-29
3-15	Typical particle motion of teleseismic P-waves at KIV and ARU.	3-31

3-16	Backazimuth deviation for 24 teleseisms recorded at KIV.	3-32
3-17	Backazimuth deviation for 23 teleseisms recorded at OBN.	3-34
4-1	Source to station paths for which data are available.	4-3
4-2	Relative location of explosions at the Semipalatinsk test range.	4-4
4-3	Explosion depth as a function of explosion yield.	4-7
4-4	Seismogram section with a typical record for each path plotted as a function of epicentral distance.	4-8
4-5	Typical amplitude response curves for the instruments at the stations.	4-10
4-6	Standard deviation of the instrument magnifications for stations BOD, NRI, and OBN for similar response curves in the period 1965-1988.	4-11
4-7	Vertical component recordings of the JVE explosion on Sep. 14, 1988, at IRIS stations and USSR station at ARTI.	4-12
4-8	Comparison of instrument response, noise, P-wave, and Lg spectra.	4-13
4-9	Panels with P-waves and Lg-waves recorded at ARU.	4-14
4-10a-e	Lg waves at USSR stations ARU, BOD, NRI, NVS, and OBN from explosions at the Semipalatinsk test range.	4-16
4-11	Comparison of Lg RMS magnitudes for common events at stations ARU, BOD, NRI, and OBN.	4-21
4-12	Comparison of Lg RMS magnitudes and yields of explosions at the Semipalatinsk test range at stations ARU, BOD, NRI, and OBN.	4-22
5-1	Location of the Balapan test site, ARU, ARCESS and NORESS arrays, and some stations of the Chinese Digital Seismic Network.	5-3
5-2	Regional data recorded at ARU.	5-5
5-3	Case 1: A 35 kt shot followed by a 40 kt shot.	5-7
5-4	Case 2: A 35 kt shot followed by a 125 kt shot.	5-8
5-5	Case 3: A 5 kt shot followed by a 35 kt shot.	5-9
5-6	Case 4: A 5 kt shot followed by a 125 kt shot.	5-10
5-7	Case 1: A 35 kt shot followed by a 40 kt shot.	5-11
5-8	Case 2: A 35 kt shot followed by a 125 kt shot.	5-12
5-9	Case 5: A 20 kt shot followed by a 45 kt shot.	5-13
5-10	Case 6: A 35 kt shot followed by a 35 kt shot.	5-14

5-11	ARCESS unfiltered data for cases 5 and 6.	5-16
5-12	Normalized yield versus delay time for cases 5 and 6 at ARCESS.	5-17
5-13	NORESS unfiltered high frequency data for case 5 at delays between 0.0 and 0.5 seconds inclusive.	5-19
5-14	Normalized yield versus delay time for case 5 for NORESS high frequency data.	5-20
5-15	Normalized yield versus delay time for case 5 for NORESS high frequency data.	5-21

1.1 THE EARTH'S CRUST AND UPPER MANTLE STRUCTURE AND ATTENUATION BENEATH IRIS STATIONS IN THE USSR

Abstract

Scientific papers and books published in the USSR on crust and upper-mantle velocity and Q-structure in the regions containing each of the five IRIS (Incorporated Research Institutions for Seismology) seismic stations have been analyzed. Three stations are located in the European part of the USSR; near Obninsk (OBN), Arti (ARU), and Kislovodsk (KIV). A fourth station is in Central Asia not far from Garm (GAR) in the Southern Tien-Shan Mountains, and a fifth at Irkutsk (IRK) near the border of the Siberian platform and the Baikal rift zone. With the exception of OBN, these stations were installed very close to the boundaries of major geological provinces having substantially different deep structure. These factors create complicated conditions for seismologists analyzing records of seismic events.

Averaged velocity sections showing the change in P-wave velocity with depth in the earth crust and upper mantle have been constructed on the basis of the most reliable results obtained from deep seismic soundings (DSS) for areas containing the five IRIS stations and the NORESS array. Tectonically active regions where the GAR (Southern Tien-Shan) and IRK (Baikal rift zone) stations were installed are generally distinguished from the East-European (NORESS array, OBN and ARU) and Scythian (KIV) platforms by lower velocities and the presence of very pronounced and thick low-velocity layers in the upper mantle. Low-velocity layers also exist in the upper mantle beneath the platforms but they are thinner and not so pronounced.

Values of the quality factor, Q , for the earth crust and upper mantle up to depths of 200-250 km vary both with depth and laterally in the range from approximately 50 to 800. A direct statistical correlation is observed between values for the velocities of seismic waves and Q . Seismic waves recorded by the IRIS stations propagate in substantially laterally inhomogeneous media, but analysis and interpretation of records of seismic events are usually based on one-dimensional velocity and Q models.

1.1.1 Introduction

Under an agreement with the Soviet Academy of Sciences, IRIS installed five seismic stations (IRIS, 1989) within the USSR (*Table 1*). Three stations are located in the European part of the USSR, one near Obninsk (OBN), a second in Arti (ARU), and a third near Kislovodsk (KIV). Stations OBN and ARU are situated in the central and eastern areas of the ancient Precambrian East-European platform, the KIV station is on the young Paleozoic Scythian platform at its border with the Greater Caucasus. A fourth station is placed, in Central Asia, near Garm (GAR) in the Southern Tien-Shan

Mountains, and a fifth not far from Irkutsk (IRK), at the border of the Precambrian Siberian platform and the Baikal rift zone.

Table 1.				
IRIS SEISMIC STATIONS in the USSR				
No.	Location	Latitude (deg.)	Longitude (deg.)	Elevation (m)
1.	Arti (Cis-Urals foredeep)	56.40N	58.60E	250
2.	Garm (South Tien-Shan)	39.00N	70.32E	1300
3.	Irkutsk (Talaya) (Baikal rift zone)	51.68N	103.64E	327
4.	Kislovodsk (Cis-Caucasus foredeep)	43.95N	42.68E	1206
5.	Obninsk (Moscow syncline)	55.10N	36.60E	'30

With the exception of OBN, these stations stand near the boundaries of major geological provinces having substantially different geological history and deep structure. These factors create complex conditions for seismologists analyzing records of seismic events.

During the past two decades, remarkable changes have occurred in Soviet seismology. Recognized internationally as one of the leaders in the study of the structure of the crust and upper mantle, the USSR has substantial achievements in spite of the fact that the country lags behind the West with respect to the technical level of conducting deep seismic investigations. The program for studying crust and upper-mantle structure on long-range deep seismic sounding (LSS) profiles is largely responsible for Soviet success in seismology. An important element of this program is the use of large industrial (including nuclear) explosions for generating seismic waves.

A map illustrating the geographical distribution of previous deep seismic studies in the Soviet Union up to the mid-1980s is presented in *Figure 1*. The

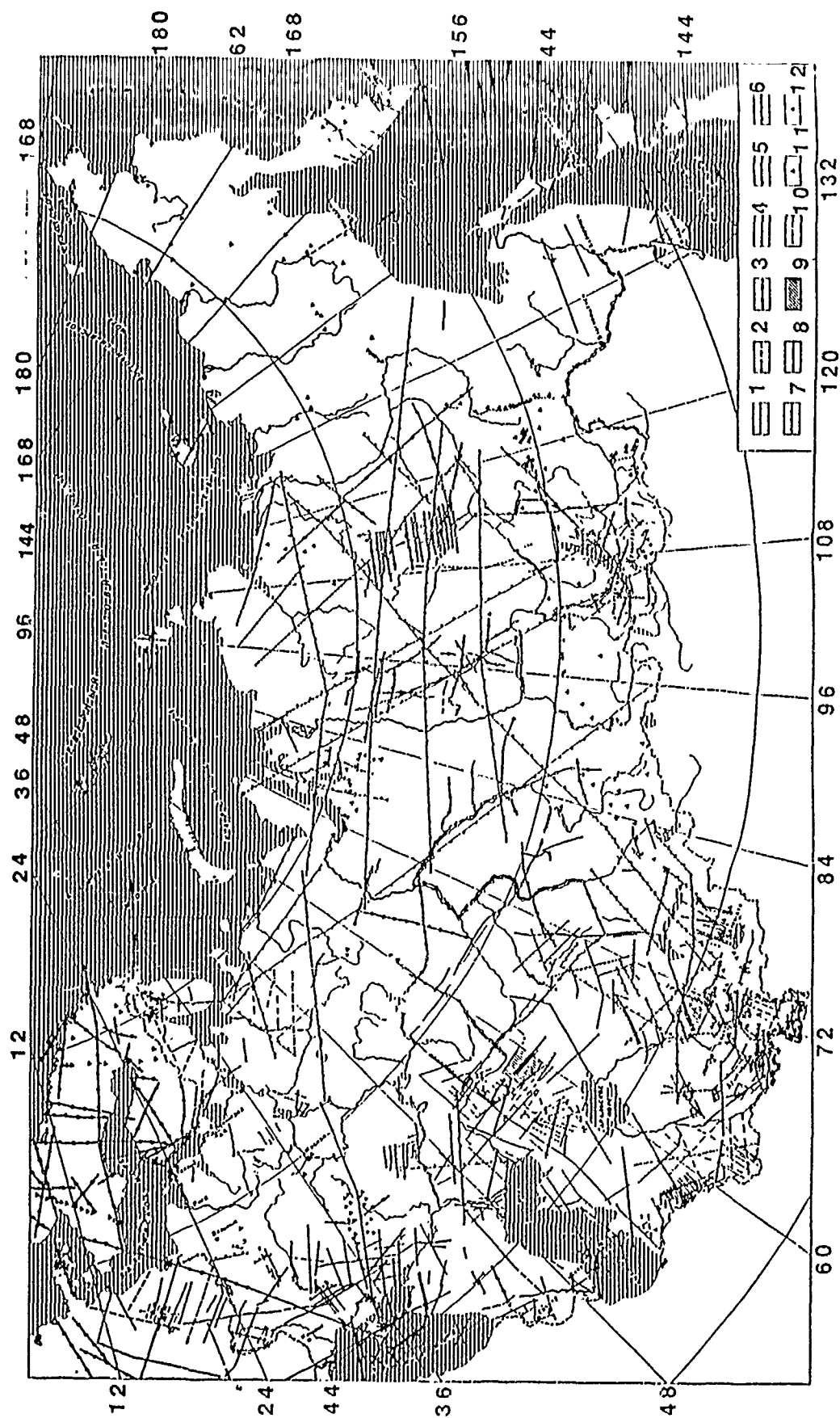


Figure 1. Geographical distribution of deep seismic studies in the USSR and neighbouring countries. 1-12 -- different kind of techniques used in crustal and upper mantle studies based on recording of explosions and earthquakes. 1 -- deep seismic sounding (DSS) on long profiles with continuous observation; 2 -- DSS on long profiles with segmented observations; 3 -- DSS on local profiles - dry land; 4 -- DSS on local profiles - marine; 5 -- DSS on long-range profiles using "large industrial (nuclear) explosions"; 6 -- DSS combined with converted wave method (CWM) using earthquakes and "large industrial explosions"; 7 -- DSS/CWM using earthquakes; 8, 9 -- CWM using local profiles (8) and areal observations (9); 10 -- correlation method for refracted waves (CMRW); 11, 12 -- point determinations of depth to Moho from observations of industrial explosions (11) and earthquakes (12). Adapted from Razinkova, Krasnopevtseva et al., 1987.

techniques used in crustal and upper mantle studies have been divided into twelve major classifications on the basis of the variations of methods of field observations for dry land and sea (the detail of the study), of the generation of seismic signals (earthquakes, explosions), and of the physical nature of recorded seismic waves (pre- and post-critical reflected, refracted and converted waves).

A variety of standard techniques were applied to acquire these data, to study of the crust and upper mantle, including:

- (1) The standard Deep Seismic Sounding (DSS) method based on observations of reflected and refracted waves. Profiles of up to 200-400 km length map the crustal structure and long-range profiles with lengths of up to 2000-4000 km that use large industrial (including nuclear) explosions as sources to probe into the upper mantle.
- (2) The Converted Wave Method is an extension of the DSS method in which various converted phases (boundary conversions of P to S) are mainly used to study the earth crust and upper mantle structure.
- (3) The Correlation Method for Refracted Waves uses densely spaced observations to track refracted wave arrivals on profiles with lengths of up to approximately 100-150 km. In this method, the primary emphasis is on determining velocities and geometry for the layers and boundaries in the earth crust and Moho
- (4) Mapping of the thickness of the earth crust using data from isolated observations of earthquakes or explosions.

The results obtained by various methods differ significantly in precision and detail. Investigations based on combinations of two or more methods were carried out frequently. To date, the most reliable information about the earth crust and upper mantle structure is produced by the DSS method using large industrial (including nuclear) explosions and based on recordings of deep refracted and reflected waves. This method is the most precise (and costly) because it utilizes a highly detailed system of field observations via explosions along reversed and overlapping profiles.

The findings were published, mainly in Russian, in hundreds of papers and dozens of monographs. Such an extensive database permits detailed analysis of crust and upper mantle structure for different geological provinces in Northern Eurasia. But it is worthwhile stressing that this database is very complicated and uneven. The published results of deep seismic studies are frequently incompatible, because they are based on different methods of field observations and interpretation of seismic records. So it is not a trivial problem to extract specific information from the mentioned database and estimate its reliability. This paper summarizes published Soviet work on crust and upper-mantle structure in the regions containing each of the IRIS stations, and presents average structural models for use in analyzing data from the stations.

1.1.2 Velocity structure

Deep seismic studies in the USSR indicate significant lateral and vertical heterogeneities in the structure of the crust and upper mantle (Borisov, 1967; Belyaevsky, 1974; Vol'vovskii and Vol'vovskii, 1975; Ryaboy, 1977, 1979, 1985, 1989). These are manifested through anomalies in travel times, amplitudes, and frequency content. In crossing from one geological structure to another, changes typically occur in both the velocities of seismic waves and the character of their distribution with depth. For this reason, we have limited our extrapolation of the results of deep seismic investigations to just those geological units in which the IRIS stations are located.

Figure 2 presents the two-dimensional velocity section of the upper mantle from the Pamirs to the Baikal rift zone, constructed more than 15 years ago and based on the interpretation of traveltimes of P-waves from earthquakes (Alekseev *et al.*, 1973). This profile connects the two IRIS stations GAR and IRK, respectively in the South Tien Shan and the Baikal rift zone. One can see that a pronounced low velocity layer in the upper mantle did not extend the length of the profile, but only beneath the Pamirs, Tien Shan and Baikal rift zone. More detailed and precise results have been obtained since the original work was published based on deep seismic soundings (DSS) along long-range explosion profiles. To characterize crust and upper-mantle structure beneath the major geological units where IRIS stations were installed we used the most accurate DSS data available (*Figure 3*).

Obninsk (OBN)

Station OBN was installed within the Precambrian East-European platform, which is one of the largest geological provinces of the territory of the USSR. This station is located in the Moscow syncline (central area of the platform). The ancient Voronezh shield lies to the south and southwest of OBN. A super long-range DSS profile crossing the European part of the territory of the USSR from south to north (from the Black sea to Polar Urals) is located approximately 250 km east of OBN (*Figure 3*). Along the northern part of this profile field observations were based on recordings of nuclear explosions, and the velocity structure of the crust and upper mantle was studied to depths 200-250 km.

This region is a typical ancient platform, with sedimentary layer thickness between 2 and 3 km and Moho depths on the average of 43-45 km (*Figure 4 and Figure 5*). Pn velocities are high, up to 8.3-8.4 km/s. An interesting feature of the upper mantle beneath the Moscow syncline is a low-velocity layer detected in the depth range of approximately 60-90 km. The crust and upper mantle parameters (e.g., velocity and depth to the main structural boundaries) vary slowly beneath the Moscow syncline in a lateral direction. However, velocities in the uppermost mantle were found to decrease at the boundary between the Moscow and Pechora

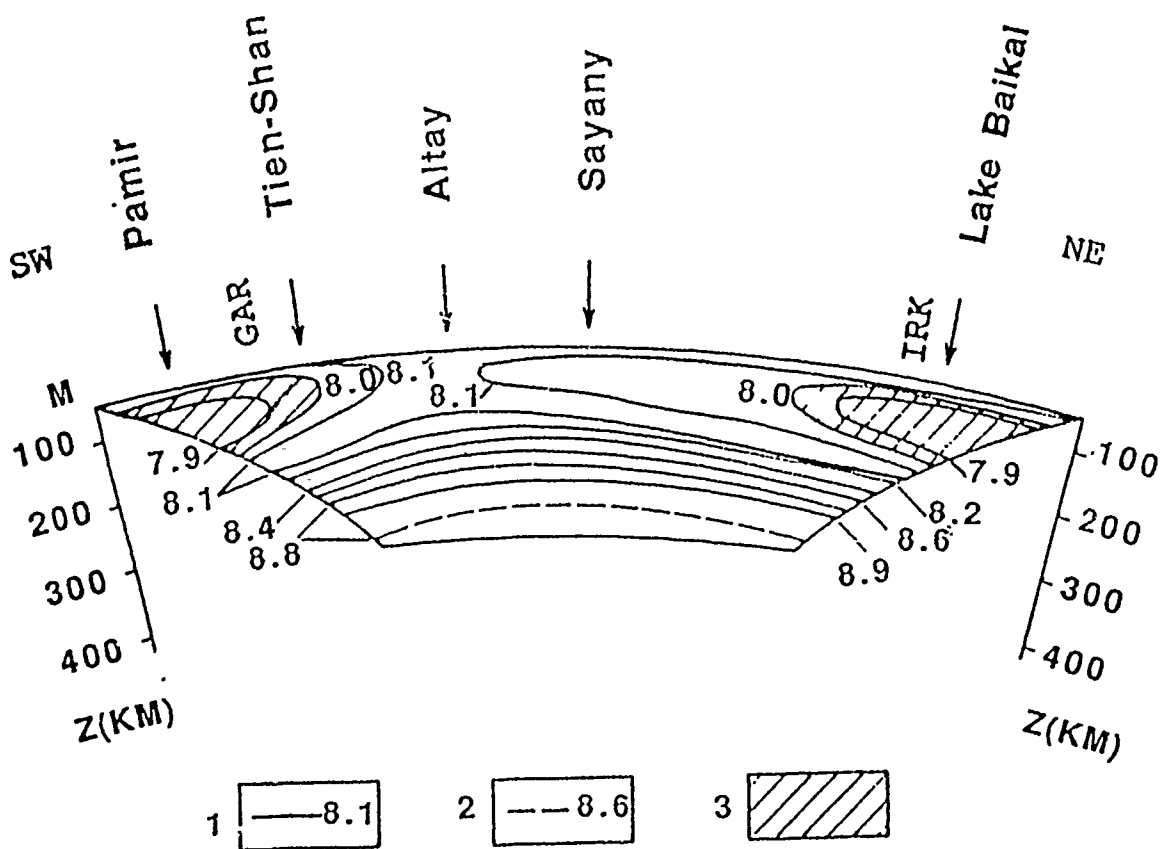


Figure 2. Velocity section of the upper mantle for the Pamir-Baikal profile based on earthquake seismology data. 1, 2 -- lines of isovelocities (km/s) according to reliable (1) and unreliable (2) data, 3 -- low velocity layer, M -- flattened Moho discontinuity, GAR and IRK -- approximate projection on the profile of the IRIS seismological stations installed in Garm (GAR) and Irkutsk (IRK). Adapted from Alekseev et al., 1973.

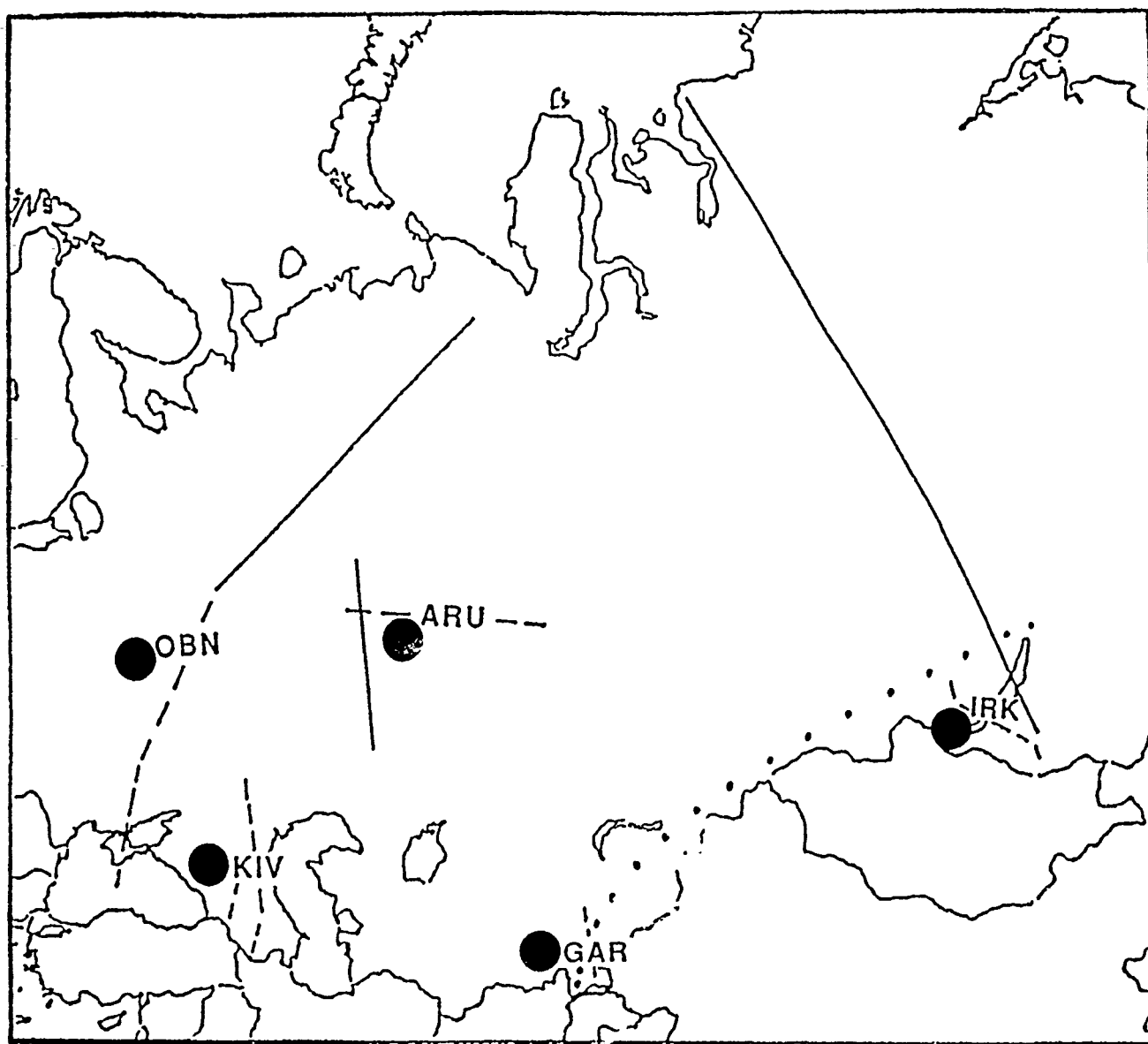


Figure 3. Location map of deep seismic profiles used in this study. Solid lines -- DSS of the earth crust and upper mantle on long-range profiles using "large industrial (nuclear) explosions", dashed lines -- DSS of the earth crust using chemical explosions, dotted line -- Pamir-Baikal profile based on earthquake seismology data. OBN, ARU, KIV, GAR, IRK - IRIS seismological stations installed within the territory of the USSR.

VORONEZH SHIELD

MOSCOW SYNECLISE

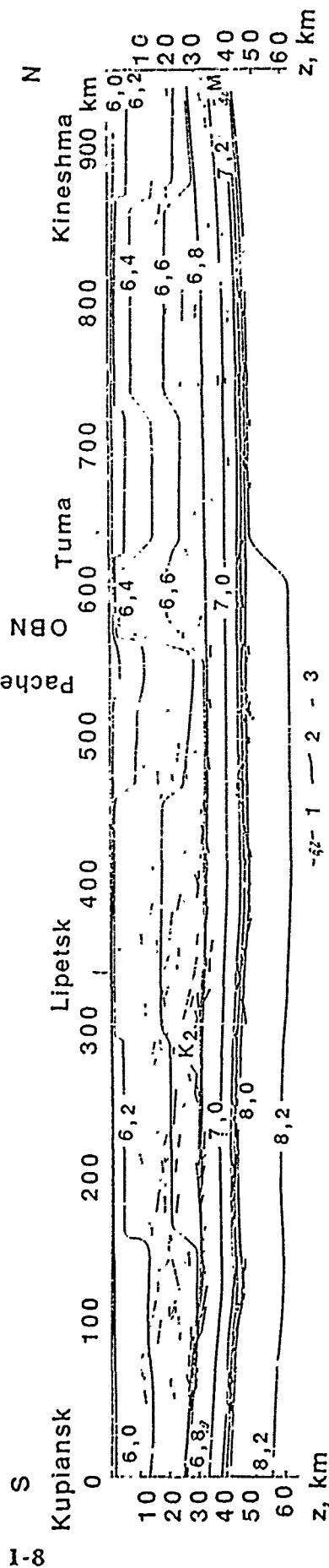


Figure 4. Seismic cross-section of the earth crust along the DSS profile from Kupiansk to Kineshma crossing central areas of the East-European platform. 1 -- lines of isovelocities in the earth crust and uppermost mantle (km/s); 2, 3 -- reflected boundaries based on reliable (2) and unreliable (3) data; OBN -- projection on the profile of the IRIS seismological station installed in Obninsk (approximately 250 km to the west of the profile). Adapted from Yurov, 1980.

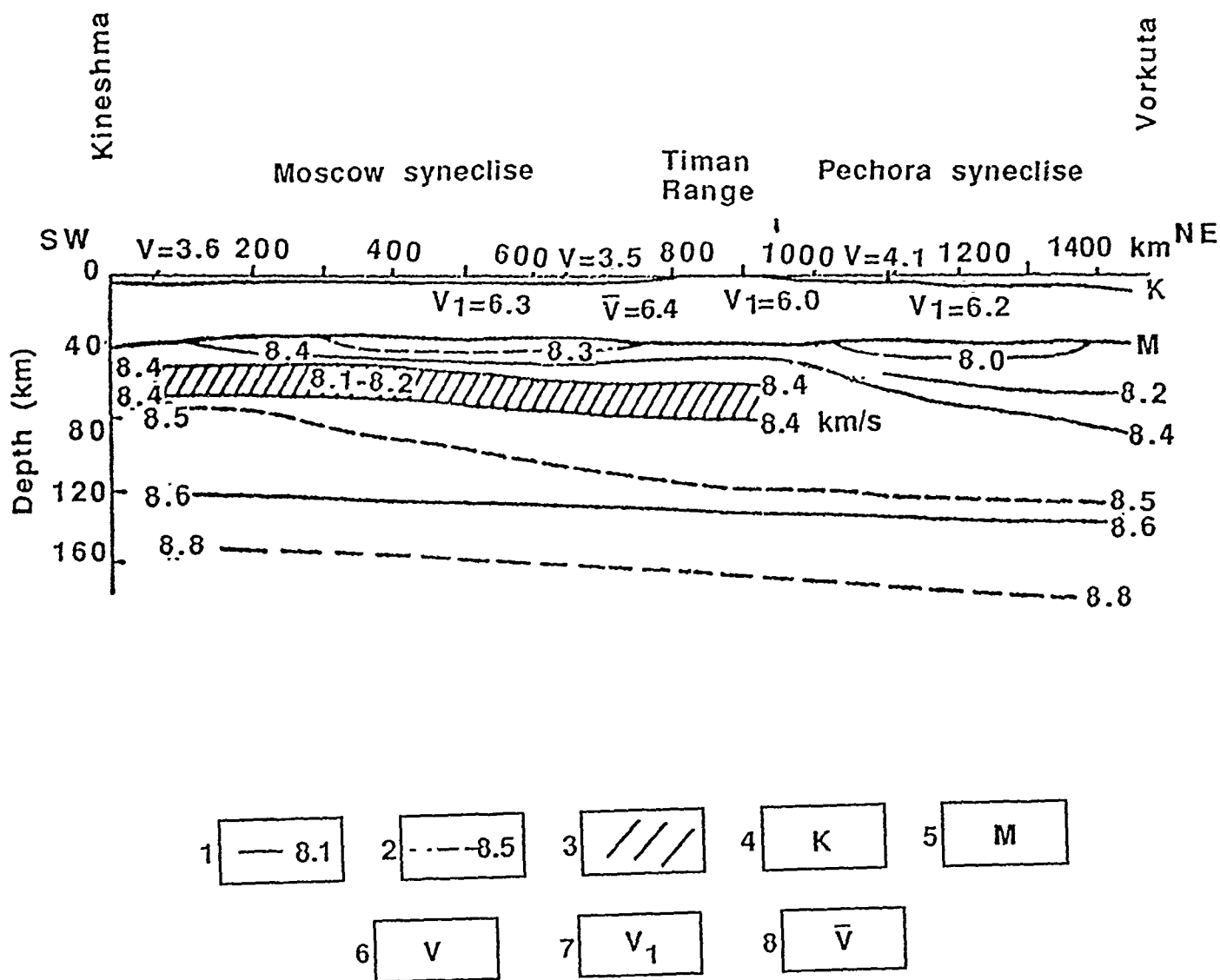


Figure 5. Seismic velocity-section of the earth crust and upper mantle along the DSS profile crossing north-eastern areas of the East European platform from Kineshma to Vorkuta. 1, 2 -- lines of isovelocities in the upper mantle (km/s) according to reliable (1) and unreliable (2) data, 3 -- low velocity layer, 4 -- basement surface, 5 -- Moho boundary; 6 -- mean velocity in the sedimentary layer, 7 -- velocity beneath the basement surface, 8 -- mean velocity in the layer between basement surface and Moho boundary. Values of velocity are given in km/s. Adapted from Ryaboy, 1979; Belyaevsky et al., 1976.

synclises, which is accompanied by an increase in sedimentary layer thickness to 5-8 km (*Figure 5*).

The sedimentary layer of the East-European platform consists mainly of carbonate rocks and is characterized by high values of mean velocity and density (up to 3.5-4.5 km/s and 2.50-2.55 g/cc respectively). A narrow and deep depression of crustal basement (Pachelmsky aulacogen) is located approximately 100 km to the south-east of OBN (Belyaevsky, 1974). This depression is traced to the south-east approximately 700-800 km to the North Caspian depression. The sedimentary layer of the Pachelmsky aulacogen is 4-5 km. thicker than under other areas of the Moscow syncline.

Arti (ARU)

Station ARU is located at the eastern margin of the East-European platform, in the Cis-Urals foredeep. ARU is near an important geological boundary between the platform and Late Paleozoic folding units of the Urals. The Urals originated from the Precambrian basement. The boundary separates regions with substantially different crust and upper mantle structure. Paleozoic platforms (West-Siberian and Turanian) adjoin to the eastern and southern borders of the Urals.

Earth crust and upper mantle velocity structure beneath the Urals and neighbouring areas of the East-European, West-Siberian and Turanian platforms was investigated along a number of DSS profiles (*Figure 1*). In the area of ARU, a detailed study of the earth crust was carried out along the east-west DSS profile from the eastern margin of the East-European platform through the Urals (at the latitude of Sverdlovsk) to the West Siberian platform. In addition, an investigation of upper-mantle structure to depths of 100-150 km was conducted along a north-south DSS profile (*Figure 3*).

The sedimentary layer thickness of the Volgo-Ural antecline and Cis-Urals foredeep is up to 5-10 km; is thicker than the Moscow syncline. This layer is approximately 6-8 km thick beneath ARU and is characterized by high mean velocities (up to 4.5 km/s) because of the influence of carbonate rocks that are widely distributed in the middle part of the geological section. Moho depths in this area are 43-45 km increasing beneath the Urals to 50 km (*Figure 6*). A low velocity layer in the lower part of the earth crust was located at approximately 25-35 km depth (Razinkova *et al.*, 1987). When crossing the boundary with the Urals, one can see basement rocks on the surface and a decrease in Pn velocity from 8.3-8.4 to 7.9-7.9 km/s. In the upper mantle of the Volgo-Ural antecline a low velocity layer similar to the layer beneath the Moscow syncline was detected at depths between 70-100 km.

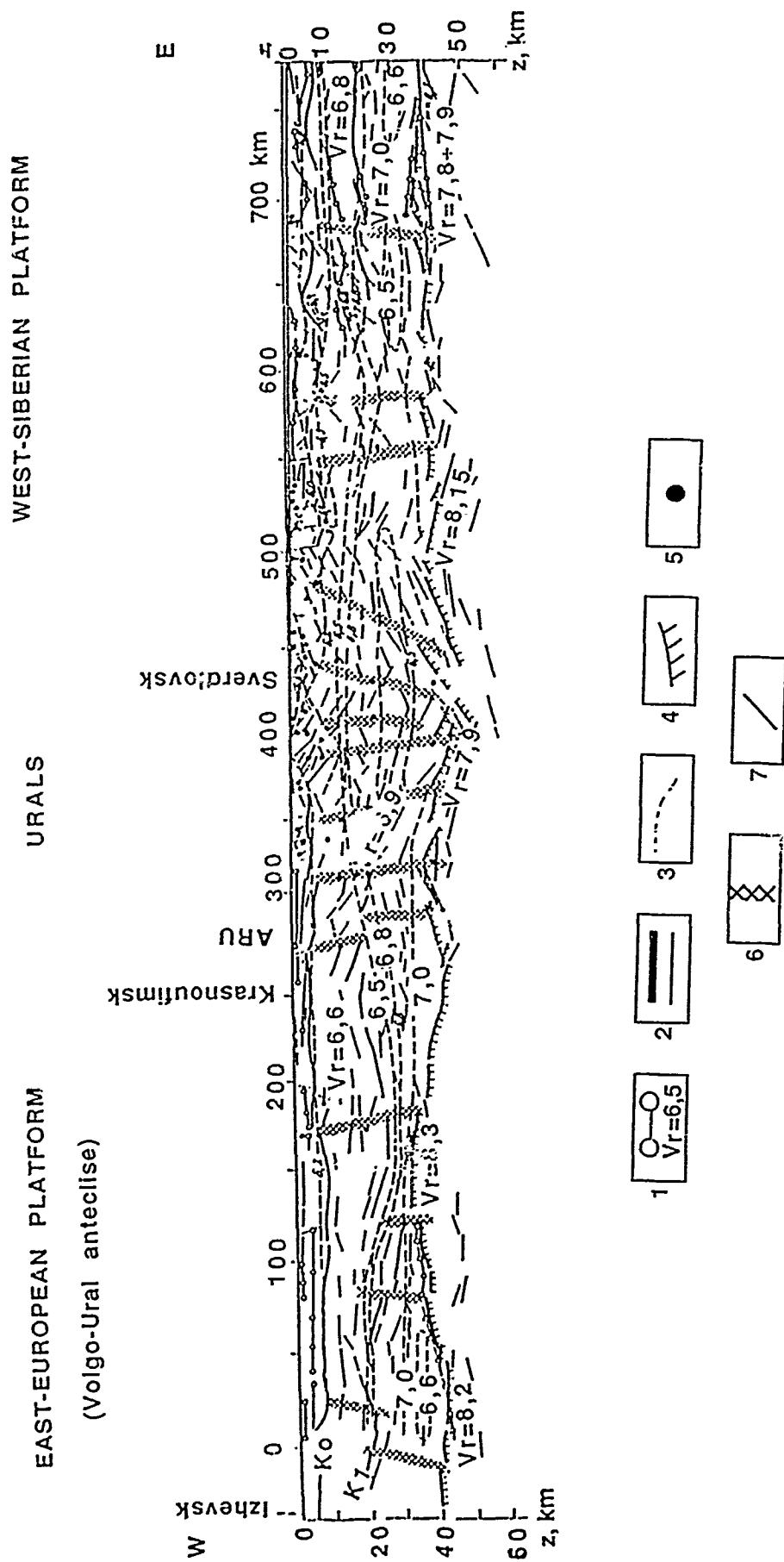


Figure 6. Seismic cross-section of the earth crust along the west-east DSS profile from the eastern margin of the East-European platform to the Urals (in the latitude of Sverdlovsk) and to the West-Siberian platform. 1 -- boundaries constructed according to refracted waves data and velocities (in km/s) beneath these boundaries; 2 -- boundaries constructed according to intensive (thick lines) and weak (thin lines) reflected waves; 3 -- lines of isovelocities (in km/s); 4 -- Moho and I_n velocity boundary; 5 -- points of diffraction; 6 -- supposed deep fault. -- faults according to geological and seismic data; ARU -- IRIS seismological station installed in Artii (foredeep of Urals). Adapted from Chalevin, Druzhinin et al., 1980.

Kislovodsk (KIV)

Station KIV is located at the southern margin of the Paleozoic Scythian platform in the Cis-Caucasus foredeep. This station is near the geological boundary between the platform and Alpine folding units of the Caucasus. These two geological provinces also have substantially different deep structure. A detailed study of the earth crust was carried out along north-south and west-east DSS profiles (*Figure 1*). Two profiles, Stepnoe-Bakuriani and Volgograd-Nahichevan, are not far from KIV. Field observations on the latter of the two extend to approximately 1000 km and were very detailed (*Figure 7*). The KIV station was installed approximately 150 km west of the Volgograd-Nahichevan profile.

The thickness of the earth crust beneath the Scythian platform and Cis-Caucasus foredeep is 43-45 km but beneath the Caucasus it thickens to 50-55 km. There is a pronounced boundary between the upper (thickness 25-30 km, velocity 5.8-6.5 km/s) and lower (thickness 10-15 km, velocity 7.0 km/s and more) crust. Usually, crustal boundaries beneath the Caucasus are not as pronounced as beneath the Scythian platform. Low velocity layers were detected in the earth crust, and these layers are thicker and more pronounced for the Caucasus, especially for the Lesser Caucasus (Alekseev *et al.*, 1973; Razinkova *et al.*, 1987). The crust of the Scythian platform (including the area of KIV) is characterized by lower velocities than the Greater Caucasus and East-European platform. A sedimentary layer beneath the Scythian platform and Cis-Caucasus foredeep is approximately 5-6 km thick and consists mainly of terrigenous rocks with mean compressional velocities between 2.5-3.5 km/s. Pn velocities for southern areas of the Scythian platform are 8.2-8.3 km/s, decreasing beneath the Caucasus to 8.0-8.1 km/s on average.

We do not have any data about the velocity structure of the upper mantle beneath the Scythian platform. Findings from studies of the upper mantle structure under the Caucasus were obtained mainly from interpretations of the P-wave travel-time curves from earthquakes (Azbel and Kondorskaya, 1974; Murusidze, 1987). Velocity sections constructed from the data show that velocity in the upper mantle increases with depth from 7.8-8.0 km/s in the uppermost mantle to 8.6-8.8 km/s at depths of 350-380 km. Two sharp velocity increases were detected at depths of 100-110 and 350-388 km. Analysis of P-wave travel-times from teleseismic earthquakes showed that the upper mantle in the western Caucasus is characterized by smaller velocities than areas to the east (Vinnik, 1976).

Garm (GAR)

Station GAR was installed in Central Asia, in the southern Tien-Shan Mountains. This region has a very complicated geological structure. The highest mountains in the USSR (Pamirs, Tien-Shans) have elevations up to 6-7 km and border on deep depressions (Fergana, South Tadzhik) where the sedimentary layer thickness

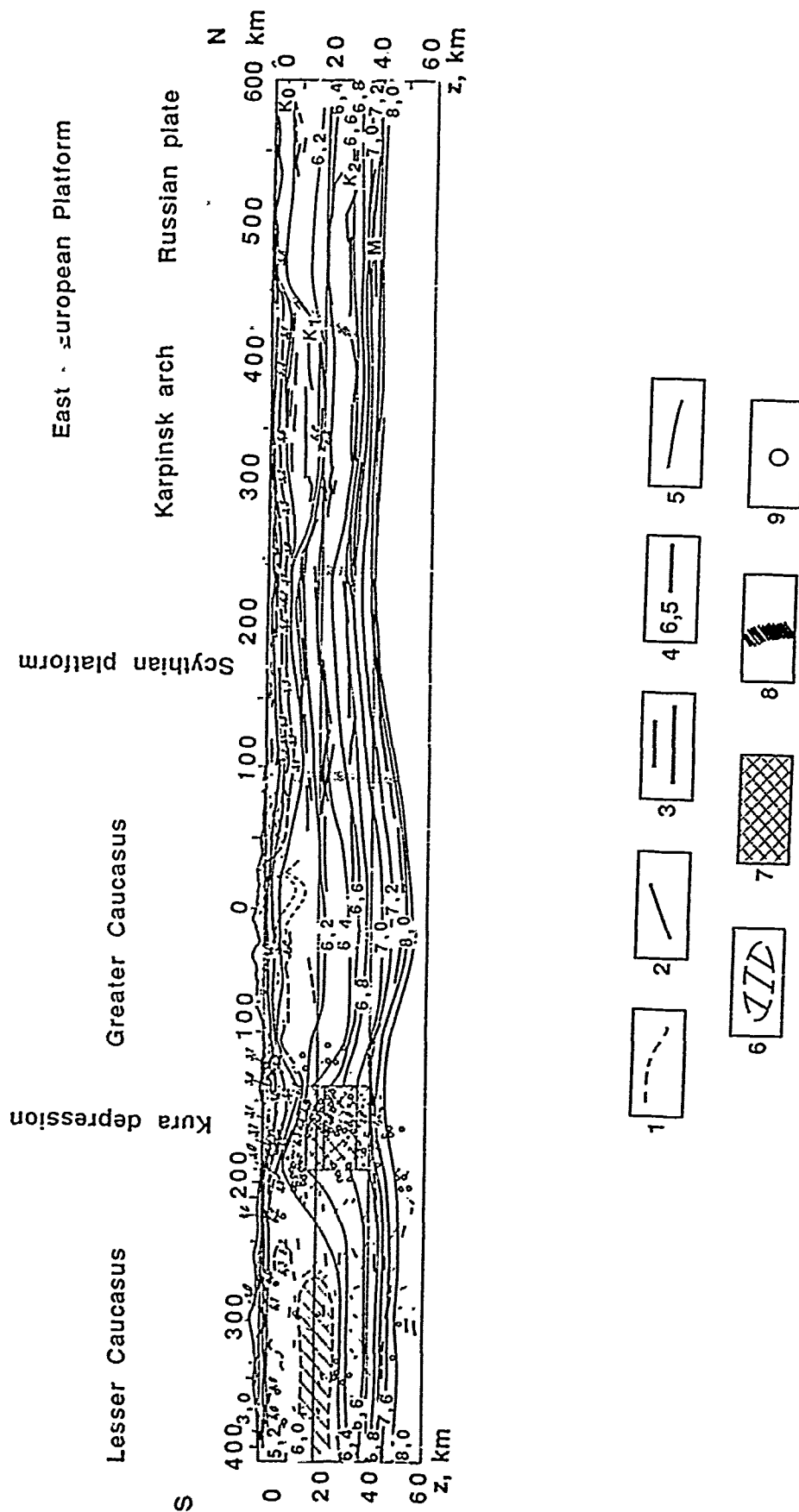


Figure 7. Seismic cross-section of the earth crust along the south-north DSS profile crossing the Caucasus area and neighbouring Scythian and East-European platform units from Nahichevan to Volgograd. 1 -- boundaries in the upper part of the earth crust according to geological data; 2 -- fractures according to geological data; 3 -- seismic boundaries according to reliable (solid lines) and unreliable (dashed lines) reflected waves data; 4 -- seismic boundaries according to refracted waves data and velocities beneath the boundaries (in km/s); 5 -- lines of isovelocity (in km/s); 6 and 7 -- zones of low (6) and high (7) velocities; 8 -- faults according to seismic data; 9 -- points of diffraction. KIV -- IRIS seismological station installed in the area of Kislovodsk (foredeep of Caucasus), approximately 150 km to the west of the profile. Adapted from Baranova, Krasnopevtseva et al., 1980.

reaches 8-10 km and more. The tectonically active area is contiguous with the Paleozoic Turanian platform to the north. Numerous studies of the earth crust and upper mantle structure were carried out in this region based on earthquake (local, far-regional and teleseismic) and explosion recordings. However, the most accurate results were obtained using explosion seismology along DSS profiles. The first DSS observations were carried out in Central Asia at the beginning of the fifties under the supervision of G. A. Gamburtsev.

An important contribution to studies of the earth crust and upper mantle of Central Asia was made in 1974-1984 during the International Pamir-Himalayas project (USSR, India, Pakistan, Italy) (Belousov *et al.*, 1984). The critical link of this project was a north-south DSS profile crossing the Himalayas, Pamirs and Tien-Shans from Srinagar (India) to Toktogul (USSR). The length of this profile is more than 1000 km, and station GAR is located approximately 250 km to the west of it.

Figure 8 shows a seismic section of the earth crust between the USSR and India. The Moho depths vary along the profile from 65-75 km beneath the southern Tien-Shans, Pamirs, and Karokoram range up to 40-50 km towards the Turanian platform and platform areas of India. Beneath the Fergana depression (the northern part of the profile) the sedimentary layer thickness is 8-10 km and the Moho depth is 45-50 km. The consolidated crust can be divided into upper and lower parts. A crustal low velocity layer beneath the southern Tien-Shan in the GAR area was detected based on the analysis of DSS and earthquake data at depth ranges of 10-21 and 12-24 km, respectively (Alekseev *et al.*, 1973; Razinkova *et al.*, 1987). The values of velocity in this layer vary from 5.6 to 6.0 km/s.

Analysis of travel times of Pn waves recorded from large industrial (including nuclear) explosions and DSS data showed that there is a very substantial difference in the upper mantle velocity structure beneath the Tien-Shan and neighboring areas of the Turanian platform. A very pronounced low velocity layer is located between 100 and 200 km below the Tien-Shan, but a similar layer probably does not exist beneath the Turanian platform (*Figure 9*). Findings for different geological units of the Tien-Shan showed (Burmakov *et al.*, 1984) that areas located west of the Talas-Fergana deep fault (TFF) (Hercynian folding) are characterized by substantially larger (up to 0.5 km/s) velocities in the upper mantle than areas located to the east (Caledonian folding) of the TFF (*Figure 9*).

Irkutsk (IRK)

Station IRK was installed near the boundary of the Baikal rift zone and the Siberian platform. Numerous studies of the crust and upper mantle velocity structure were carried out in this region using earthquake and DSS recordings. The most detailed and reliable results were also obtained by explosion seismology. *Figure 10* and *Figure 11* show findings based on DSS data.

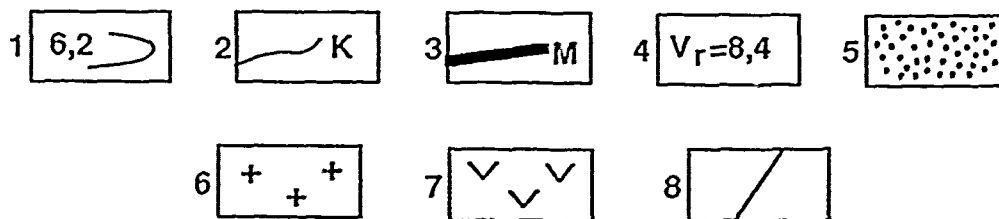
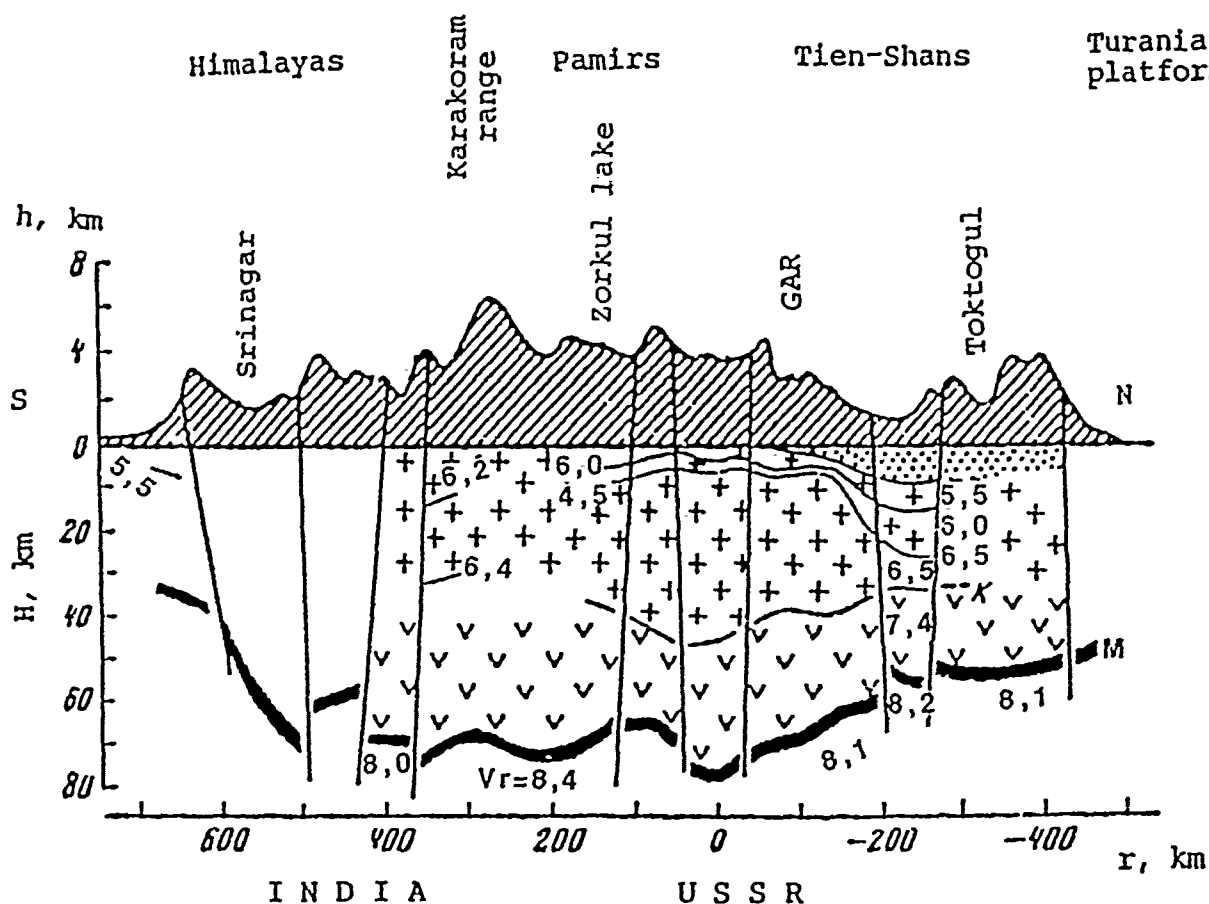


Figure 8. Seismic cross section of the earth crust along the north-south DSS profile crossing the Himalayas, Pamirs and Tien Shans from Srinagar (India) to Toktogul (USSR). 1 -- lines of isovelocities (in km/s). 2 -- a "basaltic" layer surface. 3 -- Moho boundary. 4 -- Pn velocity (in km/s). 5 -- sedimentary layer. 6 -- "granitic" layer. 7 -- "basaltic" layer. 8 -- deep faults. GAR -- IRIS seismological station installed in the area of Garm (southern Tien-Shans), approximately 250 km to the west of the profile. Adapted from Belousov, Vol'vovskii et al., 1984.

Location Map of Shot Points (SP)
Recording Stations and DSS Profiles

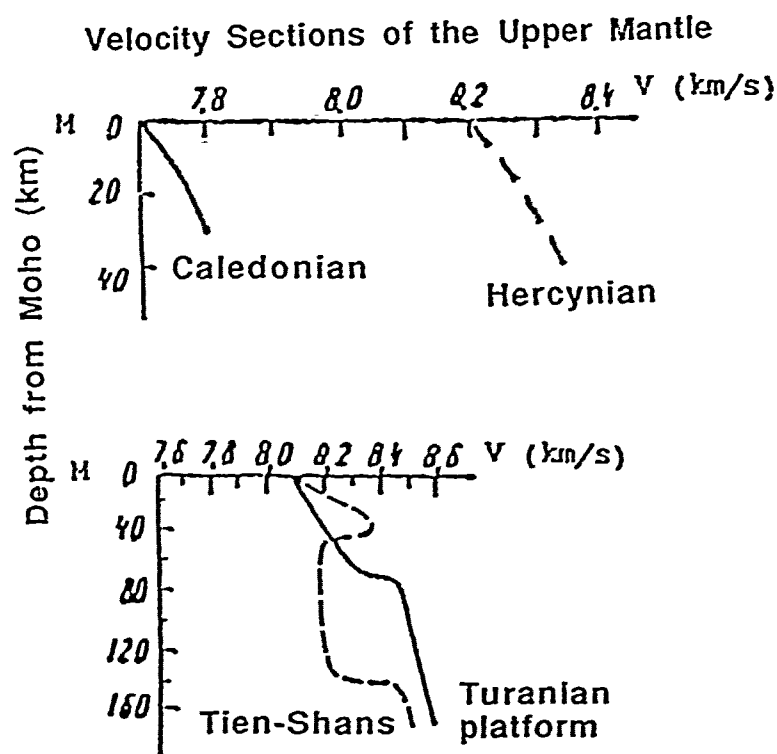
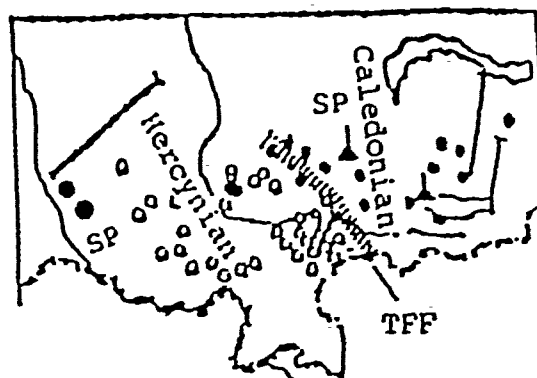


Figure 9. Results of study of the upper mantle velocity structure of the Tien Shan region and neighbouring areas of the Turanian platform by explosion seismology. Top - location map of shot points (SP) (large filled circles and triangles), recording stations (small opened and filled circles), and DSS profiles (solid lines), middle - velocity sections of the upper mantle of the Tien Shan areas to the west (Hercynian) and east (Caledonian) of the Talas Fergana deep fault (TFF), bottom - velocity sections of the upper mantle of the Tien-Shans and neighbouring areas of the Turanian platform, M - Moho boundary. Adapted from Burmakov, Vinnik et al., 1984.

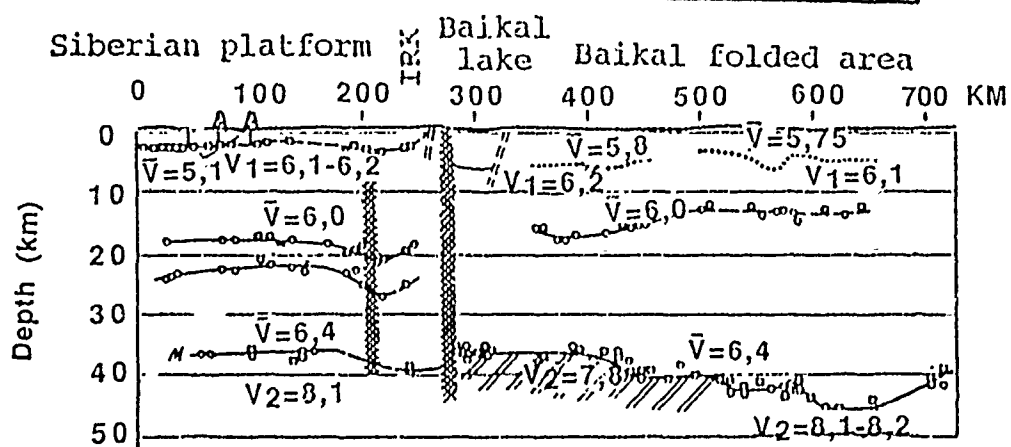
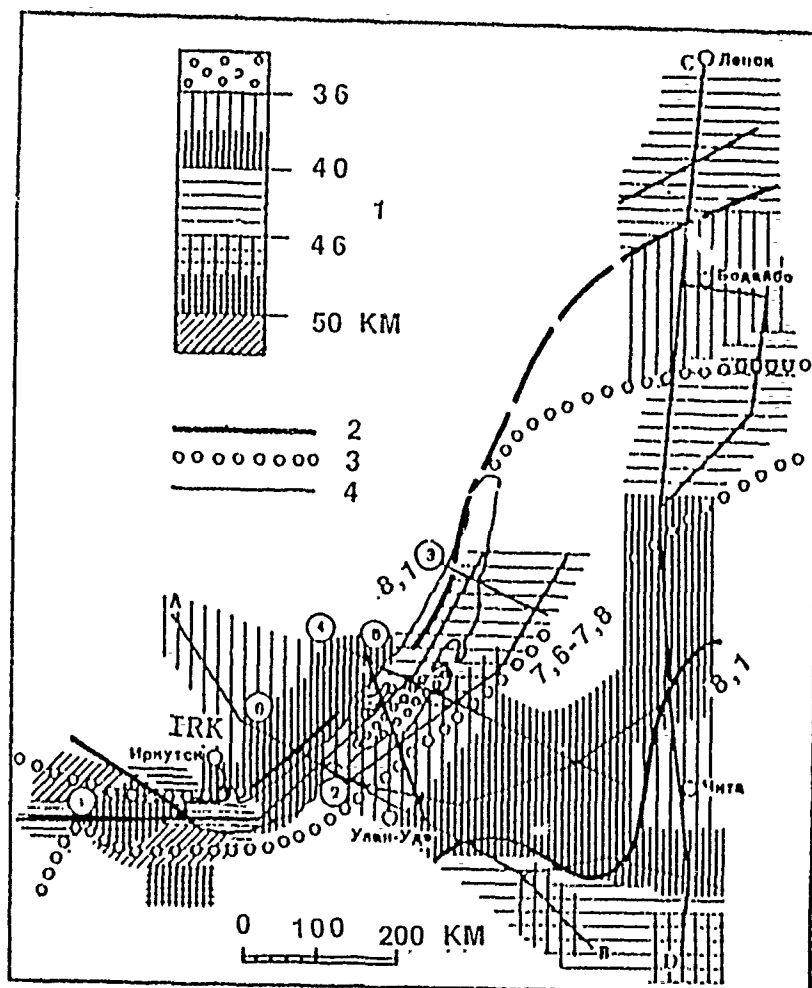


Figure 10. Results of studies of the earth crust and uppermost mantle of the Baikal rift zone by DSS. Top -- structure of the upper mantle surface (1 -- Moho depths; 2 -- boundaries of the zone characterized by low values of Pn velocity, 3 -- boundaries of the rift zone; 4 -- DSS profiles). Bottom -- seismic section of the earth crust along the A-B DSS profile. IRK -- IRIS seismological station installed in the area of Irkutsk (boundary between Baikal rift zone and Siberian platform). \bar{V} -- values of mean velocity from surface to boundaries in the earth crust and Moho, V_1 -- velocity under surface of the basement, V_2 -- Pn wave velocity. Values of velocities are given in km/s. Adapted from Puzyrev, Krylov et al., 1980.

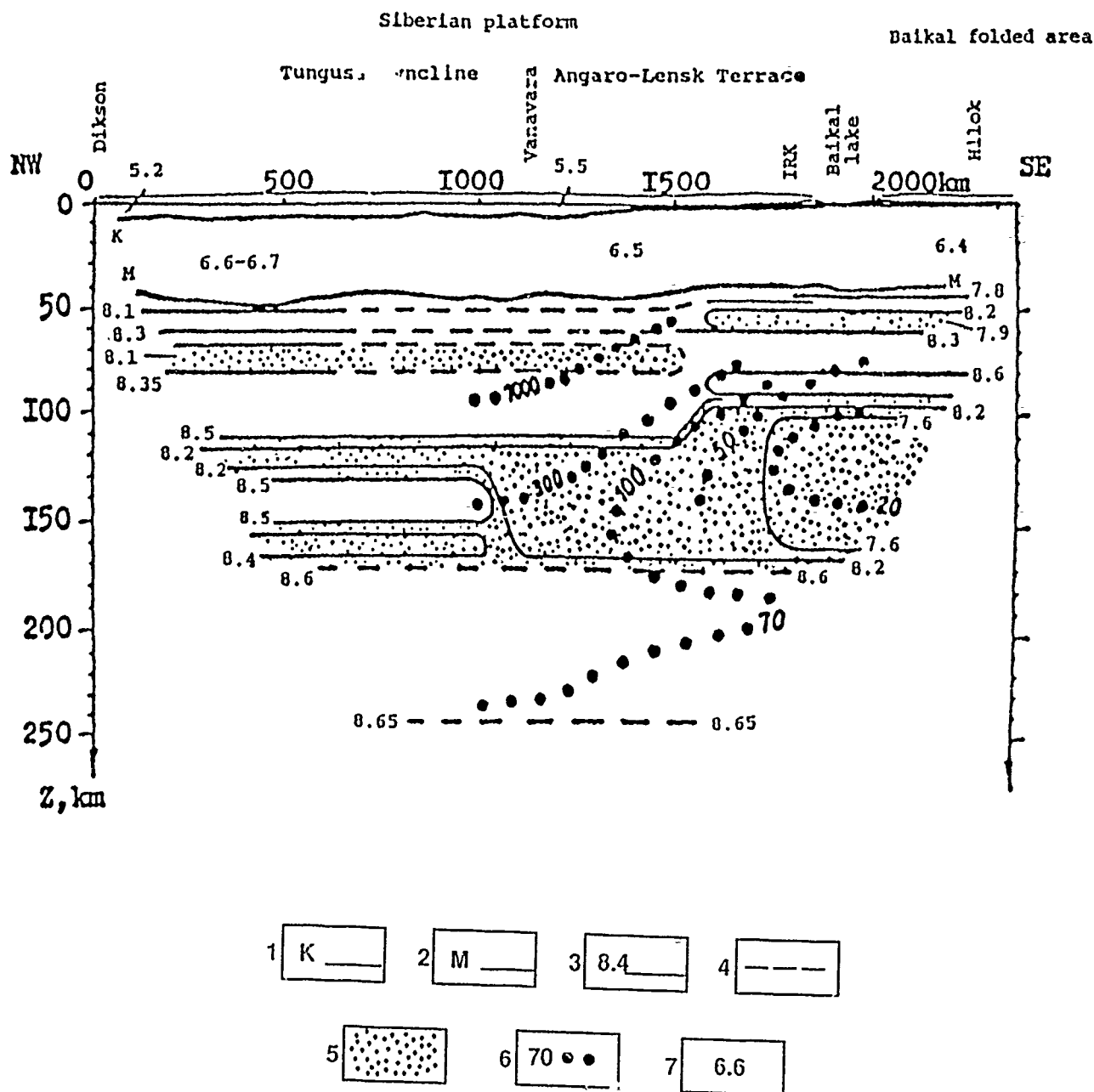


Figure 11. Comparison of a velocity section of the earth crust (after Egorkin et al., 1987, Yegorkin, Zukanov, and Chernyshev, 1984) and upper mantle (after Barkhin, et al., 1987) with deep electromagnetic data (Vanyan, Shilovskiy, 1983) for north south DSS profile crossing the Siberian platform and Baikal rift zone from Dikson to Hilok. IRK -- IRIS seismological station installed in the area of Irkutsk (approximately 200 km to the south-west of the profile). 1 -- basement surface; 2 -- Moho boundary, 3, 4 -- lines of isovelocities (km/s) according to reliable (3) and unreliable (4) data; 5 -- low-velocity layers, 6 -- isolines of electrical resistivity, Ohm.m; 7 -- values of mean velocity in the sedimentary layer and in the layer between the basement surface and Moho boundary.

The thickness of sediments and Moho depth vary beneath the Baikal rift zone between approximately 3-6 and 35-45 km, respectively. Mean velocities in the earth crust are 6.4-6.5 km/s. The uppermost mantle is characterized by low Pn velocities, 7.6-7.8 km/s and the thickness of this layer varies from approximately 8-10 to 15-20 km. This anomalous layer was also detected up to 200-400 km to the south and southeast of the Baikal rift zone at the limits of Baikal folding. A similar layer in the uppermost mantle does not exist beneath southern areas of the Siberian platform where Pn velocities are larger (8.0-8.4 km/s and sometimes locally to 8.5-8.7 km/s).

The main tectonic units of the adjacent Siberian platform (Angaro-Lensk terrace and Tunguss syncline) are located to the north of the Baikal rift zone. The crust and upper mantle of the Siberian platform are characterized, on average, by higher velocities than the Baikal rift zone. The variations are traced to depths of at least 200-250 km. Sedimentary layer thickness and Moho depths increase from 2-3 to 6-8 km and from 38-40 to 45-48 km, respectively, when crossing the boundary between the Angaro-Lensk terrace and Tunguss syncline from south to north (*Figure 11*). The sedimentary layer of the Siberian platform has higher velocities, 4.5-6.0 km/s (mean values are 5.0-5.5 km/s) than that of the Baikal rift zone. A crustal layer between the basement and Moho is characterized by a mean velocity of 6.5-6.7 km/s.

Two-dimensional velocity sections of the upper mantle were constructed for the north-south Dikson-Khilok long-range DSS profile crossing the Baikal rift zone and the Siberian platform from ray tracing results (Egorkin *et al.*, 1987, Ryaboy *et al.*, 1987) and seismic tomography (Burmakov *et al.*, 1986). Station IRK was located approximately 150 km to the west of the DSS profile (*Figure 3*). Velocity sections constructed by different methods had substantial discrepancies which were carefully analyzed (Barkhin *et al.*, 1987; Ryaboy, 1989). The two-dimensional ray tracing method of interpretation for a spherical earth was shown to produce more reliable results compared to the modification of the seismic tomographic method applied for the Dikson-Khilok profile. We will consider a velocity section of the upper mantle constructed for the DSS profile by the ray tracing method (*Figure 11*).

A layer with velocities as low as 7.6-7.7 km/s was distinctly detected in the upper mantle beneath the Baikal rift zone at a depth range of 90-100 to 160-180 km in earthquake (*Figure 2*) and explosion seismology observations (Alekseev *et al.*, 1973; Vinnik and Egorkin, 1980; Ryaboy *et al.*, 1987, Ryaboy, 1989). This layer can be traced 400-500 km north of Lake Baikal approximately to the boundary of the Angaro-Lensk Terrace. Further north, its thickness decreases significantly and the P wave velocity increases to 8.2-8.4 km/s. These conclusions conform with results of deep electromagnetic and geothermal studies. A layer of low electrical resistivity (Vanyan and Shilovskiy, 1983) was detected in the upper mantle beneath the Baikal rift zone and Angaro-Lensk Terrace at the same depth range as the low velocity layer (*Figure 11*). The temperature at the Moho discontinuity along the Dikson-

Khilok profile decreases from 800-1000 ° C (Baikal rift zone), to 500-600 ° C (Angaro-Lensk Terrace), to 350-400 ° C (Tunguss syncline) (Smirnov, 1980). It is interesting to note that beneath the Angaro-Lensk terrace fewer crustal earthquakes occurred than beneath the Baikal rift zone, and the Tunguss syncline is a non-seismic region (Razinkova, Shchukin, 1984).

1.1.3 Attenuation of seismic waves

Seismic wave attenuation in the earth crust and upper mantle of Northern Eurasia is less well determined than velocities. A number of scientific articles and monographs (Berzon *et al.*, 1962; Pasechnik, 1970; Berzon and Pasechnik, 1976; Vinik, 1976; Kopnichev, 1985) have been published on seismic wave attenuation. Many important questions, however such as the physical nature and possible mechanism for the absorption of seismic waves, and reliable methods of measuring attenuation remain unresolved. In Soviet publications, the term absorption usually implies the effect of two factors: absorption due to non-elasticity of the rocks and due to scattering by small-scale inhomogeneities. The propagation losses of the seismic energy is caused by both factors. It is difficult to reliably separate the relative shares of absorption and scattering in the total attenuation though such attempts have been made in practice (Nevskii *et al.*, 1983; Kopnichev, 1985).

Different characteristics of seismic wave attenuation are used. The basic definitions of the attenuation parameters are as follows. Attenuation of seismic waves due to absorption can be described by an exponential multiplier:

$$e^{-\alpha(f)L}, \quad (1)$$

where f is the frequency of oscillation; L is a distance along a seismic ray; α is the amplitude attenuation coefficient (its dimension is m^{-1} or km^{-1}). The attenuation coefficient α is a function of frequency:

$$\alpha(f) = Kf^n, \quad (2)$$

where "n" values vary for different kinds of rocks from 0 up to 2 (for rocks of the earth crust and upper mantle $n \approx 1$).

The logarithmic attenuation decrement ϕ is defined as

$$\phi = \alpha \lambda = \alpha VT, \quad (3)$$

where λ is the wavelength, $T = f^{-1}$ is the period, and V is the velocity of a seismic wave. The dimensionless parameter ϕ is a measure of amplitude attenuation at a distance of one wavelength.

Another parameter of attenuation well known in seismology is the dimensionless quality factor Q , which characterizes the relative amount of energy dissipated per cycle of harmonic vibrations:

$$Q = \pi \phi^{-1} = \pi (KV)^{-1}, \quad (4)$$

The main results of the seismic wave attenuation studies under platform regions adjoining IRIS stations OBN, ARU, and IRK were obtained from long-range DSS profiles. We do not have any data about attenuation parameters in the earth crust and upper mantle for station KIV.

Values for the attenuation coefficient α of P_g and P_n waves recorded from explosions for the first arrivals along DSS profiles were measured from the variation of their amplitude spectra with distance (R) from observation points to the source (Yegorkin, 1980; Yegorkin and Kun, 1978; Yegorkin *et al.*, 1981). The dependence of $A(f_i)/A(f_k)$ on R, where $A(f_k)$ is the amplitude at a certain fixed frequency, was obtained from the amplitude spectra of the recorded waves. The differences in absorption coefficients $\Delta\alpha(f_i) = \alpha(f_i) - \alpha(f_k)$ were estimated from straight lines averaging these graphs. The absolute values of the absorption coefficients and their dependence on frequency were obtained under the assumptions that $\alpha=0$ when $f=0$, and the function $\alpha(f)$ is linear in the frequency range studied (0.5 to 10 Hz for the mentioned DSS observations).

Values of Q and other parameters of attenuation were calculated using equations (3, 4) and the results of studies of the earth crust and upper mantle velocity structure along DSS profiles. The values obtained correspond to the depths of maximum ray penetration where refracted waves are propagated in a direction close to horizontal. The advantage of a method based on measurements of a ratio of spectral amplitudes, is that the effect of source spectrum, geometrical spreading of seismic rays, different gain of the recording systems and frequency response of the seismometer-soil contact on amplitudes is eliminated during the data processing.

Studies of deep seismic wave attenuation beneath geological units of Central Asia neighboring the GAR station were based on the analysis of recordings of local, regional and teleseismic earthquakes. Quantitative (Rautian and Khalturin, 1978, Rautian *et al.*, 1978, Roecker, 1981) and qualitative (Vinnik, 1976; Kopnichev, 1985) methods of analysis of body (P, S, PP, SS) and surface (L_g) waves and coda attenuation were developed. Another source of information about attenuation of seismic waves in the earth crust and upper mantle is maps of earthquake isoseismals which reflect the relative decrease of earthquake energy with epicentral distance (Anan'in *et al.*, 1975). This method is based on the assumption that at large epicentral distances, earthquake intensity mainly depends on attenuation and does not depend on hypocenter depths, source mechanism, magnitude, or epicentral distance. Isoseismals are closer to the epicenter and denser in areas where absorption of seismic wave energy is increased. Below we review the main results of attenuation studies obtained by the above mentioned methods for regions where IRIS stations are installed.

OBN, ARU, IRK

The most detailed findings have been acquired through studies of the attenuation of the P_n waves in the upper mantle from observations of long-range DSS profiles at distances from 200-300 up to 2000-3000 km. *Table 2*, based on published data (Yegorkin and Kun, 1978, Yegorkin *et al.*, 1981), lists mean values of Q for the upper mantle beneath the East-European and Siberian platforms, and the Southern Urals. The Q values in the earth crust and upper mantle vary from 50-100 to 600-800 in the depth range from basement to 200-300 km and increase on average with depth. A zone with increased absorption ($Q=130-160$) probably exists in the upper mantle at depths more than 100 km beneath the Urals and several other geological units. A similar low- Q layer was also located beneath the Baltic shield (Der *et al.*, 1986).

The mean value of Q for the upper mantle beneath the ancient East-European and Siberian platforms was calculated using the values in *Table 2*, $\bar{Q} = 314 \pm 38$. The upper mantle beneath the IRIS stations OBN, ARU (to the western direction), and IRK (to the northern direction) is probably characterized by an average $Q \approx 300$. Meanwhile the upper mantle beneath the younger geological provinces of Paleozoic folding such as the Urals (to the east, northeast and southeast of ARU), the Kazakh shield, and the Turan and Western Siberian platforms is characterized by reduced Q values on average. According to studies of spectra of P, S, PP, and SS waves from teleseismic events, the upper mantle beneath the Baikal rift zone (to the south of IRK) has anomalously high attenuation compared to the Siberian platform (Vinnik, 1976).

Observations from different geological units of the territory of the USSR showed that the average value of Q_p is approximately 1.5-2.0 times less than the average value of Q_s (Yegorkin *et al.*, 1981, Pasechnik, 1970). The observed values of Q_p and Q_s for the consolidated crust and upper mantle are characterized by considerable scatter, however, the average values of these parameters, which were obtained in various regions, are extremely close.

Table 2. Q(MEAN VALUES) OF Pn-WAVES FOR LONG-RANGE PROFILES			
No.	Distance (km)	Frequency (Hz)	Q
East-European platform (northeast of OBN)			
1.	275-535	2.5-7.5	220
2.	255-654	2.0-6.5	200
3.	867-1370	2.5-8.0	430
Southern Urals and Cis-Urals foredeep (south of ARU)			
4.	231-411	0.5-6.5	130
5.	251-618	1.0-6.5	170
6.	597-842	0.5-6.5	130
7.	638-824	2.0-7.5	280
Siberian platform (north of IRK)			
8.	189-280	2.0-8.0	530
9.	215-475	1.0-8.0	370
10.	256-351	1.0-6.0	110
11.	242-428	1.0-8.0	310
12.	309-541	1.0-5.0	300
13.	363-445	1.5-10.0	132
14.	400-488	1.0-5.5	60
15.	435-647	1.5-6.5	350
16.	483-632	1.0-6.0	200
17.	506-705	1.0-5.5	200
18.	512-728	1.0-3.0	390
19.	904-1125	1.0-6.0	410
20.	984-1270	1.0-7.0	530
21.	1211-1401	0.5-5.0	220
22.	1542-1906	0.5-5.0	280
23.	1676-1902	0.9-2.9	160
24.	2209-2382	1.0-2.6	360
25.	2307-2677	1.0-3.8	830

On the basis of DSS observations it was shown that Q is practically independent of frequency (Yegorkin and Kun, 1978). This is apparently due to the fact that

the seismic recording equipment used on the DSS profiles does not make it possible to study seismic signals over a wide frequency range. Studies of earthquake recordings carried out with more advanced equipment for a larger frequency band in tectonically active regions of Central Asia (Rautian and Khalturin, 1978; Rautian *et al.*, 1978) and the Kuril-island chain (Fedotov and Boldyrev, 1969) showed frequency dependent Q .

According to DSS data from long-range profiles, a statistical correlation exists between the attenuation parameters and P_n velocity (Figure 12); the correlation coefficient (r) is 0.6 (Yegorkin and Kun, 1978; Yegorkin, 1980). A relation between Q and P_n velocities was also shown for North America (Marshall and Springer, 1976). It should be noted that the relationship between the velocity of seismic waves and attenuation parameters has been corroborated by theoretical investigations (Gurevich, 1974), as well as by measurements of the physical properties of rock in laboratory conditions ($r=0.75$) (Volarovich *et al.*, 1969), and findings from seismic explorations (Seismorazvedka, 1981). Because upper mantle velocity structure is determined more often than attenuation, the correlation (Figure 12) can probably be used to predict values for Q . Such predictions, using this statistical approach, certainly do not replace results from direct seismic observations, but can be useful in some instances.

GAR and LIRK

Central Asia is probably the most thoroughly instrumented region of the territory of the USSR. The GAR station is located near an important geological boundary which follows the Surkhob river. North of it the rocks of the Southern Tien-Shan are crystalline, Paleozoic in age, and strongly metamorphosed. To the south in the Peter the First range, the rocks are sedimentary, highly deformed (folded and faulted), and Mesozoic to Cenozoic in age. Seismic velocities are about 10 per cent slower in the upper 10 km of the Peter the First range than in the Tien-Shan, but are quite similar at greater depths.

Studies of spectra from shallow local earthquakes yielded pronounced differences in attenuation of P- and S-waves propagating in the upper 10-15 km of the earth crust to the south and north of the Garm region. Low values of Q (≈ 100) were obtained for the sedimentary rocks of the Peter the first range compared to those in the crystalline rocks of the South Tien-Shan, $Q \approx 500$ (Rautian *et al.*, 1978). In contrast to DSS data for platforms (Yegorkin *et al.*, 1981), attenuation of P- and S-waves are comparable.

Attenuation of seismic waves in the upper mantle beneath geological units of Central Asia appears to vary laterally and with depth. High attenuation is observed under Tibet and North Tien-Shan, and weak attenuation is one of the important properties of the upper mantle of Pamir and Southern Tien-Shan. A high- Q (low

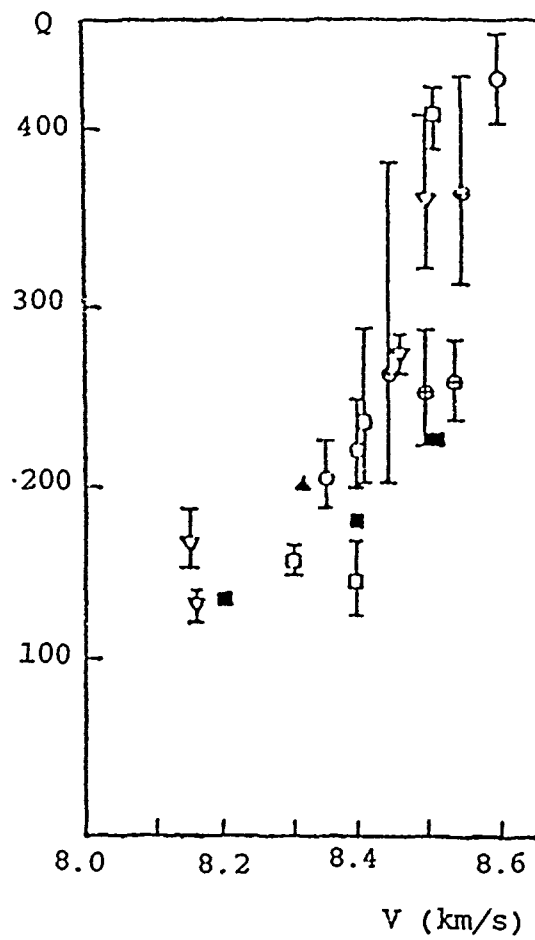


Figure 12. Relationship between quality factor Q and velocity of P waves in the upper mantle. Adapted from Yegorkin, 1980.

attenuation) zone for P- and S-waves is probably associated with the intermediate and deep earthquake zone beneath Pamir-Hindu Kush ($Q > 1000$), that is also characterized by increased velocities in the upper mantle (Vinnik, 1976; Khalturin *et al.*, 1977). A study of the spectral content and variations in time of the coda of seismic oscillations following the body and surface waves of Pamir-Hindu Kush events of intermediate depth ($H \approx 200$ km) yields increasing Q with frequency and with depth (Rautian and Khalturin, 1978). They obtained $Q(f) = 360f^{0.5}$ and $Q(f) = 900f^{0.5}$ for travel times 20-200 s and 200-2000 s, respectively. Similar results were obtained in a study of S-wave coda from shallow and intermediate Hindu Kush earthquakes of the Afghanistan region (Roecker, 1981).

Several maps of seismic wave attenuation in the upper mantle beneath the Tien-Shan and neighboring areas of the Turanian platform have been constructed. Figure 13 shows Q variations for P-waves in the lower subcrustal lithosphere of Central Asia. The map was compiled from the velocity structure of the upper mantle beneath the Tien-Shan region (Ryaboy *et al.*, 1987; Ryaboy, 1989) and the relationship between Q and P-wave velocity in the upper mantle (Figure 12). Values for Q vary roughly from 100 to 400.

The Talas-Fergana deep fault, clearly discernible on the Earth surface from geological data, divides the Southern Tien-Shan into two areas with quite different values of Q in the uppermost mantle. The Tien-Shan structures west of this fault (the Fergana depression and its northern and southern border mountain ridges) have greater values ($Q \approx 400$) than the Northern Tien-Shan ($Q \approx 100$). The Turanian plate is characterized by values of Q in the range $Q \approx 150-300$. A comparison of the map in Figure 13 with maps based on interpretation of L_g surface wave and its coda (Figure 14) and maps of isoseismals (Anan'in *et al.*, 1975) indicates a qualitative relationship between them, in that the regions located east of the Talas-Fergana fault are generally characterized by higher attenuation of seismic waves in the upper mantle than regions located to the west of the fault.

The main findings obtained for station IRK are based on a comparison of P- and S-wave spectra from teleseismic events with PP and SS spectra. According to these data, the Baikal rift zone is characterized by larger attenuation of seismic wave amplitudes than geological units of the Siberian platform (Vinnik, 1976).

1.1.4 Conclusions

Velocity sections showing the change in P-wave velocity with depth have been obtained from explosion seismology data for the areas containing the five IRIS stations and the NORESS array (Figure 15 and Table 3). One can see that the crust and upper mantle beneath these stations have different velocity structures. Tectonically active regions where the GAR (Southern Tien-Shan) and IRK (Baikal rift zone) stations were installed are generally distinguished from the East-European (NORESS

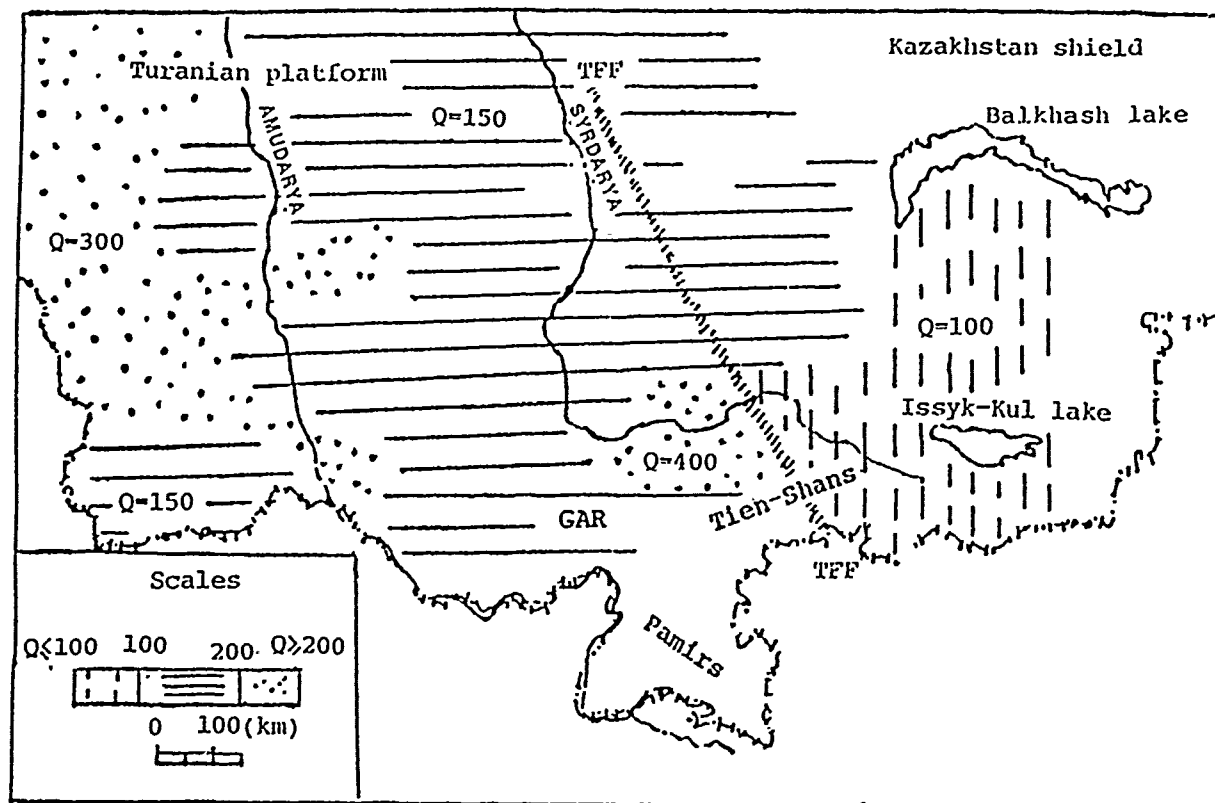


Figure 13. Map of the quality factor Q in the lower subcrustal lithosphere beneath Central Asia, determined from the correlational dependence between the Q values and P_n wave velocity. Adapted from Ryaboy, 1988, 1989.

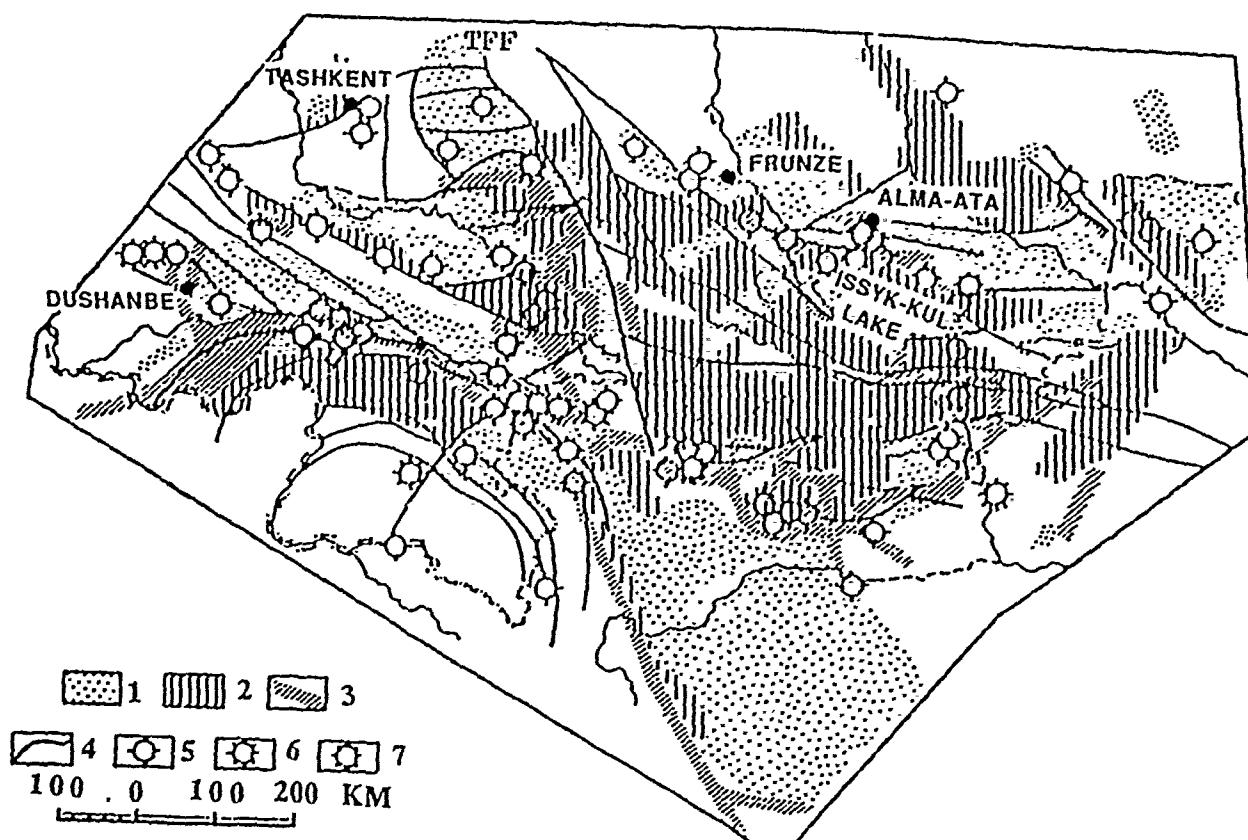


Figure 14. Map of variations in the attenuation of shear waves in the upper mantle of the Tien Shan and adjacent geological structures based on combined interpretation of L_g surface wave and its coda. 1-3 - low (1), intermediate (2), and high (3) relative absorption. 4 -- deep faults (TFF -- Talas-Fergana deep fault). 5-7 -- epicenters of strong earthquakes with magnitudes (M). 5 -- between 6 and 7, 6 -- between 7 and 8, 7 -- more than 8.0. Adapted from Kopnichev, 1985.

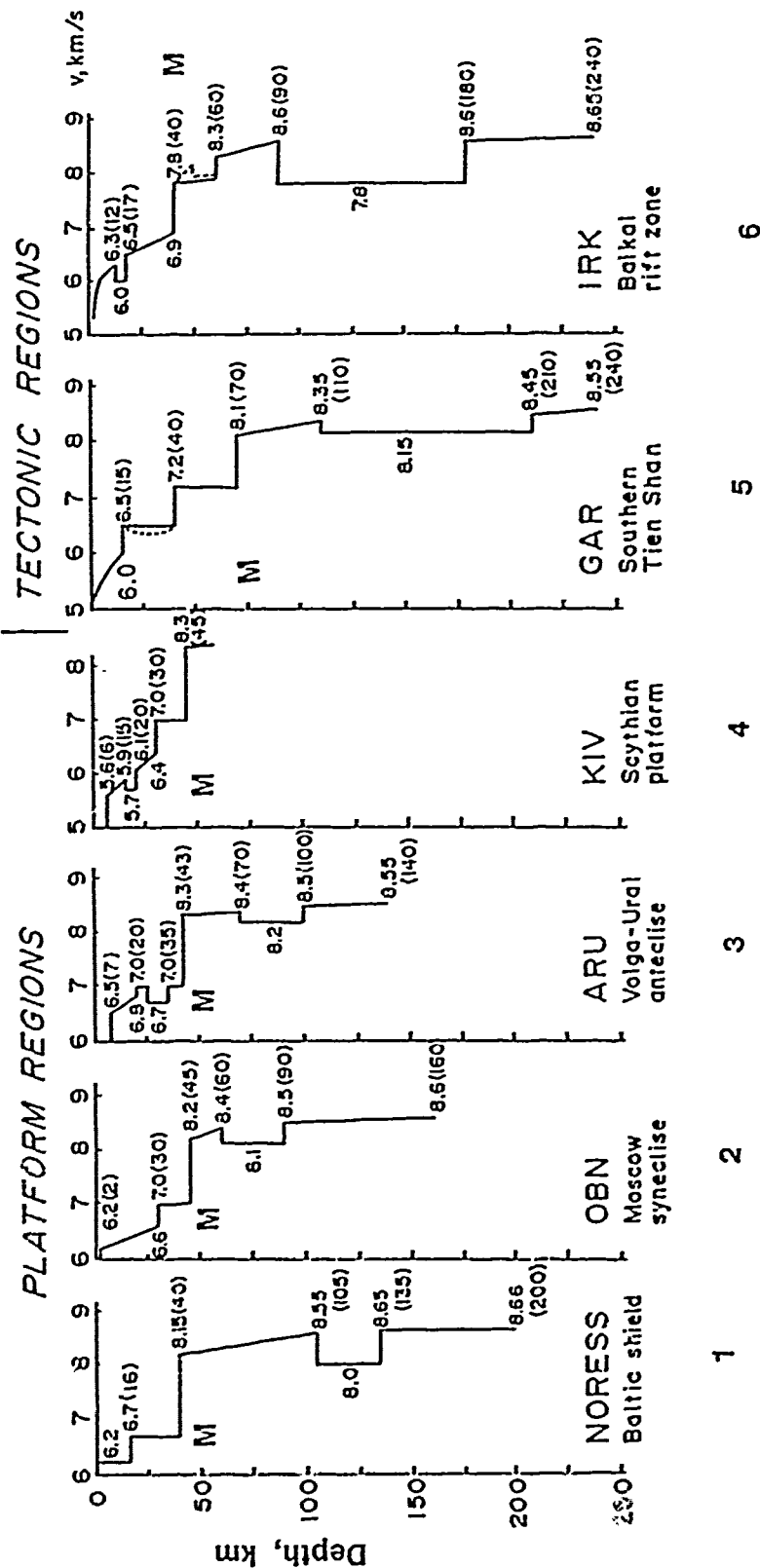


Figure 15. Seismic velocity-depth functions of the earth crust and upper mantle of major geological provinces of Northern Eurasia where NORESS array and IRIS stations were installed, based on published data. 1 -- south-eastern part of the Baltic shield, to the East of NORESS array (Ryaboy, 1990); 2 -- Moscow syncline, OBN (Yurov, 1980; Belyaevsky et al., 1976; Ryaboy, 1977); 3 -- eastern part of the Russian plate and Cis-Urals foredeep, ARU (Khalev'in et al., 1980; Ryaboy, 1979); 4 -- southern part of Scythian platform and Cis-Caucasus foredeep, KIV (Baranova, Krasnopevtseva, et al., 1980); 5 -- southern areas of the Tien-Shan, GAR (Alekseev et al., 1973; Belousov et al., 1984; Burmakov et al., 1984); 6 -- Balkal rift zone, IRK (Tsyzyrev et al., 1980; Barkhin et al., 1987). Solid lines -- exploration seismology data, dashed lines -- alternate interpretation of DSS data, dotted lines -- earthquake seismology data, M -- Moho; depths to boundaries are shown in brackets.

array, OBN and ARU) and Scythian (KIV) platforms by lower velocities and the presence of very pronounced and thick low-velocity layers in the upper mantle. Layers of reduced velocity also exist in the upper mantle beneath platforms but they are thinner and not so pronounced.

The velocity sections in *Figure 15* characterize the average crust and upper-mantle structure beneath the IRIS stations, and can be used for processing and analysis of seismic signals recorded by these stations with the following important caveat. All of the IRIS stations except OBN are located near boundaries of major geological provinces of Northern Eurasia having substantially different deep structure. The velocity and Q structure of the crust and upper mantle usually changes not only in the transition from one province to another, but also between geological units of smaller size. It is not enough to have information about deep structure only beneath the recording stations.

<p>Table 3. PARAMETERS OF THE EARTH CRUST AND UPPER MANTLE VELOCITY SECTIONS FOR IRIS STATIONS IN THE USSR AND THE NORESS ARRAY</p>						
Parameter	NORESS	OBN	ARU	KIV	GAR	IRK
crustal thickness (km)	40	45	43	45	70	40
mean crustal vel. (km/s)	6.5	6.3	6.3	5.7	6.5	6.4
depth range of crustal LVZ (km)	-	-	25-35	15-20	10-21	12-17
velocity of crustal LVZ (km/s)	-	-	6.5-6.7	5.6-5.7	5.8-6.0	6.0
Pn-wave velocity (km/s)	8.15	8.2	8.3	8.3	8.1	7.8
depth range of upper mantle LVZ (km)	105-135	60-96	70-100	-	110-210	90-180
velocity of upper mantle LVZ (km/s)	8.0	8.1	8.2	-	8.15	7.8

The relationships between observed lateral inhomogeneities in the upper mantle and geological structures in the earth crust are frequently complex and ambiguous. For instance, two large basins with sedimentary deposits down to 8-10 km and more are located at distances less than 100 km to the northeast (Fergana depression) and southwest (South Tadzhik depression) of station GAR. The distinguishing feature of the Fergana depression is that the upper mantle beneath it is

characterized by higher velocities than the South Tadjik depression. It is interesting to note that the latter is located in the Alpine Folding region of Eurasia and is believed to have been formed in a geosynclinal environment. The Fergana depression is located within the limits of the Tien-Shan which is a Paleozoic platform activated in Cenozoic time, and the depression was formed before the initiation of neotectonic activations, when platform conditions predominated in the Tien-Shan.

Q values vary both as a function of depth and laterally from 50-100 up to 600-800 when crossing boundaries between geological provinces. Tectonically active regions differ from platforms in that low-Q layers, which are pronounced in the depth range from 100 to 200 km strongly attenuate seismic waves of the active regions. However, these characteristics are only an average observation. For example, a zone with unusually low attenuation in the upper mantle at depths from 100 to 250 km ($Q \geq 1000$) was located beneath the Pamir-Hindu Kush region to the south of station GAR. This zone is also characterized by increased values of seismic wave velocities and coincides with a concentration of intermediate and deep focus earthquakes (Vinnik, 1976; Khalturin *et al.*, 1977). A direct relationship was observed between Q in the upper mantle and Pn velocities.

In studies by some American seismologists values for Q of up to 9000 are postulated for the upper mantle of platform regions of Northern Eurasia (Evernden *et al.*, 1986; Smith, 1988). These Q values exceed all previously published findings (Yegorkin and Kun, 1978; Yegorkin *et al.*, 1981; Fedotov and Boldyrev, 1969; Der *et al.*, 1986). Although the clarification of the source of these deviations in evaluations of Q values is of considerable interest, it lies outside the scope of this paper.

In conclusion, seismic waves recorded by the IRIS stations propagate in substantially laterally inhomogeneous media, but analysis and interpretation of records of seismic events are usually based on one-dimensional velocity and Q models. Overcoming this contradiction should drastically improve event locations, as well as their estimated magnitude and yield.

Vladislav Ryaboy

REFERENCES

- Alekseev, A. S., Belonosova, A. V., Burmakov, Yu. A., Krasnopevtseva, G. V., Matveeva, N. N., Nersesov, I. L., Pavlenkova, N. I., Romanov, V. G., and Ryaboy, V. Z., "Seismic studies of low-velocity layers and horizontal inhomogeneities within the crust and upper mantle on the territory of the U.S.S.R.," *Tectonophysics*, vol. 20, pp. 47-56, 1973.
- Anan'in, I. V., El'tsova, G. P., Egorova, G. A., Shchukin, Yu. K., "Zatuhanie intensivnosti zemletriasenii Srednei Azii i svyaz' ego s seismichnost'yu i geologicheskim stroeniem (Attenuation of the intensity of earthquakes in Central Asia and its connection with seismicity and geological structure)," in *Geofizicheskie polya i seismichnost' (Geophysical fields and seismicity)*, pp. 114-126, Nauka (Science) Publisher House (in Russian), Moscow, 1975.
- Azbel, I. Ya., Kondorskaya, N. V., "Ob osobennostyah skorostnykh razrezov mantii po nablyudeniym nad zemletryaseniymi SSSR (On peculiarities of velocity sections of the upper mantle according to earthquake observations in the USSR)," in *Teoreticheskaya i vychislitel'naya geofizika (Theoretical and computational geophysics)*, pp. 122-128, Nauka (Science) Publisher House (in Russian), Moscow, 1974.
- Baranova, Ye. P., Krasnopevtseva, G. V., Pavlenkova, N. I., and Radjabov, M. M., "Orogenic and rift zones. Alpine geosyncline of the Caucasus," in *Seismicheskie modeli litosfery osnovnykh geostruktur territorii SSSR (Seismic models of the lithosphere for the major geostructures of the territory of the USSR)*, pp. 110-115, Nauka (Science) Publisher House (in Russian), Moscow, 1980.
- Barkhin, G. S., Nikitina, L. N., and Ryaboy, V. Z., *Izucheniye stroyeniya verkhney mantii po materialam profil'nykh nablyudeniy GSZ (analiz metodov postroyeniya dvumernykh skorostnykh razrezov i nekotorye rezultaty) [Study of the structure of the Upper mantle based on DSS profile observations (analysis of methods for constructing two-dimensional velocity sections and several results)]*, p. 65, All-Union institute for scientific and Technical information (in Russian), Moscow, 1987.
- Belousov, V. V., Vol'vovsky, B. S., Vol'vovsky, I. S., Tal'-Virskii, B. B., and Hamrabaev, I. H., "Itogi mezhdunarodnogo Pamiro-Gimalaiskogo proekta i napravlenie budushchikh rabot (Results of the Pamir-Himalayas international project and directions of further studies)," in *Zemnaya kora i verhnayia mantiya Pamira, Gimalaev i Yuzhnogo Tian'-Shanya (The earth crust and the upper mantle of the Pamirs, Himalayas and Southern Tien-Shan)*, pp. 6-10, Nauka (Science) Publisher House (in Russian), Moscow, 1984.
- Belyaevsky, N. A., *Zemnaya kora v predelakh territorii SSSR (The earth crust within boundaries of the territory of the USSR)*, p. 280, Nedra (Interior) Publisher House (in Russian), Moscow, 1974.

- Belyaevsky, N. A., Volvovsky, B. S., Volvovsky, I. S., Yegorkin, A. V., Polshkov, M. K., Popov, Ye. A., Ryaboy, V. Z., V. B. Sollogub, Chekunov, A. V., Chernyshev, M.M., and Yurov, Yu. G., "Lithospheric structure along a profile from the Black Sea to the Polar Urals," *Tectonophysics*, no. 33, pp. 359-378, 1976.
- Berzon, I. S., Epinat'eva, A. M., Pariiskaya, G. N., Starodubrovskaya, S. P., *Akademiya Nauk SSSR (Publisher House of the Academy of Sciences of the USSR)*, in Russian, p. 511, Moscow, 1962.
- Berzon, I. S., Pasechnik, I. P., *Stroenie Zemli po dinamicheskim kharakteristikam seismicheskikh voln (Earth's structure according to dynamic characteristics of seismic waves)*, p. 236, Nauka (Science) Publisher House (in Russian), Moscow, 1976.
- Borisov, A. A., *Glubinnaya struktura SSSR po geofizicheskim dannym (Deep structure of the USSR territory according to geophysical data)*, p. 303, Nedra (Interior) Publisher House (in Russian), Moscow, 1967.
- Burmakov, Yu. A., Vinnik, L. P., Ryaboy, V. Z. et al., "Study of the upper mantle structure of the Central Asia and Kazakhstan by explosion seismology," in *Issledovaniya zemnoi kory i verkhnei mantii seismoopasnykh zon territorii SSSR (Investigation of the earth crust and upper mantle in seismically hazardous zones of the territory of the USSR)*, pp. 70-98, Nauka (Science) Publisher House (in Russian), Moscow, 1984.
- Burmakov, Yu. A., Vinnik, L. P., Egorkin, A. V., and Chernyshev, N. M., "Issledovaniye podkorovoi litosfery Sibiri metodom seismicheskoy tomografii (Investigation of the subcrustal lithosphere of Siberia by the seismic tomography method)," *Doklady AN SSSR (Reports of the USSR Academy of Sciences)*, (in Russian), vol. 287, no. 1, pp. 78-82, 1986.
- Der, Z. A., Lees, A. C., and Cormier, V. F., "Frequency dependence of Q in the mantle underlying the shield areas of Eurasia, part 1: the Q model," *Geophys. Journ. astr. Soc.*, vol. 87, pp. 1103-1112, 1986.
- Evernden, J. F., Archambeau C. B., and Cranswick E., "An evaluation of seismic decoupling and underground nuclear test monitoring using high-frequency data," *Rev. Geophysics*, vol. 24, no. 2, pp. 143-215, 1986.
- Egorkin, A. V., Zukanov, S. K., Pavlenkova, N. A., and Chernyshev, N. M., "Results of lithospheric studies from long-range profiles in Siberia," *Tectonophysics*, vol. 140, pp. 29-47, 1987.
- Fedotov, S. A. and Boldyrev, S. A., "Frequency dependence of the body wave absorption in the crust and upper mantle of the Kuril island chain," *Izvestiya Academy of sciences, USSR. Physics of the solid Earth (English edition)*, no. 9, pp. 553-562, 1969.

- Gurevich, G. I., *Deformatsii sredy i rasprostranenie seismicheskikh voln* (Deformability of media and propagation of seismic waves), p. 230, Nauka (Science) Publisher House (in Russian), Moscow, 1974.
- IRIS,, *Some data sets of the IDA/IRIS data collection center*, p. 13, IRIS, 1989.
- Khalevin, N. I., Druzhinin, V. S, et al., "Orogenic and rift zones. The Urals.," in *Seismicheskie modeli litosfery osnovnykh geostruktur territorii SSSR* (Seismic models of the lithosphere for the major geostructures on the territory of the USSR), pp. 102-110, Nauka (Science) Publisher House (in Russian), Moscow, 1980.
- Khalturin, V. I., Rautian, T. G. , and Molnar, P. , "The spectral content of Pamir-Hindu Kush intermediate depth earthquakes. evidence for a high-Q zone in the upper mantle ," *Journ. Geoph. Res.* , vol. 82 , no. 20 , pp. 2931-2943, 1977 .
- Kopnichen, Yu. F., *Korotkoperiodnye seismicheskie volnovye polya* (Short period seismic wave fields), p. 176, Nauka (Science) Publisher House (in Russian), Moscow, 1985.
- Marshall, P. D. and Springer, D. L., "Is the velocity of Pn an indication of Q?," *Preprint UCRL-78701*, 1976.
- Murusidze, G. Ya., *Skorostnaya model verkhnei mantii na territorii Kavkaza i prilgayushchih regionov* (Velocity section of the upper mantle beneath the Caucasus and adjoining regions), p. 134, Metsnireba Publisher House (in Russian), Tbilisi, 1987.
- Nevskii, M. V., Nikolayev, A. V, and Rznichenko, O. Yu., "Scattering and absorbtion of longitudinal seismic waves in the Earth's crust," *Izvestiya Academy of Sciences, USSR (English edition)*, vol. 18, no. 10, pp. 754-761, 1983.
- Pasechnik, I. P., *Haracteristika seismicheskikh voln pri yadernykh vzryvakh i zemletryasenyakh* (Characteristics of the seismic waves recorded from nuclear explosions and earthquakes), p. 191, Nauka (Science) Publisher House (in Russian), Moscow, 1970.
- Puzyrev, N. N., Krylov, S. V., et al., "Orogenic and rift zones. The Baikal rift zone.," in *Seismicheskie modeli litosfery osnovnykh geostruktur territorii SSSR* (Seismic models of the lithosphere for the major geostructures on the territory of the USSR) , pp. 126-132, Nauka (Science) Publisher House (in Russian) , Moscow, 1980.
- Rautian, T. G. and Khalturin, V. I., "Thé use of the coda for determination of the earthquake source spectrum," *Bull. Seism. Soc. Am.*, vol. 68, no. 4, pp. 923-948, 1978.

Rautian, T. G., Khalturin, V. I., Martynov, V. G., and Molnar, P., "Preliminary analysis of the spectral content of P and S waves from local earthquakes in the Garm, Tadzhikistan region," *Bull. Seism. Soc. Am.*, vol. 68, no. 4, pp. 949-971, 1978.

Razinkova, M. I., Krasnopevtseva, G. V. et al., "Seismic studies of the earth crust," in *Glubinnoye stroeniye slaboseysmichnykh regionov SSSR (Deep structure of weak seismic regions of the USSR)*, pp. 6-62, Nauka (Science) Publisher House (in Russian), Moscow, 1987.

Razinkova, M. I. and Shchukin, Yu. K., "Geofizicheskaya kharakteristika i osobennosti stroeniya zemnoi kory i verkhnei mantii Yuga Sibiri (Geophysical features and peculiarities of the earth crust and upper mantle of southern Siberia)," in *Issledovaniye zemnoy kory i verkhney mantii seysmoopasnykh zon territorii SSSR (Investigations of the earth crust and upper mantle in seismically hazardous zones of the territory of the USSR)*, pp. 115-132, Nauka (Science) Publisher House (in Russian), Moscow, 1984.

Roecker, S. W., "Seismicity and tectonics of the Pamir-Hindu Kush region of Central Asia," *Ph.D. thesis*, p. 297, Mass. Inst. of Tech., 1981.

Ryaboy, V. Z., "Study of the structure of the lower lithosphere by explosion seismology in the USSR," *Journ. of Geophysics*, vol. 43, no. 4, pp. 593-610, 1977.

Ryaboy, V. Z., *Struktura verkhney mantii territorii SSSR po seismicheskim dannym (The upper mantle structure of the territory of the USSR according to seismic data)*, p. 245, Nedra (Interior) Publisher House (in Russian), Moscow, 1979.

Ryaboy, V. Z., "Lower lithosphere and asthenosphere of central and eastern regions of northern Eurasia based on seismic data," *Izvestiya Academy of Sciences, USSR, Physics of the Solid Earth (English edition)*, vol. 21, no. 2, pp. 100-110, 1985.

Ryaboy, V. Z., *On feasibility of compiling a map of seismic waves attenuation of the USSR territory (manuscript)*, p. 53, USGS, Reston Va, 1988.

Ryaboy, V. Z., *Upper mantle structure studies by explosion seismology in the USSR*, p. 154, DELPHIC associates, 1989.

Ryaboy, V. Z., "Upper mantle structure along a profile from Oslo (NORESS) to Helsinki to Leningrad, based on explosion seismology," *Bul. Seism. Soc. Am., Proceedings from the NORSAR symposium on Regional Seismic Arrays and Nuclear Test Ban Verification (in press)*, 1990.

Ryaboy, V. Z., Yu. A. Burmakov, S. V. Potap'ev, and L. N. Nikitina, "The main features of the velocity structure of the upper mantle," in *Glubinnoye stroeniye slaboseysmichnykh regionov SSSR (Deep structure of weak seismic regions of the USSR)*, pp. 86-117, Nauka (Science) Publisher House (in Russian), Moscow, 1987.

- Seismorazvedka. Spravochnik geofizika, (*Seismic exploration. Handbook*), p. 464, Nedra (Interior) Publisher House (in Russian), Moscow, 1981.
- Smirnov, Ya. B., *Teplovoe pole territorii SSSR (Heat field in the territory of the USSR)*, p. 150, GUGK SSSR Publisher House (in Russian), Moscow, 1980.
- Smith, A. T., "Estimating high-frequency crustal attenuation in Eastern Kazakhstan, USSR, using reversed spectral ratios of Pg and Pn," *Preprint*, pp. 19, 1988.
- Van'yan, L. L. and Shilovskiy, P. P., *Glubinnaya elektroprovodnost okeanov i kontinentov (Deep electrical conductivity of oceans and continents)*, p. 86, Nauka (Science) Publisher House (in Russian), Moscow, 1983.
- Vinnik, L.P., *Issledovaniya mantii Zemli seismicheskimi metodami (Seismic studies of the earth's upper mantle)*, p. 198, Nauka (Science) Publisher House (in Russian), Moscow, 1976.
- Vinnik, L. P. and Egorkin, A. V., "Volnovye polya i modeli litosfery-astenosfery po dannym seismicheskikh nablyudeniy v Sibiri (Wave fields and models of the lithosphere-asthenosphere, according to seismic observations in Siberia)," *Doklady AN SSSR (Reports of the USSR Academy of Sciences)*, (in Russian), vol. 250, no. 2, pp. 318-323, 1980.
- Volarovich, M. P., Gzovskiy, M. V., Levykin, A. L., and Osokina, D. N., "The correlation dependance between attenuation decrements and elasticity modules of rocks," *Izvestia Academy of Sciences, USSR. Physics of the Solid Earth (English edition)*, vol. 14, no. 4, pp. 741-746, 1969.
- Vol'vovsky, I. S. and Vol'vovsky, B. S., *Razrezy zemnoi kory territorii SSSR po dannym glubinnogo seismicheskogo zondirovaniya (Cross-sections of the earth crust in the territory of the USSR according to deep seismic soundings)*, p. 268, Sovetskoe Radio (Soviet Radio) Publisher House (in Russian), Moscow, 1975.
- Yegorkin, A. V., "General features of mantle structure," in *Seismicheskie modeli litosfery osnovnykh geostruktur territorii SSSR (Seismic models of the lithosphere for the major geostructures on the territory of the USSR)*, pp. 161-170, Nauka (Science) Publisher House (in Russian), Moscow, 1980.
- Yegorkin, A. V. and Kun, V. V., "Absorption of longitudinal waves in the Earth's upper mantle," *Izv. (Bull.) Acad. Sci. USSR, Physics of the solid Earth, AGU Transl.*, vol. 14, no. 4, pp. 262-270, 1978.
- Yegorkin, A. V., Kun, V. V., and Chernyshev, N. M., "Absorption of longitudinal and transverse waves in the crust and upper mantle of the West Siberian plate and the Siberian platform," *Izv. (Bull.) Acad. Sci. USSR, Physics of the solid Earth, AGU Transl.*, vol. 17, no. 2, pp. 105-115, 1981.

Yegorkin, A. V., Zyuganov, S. K., and Chernyshev, N. M., "Verkhnyaya mantiya Sibiri (The upper mantle of Siberia)," in *27-y mezhdunarodnyi geologicheskii kongress, Geofizika (27th International geological congress, Geophysics)*, vol. 8, pp. 27-42, Nauka (Science) Publisher House (in Russian), Moscow, 1984.

Yurov, Yu. G., "Kristallicheskie massivy i platformennye plity. Regional'noe sechenie cherez Russkuiy platformy, profil' Kupiansk-Kineshma (Crystalline massifs and platform plates. Regional section across the Russian plate, Kupiansk-Kineshma profile)," in *Seismicheskie modeli litosferi osnovnykh geostruktur territorii SSSR (Seismic models of the lithosphere for the major geostructures on the territory of the USSR)*, pp. 50-60, Nauka (Science) Publisher House (in Russian), Moscow, 1980.

Zunnunov, F. H., Ryaboy, V. Z., et al., "Izuchenie stroeniya zemnoi kory i verhnei mantii metodom GSZ (Study of the earth crust and upper mantle structure by DSS)," in *Zemnaya kora i verkhnyaya mantia Srednei Azii (The earth crust and upper mantle of Central Asia)*, pp. 79-105, Nauka (Science) Publisher House (in Russian), Moscow, 1977.

1.2 LATERAL INHOMOGENEITIES OF THE UPPER MANTLE BENEATH NORTHERN EURASIA INFERED FROM Pn-WAVE EXPLOSION SEISMOLOGY OBSERVATIONS

Abstract

This paper presents a review of published Soviet data on travel-times, amplitudes, and waveforms of Pn-waves based on explosion seismology. Large industrial (including nuclear) explosions were recorded by portable instruments used in long-range deep seismic sounding profiles (DSS) and seismological networks up to epicentral distances of 3000 km. Pn-wave travel-times that have been corrected for lateral velocity variations in the earth's crust differ by as much as 5-6 seconds between different regions. Such large differences are attributed to differences in the velocity structure of the upper mantle.

A complex but distinct relationship has been observed between Pn-wave travel-times and subsurface geology. The ancient Pre-Cambrian platforms (East-European and Siberian) are characterized by early Pn-wave arrivals, whereas the largest travel-times of these waves are observed for tectonically active regions (Tien-Shan and Baikal rift zone). Pn-wave travel-time curves constructed for Paleozoic platform plates (Turan and West-Siberian) occupy an intermediate position. Pn-wave travel-time deviations are also observed for the ray paths located basically within the limits of substantially smaller geological structures (individual basins, lifts, mountain ridges).

The scale of horizontal velocity heterogeneities in the upper mantle beneath Northern Eurasia is quite variable. Linear dimensions of the inhomogeneities reliably detected by Pn-waves are on the order of 100 to 2000 km with velocity contrasts averaging $\pm(4-5)\%$.

1.2.1 Introduction

The central and eastern regions of Northern Eurasia considered in this paper extend from the western boundary of the East-European platform (Teisseyre-Tornquist zone) to the transition from the Eurasian continent to the Pacific Ocean in the east, and from the Alpine zone in the south to the Arctic basin in the north. Within these boundaries geological provinces are found that are different in their development (old Pre-Cambrian platforms, young Paleozoic platform plates, folded mountain systems, deep depressions and rift zones) and in their crust and upper mantle velocity structure.

One of the main findings of Northern Eurasian seismic studies performed over the past ten to fifteen years is the presence of significant lateral velocity heterogeneities in the upper mantle up to depths of at least 200-300 km (Vinnik, 1976,

Ryaboy, 1979). These are manifested through anomalies in travel times, amplitudes, and frequency content and have obvious implications for the fundamental and applied problems of geology and geophysics, including seismic monitoring and verification.

The first hypotheses about the presence of horizontal velocity heterogeneities in the upper mantle were proposed in the late 1930s by J. Macelwain (1937) and Y. Savarenskiy (1940) who showed that discrepancies between observed travel-time curves and velocity sections of the upper mantle constructed for different regions of the world significantly exceeded their possible errors. At that time, the opinions of Macelwain and Savarenskiy were not widely accepted as there was no convincing evidence to support their postulates.

Failing to consider the influence of horizontal velocity inhomogeneities in the medium can result in significant interpretation errors for deep seismic sounding profiles. For example, *Figure 1* shows reversed synthetic travel-time curves for waves refracted in a two-dimensional upper mantle velocity model $V(x,z)$. For each of these travel-time curves, the one-dimensional upper mantle velocity section was constructed by the ray-trace method. These one-dimensional velocity sections differ significantly, and both inappropriately characterize the actual distribution of velocity. When interpreting the travel-time curve from shot point 1, a nonexistent low-velocity layer is inferred; but for the travel-time curve from shot point 2, a sharp velocity increase with respect to depth is detected. These features are absent in the original model. Lateral velocity inhomogeneities can cause significant errors in interpretation if one dimensional structure is assumed.

Figure 2 compares refracted wave ray paths calculated for two-dimensional (*Figure 2A*) and one-dimensional (*Figure 2B*) upper mantle velocity models. The ray path density qualitatively characterizes the energy distribution of the seismic waves recorded in the first arrivals. One can see substantial differences in the ray path trajectories in *Figures 2A and 2B*. Velocity heterogeneities can focus and diffuse seismic wave energy causing amplitude anomalies which influence the estimated magnitude and yield of events.

The upper mantle velocity structure of the USSR has been studied using recordings from long-range deep seismic sounding (DSS) profiles and recordings of the DSS explosions obtained with both temporary and permanent seismic networks. In recent years a considerable amount of DSS research has been carried out (Razin-kova, Krasnopevtseva, 1987). This paper deals with the analysis of Pn travel-times, amplitudes, and waveforms recorded from DSS chemical and large industrial (including nuclear) explosions at regional distances up to 1500-2000 km. Our main aim is to study general features of the three-dimensional upper mantle velocity model under major geological provinces of Northern Eurasia.

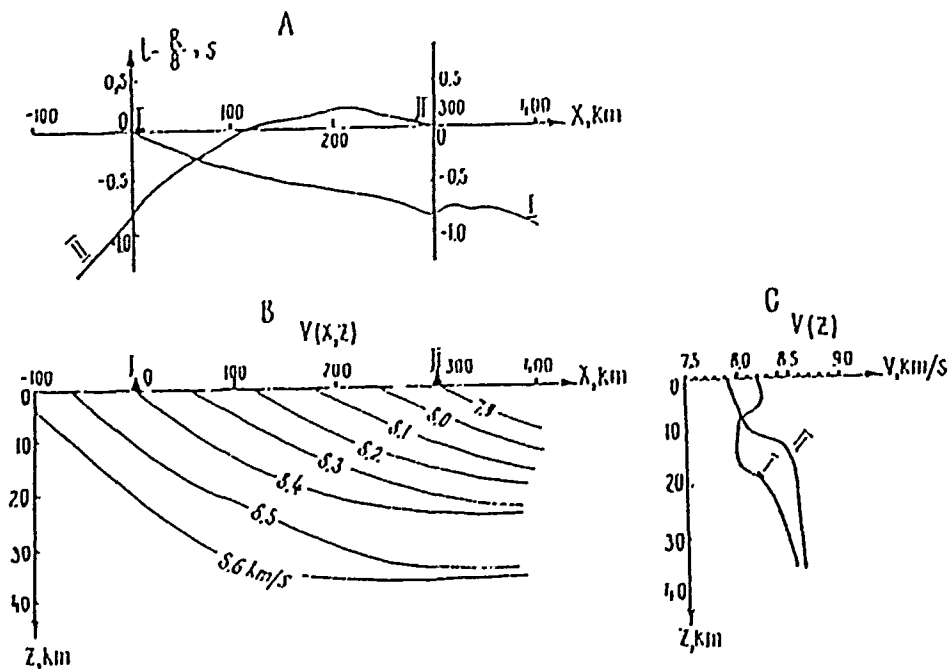


Figure 1. The effect of lateral heterogeneities on the resulting upper mantle velocity sections. Depths are measured with reference to the Moho. A). Theoretical travel-time curves of refracted waves for the horizontally heterogeneous velocity model of the upper mantle $V(x,z)$ shown in B). I, II - shotpoints and respective reversed travel-time curves, reduced with a velocity of 8.0 km/s. C). Velocity versus depth curves $V(z)$, constructed using the ray tracing method for I and II travel-time curves in A. (Adapted from Ryaboy, 1977).

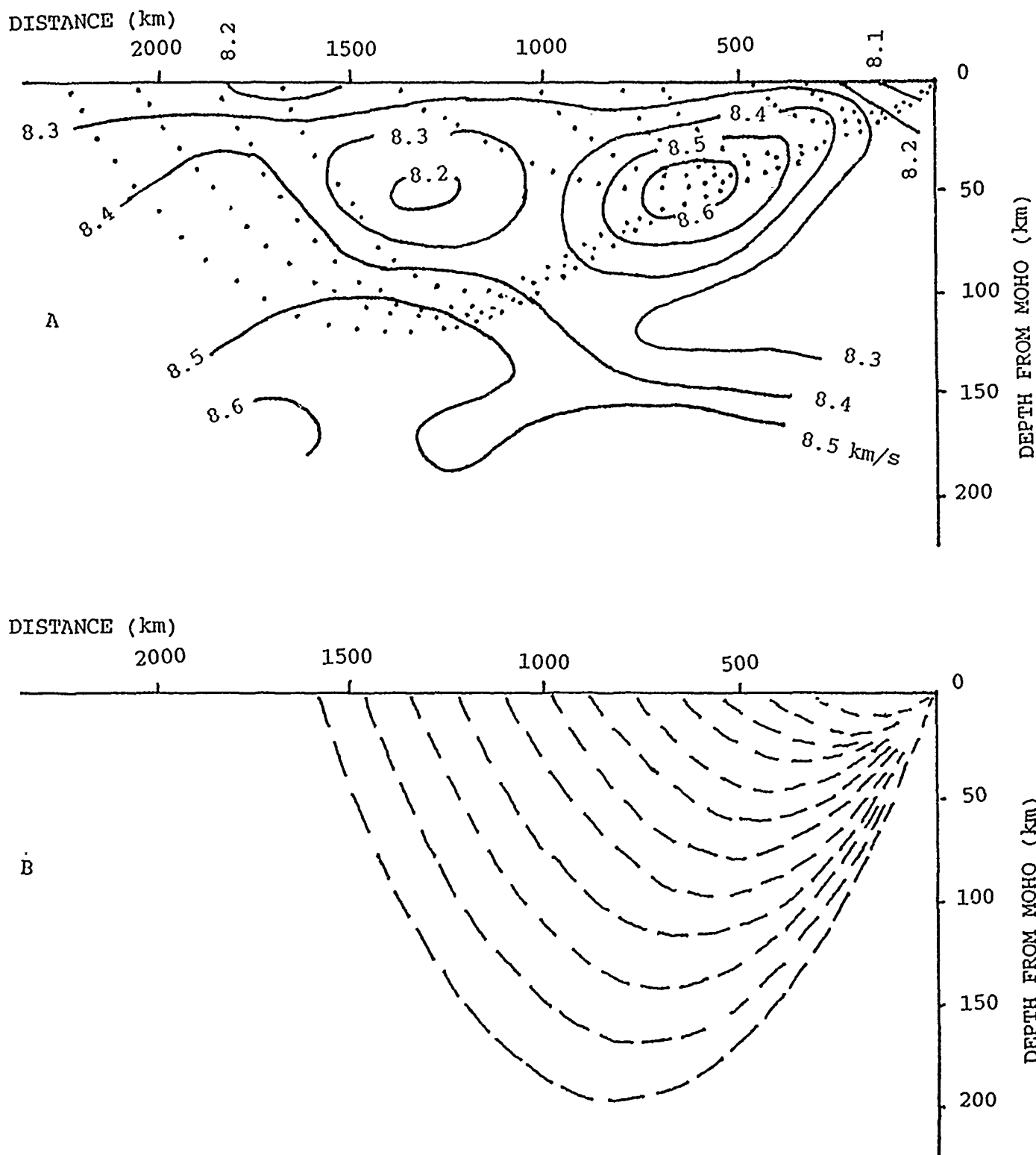


Figure 2. A comparison of refracted wave ray paths for. A) a laterally inhomogeneous $V(x,z)$ and B) an one-dimensional velocity model $V(z)=8.1(1+0.0005z)$ of the upper mantle. Solid lines are isovelocity contours in the upper mantle. Dotted (A) and dashed (B) lines are ray paths for two- and one dimensional velocity models respectively. (Adapted from Baikhin *et al.*, 1987; Ryaboy, 1989).

1.2.2 Waveforms and amplitudes of Pn-waves

Pn-waves were recorded as first arrivals at ranges between 130 up to 2000 km along numerous reversed and overlapping long-range profiles. These observations showed that the Pn-wave has a very complicated structure and consists of several arrival groups. First arrivals are typically characterized by small amplitudes and relatively high frequencies, these are followed by secondary arrivals with substantially larger amplitudes and lower frequencies. In general, recognizing the weak first arrivals is very difficult.

Apparent velocities tend to increase from 7.7-8.2 to 8.8-9.0 km/s and more as distance increases from 1500 to 2000 km. In this distance range Pn-wave first arrivals are interpreted as being refracted in the upper mantle at depths of 200-300 km. At the crossover range of two different velocity arrivals a gradual change in the waveforms of the first arrivals is observed. Occasionally, this is accompanied by an attenuation of the first waves, a break in the travel-time curve, and an offset to later time. The magnitude of such an offset can reach 1-3 seconds.

Figure 3a is a record section of Pn-waves for the Kazakh shield where one can see the offset at a range of approximately 500 km. A similar cut-off is observed in record sections of overlapping and reversed profiles of Pn-waves recorded within the Moscow (*Figure 3b*) and North Caspian depressions (*Figure 3c*) of the East-European platform. Cut-offs of Pn-waves at larger distances (800-850 km) were observed in the record sections from the northern region of the West-Siberian platform plate (*Figure 3d*) and southern Baltic shield (*Figure 3e*). Offsets of this kind when accompanied by similar offsets at approximately the same distances on reversed profiles are characteristic of low-velocity layers in the upper mantle. For offsets due to low-velocity layers, Pn-wave first arrivals are usually characterized by increased magnitude and lower frequencies due to the influence of the low-velocity layers at ranges greater than the crossover distance.

The 400 and 650 km discontinuities cause offsets in the data at ranges greater than 1600-2000 km. Arrivals from the higher velocity material (apparent velocities of 10.0-11.5 km/s) are seen as large amplitude later arrivals at ranges less than the crossover distance (*Figure 3f*).

Amplitude vs. distance plots of Pn-wave first arrivals vary in the different geological provinces of the USSR. *Figures 4* and *5* show that amplitudes can vary by factors of five to ten along DSS profiles within the East-European and Siberian Precambrian platforms, the Turanian and West-Siberian platform plates, and the Kazakh shield. The magnitudes and distances of these amplitude anomalies are not consistent between the different geological provinces. The linear dimensions of the zones of increased or decreased Pn-wave amplitudes are usually 300-500 km.

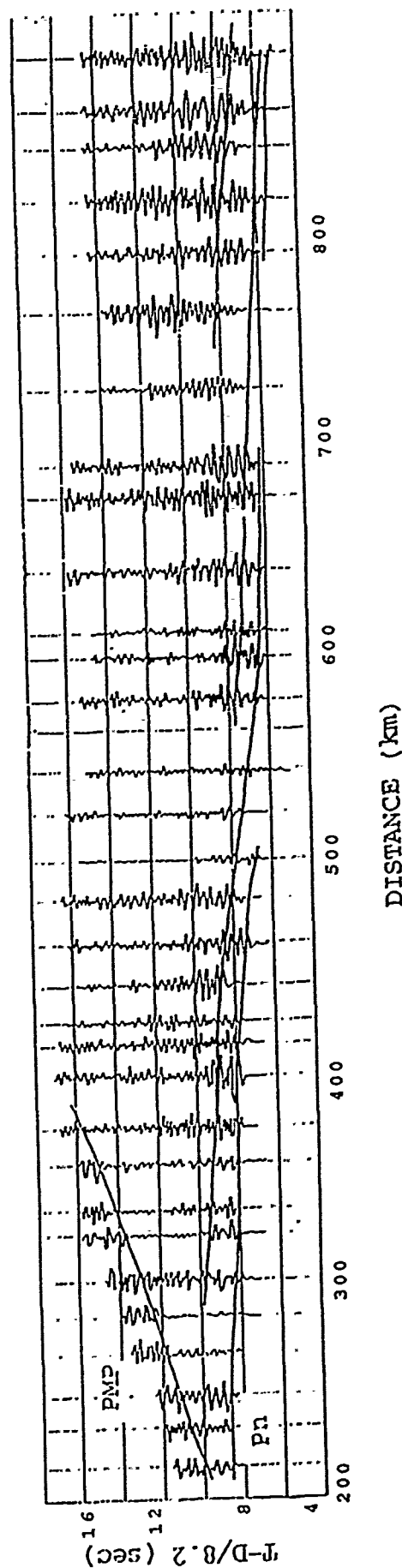


Figure 3a-f. P_n wave seismic record sections constructed for long-range DSS profiles within major geological provinces of Northern Eurasia: a) -- Kazakh shield (Ryaboy, 1979); b) -- Moscow depression (East-European platform) (Vinnik, Ryaboy, 1981), top and bottom are record sections for overlapping profiles; c) -- North-Caspian depression (East-European platform) (Vinnik, Ryaboy, 1981), top and bottom are record sections for reversed profiles; d) -- West-Siberian platform plate (Vinnik, Egorkin, 1980); e) -- southern areas of the Baltic shield, profile Oslo-Helsinki-Leningrad (Ryaboy, 1990a); f) -- Siberian platform, north-south profile Dikson-Khilok (Egorkin, Pavlenkova, 1981). Amplitudes are trace-normalized.

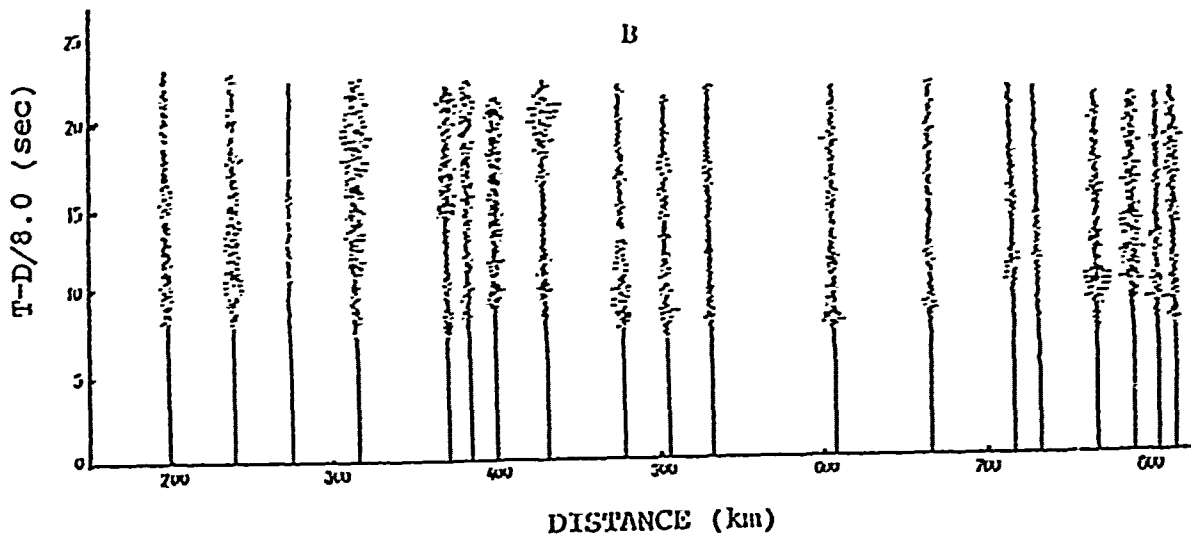
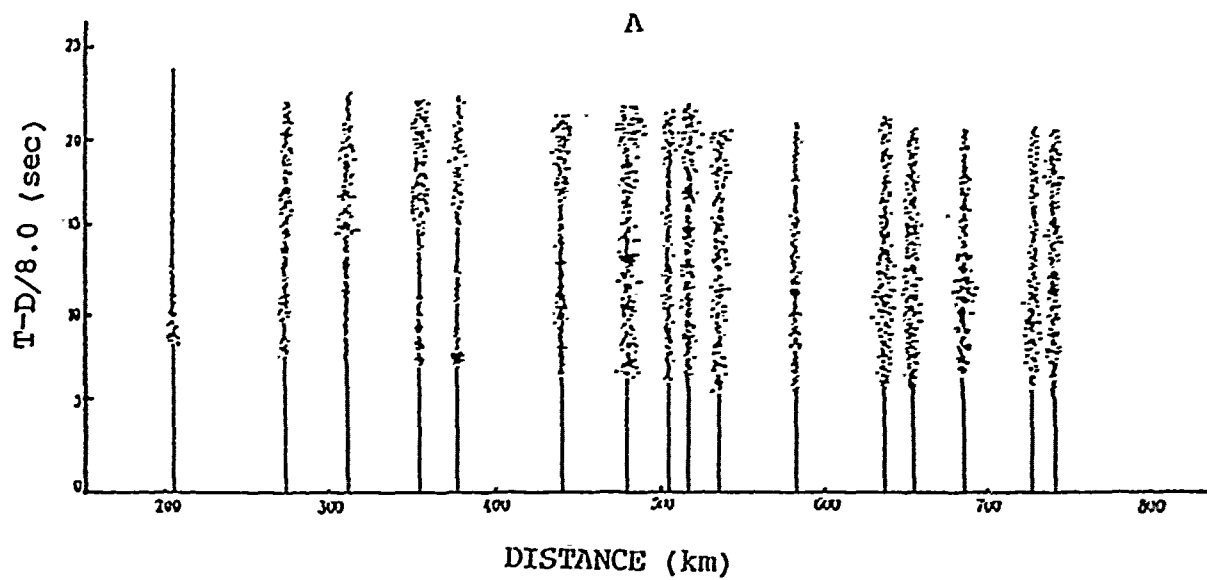


Figure 3b.

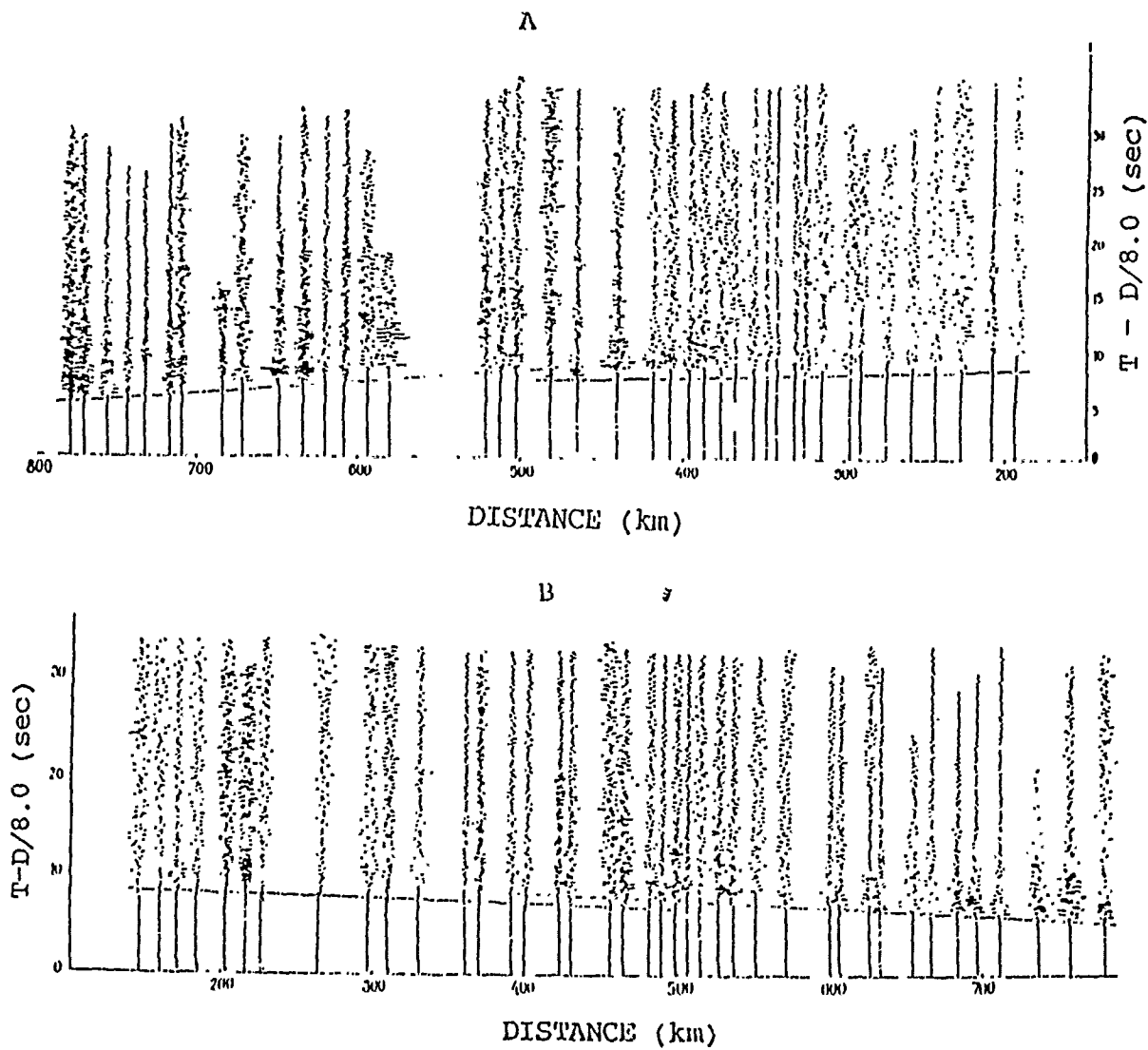


Figure 3c.

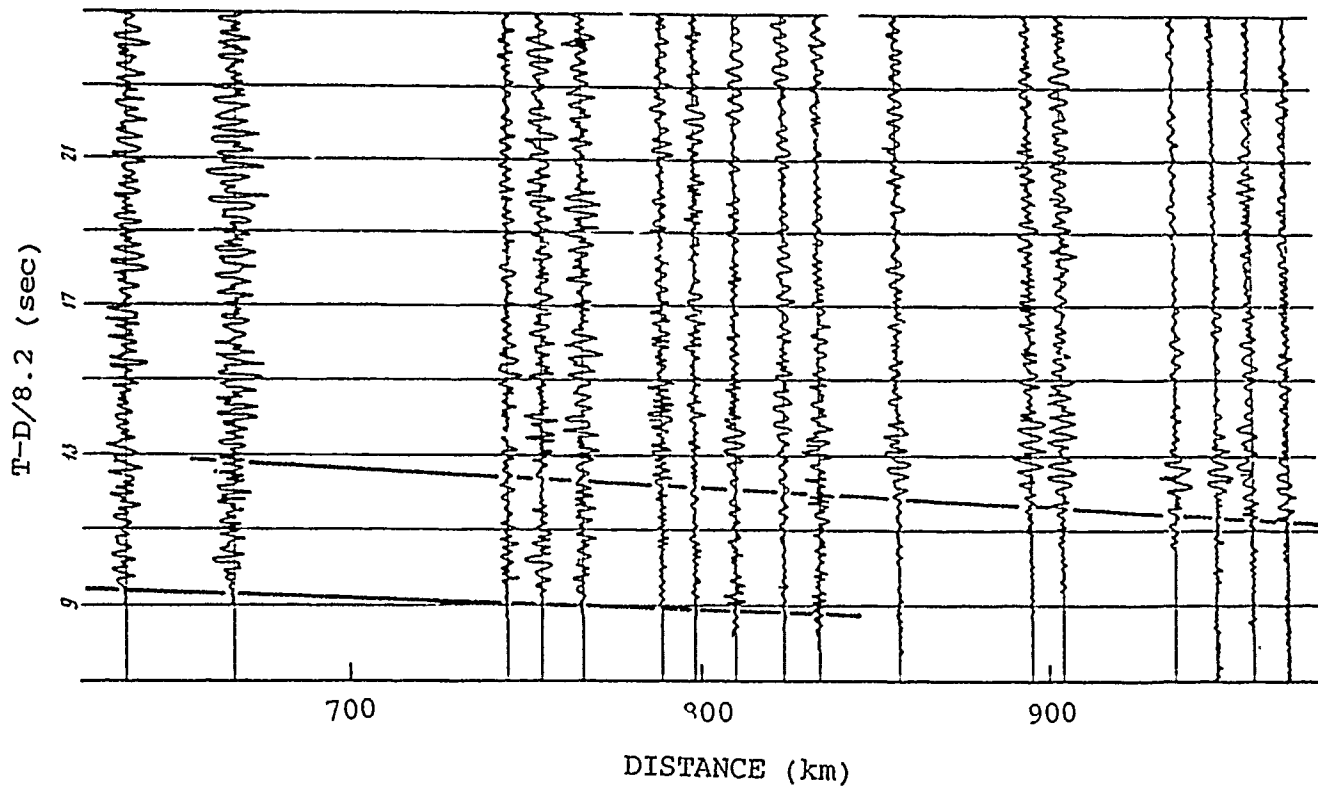


Figure 3d.

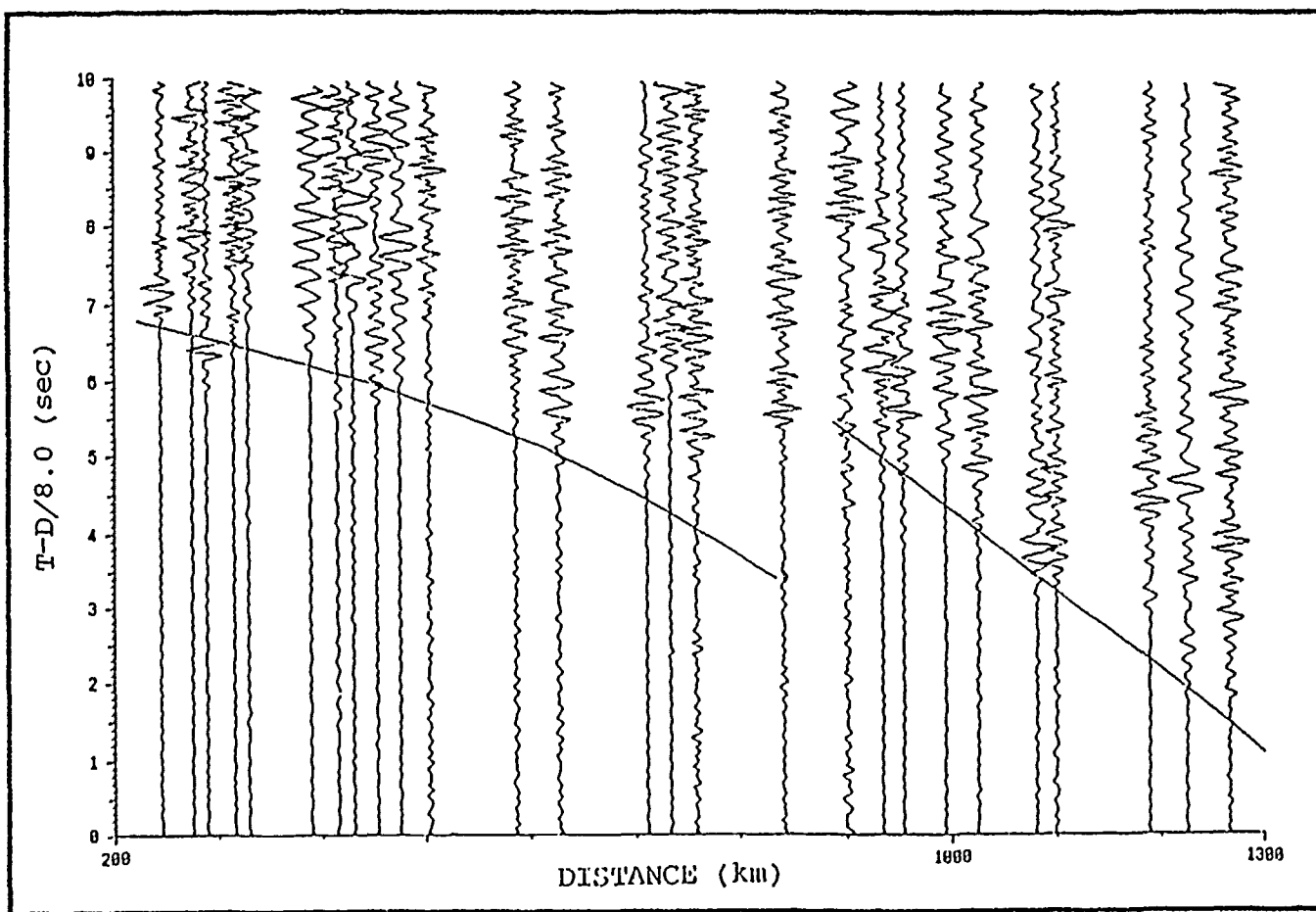


Figure 3c.

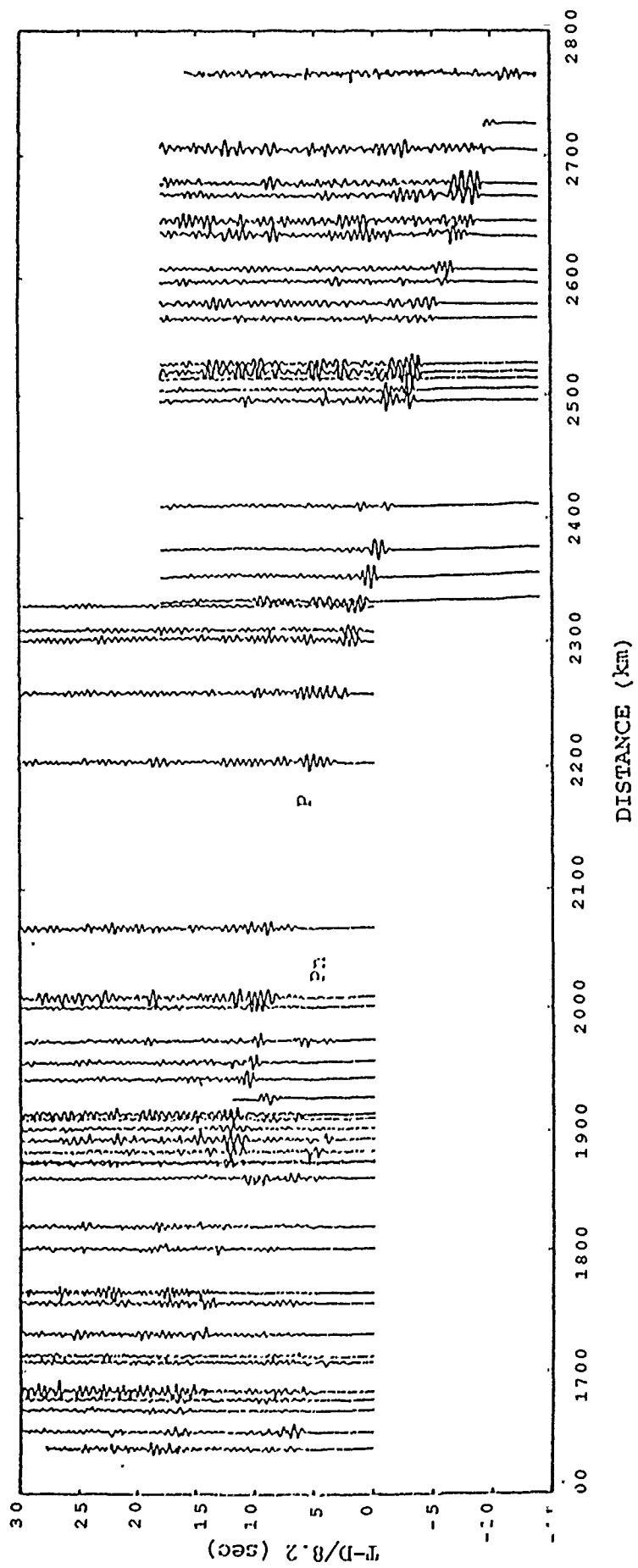


Figure 3f.

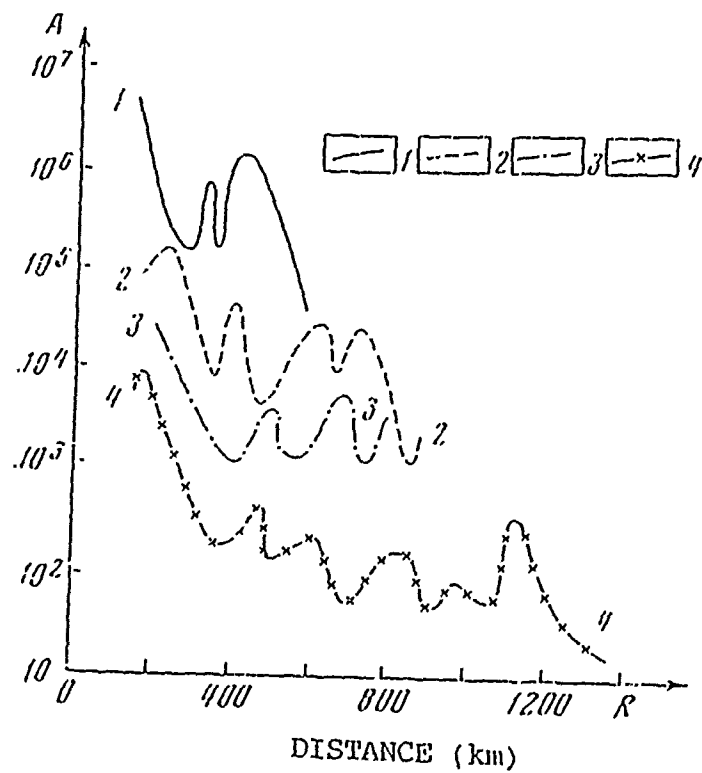


Figure 4. Averaged P_n wave amplitude versus distance variations for different geological provinces of Northern Eurasia: 1 -- Turanian platform plate, 2 -- Kazakh shield, 3 -- North-Caspian depression (East-European platform), 4 -- Moscow depression (East-European platform). (Adapted from Ryaboy, 1979).

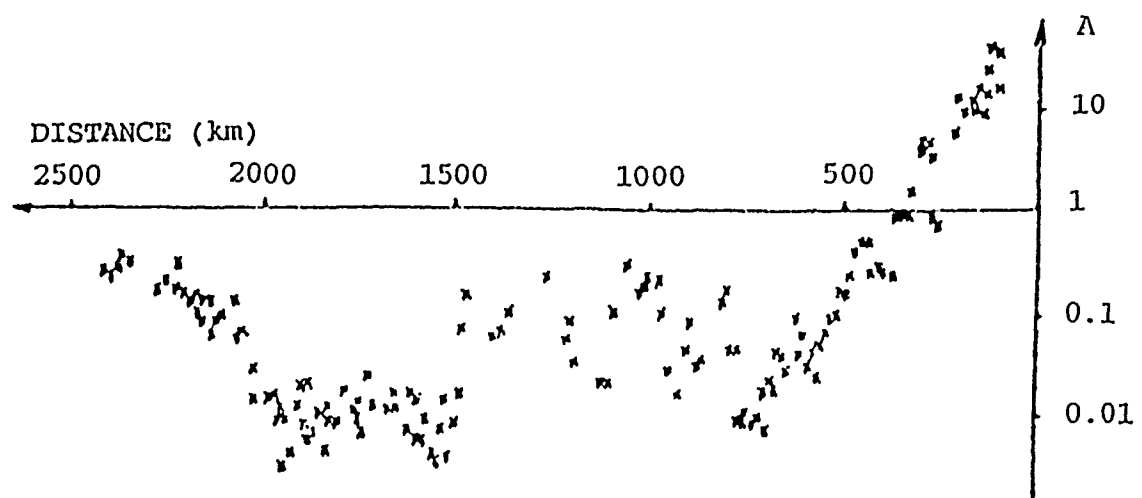


Figure 5. P_n wave amplitude versus distance for west-east Khanty-Mansiisk - Lena river long range DSS profile (West Siberian platform plate and Siberian platform). (Adapted from Barkhin *et al.*, 1987).

Pronounced Pn-wave amplitude anomalies can be qualitatively explained by the influence of vertical and lateral velocity inhomogeneities of the upper mantle. *Figure 6* shows the observed amplitude vs. distance plot for the Pn phase of the Barnaul-Tura DSS profile and a suite of rays calculated for the laterally inhomogeneous velocity section of the upper mantle derived for this area. The two-dimensional upper mantle velocity section not only produces a good fit to the travel-time curve for the Pn-waves, but also the amplitudes inferred from the horizontal ray density qualitatively fit the amplitude vs. distance plot. Results like these indicate that we can qualitatively predict Pn-wave amplitude anomalies based on detailed studies of the upper mantle velocity structure.

1.2.3 Travel-times of Pn-waves

Precise information on the velocity structure of the upper mantle may be obtained from Pn-wave travel-times. Reference travel-time curves of Pn-waves for different geological provinces of Northern Eurasia have been constructed based on the extensive explosion seismology database available in the USSR. We shall consider the results obtained for the Central Asian and Siberian regions in more detail.

Burmakov et al. (1984) derived the upper mantle velocity structure under Central Asia and southern Kazakhstan regions using Pn-wave travel-times. The Pn-waves from 10 large industrial explosions (including nuclear explosions) were recorded at epicentral distances up to 1500-1600 km on long-range DSS profiles and by a seismic network consisting of 85 temporary and permanent recording stations. *Figure 7A* shows the locations of the DSS profiles, seismological stations, and shot points. The geometry of the shot points and recording stations made it possible to study Pn-wave travel-times for ray paths crossing major geological units of Central Asia (Tien Shan and Turanian platform plate) in different directions.

Observed Pn-wave travel-times for the same distance but for different paths are up to 6 seconds different (*Figure 7B*). One possible explanation for this discrepancy is that the thickness of the earth's crust beneath different geological units of Central Asia varies from 35-40 up to 55-65 km (Belyaevsky, 1974, Khamrabaev, 1977; Zverev, Kosminskaya, 1980; Khamrabaev, Zunnunov, 1984). The misleading effects of the earth's crust were removed by recomputing the Pn-wave travel-times with the crust removed to a depth of 40 km. The computation was based on ray theory and the crustal velocity data available (Ryaboy, 1979).

Figure 7C shows average Pn-wave travel-times for the Tien Shan and the Turanian platform, recalculated to a flattened Moho. The maximum difference between the Pn-wave travel-times for the same distance on this figure is 7 seconds. This is approximately 10 times larger than the possible errors due to poor picks and demonstrates the existence of lateral changes in the upper mantle velocity structure. The travel-time curve constructed for Tien-Shan at distances more than

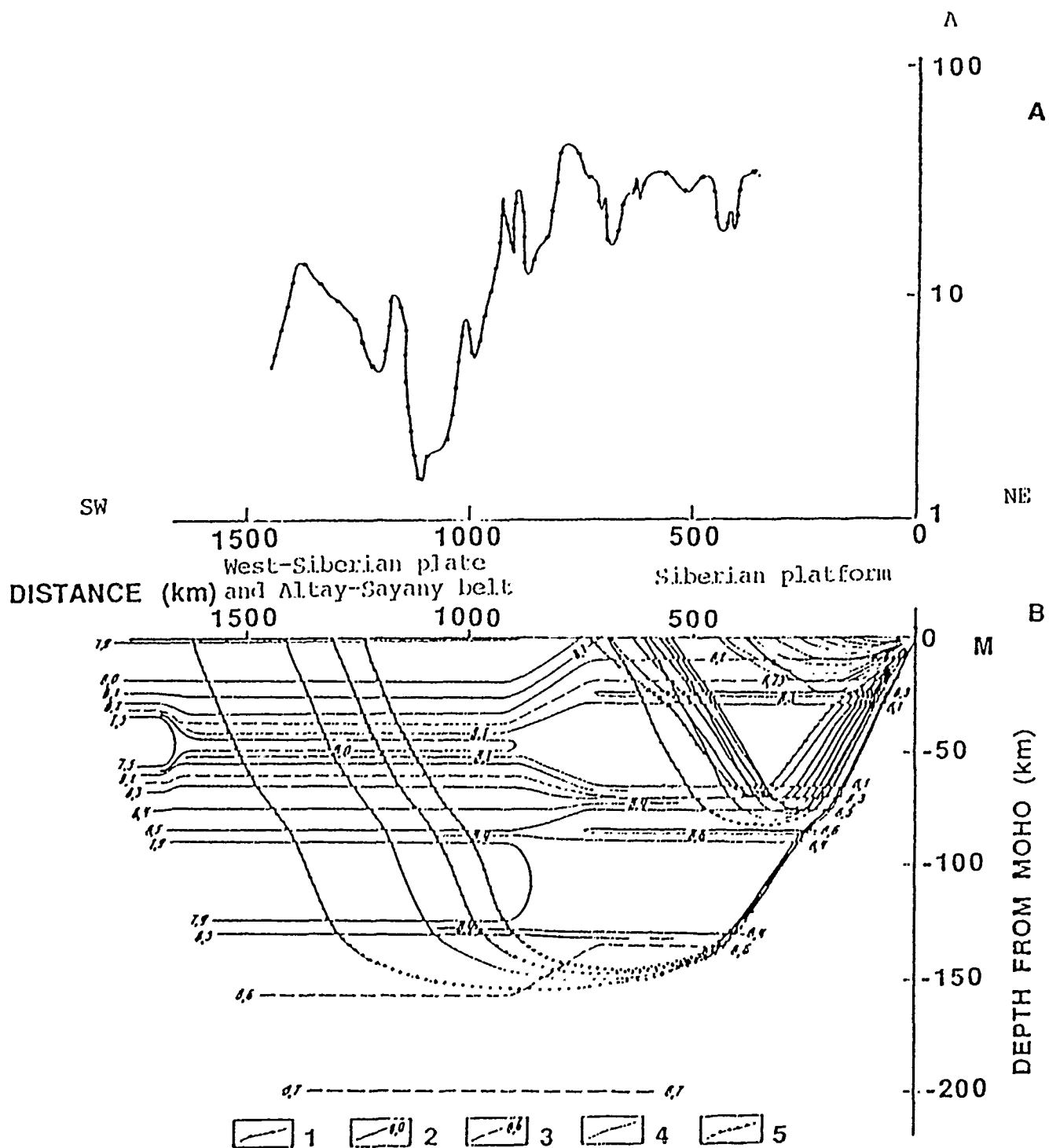


Figure 6. Barnaul-Tura long-range DSS profile (southern Siberia). A comparison of the observed amplitude versus distance plot $A(R)$ for the P_n wave (top) and the ray paths (bottom) calculated for a laterally heterogeneous upper mantle velocity model of the profile at regularly spaced interval in the angle of radiation from the source. 1 -- amplitude versus distance graph, 2 and 3 -- isovelocity contours from reliable (2) and unreliable (3) data, 4 and 5 -- ray paths of refracted waves calculated at one degree intervals in the angle of radiation (4) and for intermediate values of the angle (5). The density of the emergent rays is proportional to amplitude. (Adapted from Ryaboy *et al.*, 1987).

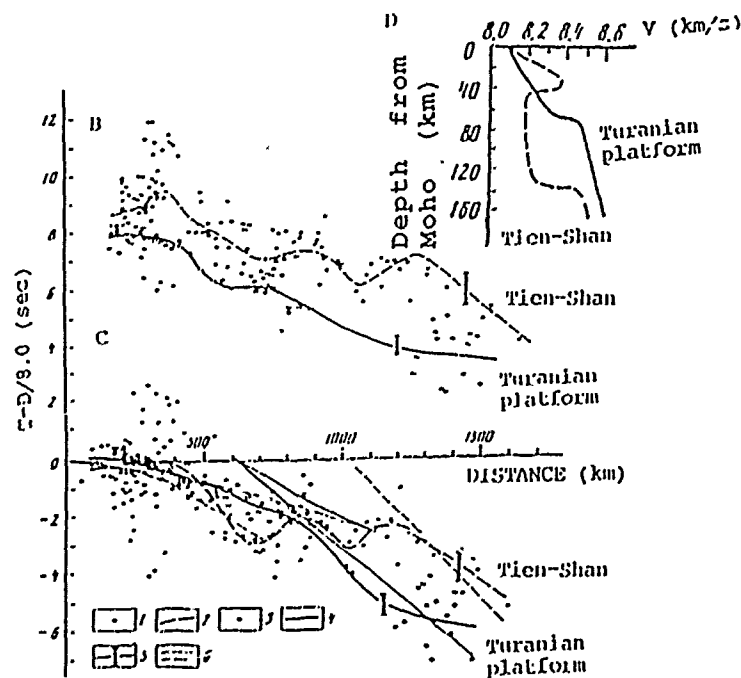
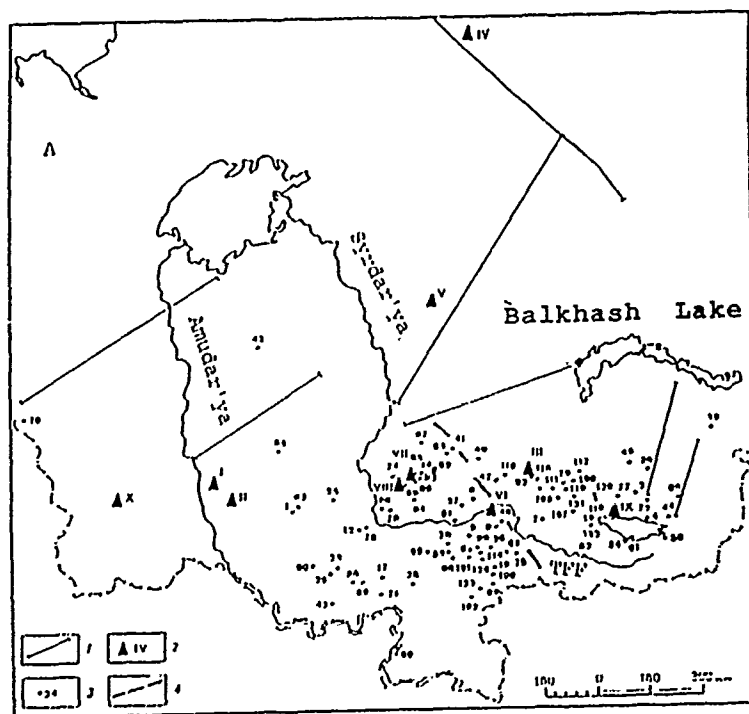


Figure 7. Results of studies of the upper mantle velocity structure beneath major geological provinces of Central Asia by explosion seismology. A). Location map (1 -- DSS profiles, 2 -- shot points of large industrial explosions, 3 -- recording stations, 4 -- Talasa-Fergana fault, TFF). B). Observed P_n wave travel-times, and C) recalculated to a smoothed Moho , for Turanian platform plate and Tien-Shan. D). Velocity versus depth variations in the upper mantle beneath the Turanian plate and Tien-Shan (1 and 2 -- P_n wave travel-times and averaged travel-time curve for Tien-Shan respectively; 3 and 4 -- the same as 1 and 2 but for the Turanian plate; 5 -- error of the averaged travel-time curves; 6 -- theoretical travel-time curves calculated for velocity sections in Figure 7B, the travel-time curves and velocity sections are designated similarly). (Adapted from Burmakov *et al.*, 1984).

1000 km is characterized by a 2-3 second shift relative to the travel-time curve for the Turanian plate. Inversion of the Pn travel-time curves using a ray tracing method shows the existence of a pronounced low-velocity layer in the upper mantle beneath Tien Shan and the lack of a similar layer under the Turanian plate (*Figure 7D*).

Figure 7C showed the presence of significant anomalies in the Pn-wave travel-times which are probably caused by small geological structures (individual basins, uplifts, and mountain ranges). As an example, Pn-waves travelling in the upper mantle beneath Tien Shan to the east of the Talasa-Fergana Fault (TFF) are delayed at distances of 300-400 km by 3 to 3.5 seconds relative to those in the western region of Tien Shan (*Figure 8*). This travel-time anomaly can be generated by lateral velocity variations in the upper mantle on the order of 0.5 km/sec. Interpretation of teleseismic observations by Vinnik et al. (1983) confirmed the results of explosion seismology data and also illustrated that the velocity variations must occur at depths of no less than 150-200 km.

Two large scale velocity inhomogeneities of the upper mantle with linear size more than 1000 km exist in Central Asia beneath the Tien Shan and the Turanian platform. Smaller sized velocity inhomogeneities were also located under western and eastern areas of Tien Shan and other geological units of the Turanian plate. For example, Pn-waves are locally faster beneath the Cis-Kopetdagh foredeep according to observations on the long-range DSS profile from the Kopetdag mountains to the Aral sea (Ryaboy, 1979).

Detailed seismic studies of the upper mantle based on DSS profiles using nuclear explosions as sources have been completed in Siberia. *Figure 9* shows the location of these profiles which cross all of the major geological provinces of Siberia (West-Siberian Hercynian plate and Pre-Cambrian Siberian platform) and neighboring regions (Egorkin et al., 1984, 1987; Vinnik, Egorkin, 1980, Pavlenkova, Egorkin, 1983; Ryaboy, 1985; Ryaboy et al., 1987; Barkhin et al., 1987). The average distance between shot points was 150-200 km and the length of the standard profiles (each reversed and overlapped) was 250-300 km. In addition, three to four reversed and overlapping profiles, each 1000-3000 km long, were obtained at 500-1000 km spacing for the nuclear shots. The explosions were recorded by three-component seismic stations with 10-20 km spacings between receivers.

Let us examine the Pn-wave travel-time curves for two long-range profiles, the Khanty-Mansiisk - Lena River profile, crossing the West-Siberian plate and Siberian platform, and sub-meridional Dikson-Khilok profile crossing the Siberian platform and Baikal rift zone (see profiles III-III and V-V accordingly on *Figure 9*). *Figure 10* shows the observed Pn-wave travel-time curves constructed for these profiles. The individual travel-time curves are very complicated and include shadow zones, sharp attenuation of the first arrivals, and breaks in the curves with offsets to later times.

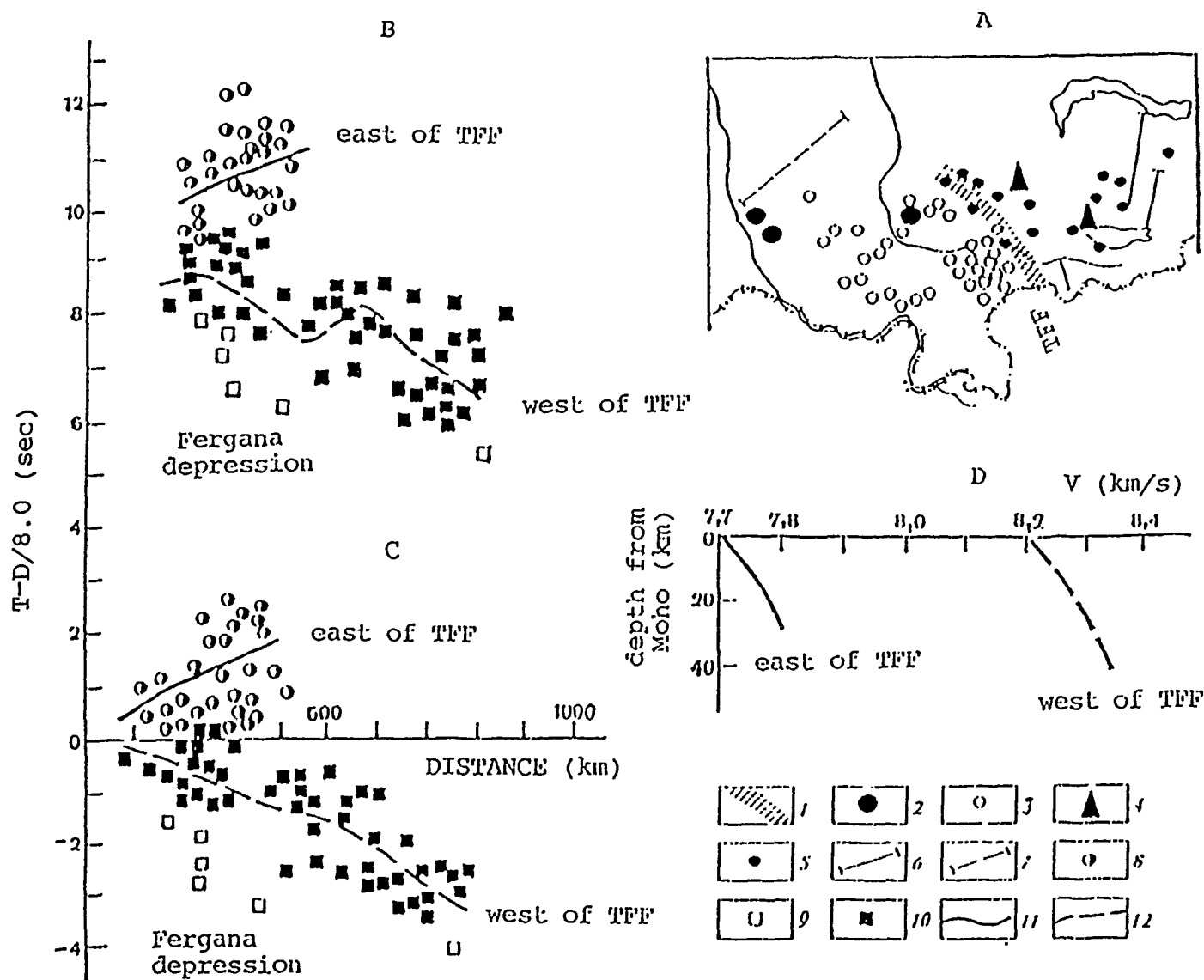


Figure 8. Results of studies of the upper mantle velocity structure of Tien-Shan by explosion seismology A). Location map. B). Observed P_n wave travel-times, and C) recalculated to smoothed Moho. D). Velocity versus depth variations in the upper mantle (depths are given from the Moho). 1 -- Talasa-Fergana fault (TFF); 2 -- shot points of large industrial explosions to the west of TFF; 3 -- seismic recording stations to the west of TFF; 4 -- the same as 2 but to the east of TFF; 5 -- the same as 3 but to the east of TFF; 6 -- DSS profiles used in constructing the velocity section for that region of Tien-Shan to the east of TFF; 7 -- the same as 6 but to the west of TFF; 8 -- P_n wave travel-times for that region of Tien-Shan to the east of TFF; 9 and 10 -- the same as 8 but to the west of TFF (9 -- for Fergana depression); 11 and 12 -- averaged travel-time curves and velocity sections corresponding to regions east (11) and west (12) of TFF. (Adapted from Burmakov *et al.*, 1984).

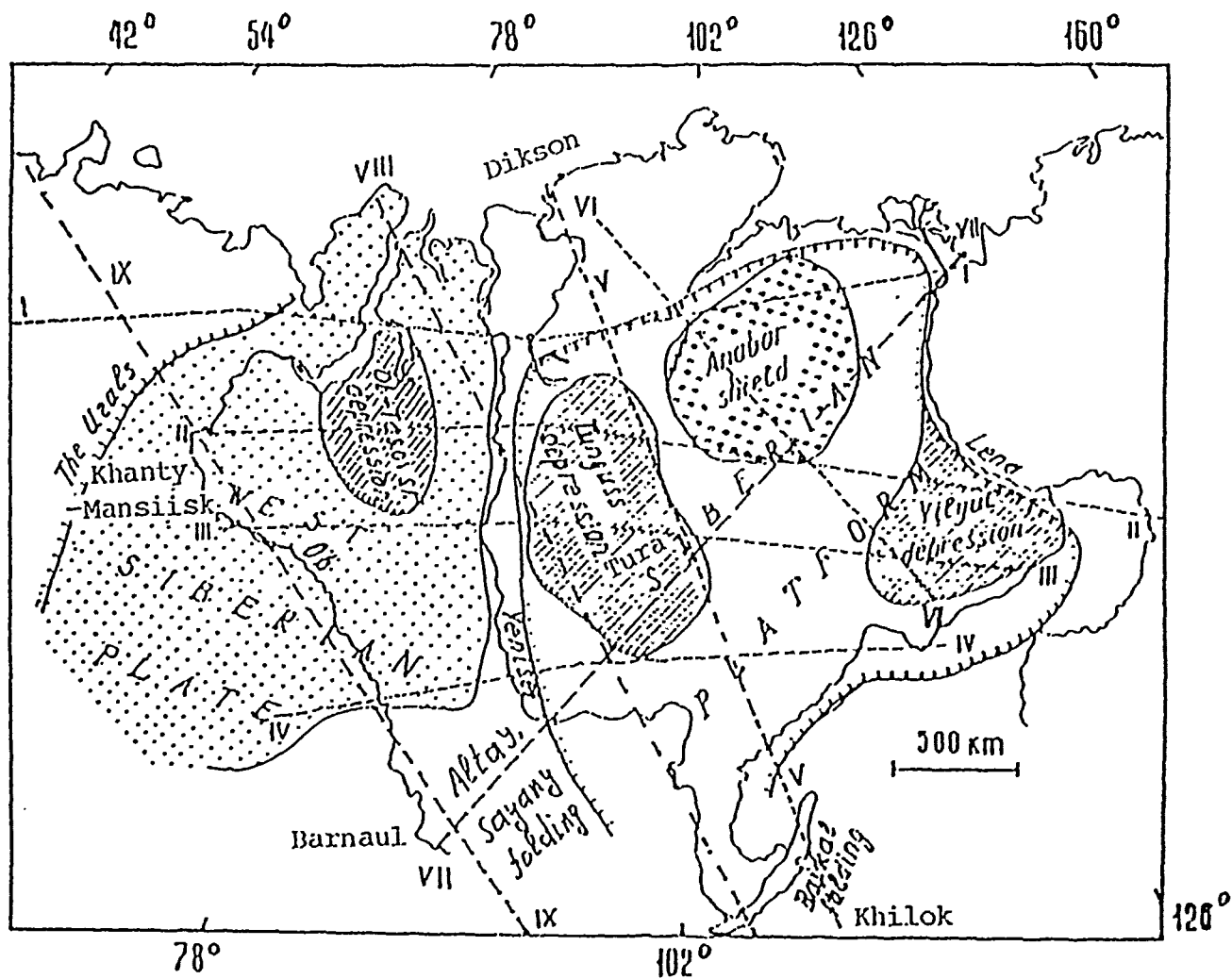


Figure 9. Location map of long range DSS profiles in Siberia. (Adapted from Egorkin *et al.*, 1987 with additions of V. Ryaboy).

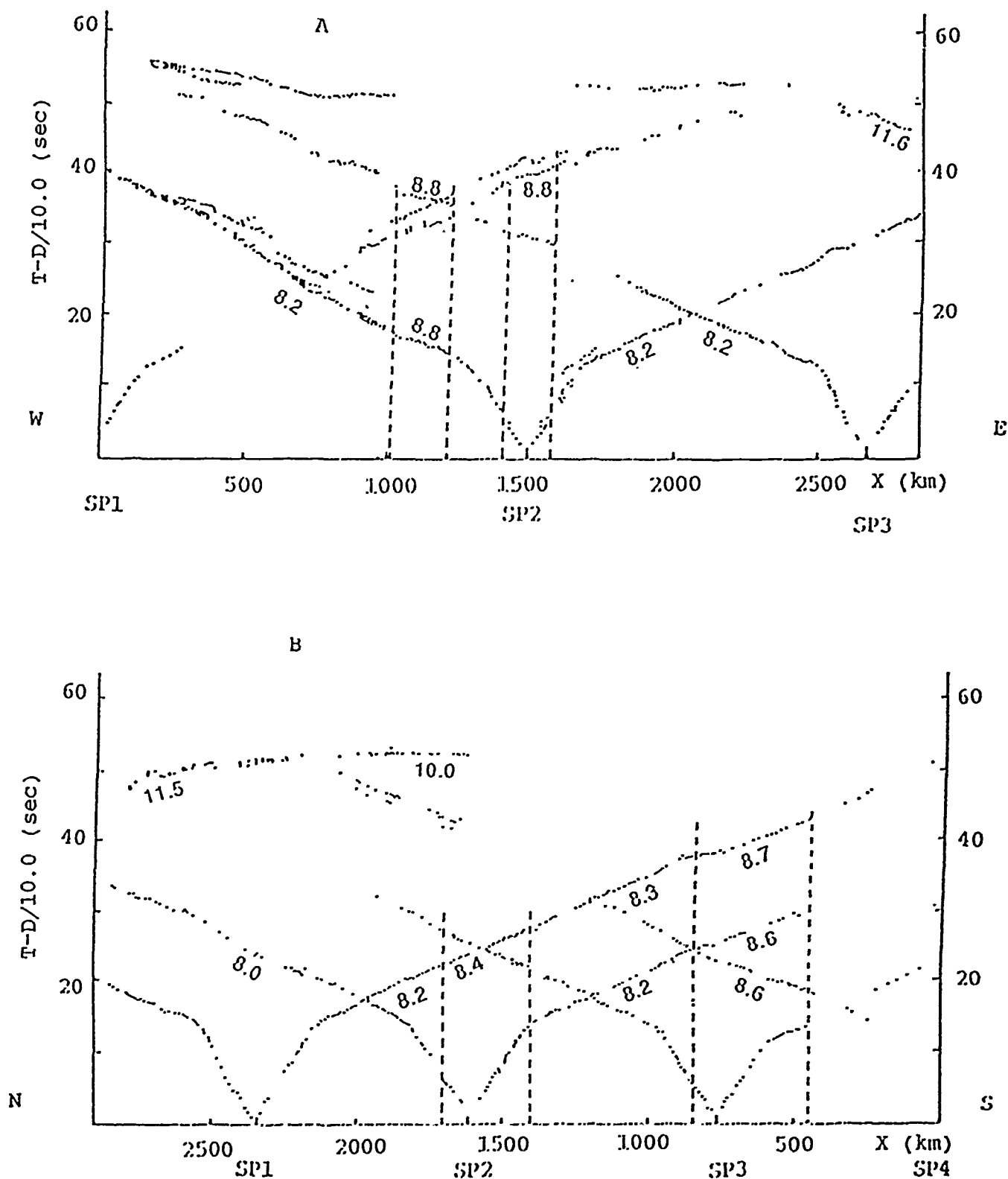


Figure 10. Observed travel-time curves of P_n and P waves recorded along two long-range DSS profiles in Siberia. A). West-East Khanty-Mansiisk - Lena River profile (Egorkin *et al.*, 1987). B). North-South Dikson-Khilok profile (Pavlenkova, Egorkin, 1983). Vertical dashed lines show elements of P_n wave travel-time curves with increased apparent velocity, depicted by numbers.

The apparent velocities range from 7.8-8.0 to 10.0-11.6 km/s and certain elements of the travel-time curves show locally increasing apparent velocities. Some of these elements were also observed at identical intervals of the profiles for reversed and overlapping travel-time curves, indicating strong small scale horizontal velocity variations in the upper mantle (from 7.8 to 8.6 km/s). Dashed lines on *Figure 10* show elements of Pn-wave travel-time curves with increased apparent velocities. The linear dimensions of these zones vary from 100 to 300 km. This is probably a conservative estimate of the smallest lateral velocity inhomogeneity located in the upper mantle that can be observed with Pn-waves. A similar high-velocity body in the lower lithosphere has also been detected in southern Sweden along the Oslo-Helsinki-Leningrad profile (Ryaboy, 1990) and in many other regions of Northern Eurasia.

Pn-wave travel-times for different geological units of Siberia vary substantially. *Figure 11* shows a comparison of the reversed Pn-wave travel-time curves recomputed to the Moho for the two long-range profiles mentioned above. One can see that the discrepancy between the travel-time curves constructed for the West-Siberian plate and the Siberian platform is 3-4 seconds (*Figure 11A*). For the northern and southern regions of the Siberian platform the difference is 1-2 seconds (*Figure 11B*).

The travel-time characteristics of the two reversed profiles are due to differences in the upper mantle velocity structure of the two regions. The Pn-wave travel-time curve for the southern areas of the Siberian platform, which includes the tectonically active Baikal rift zone, is characterized by a very long shadow zone within the 600 to 1200 km distance range. On the reversed profile covering the northern areas of Siberian platform (mainly the Tunguss depression) the shadow zone is substantially shorter.

The differences in the travel-time curves of the reversed profiles can be attributed to a low velocity layer (7.6 km/s) located beneath the Baikal rift zone and southern areas of the Siberian platform (Angaro-Lensk Terrace) at a depth range of 90 to 180 km. Further north, beneath the Tunguss depression, its thickness decreases significantly and the velocity increases to 8.2-8.4 km/s, which is typical for platforms of Northern Eurasia (Barkhin et al., 1987; Ryaboy, 1989).

Reference travel-time curves for Pn-waves were constructed to characterize and compare the average upper mantle velocity structure beneath major geological provinces of Northern Eurasia. These curves, based on explosion seismology data, were calculated by statistical smoothing of Pn-wave travel-times observed on long-range DSS profiles and regional seismic networks (*Figure 12A*). To make the effects of the upper mantle heterogeneities more evident, the earth's crust was "stripped off" and travel times were recomputed relative to a smoothed Moho (*Figure 12B*). The ancient Pre Cambrian platforms (East-European and Siberian) are characterized

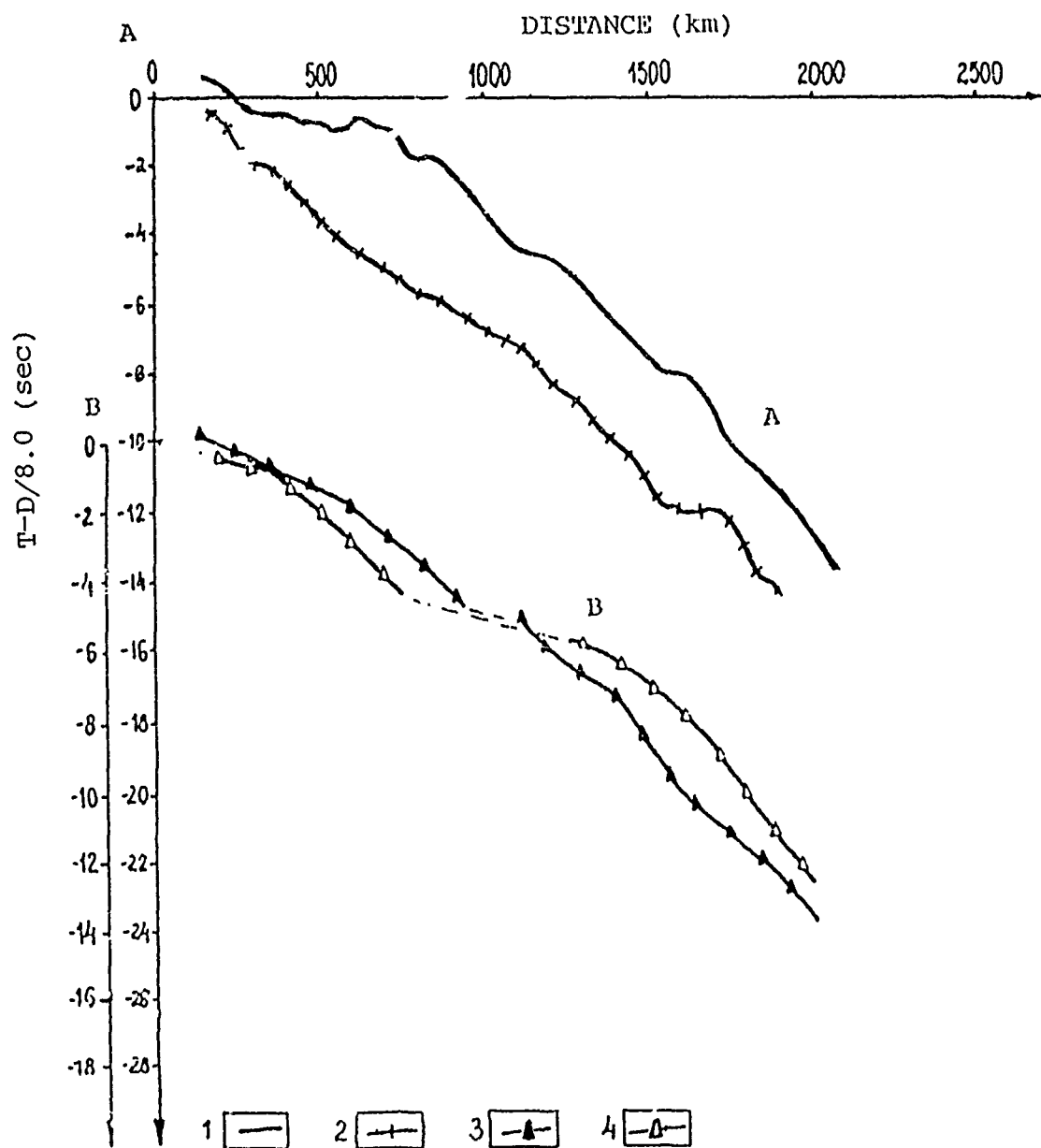


Figure 11. A comparison of reversed P_n travel-time curves for long-range DSS profiles in Siberia. A). West-East Khanty-Mansiysk - Lena River profile (1,2 -- travel-time curves for the West-Siberian platform plate and the Siberian platform respectively). B). North-South Dikson-Khilok profile (3,4 -- travel-time curves for northern and southern areas of Siberian platform including Baikal rift zone respectively). P_n wave shadow zones are depicted by dashed lines. (Adapted from Barkhin *et al.*, 1987).

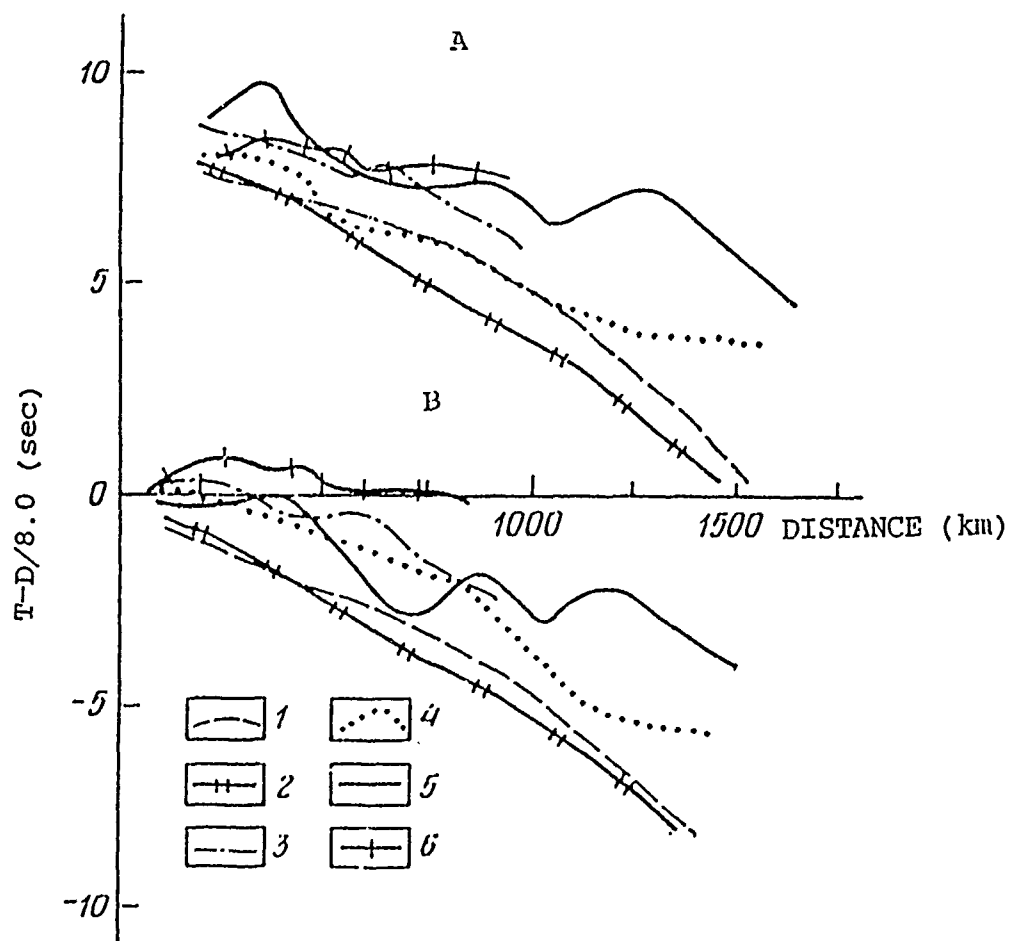


Figure 12. Averaged travel-time curves of P_n waves for major geological provinces of Northern Eurasia, according to explosion seismology data. A). P_n wave travel-times, observed and B) recalculated to a smoothed Moho. 1 -- East-European platform, 2 -- Siberian platform, 3 -- West-Siberian platform plate, 4 -- Turanian platform plate, 5 -- Tien-Shan, 6 -- Baikal rift zone. (Adapted from Ryaboy, 1985).

by the shortest travel-times, the tectonically active areas (Tien-Shan and Baikal rift zone) are characterized by the largest. Travel-time curves for the Turanian and West-Siberian platform plates occupy an intermediate position.

The differences between the travel-time curves shown in *Figure 12B* are as large as 5 seconds. This is substantially larger than the possible errors and suggests that there are large scale velocity inhomogeneities in the upper mantle related to the distribution of the major geological provinces of Northern Eurasia. The linear dimensions of the heterogeneities in the upper mantle detected in a such a manner are on the order of 1000 km or more, and they can be traced to depths of at least 200-300 km. The estimated contrast in the upper mantle necessary to explain the observed differences in Pn-wave travel-times is $\pm(4-5)\%$.

1.2.4 Conclusions

In the upper mantle of Northern Eurasia, observations from explosion seismology have revealed lateral velocity inhomogeneities at depths of not less than 200-300 km. The linear dimensions of the heterogeneities located using Pn-wave travel-time and amplitude observations vary from 100 km up to 1000 km and more, and the velocity contrast necessary to explain these observations varies between $\pm(4-5)\%$ relative to the mean velocity values. The velocity structure of the upper mantle usually changes with the transition from one geological province to another. The relationship between the velocity structure of the upper mantle and the distribution of geological units is complex and ambiguous.

The study of lateral inhomogeneities in the upper mantle is very important for a complete understanding of travel-times, amplitudes, and frequency content of seismic waves recorded at regional and teleseismic distances (McLaughlin et al., 1989; Barker and Murphy, 1989). Seismic waves recorded at regional and teleseismic distances propagate in substantially inhomogeneous media, but the analysis and interpretation of seismic records is usually based on one-dimensional velocity models. Overcoming this contradiction should improve the location and timing of events, as well as their estimated magnitude and yield.

Vladislav Ryaboy

REFERENCES

- Bache, T. C., S. R. Bratt, Wang, J., Fung, R. M., Cobryn, C., and Given, J. W., "The Intelligent Monitoring System," *Bull. Seism. Soc. Am. (in press)*, p. 18, 1990.
- Barker, B. W. and J. R. Murphy, "A lithospheric velocity anomaly beneath Shagan River test site: Part 1. Detection and Location with Network Magnitude Residuals," *Seismological research letters*, vol. 60, no. 1, p. 5, 1989.
- Barkhin, G. S., Nikitina, L. N., and Ryaboy, V. Z., *Izucheniye stroyeniya verkhney mantii po materialam profilnykh nablyudeniy GSZ (analiz metodov postroyeniya dvumernykh skorostnykh razrezov i nekotorye rezultaty)* [Study of the structure of the Upper mantle based on DSS profile observations (analysis of methods for constructing two-dimensional velocity sections and several results)], p. 65, All-Union institute for scientific and Technical information (in Russian), Moscow, 1987.
- Belyaevsky, N. A., *Zemnaya kora v predelakh territorii SSSR (The earth crust within boundaries of the territory of the USSR)*, p. 280, Nedra (Interior) Publisher House (in Russian), Moscow, 1974.
- Bratt, S. R., Swanger, H. J., Stead, R. J., Ryall, F., and Bache, T. C., "Initial results from the Intelligent Monitoring System," *Bull. Seism. Soc. Am. (in press)*, p. 29, 1990.
- Burmakov, Yu. A., Vinnik, L. P., and al., V. Z. Ryaboy et, "Study of the upper mantle structure of the Central Asia and Kazakhstan by explosion seismology," in *Issledovaniya zemnoi kory i verkhnei mantii seismoopasnykh zon territorii SSSR (Investigation of the earth crust and upper mantle in seismically hazardous zones of the territory of the USSR)*, pp. 70-98, Nauka (Science) Publisher House (in Russian), Moscow, 1984.
- Egorkin, A. V. and Pavlenkova, N. I., "Studies of mantle structure of the USSR territory on long-range seismic profiles," *Phys. Earth Planet Inter.*, no. 25, pp. 12-26, 1981.
- Egorkin, A. V., Zukanov, S. K., Pavlenkova, N. A., and Chernyshev, N. M., "Results of lithospheric studies from long-range profiles in Siberia," *Tectonophysics*, vol. 140, pp. 29-47, 1987.
- Khamrabaev, I. Kh. (editor), *Zemnaya kora i verkhnya mantia Srednei Azii (The earth crust and upper mantle of the Central Asia)*, p. 210, Nauka (Science) Publisher House (in Russian), Moscow, 1977.
- Khamrabaev, I. Kh. and Zunnunov, F. Kh. (editors), *Zemnaya kora i verhnaya mantiya Pamira, Gimalaev i Yuzhnogo Tian'-Shanya (The earth crust and the upper mantle of the Pamirs, Himalayas and Southern Tien-Shan)*, p. 160,

- Nauka (Science) Publisher House (in Russian), Moscow, 1984.
- Macelwain, J. B., "Roots of mountains or roots of continents?," *Bull. Seism. Soc. Amer.*, vol. 27, no. 1, pp. 29-34, 1937.
- McLaughlin, K. L., J. R. Murphy, and B. W. Barker, "A lithospheric velocity anomaly beneath Shagan River test site: Part 2. Imaging and Inversion with Amplitude Transmission Tomography," *Seismological research letters*, vol. 60, no. 1, p. 5, 1989.
- Murphy, J. R., "A new system for seismic yield estimation of underground explosions," *Seismological Research letters*, vol. 61, no. 1, p. 19, 1990.
- Pavlenkova, N. I. and Yegorkin, A. V., "Upper mantle heterogeneity in the northern part of Eurasia," *Physics of the Earth and Planetary Interiors*, vol. 33, no. 3, pp. 180-193, 1983.
- Razinkova, M. I. and Krasnopevtseva, G. V., "Geographical distribution of seismic studies of the earth crust and upper mantle," in *Glubinnoye stroenie slaboseysmichnykh regionov SSSR (Deep structure of weak seismic regions of the USSR)*, pp. 6-9, Nauka (Science) Publisher House (in Russian), Moscow, 1987.
- Ryaboy, V. Z., "Study of the structure of the lower lithosphere by explosion seismology in the USSR," *Journal of Geophysics*, pp. 593-610, 1977.
- Ryaboy, V. Z., *Struktura verkhney mantii territorii SSSR po seismicheskim dannym (The upper mantle structure of the territory of the USSR according to seismic data)*, p. 245, Nedra (Interior) Publisher House (in Russian), Moscow, 1979.
- Ryaboy, V. Z., "Lower lithosphere and asthenosphere of central and eastern regions of Northern Eurasia based on seismic data," *Izvestiya Academy of Sciences, USSR, Physics of the Solid Earth (English edition)*, vol. 21, no. 2, pp. 100-110, 1985.
- Ryaboy, V. Z., *Upper mantle structure studies by explosion seismology in the USSR*, p. 154, DELPHIC associates, 1989.
- Ryaboy, V. Z., "Upper mantle structure along a profile from Oslo (NORESS) to Helsinki to Leningrad, based on explosion seismology," *Bul. Seism. Soc. Am., Proceedings from the NORSAR symposium on Regional Seismic Arrays and Nuclear Test Ban Verification (in press)*, 1990a.
- Ryaboy, V. Z., "Crust-Upper mantle structure beneath IRIS stations in the USSR," *unpublished manuscript, Center for Seismic Studies*, p. 20, 1990b.

- Ryaboy, V. Z., Burmakov, Yu. A., Potap'ev, S. V., and al., L. N. Nikitina et, "The main features of the velocity structure of the upper mantle," in *Glubinnoye stroenie slaboseysmichnykh regionov SSSR (Deep structure of weak seismic regions of the USSR)*, pp. 86-117, Nauka (Science) Publisher House (in Russian), Moscow, 1987.
- Savarenskiy, Y. F., "K voprosu o neodnorodnosti v glubinnom stroenii Zemli (On the inhomogeneity in the deep structure of the Earth)," *Doklady AN SSSR (Reports of the USSR Academy of Sciences)*, (in Russian), vol. 27, no. 1, pp. 18-22, 1940.
- Vinnik, L. P., *Issledovaniya mantii Zemli seismicheskimi metodami (Seismic studies of the earth's upper mantle)*, p. 198, Nauka (Science) Publisher House (in Russian), Moscow, 1976.
- Vinnik, L. P. and Egorkin, A. V., "Volnovye polya i modeli litosfery-astenosfery po dannym seismicheskikh nablyudeniy v Sibiri (Wave fields and models of the lithosphere-asthenosphere, according to data from seismic observations in Siberia)," *Doklady AN SSSR (Reports of the USSR Academy of Sciences)*, (in Russian), vol. 250, no. 2, pp. 318-323, 1980.
- Vinnik, L. P. and Ryaboy, V. Z., "Deep structure of the East European platform according to seismic data," *Phys. Earth Planet. Inter.*, vol. 25, pp. 27-37, 1981.
- Vinnik, L. P., Sayipbekova, A. M., and Yudakhin, F. N., "Glubinnaya struktura i dinamika litosfery Tien Shanya (Deep structure and dynamics of the lithosphere of Tien Shan)," *Dokl. Akad. Nauk SSSR (in Russian)*, vol. 268, no. 1, pp. 143-146, 1983.
- Yegorkin, A. V., Zukanov, S. K., and Chernyshev, N. M., "Verkhnyaya mantiya Sibiri (The upper mantle of Siberia)," in *27-y mezhdunarodnyi geologicheskii kongress, Geofizika i a (27th International geological congress, Geophysics)*, vol. 8, pp. 27-42, Nauka (Science) Publisher House (in Russian), Moscow, 1984.
- Zverev, S. M. and Kosminskaya, I. P. (editors), *Seismicheskie modeli litosfery osnovnykh geostruktur territorii SSSR (Seismic models of the lithosphere for the major geostructures on the territory of the USSR)*, p. 184, Nauka (Science) Publisher House (in Russian), Moscow, 1980.

2.1 THREE-COMPONENT ANALYSIS OF REGIONAL PHASES AT NORESS AND ARCESS: POLARIZATION AND PHASE IDENTIFICATION

ABSTRACT

Particle motion characteristics of short-period three-component (3-C) data are compared for various seismic phases at NORESS and ARCESS, and their usefulness for phase identification is evaluated. Continuous recordings at the arrays of 3-C elements were processed during routine operation of the *Intelligent Monitoring System (IMS)*. The data set used in this study consists of 3822 arrivals extracted from the *IMS* database, and covers a period of about 2.5 months. First, polarization attributes and azimuth of the dominant linear motion are compared for local/regional phases (P_n, P_g, S_n, L_g) at the two arrays. P -type arrivals have larger angles of incidence at ARCESS than at NORESS, on average, for similar ranges of distance and signal-to-noise ratio (SNR). This can be partly explained by higher crustal velocities under the ARCESS array. Also, at ARCESS the ratio of horizontal to vertical power is similar for S_n and L_g , on average, while at NORESS it is larger for S_n . S_n and L_g azimuths at ARCESS (and L_g azimuth at NORESS, with more scatter) provide good estimates of backazimuth (with a 180° ambiguity), and indicate predominance of SH motion at ARCESS. In the second part of this study multivariate data analysis is performed to obtain phase identifications (with associated confidence), using polarization attributes as predictors. P - and S -type phases are distinguished with a success rate of 82% at NORESS and 89% at ARCESS. The performance is even better for P -type arrivals with 3-C SNR > 2 (96% and 98%, respectively). S_n and L_g are correctly identified for 74% of S -type phases at NORESS and 64% at ARCESS. Contamination of L_g by S_n coda at shorter ranges, and dominant SH motion for both S -type phases at ARCESS affect the performance. This study shows the importance of evaluating each 3-C station individually.

2.1.1 Introduction

With the advent of three-component (3-C) stations located within the USSR, such as the new IRIS stations (Given, 1990), the importance of 3-C data for detection, location and identification of seismic events must be evaluated. This is particularly relevant to the automated processing of continuous data, as performed in the *Intelligent Monitoring System (IMS)* (Bache *et al.*, 1990). The noise reduction and added information from frequency-wavenumber (F-K) analysis of array data (e.g., Kvaerna and Ringdal, 1986) are not available at single 3-C stations, so greater emphasis must be placed on polarization. Polarization, along with other signal properties, such as frequency, duration, envelope, and relative arrival time and amplitude, is a possible indicator of phase type. For some phase types, it has been used to estimate backazimuth and slowness (US/GSE/49, 1987; Magotra *et al.*, 1987;

Jurkevics, 1988; Ruud *et al.*, 1988, Suteau-Henson, 1990; Walck and Chael, 1991; Jarpe and Dowla, 1991) Studies of backazimuth estimation from polarization at RSTN stations (US/GSE/49, 1987; Walck and Chael, 1991) indicate that the near-surface geology can strongly affect the scatter in the estimates. In practice, polarization is site-dependent, and its use for seismic monitoring must be examined in this context.

In this study, polarization of regional phases and its use for phase identification are compared at the 3-C arrays of NORESS and ARCESS (four of the 25 elements are 3-C at each array). The data set used is extensive, 3822 arrivals, and was extracted from the *IMS* database from about 2.5 months of routine operation. Therefore, it is typical of a continuous monitoring situation. Another advantage is that, from combining the results of F-K analysis, single- or multiple-array locations, and comparison with known mine locations, event locations are generally well constrained. Bratt *et al.* (1990) compared *IMS* solutions to those from the Finnish local network, and found a median location separation of 23.5 km, the largest discrepancies usually being due to low signal-to-noise ratio (SNR). Also, the SNR at both NORESS and ARCESS is particularly good, on average, for regional phases over a wide frequency band, and the use of four 3-C elements available at each array provides further noise reduction. Therefore, this is an appropriate data set to begin evaluating the use of 3-C data in the *IMS*.

In the first part of this study, the polarization characteristics of regional phases (*Pn*, *Pg*, *Sn*, *Lg*) recorded at the arrays of 3-C elements at NORESS and ARCESS are compared. This study is an extension of the work of Jurkevics (1988) who investigated the particle motion of regional phases at NORESS, based on a data set of 93 events of various types, with good coverage in distance, azimuth, and SNR. His study focused on the effects of SNR and the frequency band used in the analysis. We study the ARCESS site and use a data set that is much larger and more representative of a seismic monitoring situation. Also, the important effect of epicentral distance is investigated, as well as backazimuth estimation for all phase types. The method developed by Jurkevics was previously adapted for use in the automated processing of the *IMS* (Bache *et al.*, 1990).

Polarization plays a major role in phase identification of 3-C data. The need to improve this capability in the *IMS* for arrays and to develop it for 3-C single stations motivated the second part of this study, where an approach for automated phase identification based on signal characteristics is described. It uses classical methods of multivariate data analysis. Similar techniques have been used, for example, in oil exploration (Mason and Full, 1986), as well as in seismic event discrimination (e.g., Dysart and Pulli, 1990). The procedure described in this paper can be integrated within the phase identification software of the *IMS*.

Finally, as an application of this approach, the capabilities of polarization for identifying regional phases at NORESS and ARCESS are investigated. Polarization is only one among other signal properties that are useful for phase identification in the *IMS*, especially at array stations. However, the method proposed in this study can easily use other predictors of phase type. Also, the experience acquired with this well-controlled data set will be informative when applying such techniques to single stations in more complex situations, such as the IRIS stations in the USSR.

2.1.2 The Data

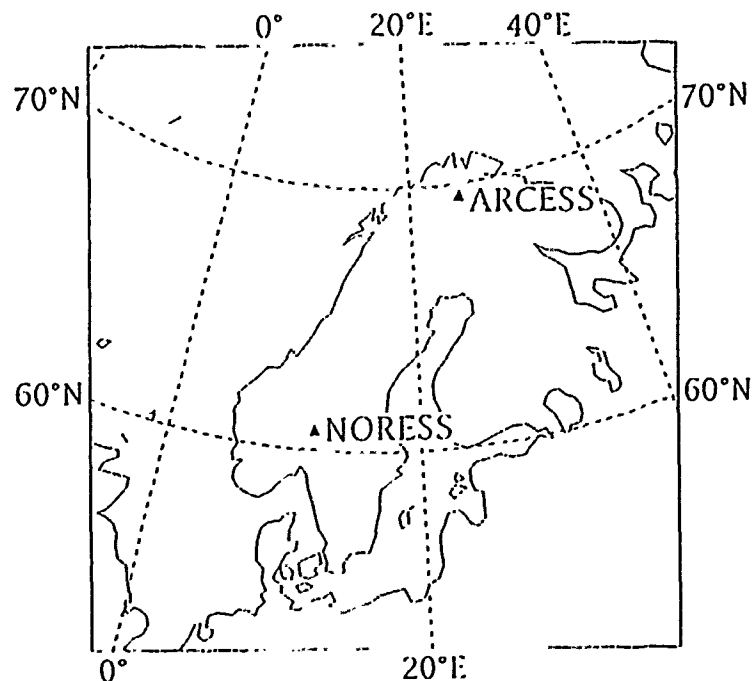
The data set used for this study was extracted from the *IMS* database, and covers about 2.5 months of routine processing of continuous data from NORESS and ARCESS (from November 7 to 25, 1989 and from January 16 to March 11, 1990). All selected arrivals are from *IMS* "final event solutions" that have been reviewed by an analyst. Detected arrivals with final phase identification *Pn*, *Pg*, *Sn*, or *Lg* (see Bache *et al.*, 1990) were used, with the exception of those from events identified as "multiple" or "mixed" by the analyst (i.e., those contaminated with signals from interfering events). Arrivals added by the analyst were not included because their polarization attributes were not measured.

A total of 3822 arrivals were analyzed: 1391 from NORESS (473 *Pn*, 234 *Pg*, 97 *Sn*, 587 *Lg*), and 2431 from ARCESS (1029 *Pn*, 156 *Pg*, 223 *Sn*, 1023 *Lg*). Figure 1 shows a map with the locations of the arrays (*top*), and histograms of the distance and SNR distributions (see next section for a definition of "3-C SNR") for these arrivals (*bottom*). Because this data set reflects the seismicity recorded at the arrays over a given period of time, its coverage (in distance, azimuth, and SNR) is not uniform. The seismicity is dominated by local ($< 2^\circ$ epicentral distance) and near-regional events ($< 5^\circ$). The NORESS set includes a larger proportion of local and far-regional (between 5° and 14°) events than the ARCESS data. Most arrivals have 3-C SNR < 10 ; at NORESS the average is 2.5 and at ARCESS it is 2.8. The difference in SNR between the two arrays is due to relatively more arrivals with very low SNR (< 1.6) at NORESS. The characteristics of events processed by the *IMS* are described in detail in Bratt *et al.* (1990).

2.1.3 Polarization of Regional Phases at NORESS and ARCESS

The Polarization Measurements

During the *IMS* processing a set of polarization measurements is made and stored in the database for each detection (Bache *et al.*, 1990). Polarization analysis is performed using the method developed by Jurkevics (1988). Its adaptation to automated processing is described in Suteau-Henson (1990), and is summarized below. The covariance matrix is calculated for a set of overlapping time windows. The axes of the "polarization ellipsoid" are found by solving the eigenproblem for



NORESS

ARCESS

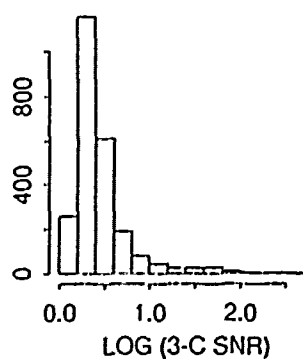
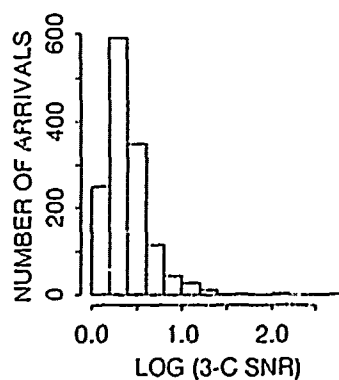
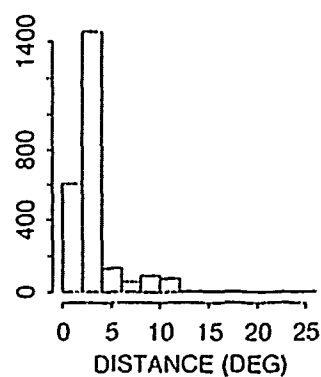
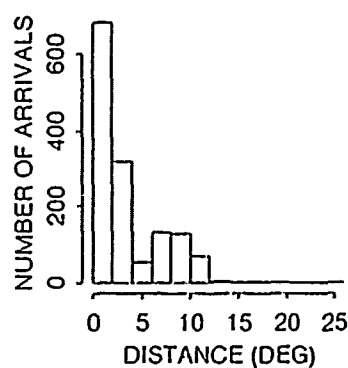


Figure 1. The map (*top*) shows the study area, with the locations of NORESS (60.735° N, 11.541° E) and ARCESS (69.535° N, 25.506° E). Histograms (*bottom*) show the distributions of epicentral distance and 3-C SNR for the 3822 arrivals at NORESS and ARCESS used in this study.

the covariance matrix (Jurkevics, 1988). Each of the time windows is two-seconds long, and the set of windows covers an eight-second segment, centered on the onset time determined from automated processing. This calculation is performed in each of the frequency bands 1-2, 2-4, 4-8, and 8-16 Hz. The bands with 3-C SNR above 1.5 (or the band with the largest 3-C SNR below 1.5) are selected. The "3-C SNR" estimate is defined as the ratio of maximum signal to average (mean) noise 3-C amplitude, where the 3-C amplitude is the sum of amplitudes on all three axes of the polarization ellipsoid. Pre-arrival noise, measured in an eight-second segment, starting 20 seconds before the arrival, is used. The length of the noise segment is the same as that of the signal segment. It must be long enough to provide stable estimates. However, a longer window would be more likely to include seismic phases along with pre-event or signal-generated noise. Also, the noise segment must be positioned so as not to include the onset of signal. The covariance matrices are averaged over the selected frequency bands, and also over the array of four 3-C elements. "Polarization attributes" are derived from the axes of the polarization ellipsoid. Some of them are more relevant to *P*-type phases, and are measured at the time of maximum rectilinearity for the arrival. They are: rectilinearity (*rect*, defined as $(1 - (\lambda_2 + \lambda_3) / 2\lambda_1)^2$, where the λ_i 's represent the power along the principal axes, and are ordered so that $\lambda_1 \geq \lambda_2 \geq \lambda_3$), and incidence angle (*inc1*) and azimuth of the long axis (i.e., direction of principal rectilinear motion). Our definition of rectilinearity is similar to that of Jurkevics (1988), who uses amplitude instead of power for the λ_i 's and does not square the expression. Others are "S-type" attributes, and are measured at the time of maximum 3-C amplitude. They are: planarity (*plan*, defined as $(1 - \lambda_3 / \lambda_2)^2$), ratio of horizontal to vertical power (*H/V*), and incidence angle of the short axis (*inc3*). The latter represents the incidence angle of the normal to the plane of principal planar motion; therefore, a small (large, respectively) value indicates particle motion mostly in a near-horizontal (near-vertical, respectively) plane. Our definition of planarity differs from that of Jurkevics (1988). It has the advantage of being independent of the amplitude of the long axis. With this definition, planarity will be large if the short axis is small compared to the middle axis, which indicates planar motion, regardless of the degree of rectilinearity. These six polarization attributes are useful for characterizing regional phases.

In addition to the polarization measurements, 3-C SNR averaged over the selected frequency bands and frequency (center of the wide band used in the analysis) were extracted from the database. The backazimuth and epicentral distance obtained for the final event solution are also used, the former for comparison with the azimuth from polarization analysis, and the latter to study its influence on polarization.

Polarization of P-Type Phases

In this section, the polarization characteristics of P_n and P_g are compared at NORESS and ARCESS. Then, the influence of SNR and distance is investigated. Finally, backazimuth estimation is evaluated at the two arrays.

Polarization Characteristics.

In Table 1 the distributions of polarization attributes are compared for P_n and P_g , at NORESS and ARCESS. At both arrays and for both phases, rectilinearity averages about 0.6 and planarity 0.1. Low planarity is expected for P -type phases. $inc3$ has a median close to 80° , indicating a near-vertical plane of principal motion, as expected.

Significant differences between NORESS and ARCESS are observed for the attributes $inc1$ and H/V , which are highly correlated for P -type phases. For example, $inc1$ for P_n has median values 12° lower at NORESS than at ARCESS. Similarly, the medians for the distribution of H/V are 0.65 at NORESS and 0.86 at ARCESS. Therefore, P -type local and regional phases have larger incidence angles (relatively more horizontal motion) at ARCESS than at NORESS.

Effect of SNR and Distance.

The observed differences between NORESS and ARCESS could simply reflect differences in SNR and/or distance coverage. Therefore, the effects of SNR and distance on $inc1$ and H/V were investigated. Figure 2 shows $inc1$ as a function of 3-C SNR for P_n and P_g , at the two arrays. A large scatter is observed for 3-C SNR < 2 , which could bias the results. However, if only arrivals with 3-C SNR > 2 are included, the median of $inc1$ becomes 38° for P_n and 39° for P_g at NORESS, and 51° for P_n and 55° for P_g at ARCESS, and therefore, is not significantly different from that obtained for the entire SNR range.

In Figure 3 $inc1$ is plotted as a function of epicentral distance for arrivals with 3 C SNR > 2 . Most arrivals are from local or near-regional events ($< 5^\circ$). The cross-over distance between P_g and P_n is about 1.7° . Beyond the cross-over distance, P_g is contaminated by P_n coda, and by 5° is generally not observed. This contamination explains why P_n and P_g have similar polarization characteristics in the near-regional range. At both arrays, there is a difference between near-regional and far-regional P_n arrivals. At far-regional distances $inc1$ is smaller, as expected. However, the observed systematic difference between the median of $inc1$ at NORESS and ARCESS persists for both P_n and P_g , regardless of distance. This indicates that it is probably a site effect, which could be caused by different velocity structures beneath the two arrays.

TABLE I
DISTRIBUTIONS OF POLARIZATION ATTRIBUTES

Attribute	Symbol		NORESS				ARCESS			
			<i>P_n</i>	<i>P_g</i>	<i>S_n</i>	<i>L_g</i>	<i>P_n</i>	<i>P_g</i>	<i>S_n</i>	<i>L_g</i>
Rectilinearity	<i>rect</i>	Mean	0.55	0.58	0.34	0.38	0.60	0.60	0.36	0.43
		Median	0.57	0.59	0.32	0.36	0.62	0.63	0.35	0.42
		S.D.	0.17	0.15	0.14	0.14	0.16	0.12	0.11	0.14
Planarity	<i>plan</i>	Mean	0.12	0.13	0.16	0.13	0.15	0.12	0.08	0.09
		Median	0.10	0.10	0.13	0.11	0.11	0.11	0.06	0.08
		S.D.	0.10	0.10	0.12	0.11	0.13	0.09	0.07	0.07
Horizontal/Vertical	<i>H/V</i>	Mean	0.65	0.58	1.51	1.11	0.88	0.90	1.36	1.39
		Median	0.65	0.58	1.53	1.12	0.86	0.91	1.39	1.38
		S.D.	0.29	0.19	0.57	0.39	0.31	0.23	0.36	0.44
Incidence Angle	<i>inc 1</i>	Mean	43°	41°	75°	71°	52°	54°	79°	79°
		Median	40°	38°	79°	78°	52°	54°	82°	82°
		S.D.	17°	14°	15°	19°	13°	10°	11°	12°
Short-Axis Incidence	<i>inc 3</i>	Mean	71°	75°	34°	60°	70°	76°	54°	63°
		Median	77°	80°	24°	65°	78°	82°	56°	70°
		S.D.	17°	14°	25°	22°	19°	13°	24°	22°

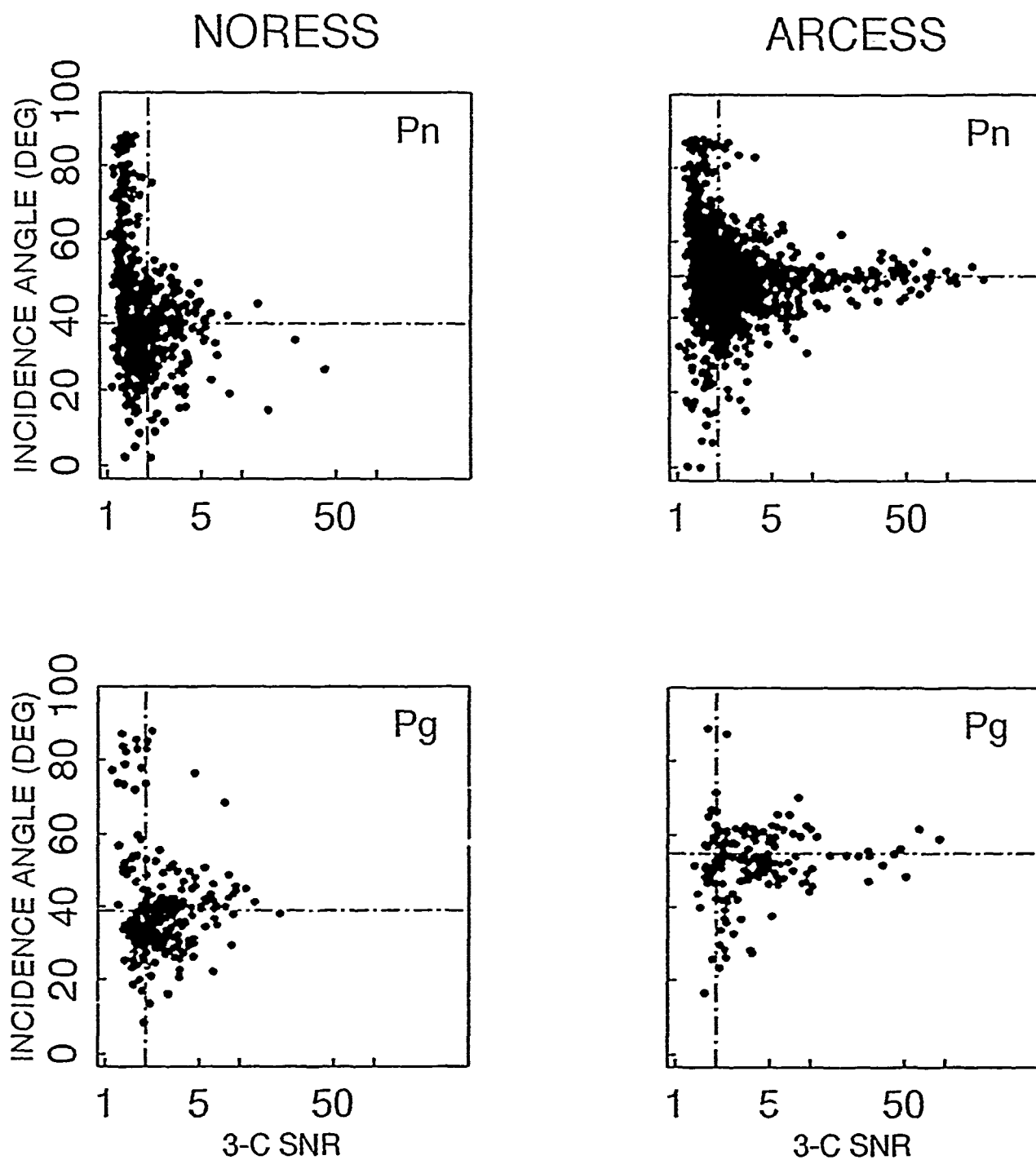


Figure 2. Incidence angle ($inc\ I$) is plotted against three component signal to noise ratio ("3-C SNR") for Pn (top) and Pg (bottom) arrivals, at NORESS (left) and ARCESS (right). Large scatter is observed for 3-C SNR < 2 (left of dashed vertical line). The dashed horizontal line denotes the median of the observations.

NORESS

ARCESS

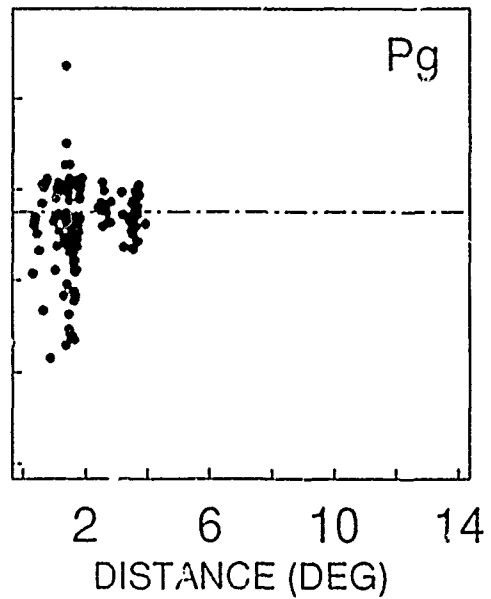
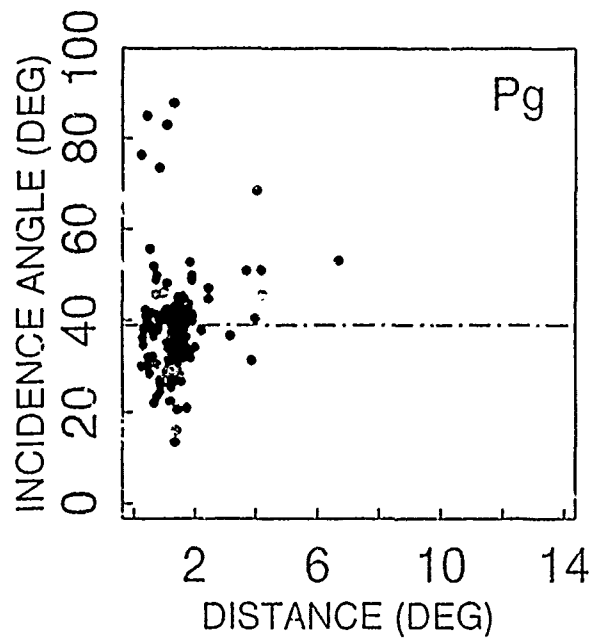
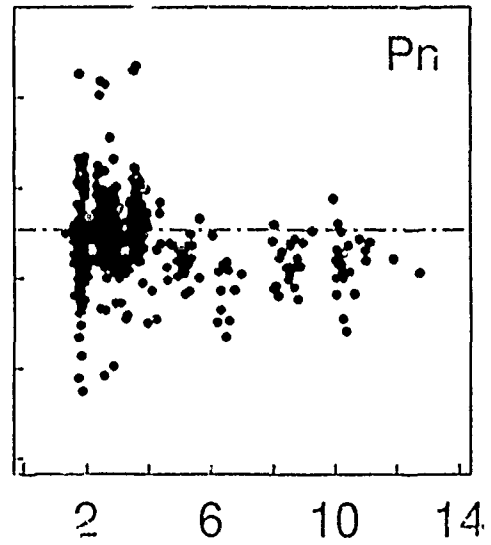
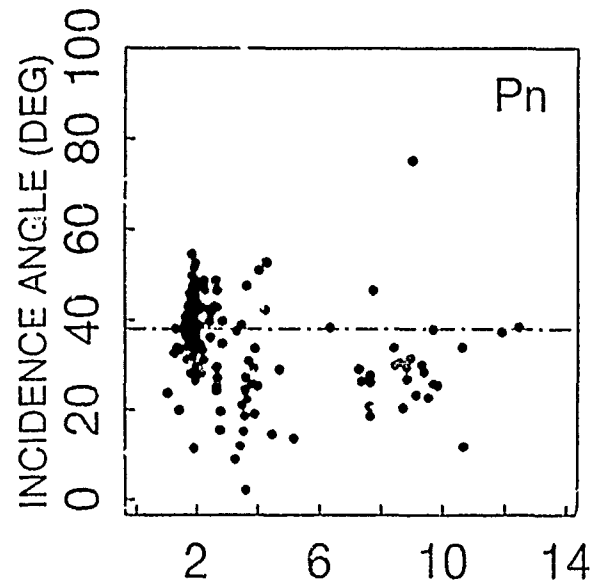


Figure 3. Incidence angle (*inc1*) is plotted against epicentral distance for *Pn* (top) and *Pg* (bottom) arrivals with 3-C SNR > 2, at NORESS (left) and ARCESS (right). The dashed horizontal line denotes the median of the observations.

Such differences in the polarization of *P*-type arrivals between the two arrays are rather surprising, since both are located on hard rock. The larger average incidence angle at ARCESS could be due to a larger ratio of upper-crust to upper-mantle velocity. Assuming similar upper-mantle velocities for the two arrays (Ryaboy, personal communication, 1990), this would be consistent with a higher upper-crustal velocity at ARCESS. The local geology is different at the two arrays. It is more complex at NORESS, where the 3-C array is located in an area of granites and rhyolites, with gabbro intrusions of contrasting properties (Ruud and Husebye, 1991). The average *P*-wave velocities are 5.5 to 6.0 km/s (Mykkeltveit *et al.*, 1990). A seismic reflection profile indicates the presence of a dipping reflector (Mykkeltveit, 1987). The ARCESS array is located entirely on gabbro outcrops which are characterized by high density and high velocity. Assuming a *P*-wave velocity of 5.91 km/s for granite at NORESS and 6.74 km/s for gabbro at ARCESS (Mykkeltveit, 1987), the corresponding velocity ratio is 0.88. For comparison, the ratio of the sines of "true" incidence angle (derived from the observed apparent incidence angle, assuming a Poisson's ratio of 0.25) is 0.74 for the median of the observations. Other site effects, such as dipping layers and other lateral variations in structure, may bias the measurements.

Backazimuth Estimation.

At the top of *Figure 4* the azimuth residuals (the difference between the backazimuth from polarization and that from the final event solution) are plotted as a function of 3-C SNR for all *P*-type arrivals at each array. For arrivals with 3-C SNR > 2, their distribution has more outliers at NORESS than at ARCESS. The bottom of *Figure 4* shows histograms for the subset of azimuth residuals smaller than 90° at each array. The scatter is larger at NORESS. Therefore, backazimuth estimation using *P_n* or *P_g* is more stable at ARCESS than at NORESS (fewer outliers and less scatter). The standard deviation for the subset with 3-C SNR > 2 and residual less than 60° is 11° for *P_n* and 10° for *P_g* at NORESS, compared to 7° for both *P_n* and *P_g* at ARCESS. This estimate of 11° for *P_n* at the array of 3-C elements at NORESS is similar to those obtained by Jurkevics (1988): 10°-14°, around 4 to 10 Hz. It is also close to the estimate of 14°, at a 3-C element, found in a previous study that used a smaller data set (Suteau-Henson, 1990).

The results from this study confirm previous theoretical and empirical ones (e.g., Harris, 1990; Jurkevics, 1988; Suteau-Henson, 1990), which showed SNR is a major factor controlling the variance on the estimates of polarization and backazimuth for *P*-type phases. Although much of the scatter observed for 3-C SNR < 2 is probably due to limitations of the automated data processing and might be reduced through parameter optimization, such a threshold appears to be an intrinsic property of direction estimation using 3-C data (Harris, 1990; Walck and Chael, 1991).

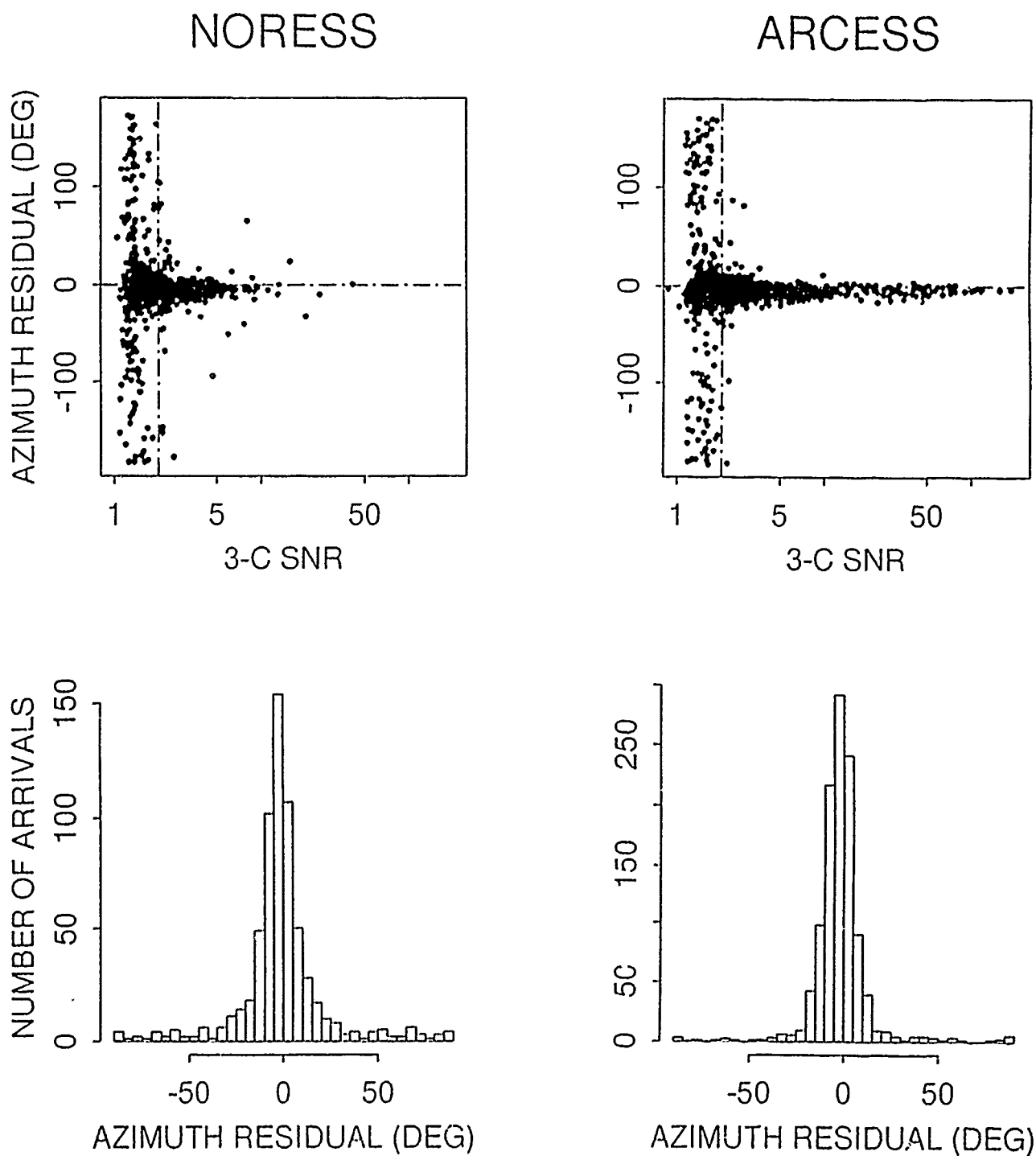


Figure 4. At the *top*, azimuth residuals (backazimuth from polarization minus backazimuth from the *IMS* final event solution) are plotted against 3 C SNR for *P*-type arrivals (*Pn* and *Pg*), at NORESS and ARCESS. The dashed vertical li. denotes a 3-C SNR of 2. At the *bottom*, histograms show the distributions of azimuth residuals between -90° and $+90^{\circ}$, at NORESS (*left*) and ARCESS (*right*).

Polarization of *S*-Type Phases

The polarization characteristics of *Sn* and *Lg* are compared at the two arrays, and the effect of SNR and distance investigated in this section. The differences in frequency content and their impact on the observed polarization are also studied. Finally, the capabilities for backazimuth estimation are evaluated.

Polarization Characteristics.

The distributions of attributes for *Sn* and *Lg* at NORESS and ARCESS are given in Table 1. At both arrays, the *S*-type phases have lower rectilinearity than the *P*-type phases due to their more complex particle motion. *incl* is large (median of about 80°), indicating near-horizontal dominant linear motion. Planarity has a large variance for all phases, so that the actual differences between phases are small. This is due to the fact that its value strongly depends on the length of the short axis of the polarization ellipsoid, and, therefore, on the noise level and SNR. The largest difference observed is between *Sn* at NORESS and ARCESS.

Significant differences between the two arrays are found in the relative amount of vertical motion. At NORESS *H/V* has a median of 1.1 for *Lg*, indicating nearly equal amounts of horizontal and vertical motion, while for *Sn* it is 1.5, i.e., horizontal motion dominates. In contrast, at ARCESS, both phases have medians of 1.4, which shows predominantly horizontal motion. Further differences are observed in the *inc3* distributions, although the scatter is rather large. The median for *Lg* is 65° at NORESS and 70° at ARCESS, indicating a near-vertical plane of dominant motion. However, for *Sn* at NORESS, the median is 24° (i.e., particle motion mostly in a near-horizontal plane), while it is 56° at ARCESS. This difference is significant in spite of the large scatter. Our results for NORESS confirm those of Jurkevics (1988): *Sn* and *Lg* have significantly different polarization, and therefore, should be distinguishable on the basis of their polarization attributes, especially *H/V* and *inc3*. Differences between *Sn* and *Lg* polarization are not as strong at ARCESS: mostly, rectilinearity is slightly higher and the plane of dominant motion more near-vertical for *Lg*. This implies that an *Sn* / *Lg* discriminant based on the polarization results of NORESS data would not work at ARCESS, and illustrates the site dependence of such a discriminant.

The effects of near-surface geology (velocities, lateral heterogeneity) on the particle motion of *S*-type phases are difficult to assess, due to their complexity. Such effects have been studied in strong-motion seismology (e.g., Vidale, 1986). *SV* motion can be complicated by non-linear *SV*-to-*P* conversions, and become elliptical. More work is needed to determine if differences in receiver structure at NORESS and ARCESS can account for the observed polarization properties of both *P*-type and *S*-type phases.

Effect of SNR and Distance.

Most *S*-type phases at both arrays have 3-C SNR between 1.6 and 5, and the main effect of low SNR is to increase the scatter in the estimates. Distance, however, strongly affects polarization. *Figure 5 (top)* shows H/V as a function of epicentral distance at the two arrays for *Sn* and *Lg*. Between the cross-over distance (about 1.7°) and a distance of about 5° , *Lg* is contaminated by *Sn* coda. Since the noise window used to select the frequency band for the analysis is taken before the *Sn* onset, polarization measurements are made at frequencies including a significant component of *Sn* coda and are thus contaminated. This results in considerable overlap between the H/V distributions for *Sn* and *Lg* in that distance range for both arrays. At NORESS, the far-regional *Lg* (distance $> 5^\circ$) has more vertical amplitude than local *Lg*, on average, with a mean of 0.84 for H/V , compared to 1.18. This strong effect is not observed at ARCESS. At far-regional distances, the *Sn* and *Lg* populations tend to separate, much more so at NORESS than at ARCESS. Similar effects are observed for *inc3* (*Figure 5, bottom*). At large distances, the plane of dominant motion is mostly near-vertical for *Lg* at both arrays (but more so at NORESS), while it is closer to horizontal, on average, for *Sn* at NORESS: for distances $> 5^\circ$, the distribution of *inc3* for *Lg* (*Sn*, respectively) at NORESS has a mean of 74° and a standard deviation of 14° (32° and 25° , respectively). Contamination of *Lg* by *Sn* contributes to the scatter of *inc3* for *Lg* at smaller distances. The scatter for *Sn* may also reflect contamination by the coda of *P*-type phases. At larger distances ($> 5^\circ$), because the contamination of *Lg* by *Sn* coda is minimized by selecting the frequency band for which the ratio of *Lg* to *Sn* coda is above a given threshold, and the time separation between the two phases is greater, it will be easier to distinguish *Sn* from *Lg* using polarization, especially at NORESS.

Frequency Characteristics.

The contamination of *Lg* by *Sn* coda at shorter ranges is illustrated by the variation in frequency content at the time of *Lg* arrival, as a function of distance. *Figure 6* shows the center of the frequency band used in polarization analysis (i.e., the wide band including all bands with 3-C SNR > 1.5 , or the band with largest 3-C SNR < 1.5), plotted against epicentral distance for *Sn* and *Lg*, at the two arrays. A center frequency above 8 Hz indicates the high-frequency band (8-16 Hz) was used, while a center frequency below 4 Hz indicates that no frequencies above 4 Hz were included. At both arrays, *Sn* tends to keep its high-frequency content in the far-regional range (beyond 5° distance), with a mean of 6.3 Hz (standard deviation, "s.d.", of 2.6 Hz) at NORESS and 8.4 Hz (s.d. of 1.8 Hz) at ARCESS. In contrast, far-regional *Lg* is generally depleted in high frequencies, with a mean of 2.9 Hz (s.d. of 1.3 Hz) at NORESS and 4.1 Hz (s.d. of 2.7 Hz) at ARCESS. As mentioned above, the polarization measurements for near-regional *Lg* (between about 2° and 5°) are not corrected for contamination by *Sn* coda, which probably accounts for the high frequencies (> 8 Hz) observed in that distance range.

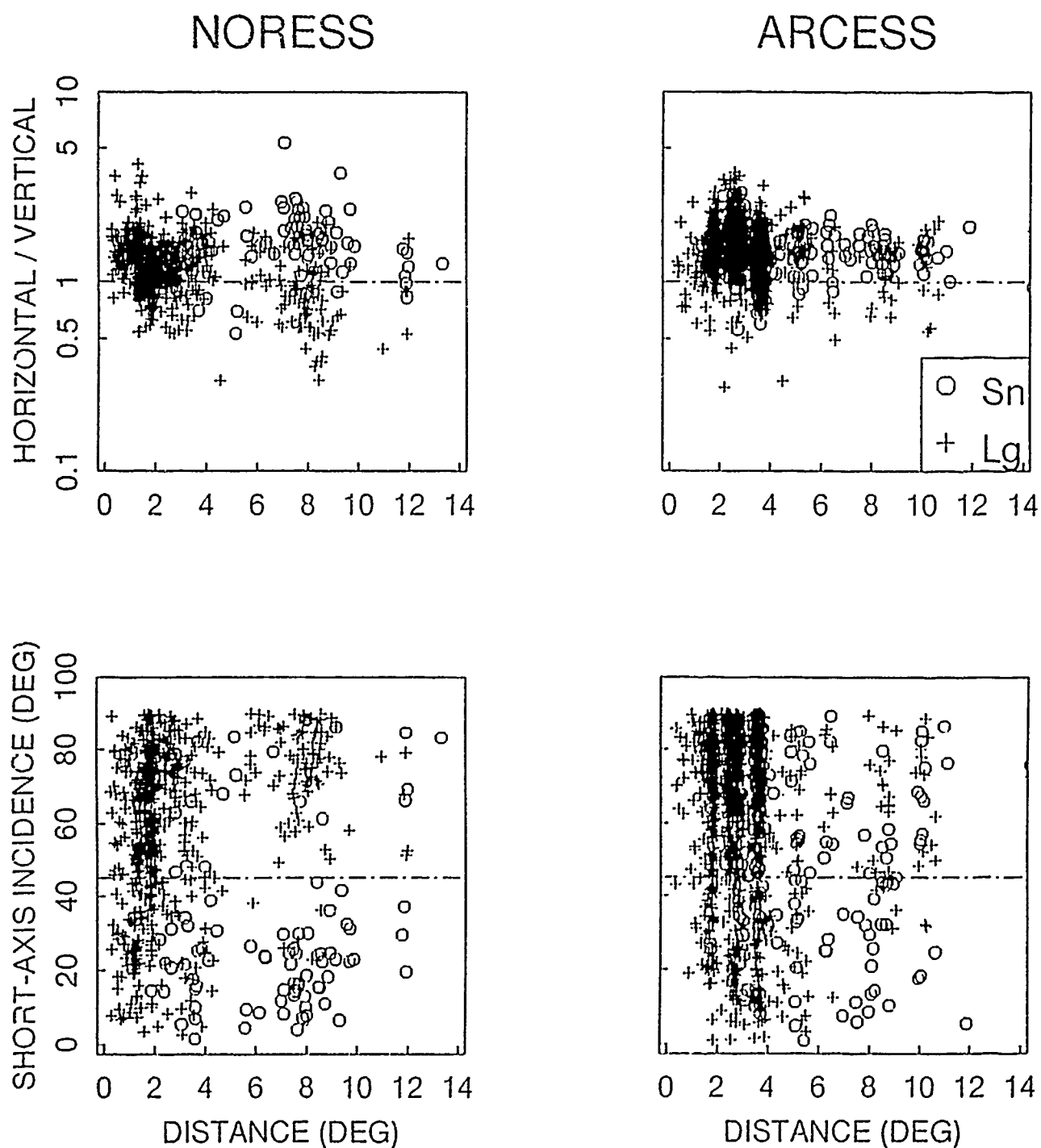


Figure 5. At the *top* the ratio of horizontal to vertical power (" H/V ") is plotted on a log scale versus epicentral distance, for *Sn* (circles) and *Lg* (plus signs), at NORESS (*left*) and ARCESS (*right*). The dashed horizontal line denotes a ratio of 1, i.e., equal horizontal and vertical amplitudes. At the *bottom*, short-axis incidence (*inc3*) is plotted instead. The dashed horizontal line represents an angle of 45°.

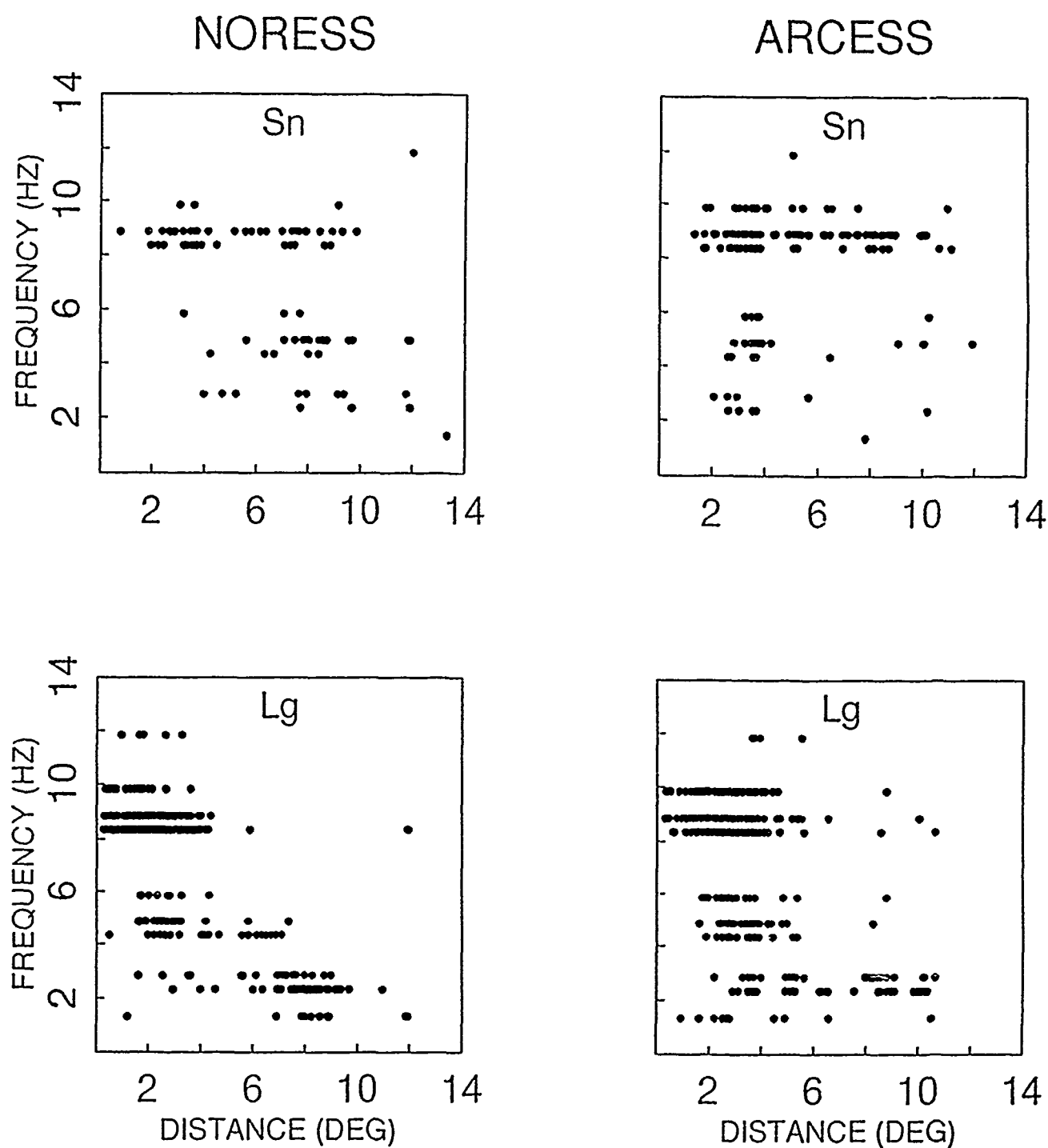


Figure 6. The center frequency of the wide band used for polarization analysis is plotted against epicentral distance for *Sn* (top) and *Lg* (bottom), at NORESS (left) and ARCESS (right).

The results from this study are in agreement with the observation by Jurkevics (1988) that the contamination of *Lg* polarization by *Sn* increases with frequency. In the *IMS* automated processing, this effect is much stronger in the near-regional than in the far-regional range. At distances beyond about 5°, different frequency characteristics are observed for *Sn* and *Lg*, and consequently, this property could be used to distinguish between the two phases.

For this data set there appears to be a critical distance at which polarization characteristics change (about 5°). The observed frequency content at the time of *Lg* arrival is also quite different beyond that distance. This contrasts with observations of contamination of secondary phases by the coda of preceding arrivals throughout the entire regional range, as seen on sonograms (e.g., Suteau-Henson, 1989). However, close inspection of the procedure used to select the frequency band for the analysis showed that *Pg* (respectively, *Lg*) is not corrected for *Pn* (respectively, *Sn*) coda contamination at distances less than about 5°. Therefore, this particular distance appears to be an artifact of the automated processing. The distance range for which frequency selection is improved could possibly be extended by taking a shorter noise window, positioned closer to the phase onset. However, the limitations of automated processing are such that it will remain very difficult to correct for this effect in the near-regional range, close to the cross-over distance.

Backazimuth Estimation.

Regional *S*-type phases recorded at 3-C stations are not generally considered to be very useful for backazimuth estimation because of their complex particle motion. This is in contrast with such phases recorded at arrays, that provide estimates of backazimuth from F-K analysis. Few attempts have been made to evaluate their potential for that purpose. Jurkevics (1988) found that *Sn* waves at the NORESS 3-C array did not yield reasonable azimuth estimates. He was able to compute an *Lg* azimuth using the orientation of the minimum horizontal motion. At NORESS also, Ruud *et al.* (1988) assumed a simplified particle motion model, such as *SV* only (no transverse component), to estimate the azimuth of regional shear waves as a function of time. At the 3-C high-frequency element of NORESS, Jarpe and Dowla (1991) found that the correct particle motion model for the *Lg* phase can be either *SV* or *SH*, resulting in 90° or 180° ambiguities. The *SV* model was correct most of the time and they obtained a minimum standard deviation of about 7° in the 15-25 Hz band, for a particular source location and optimum parameters. In this study, the azimuth of dominant rectilinear motion (automatically calculated and stored by the *IMS*, regardless of phase type) was extracted, and compared to the backazimuth derived from the final event solution. We make the assumption that the direction of dominant rectilinear motion is transverse, so that it differs by $\pm 90^\circ$ from the actual backazimuth. If the difference (backazimuth from polarization minus backazimuth from event solution) is positive (respectively, negative), 90° are

subtracted (respectively, added) to obtain an azimuth residual. The distributions of these residuals are plotted in Figure 7 for S_n and L_g , at the two arrays. It shows that at ARCESS, both S_n and L_g give reasonable backazimuth estimates with standard deviations of 18° and 19° , respectively. The estimates for L_g at NORESS have more scatter (s.d. of 25°). This compares well with the results obtained by Jurkevics (1988), who found L_g azimuth errors at NORESS were a strong function of frequency, with standard deviations of 16° , 27° , and 36° around 4, 6, and 10 Hz, respectively. The scatter for S_n at NORESS is very large (s.d. of 42°).

These results indicate that backazimuth from polarization can be used for both S_n and L_g at ARCESS, with a 180° ambiguity. This would be particularly useful for associating an S -type phase with a preceding P -type arrival, in the absence of information from F-K analysis. At NORESS, 3-C L_g backazimuth estimates could also be used for phase association, although with somewhat less confidence.

Another interesting result is that the dominant linear motion is transverse (i.e., SH motion) at ARCESS for both phases, and at NORESS for L_g , to a lesser degree. Based on this data set, S_n at NORESS does not show as strong a preference in orientation of dominant horizontal motion. The lack of predominance of either SH or SV motion for this phase contributes to its poor backazimuth estimation. These results, combined with those described in the section on polarization characteristics, confirm those previously obtained by Jurkevics (1988) that, on average, NORESS S_n has about equal amounts of transverse and radial motion (and little vertical motion), and L_g has transverse and vertical components of comparable amplitude. The results presented in this paper indicate slightly more transverse motion, especially for L_g .

2.1.4 Method For Phase Identification

The preceding section shows that polarization characteristics are potentially useful for identifying regional phases at NORESS and ARCESS. Other signal properties (such as frequency, amplitude, duration, shape of the envelope) could also be indicators of phase type. In this section, a method is devised to automatically identify a new arrival by comparing its characteristics to those of arrivals in a training set. It uses classical techniques of statistical multivariate data analysis (e.g., Cooley and Lohnes, 1971), and is briefly described below. In the next section, it will be applied to the identification of regional phases at NORESS and ARCESS, based on polarization. Other methods have proven useful to solve classification problems. Anderson (1990), for example, describes and applies various techniques to phase identification for IMS array data. Neural networks could also be used in a way similar to that proposed by Dysart and Pulli (1990) for source discrimination. The technique used here presents some advantages. Not only is it not computationally intensive, but also the classification results are directly related to the statistical distributions of the data. Therefore, as will be shown below the results can be

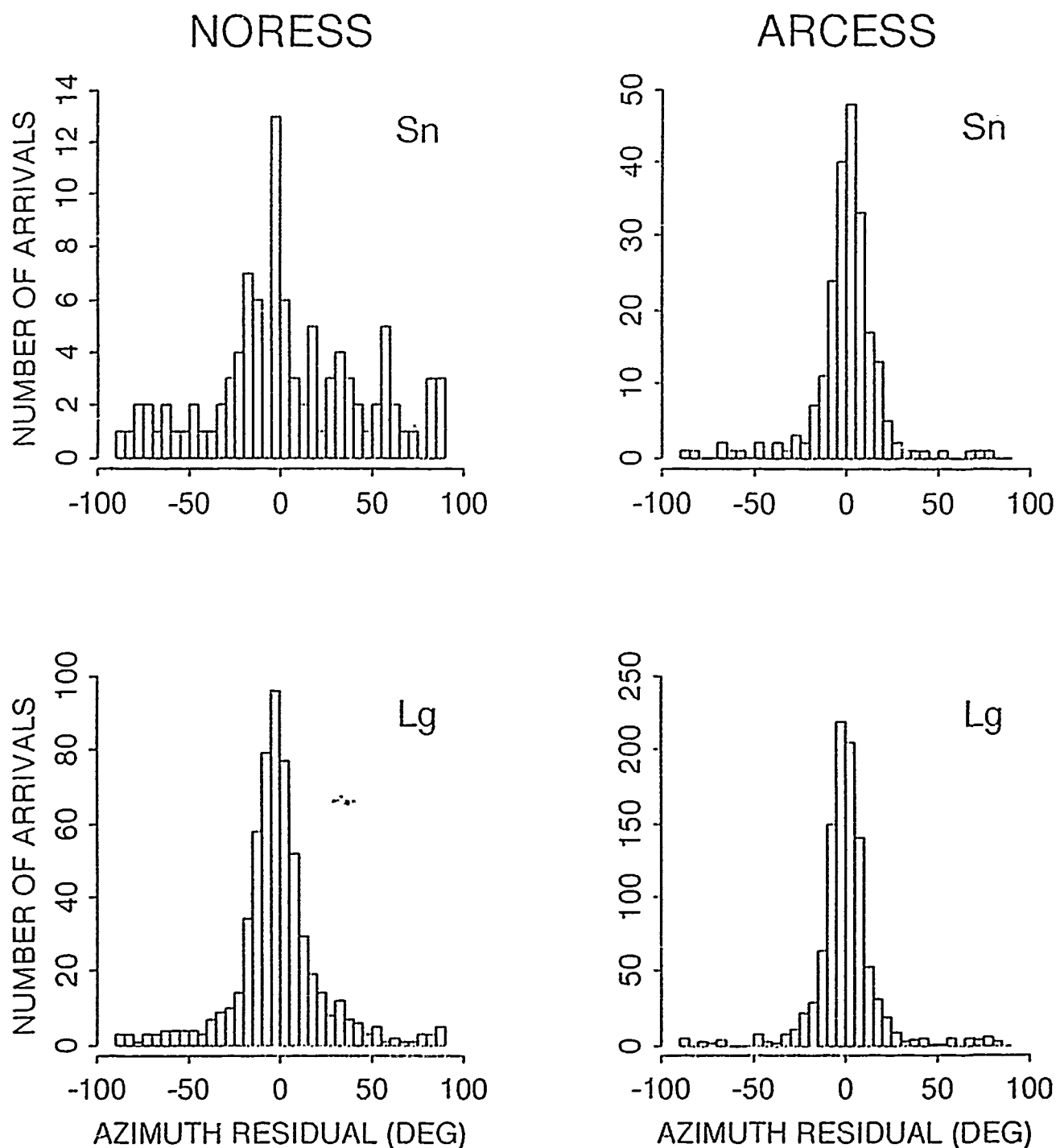


Figure 7. Histograms of azimuth residuals are plotted for *Sn* (top) and *Lg* (bottom), at NORESS (left) and ARCESS (right). These azimuth residuals represent the difference between backazimuth from polarization (assuming dominant rectilinear motion is transverse) and backazimuth from the *IMS* final event solution, and a $\pm 90^\circ$ correction has been applied.

explained in terms of the physical properties of the data, such as the polarization characteristics described in the previous section.

Figure 8 summarizes the various steps followed. Up to the classification procedure, they are similar to those described by Mason and Full (1986), who applied this method to predict oil well production. In the first step a representative data set is selected. As the problem consists of distinguishing between arrivals belonging to g groups (such as P -type / S -type, or S_n / Lg , or teleseismic P / regional P / regional S), there must be a large enough number of arrivals in each group to insure a reliable and stable statistical analysis. Then, the data are divided into a "norming" (or "training") sample and a "replication" (or "testing") sample, randomly selected and of about equal sizes. The object is to find a function discriminating between the g groups of the norming sample. The same function will be applied to the replication sample, and the results compared. This provides a test of the validity of the discriminant function (good results for the replication sample will not differ much from those for the norming sample).

After dividing the data into the norming and replication populations, a set of p measurements ("predictors") made on the data is selected (such as a set of polarization attributes). These are transformed to improve the normality of their distributions (for example, incidence angle is replaced by the logarithm of its tangent). Then, their distributions for the norming sample are standardized.

Principal Component Analysis ("PCA", e.g., Cooley and Lohnes, 1971) is performed on the norming sample to rotate the transformed variables into a new set ("principal components"), with the following properties. they are orthogonal, and ordered so that the first accounts for most of the variance in the data, the second, for most of the remaining variance, etc. Therefore, any correlation present in the original measurements is removed (such as between $inc1$ and H/V). Also, the number of useful variables can be reduced, as only the most important principal components need be used. Then, the replication sample is standardized (using the means and variances obtained for the norming sample), and the eigenvectors resulting from PCA are applied to it, to obtain principal component scores.

In the next step, Discriminant Analysis is performed on the principal component scores for the norming sample. It finds a discriminant function that is a linear combination of the principal components, with the following properties. it maximizes the separation between groups (such as P and S), while minimizing the dispersion of the resulting discriminant scores within each group. Note that its rank is the smaller of $g-1$ and p . This function is also applied to the replication sample, so that discriminant scores are obtained for both samples. The centroid and dispersion of the distribution of discriminant scores are calculated for each group in the norming sample.

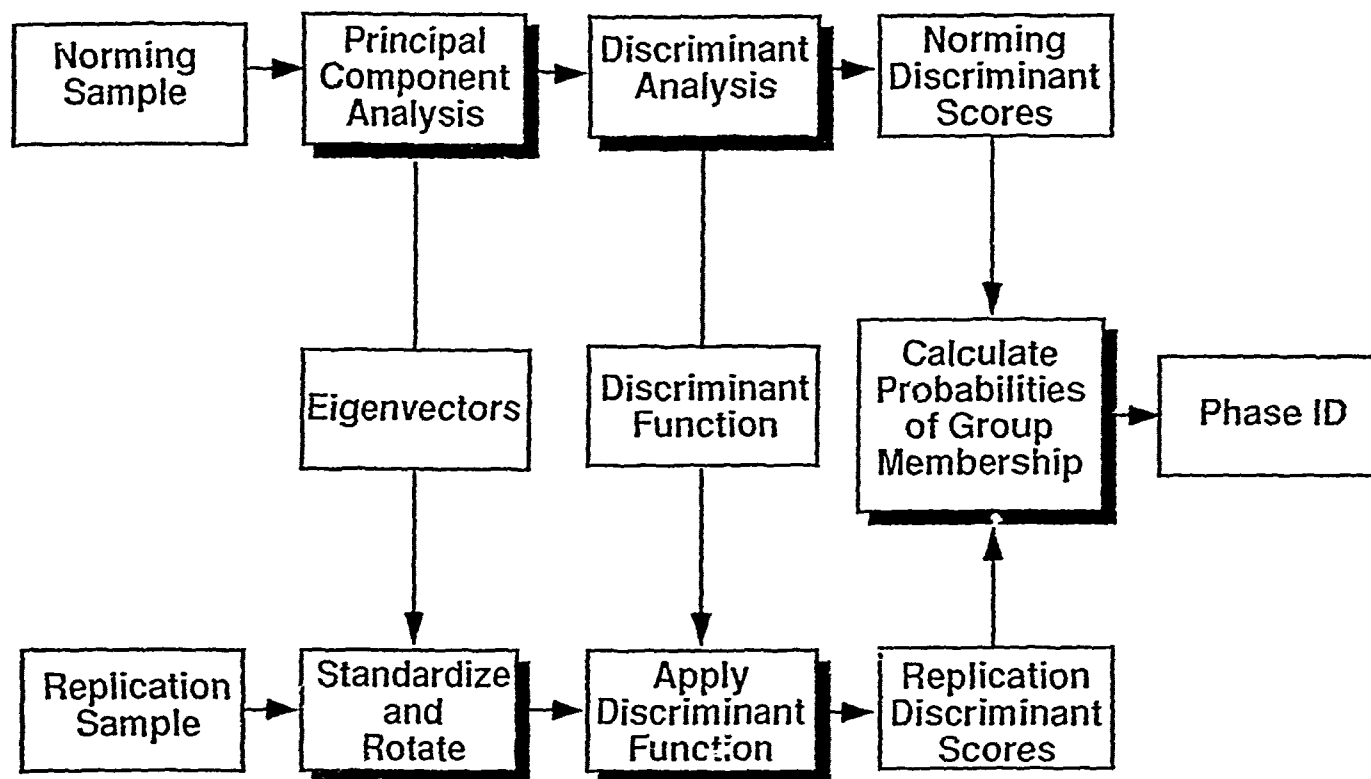


Figure 8. Flow chart describing the method for automated phase identification using signal characteristics (adapted from Mason and Full, 1986).

The probability of membership in a group is estimated for each arrival in each sample, using some classification procedure. Here, Geisser's model is used (Cooley and Lohnes, 1971, page 269). It is based on the distance between the discriminant score for an arrival and the centroid of a given group (and also depends on the dispersion and number of arrivals in the group, and the total number of arrivals in the norming sample). The probabilities are normalized so that, for each arrival, the sum of the probabilities of membership in all groups is 100%. These probabilities are used to perform phase identification: each arrival is assigned to the phase group for which it has the highest probability of membership. This probability is a measure of the confidence in the identification.

The performance of the discriminant function can be evaluated by comparing the phase assignment with the actual phase identification (as stored in the database) for each arrival. The number of correctly identified ("hits") and incorrectly identified ("misses") arrivals can be calculated for each group in each sample, and the results compared. If the performance significantly decreases for the replication sample, the discriminant function is not validated. In practice, especially for small samples, performing the analysis on several randomly selected samples and averaging may help stabilize the results.

Identification of Regional Phases at NORESS and ARCESS

In this section, the method for automated phase identification described above is applied to regional phases at NORESS and ARCESS, using polarization characteristics as predictors. The attributes studied in the section on polarization (with the exception of azimuth) are selected as the measurements. First, their normality is increased, as this method is based on theory assuming normal distributions. The following transformations improved the normality of the distributions:

$$rect \rightarrow \sqrt{rect}$$

$$plan \rightarrow \sqrt{plan}$$

$$H/V \rightarrow \log_{10}(H/V)$$

$$inc1 \rightarrow \log_{10}(\tan inc1)$$

$$inc3 \rightarrow \log_{10}(\tan inc3)$$

In the *IMS*, phase identification is performed in two stages (Bache *et al.*, 1990): *initial* phase identification (e.g., signal vs. noise, teleseismic vs. regional, *P*-type vs. *S*-type), then *refining* phase identification (e.g., *Pn*, *Lg*, *Rg*, *P*). Therefore, in the following, the data are used to distinguish, first between *P*-type and *S*-type phases, then, between *Pn* and *Pg*, and between *Sr* and *Lg*.

Initial Phase Identification

The discriminant scores were calculated for the group of *P*-type phases and the group of *S* type phases, for the norming and replication samples, at NORESS and ARCESS. Figure 9 displays the densities of the discriminant scores for each group. The norming samples at NORESS and ARCESS are compared in the top two plots. Better group separation is achieved at ARCESS. This can be explained by the stronger *SH* polarization of *S*-type arrivals at this array, which contrasts with *P*-type particle motion. The right two plots compare the norming and replication samples at ARCESS. The larger variance of the *S*-type group for the replication sample (also observed at NORESS) may be due to its lack of homogeneity (the polarization characteristics of *Sn* and *Lg* are less alike than those of *Ph* and *Pg*). The discriminant densities are also plotted for the subset of the NORESS norming sample with 3-C SNR > 2 (*bottom left*). Compared to those for the entire data set (*top left*), the variance is reduced, especially for the *P*-type group, resulting in significantly better group separation. This effect is also observed at ARCESS, and is due to the sharp decrease in the scatter of polarization characteristics for 3-C SNR > 2 (see Figure 2).

Histograms for the probabilities of membership in the *P*-type group are plotted in Figure 10 for the norming sample at NORESS and ARCESS. It shows that the confidence in the phase assignment is higher at ARCESS than at NORESS as expected from the discriminant densities. It is also higher for *P*-type than for *S*-type arrivals, especially at NORESS, which may be due to the less homogeneous *S*-type population at this array (i.e., larger differences between *Sn* and *Lg* polarization).

The "hits" and "misses", i.e., the number of arrivals correctly and incorrectly identified, for the *P*- and *S*-type groups at each array, are shown to the left of Figure 11a and 11b. The results for the norming and replication samples have been combined. The subset for 3-C SNR > 2 is also shown in the middle of each figure. The performance of the discriminants obtained to distinguish between *P*- and *S*-type arrivals can be summarized as follows:

- Slightly fewer arrivals are correctly identified at NORESS (82%) than at ARCESS (89%).
- The percentage of hits is slightly higher for *P*-type arrivals (84% at NORESS and 90% at ARCESS) than for *S*-type arrivals (80% and 88%, respectively).
- The performance is improved for arrivals with 3-C SNR > 2 (88% at NORESS and 93% at ARCESS).
- This improvement is particularly remarkable for *P*-type arrivals, that have a success rate of 96% at NORESS and 98% at ARCESS, indicating that low SNR is the major cause of misidentification of *P*-type phases with this procedure.

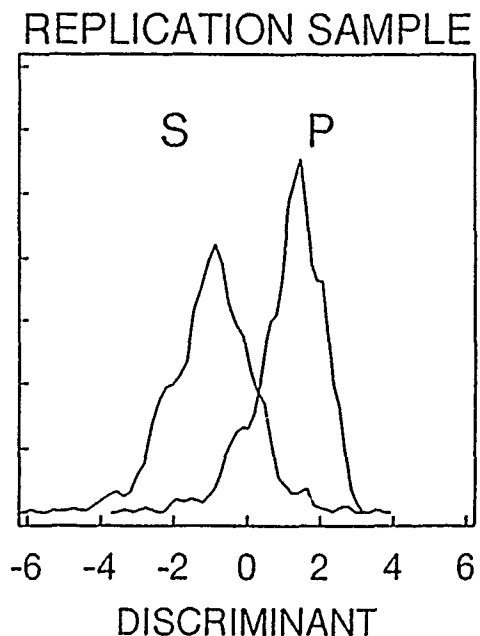
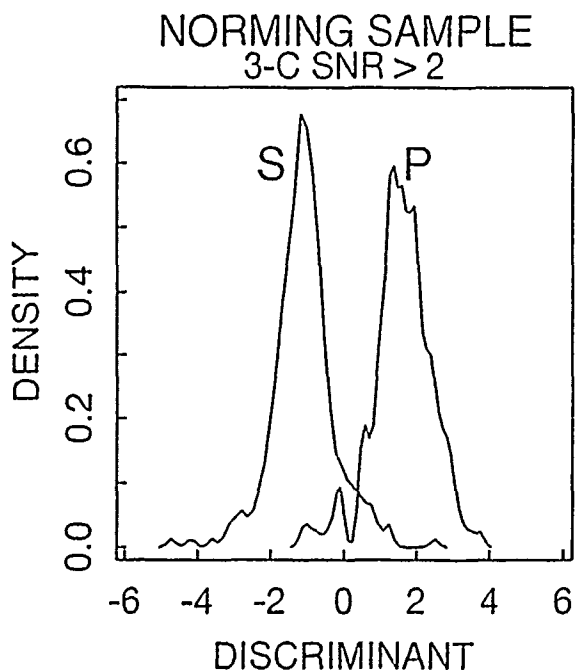
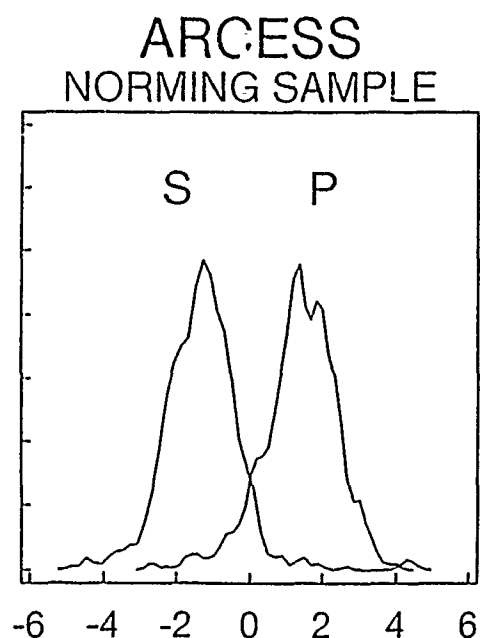
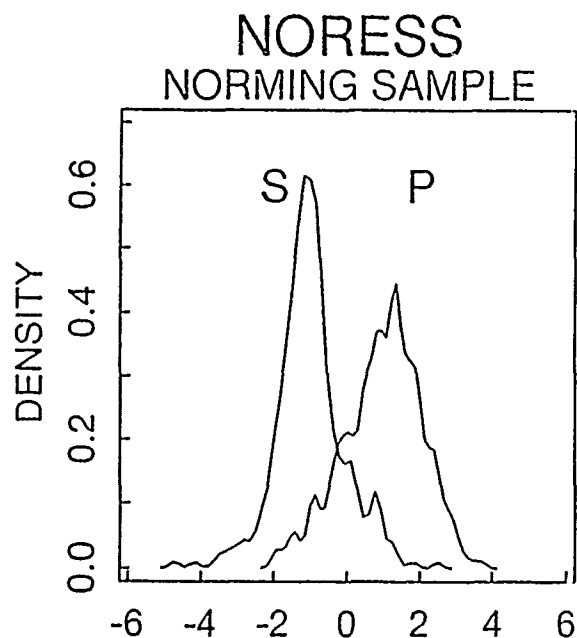


Figure 9. The density of the discriminant scores for arrivals in the *P*-type (*P_n* and *P_g*) and *S*-type (*S_n* and *L_g*) groups is plotted as a function of the discriminant value for various subsets of the data: *top left* - NORESS norming sample, *top right* - ARCESS norming sample, *bottom left* - subset of the NORESS norming sample with 3-C SNR > 2, and *bottom right* - ARCESS replication sample.

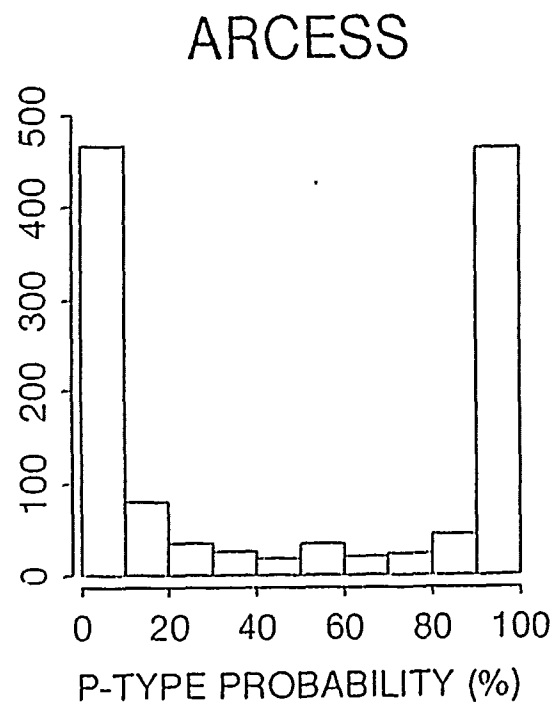
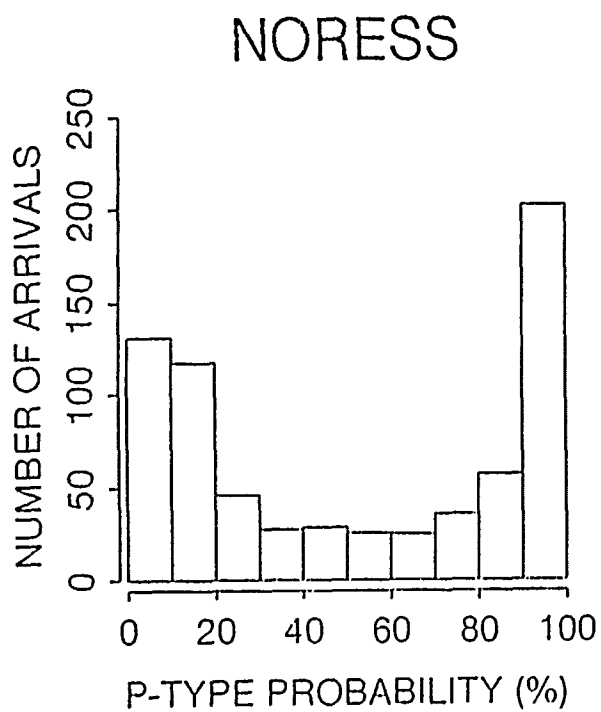


Figure 10. Histograms of the probability (in percent) of membership in the *P*-type group are plotted for the norming sample at NORESS (*left*) and ARCESS (*right*). Note that the probability (in percent) of membership in the *S*-type group is $100 - P\text{-type probability (\%)}$.

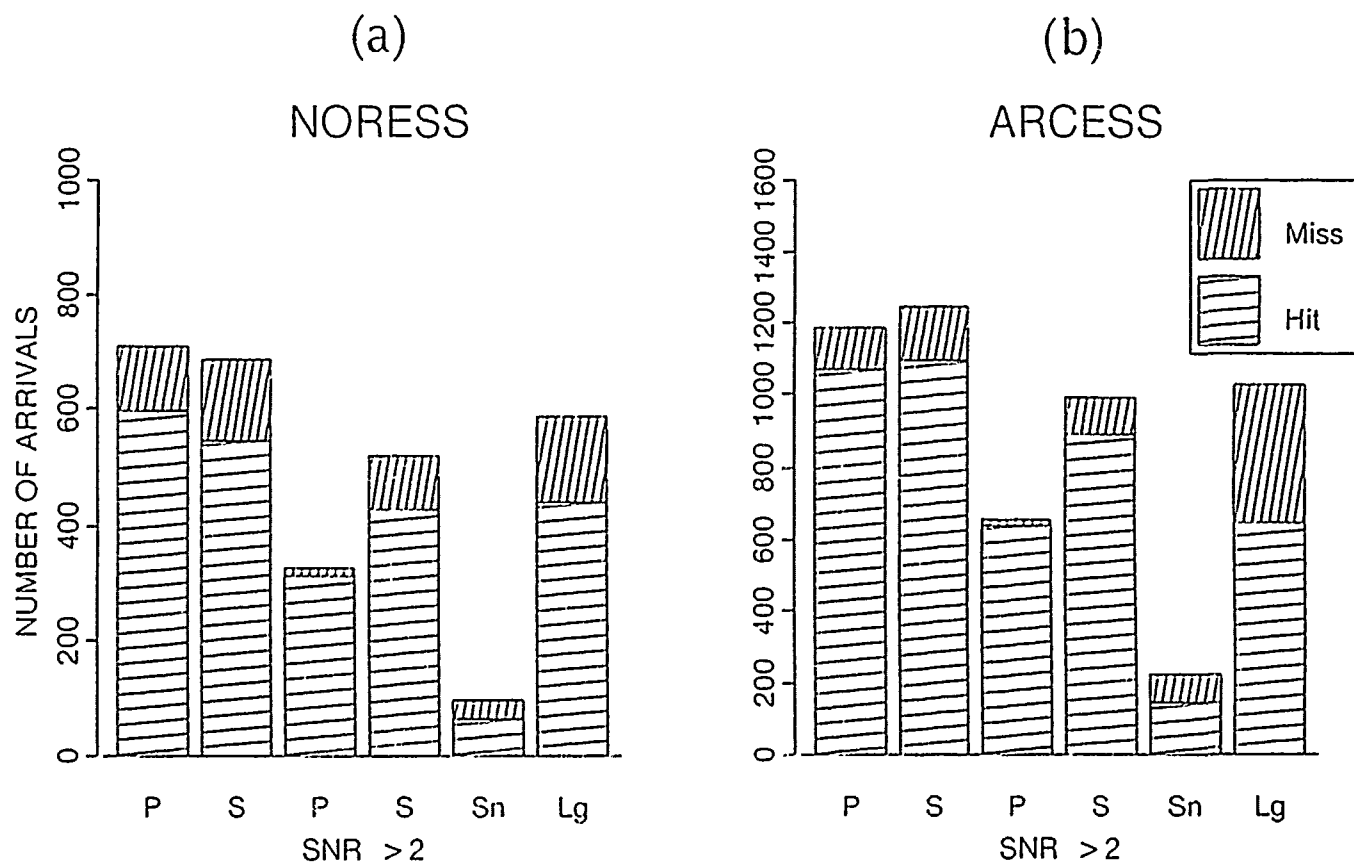


Figure 11. Barplots show the number of arrivals correctly ("hit") and incorrectly ("miss") identified, a) at NORESS and b) at ARCESS, for various phase identification problems. From left to right, *P*-type versus *S*-type, same except only arrivals with 3-C SNR > 2 are shown, and *Sn* versus *Lg*.

It is interesting to compare the results from this section to those from the polarization section above. The weights applied to each of the five polarization attributes, after normalization and standardization, to form the discriminant functions are shown in *Table 2 (first line)*. The attributes that were given the largest weights by the automated procedure are *rect*, *inc1*, and *H/V*. *P*-type phases are identified based on their higher rectilinearity, smaller incidence angle, and smaller *H/V*. This is expected from the differences in polarization between *P*-type and *S*-type phases from both theoretical models and the observations in this study.

TABLE 2
WEIGHTS OF DISCRIMINANT FUNCTIONS

Groups	NO. .SS					ARCESS				
	<i>rect</i>	<i>plan</i>	<i>H/V</i>	<i>inc1</i>	<i>inc3</i>	<i>rect</i>	<i>plan</i>	<i>H/V</i>	<i>inc1</i>	<i>inc3</i>
<i>P</i> vs. <i>S</i>	0.57	-0.16	-0.76	-0.49	-0.14	0.82	-0.03	-0.66	-0.85	-0.27
<i>Pn</i> vs. <i>Pg</i>	-0.33	-0.38	0.75	0.01	0.13	0.04	-0.74	0.47	0.28	0.89
<i>Sn</i> vs. <i>Lg</i>	-0.36	0.42	0.70	-0.23	-0.47	-0.89	-0.07	0.14	0.06	-0.42

Defining Phase Identification

In the previous section it was found that it is possible to distinguish between *P*-type and *S*-type phases using polarization alone, with success rates varying from 80% to 98%, depending on site, phase type, and SNR range. Next, the capabilities of this approach to distinguish, first between *Pn* and *Pg*, and then between *Sn* and *Lg*, are evaluated.

P-Type Phases.

A discriminant analysis, similar to that used for initial phase identification, was performed on the subset of the data including only the *P*-type arrivals. The two groups considered were *Pn* and *Pg*. Their observed polarization characteristics are not very different (see *Figure 2*, *Figure 3* and *Table 1*), due in part to contamination of *Pg* by *Pn* coda beyond the cross-over distance. Therefore, the resulting discriminants did not have a high success rate. However, *Pn* has more distinct polarization at far-regional ranges (see *Figure 3*). Therefore, the performance was also evaluated for the subset of the *Pn* data with distances $> 3^\circ$. The weights applied to the

polarization attributes to form the discriminant functions are given in *Table 2* (*second line*). We find that:

- Fewer arrivals are correctly identified at NORESS (57%) than at ARCESS (65%), which may be due to the low SNR for many *Pn* (and some *Pg*) arrivals at NORESS.
- The performance is slightly better for *Pn* (59% at NORESS and 66% at ARCESS) than for *Pg* (54% and 57%, respectively).
- For *Pn* with distances $> 3^\circ$, the performance increases to 67% at NORESS and 70% at ARCESS.

S-type Phases.

Discriminant analysis was also performed on the *S*-type arrivals to distinguish between *Sn* and *Lg*. The performance obtained at the two arrays for *Sn* and for *Lg* is shown to the right of *Figure 11a* and *11b*, and the main results are as follows:

- The overall success rate is higher at NORESS (74%) than at ARCESS (64%) due to the fact that at ARCESS both *Sn* and *Lg* are characterized by dominant *SH* motion, while at NORESS, their polarization properties are more distinct (see *Figure 5* and *Table 1*).
- The percentage of hits is 66% for *Sn* at both arrays, while for *Lg*, it is 75% at NORESS and 63% at ARCESS (the relatively low percentage for *Sn* at NORESS reflects poor results obtained for the replication sample, due to a small population).

As expected from the study of polarization described in a previous section (see *Table 1*), the set of attributes contributing most to the discriminant function is different for the two arrays (*Table 2, third line*). At ARCESS the dominant attribute is rectilinearity, which is somewhat larger for *Lg*, due to a stronger *SH* component. Another is *inc3*, the plane of principal motion being less near-vertical for *Sn*. At NORESS the main predictors are *H/V* and *inc3*.

2.1.6 Discussion

Arrays of four 3-C elements were used to obtain polarization and direction parameters in this study as such arrays are systematically used for the purpose of noise reduction in the *IMS*, and no estimates are made from individual 3-C elements. In practice, however, such parameters must often be estimated at single 3-C stations. In a theoretical study, Jurkevics (1988) shows that averaging the covariance matrices computed at the individual sensors of an array corresponds to ensemble averaging. It reduces the standard deviation of the direction estimates by \sqrt{N} , where *N* is the number of sensors. This, however, is based on the assumption that noise and local scattering effects are uncorrelated between array sensors. The

reduction in scatter attainable in practice is usually lower. As array-averaging will also produce an increase in SNR, no overall change in the distributions as a function of SNR should result. Another effect would be to reduce any bias and/or scatter due to receiver structure at a particular 3-C element. Therefore, more bias and scatter in polarization and direction estimates, and as a result, more uncertainty in phase identification, might be expected at a single 3-C station such as the IRIS stations in the USSR.

The study of systematic variations in polarization characteristics for different sources (earthquakes vs. explosions), various source depths, or different paths, is beyond the scope of this paper. Source type is expected to somewhat affect polarization because of changes in the average SNR for a given phase, resulting from different relative excitation of wave types for a given magnitude. Source depth will influence polarization by affecting the phase type (e.g., P_n vs. direct P), incidence angle, and related parameters. The effect of velocity structure on polarization can be strong: it can modify the type of polarization (rectilinear vs. elliptical), produce phase conversions, and introduce scatter and systematic bias in polarization attributes, including azimuth. Although such factors can influence polarization characteristics of a given wave type, their effect can be reduced by evaluating each site individually and using some regionalization if necessary.

The method described in this paper for automated phase identification using signal characteristics of individual arrivals was applied to the identification of regional phases based on polarization. Clearly, this analysis could easily be extended to include other signal properties, such as frequency, presumably resulting in improved performance. "Context information" has also proven useful, especially for defining phase identification: for example, relative timing and amplitude of signals arriving within a certain time window (Bache *et al.*, 1990). More work is needed to determine if the approach described in this study could be extended to include such context information. An alternative is to perform preliminary phase identifications (with an associated confidence) using individual predictors (such as polarization), then merge the results obtained for several predictors, in a way similar to that used by Baumgardt and Young (1990) for event identification.

The strong effect of distance on polarization should be reflected in improved phase identification for arrivals in some distance ranges if the distance is known. In the *IMS*, epicentral distance is not known at the time of phase identification. However, some context information, such as $S-P$ time can be inferred. If such an estimate of distance is available, further control can be obtained. For example, S_n vs. Lg phase identification based on polarization should be easier at distances $> 5^\circ$.

Phase identification in the *IMS* raises some issues that were not addressed in this preliminary study. For example, initial phase identification must not only distinguish between P and S , but also between signal and noise, and teleseismic and

regional phases. Also, some phases are identified in the database as being of *P*-type, but have no defining phase identification (*Px*). Clearly, the approach described in this paper could be used on a data set including all types of detections. Also, although this method was applied to a large database, some subsets, such as *Sn* at NORESS and *Pg* at ARCESS, were relatively small. Fewer data were available at far-regional distances. Supplementing this data set would help strengthen some of the results. With a suitable data set it would also be possible to further subdivide the phase groups on the basis of various factors: for example, treat *P*-type arrivals with 3-C SNR > 2, or *S*-type arrivals with estimated distance > 5° separately. Such refinement of the analysis is easy in the context of the *IMS*, where knowledge can be acquired on a regular basis by analyzing new data (Bache *et al.*, 1990). This new knowledge can in turn be used to improve specific functions, such as phase identification, resulting in better overall performance of the system.

2.1.7 Conclusions

Polarization of local/regional phases were compared at NORESS and ARCESS, two hard-rock sites. The analysis showed that there are significant differences in the particle motion characteristics between the two arrays for each of the four phases studied (*Pn*, *Pg*, *Sn* and *Lg*), even within similar ranges of SNR and epicentral distance. Particle motion is critical for backazimuth estimation. This study indicates that ARCESS provides better backazimuth estimates than NORESS for the four regional phases studied.

Polarization was found useful for phase identification at both sites, although some differences were observed. The same discriminants cannot be used at both arrays, as the polarization attributes and associated weights that best distinguish two given phase groups at NORESS (for example, *H/V* and *inc3* for *Sn* and *Lg*) do not constitute the optimal set at ARCESS. This illustrates the site dependence of phase identification using 3-C data. Site effects are expected to be even stronger at stations more affected by low subsurface velocities and/or significant lateral heterogeneity, such as the IRIS station in the USSR (Ryaboy, 1990). Therefore, the knowledge acquired at one 3-C station or array cannot simply be transposed to another, and each station must be evaluated individually.

Finally, the strong effects of SNR and epicentral distance on polarization are reflected in improved phase identification for arrivals within certain ranges of those parameters. For example, *P*-type phases with 3-C SNR > 2 are more easily distinguished from *S*-type phases. Also, *Sn* and *Lg* are easier to identify at far-regional distances. This, in turn, results in a higher confidence in their phase assignment. In particular, this study shows the importance of high SNR for reliable phase identification of regional *P*-type phases using 3-C data. Therefore, noise conditions will strongly affect this capability at 3-C stations.

ACKNOWLEDGMENTS

The data used in this study were extracted from the *IMS* database, and the author wishes to thank the *IMS* operation staff, both at the Center for Seismic Studies and at NORSAR, for making it available to her. R. Stead, in particular, kindly helped in selecting the data. I am grateful for the encouragement provided by A. Ryall, T. Bache, and S. Bratt. I also thank J. Carter, S. Bratt, J. Vidale and two anonymous reviewers for their helpful review of the manuscript. This research was supported by the Air Force Geophysics Laboratory, under Contract F19628-89-C-0203.

Anne Suteau-Henson

References

- Anderson, K. R. (1990). Programming as a Geophysical Inverse Problem, *Bull. Seism. Soc. Am.* **80**, Part B, 1893-1909.
- Bache, T. C., S. R. Bratt, J. Wang, R. M. Fung, C. Kobryn, and J. W. Given (1990). The Intelligent Monitoring System, *Bull. Seism. Soc. Am.* **80**, Part B, 1833-1851.
- Baumgardt, D. R. and G. Young (1990). Design and Development of an Intelligent Event Identification System (ISEIS), in *Proceedings of the Twelfth Annual DARPA/GL Seismic Research Symposium (18 - 20 September 1990)*, GL-TR-90-0212, 1-9.
- Bratt, S. R., H. J. Swanger, R. J. Stead, F. Ryall, and T. C. Bache (1990). Initial Results From the Intelligent Monitoring System, *Bull. Seism. Soc. Am.* **80**, Part B, 1852-1873.
- Cooley, W. W. and P. R. Lohnes (1971). *Multivariate Data Analysis*, John Wiley & Sons, Inc., 364 pp.
- Dysart, P. S. and J. J. Pulli (1990). Regional Seismic Event Classification at the NORESS Array: Seismological Measurements and the Use of Trained Neural Networks, *Bull. Seism. Soc. Am.* **80**, Part B, 1910-1933.
- Given, H. K. (1990). Variations in Broadband Seismic Noise at IRIS/IDA Stations in the USSR With Implications for Event Detection, *Bull. Seism. Soc. Am.* **80**, Part B, 2072-2088.
- Harris, D. B. (1990). Comparison of the Direction Estimation Performance of High-Frequency Seismic Arrays and Three-Component Stations, *Bull. Seism. Soc. Am.* **80**, Part B, 1951-1968.
- Jarpe, S. and F. Dowla (1991). Performance of High-Frequency Three-Component Stations for Azimuth Estimation From Regional Seismic Phases, submitted to *Bull. Seism. Soc. Am.*
- Jurkevics, A. (1988). Polarization Analysis Of Three-Component Array Data, *Bull. Seism. Soc. Am.* **78**, 1725-1743.
- Kvaerna, T. and F. Ringdal (1986). Stability of Various F-K Estimation Techniques, in *NORSAR Semiannual Technical Summary, 1-86/87*, Kjeller, Norway, 29-40.
- Magotra, N., N. Ahmed, and E. Chael (1987). Seismic Event Detection and Source Location Using Single-Station (Three-Component) Data, *Bull. Seism. Soc. Am.* **77**, 958-971.
- Mason, K. L. and W. E. Full (1986). Multivariate Statistical Techniques Used in Exploration, *Geobyte Fall '86*, 40-46.

- Mykkeltveit, S. (1987). Local Geology of the Regional Array Sites in Norway, in *NOR-SAR Semiannual Technical Summary 1-87/88*, Kjeller, Norway, 123-129.
- Mykkeltveit, S., F. Ringdal, T. Kvaerna, and R. W. Alewine (1990). Application of Regional Arrays in Seismic Verification Research, *Bull. Seism. Soc. Am.* **80**, Part B, 1777-1800.
- Ruud, B. O., E. S. Husebye, S. F. Ingate, and A. Christoffersson (1988). Event Location at Any Distance Using Seismic Data From a Single, Three-Component Station, *Bull. Seism. Soc. Am.* **78**, 308-325.
- Ruud, B. O. and F. S. Husebye (1991). Exploring the Upper Crystalline Crust: a Joint Interpretation of 3D Imaging and Reflection Profiling at the NORESS Array, *Tectonophysics* (in press).
- Ryaboy, V. (1990). The Earth's Crust and Upper Mantle Structure and Attenuation Beneath IRIS Stations in the USSR, in *Center for Seismic Studies Technical Report C90-04*, Arlington, Virginia, 1-1 - 1-37.
- Suteau-Henson, A. (1989). Characterization of Regional Events Recorded at NORESS and the NRDC Stations, in *Center for Seismic Studies Technical Report C89-01*, Arlington, Virginia, 4-43 - 4-64.
- Suteau-Henson, A. (1990). Estimating Azimuth and Slowness From Three-Component and Array Stations, *Bull. Seism. Soc. Am.* **80**, Part B, 1987-1998.
- US/GSE/49 (1987). A Recommendation for Inclusion of Azimuth as a Reportable Parameter for Three-Component Stations, *United States Delegation to the Conference on Disarmament*, Geneva, Switzerland, 37 pp.
- Vidale, J. E. (1986). Complex Polarization Analysis of Particle Motion, *Bull. Seism. Soc. Am.* **76**, 1393-1405.
- Walck, M. C. and E. P. Chael (1991). Optimal Back-azimuth Estimation for Three-Component Recordings of Regional Seismic Events, *Bull. Seism. Soc. Am.* **81**, 643-666.

2.2 COMPARATIVE ANALYSIS OF THE HELSINKI AND IMS BULLETINS FOR SELECTED EVENTS ALONG THE ARCESS - FINESA PROFILE

The University of Helsinki (HEL) has operated a network of seismic stations in Finland and other scandinavian countries that is used to produce a seismic event bulletin. This bulletin has been the source of "truth" for calibrating the location capabilities of the Intelligent Monitoring System (IMS) (Bache et al., 1990). The IMS used data from the NORESS and ARCESS arrays in formulating its bulletin for the period studied. This short paper compares the two bulletins and assesses the location capabilities of the IMS. 103 events recorded by the IMS during the period from September to November 1989 were selected for the comparison of the seismological bulletins. These events were listed and identified as possible mine explosions in the both HEL and IMS bulletins (Bratt et al., 1990). The events are located south and southeast of the ARCESS array in the eastern part of the Baltic shield, mainly within the northwestern areas of the USSR, and partially within Finland and Sweden (*Figure 1*). The events were in the range of epicentral distances from 200 to 1,200 km from ARCESS and had magnitudes (*ML*) 2.0-2.9.

A comparison of distances (*DIST*) and azimuths (*AZ*) from the ARCESS array to the events, and estimated origin times (*T*) based on the HEL and IMS bulletins is given in *Table 1*. A statistical analysis of the data in *Table 1* was made and included calculations of density plots, coefficients of linear correlation, normal quantile - quantile plots, and other statistical characteristics. These results show that the discrepancy between the HEL and IMS bulletins for approximately 95% of the events are: 0.16 ± 5.08 sec., 5.91 ± 36.98 km, and $0.25^\circ \pm 4.20^\circ$ for origin time, epicentral distance, and backazimuth, respectively (*Table 2*).

The differences between backazimuths from ARCESS calculated from locations in the IMS and HEL bulletins can be approximated by a normal distribution. The distributions of the epicentral distance and estimated origin time differences are not as clear (*Figure 2*). The analysis shows a negative, statistically significant relation between the distance differences and the origin time differences based on the two bulletins. Qualitatively similar results were obtained for a comparison of the NORESS and HEL bulletins for events recorded by the NORESS array along the Oslo(NORESS)-Helsinki-Leningrad profile (Ryaboy, 1990).

It is noteworthy that discrepancies between the HEL and IMS bulletins are substantially less than the discrepancies between the HEL and NORESS bulletins (*Table 2*, *Figure 2*). This leads us to conclude that the location parameters and origin times in the IMS bulletin have less error than those based only on NORESS recordings alone. A similar result was obtained by Bratt et al. (1990) for a larger number of events. This obvious conclusion does not assist us in determining whether the HEL or IMS bulletin is more accurate.

LOCATION MAP OF SELECTED EVENTS FOR ARCESS-FINESA PROFILE

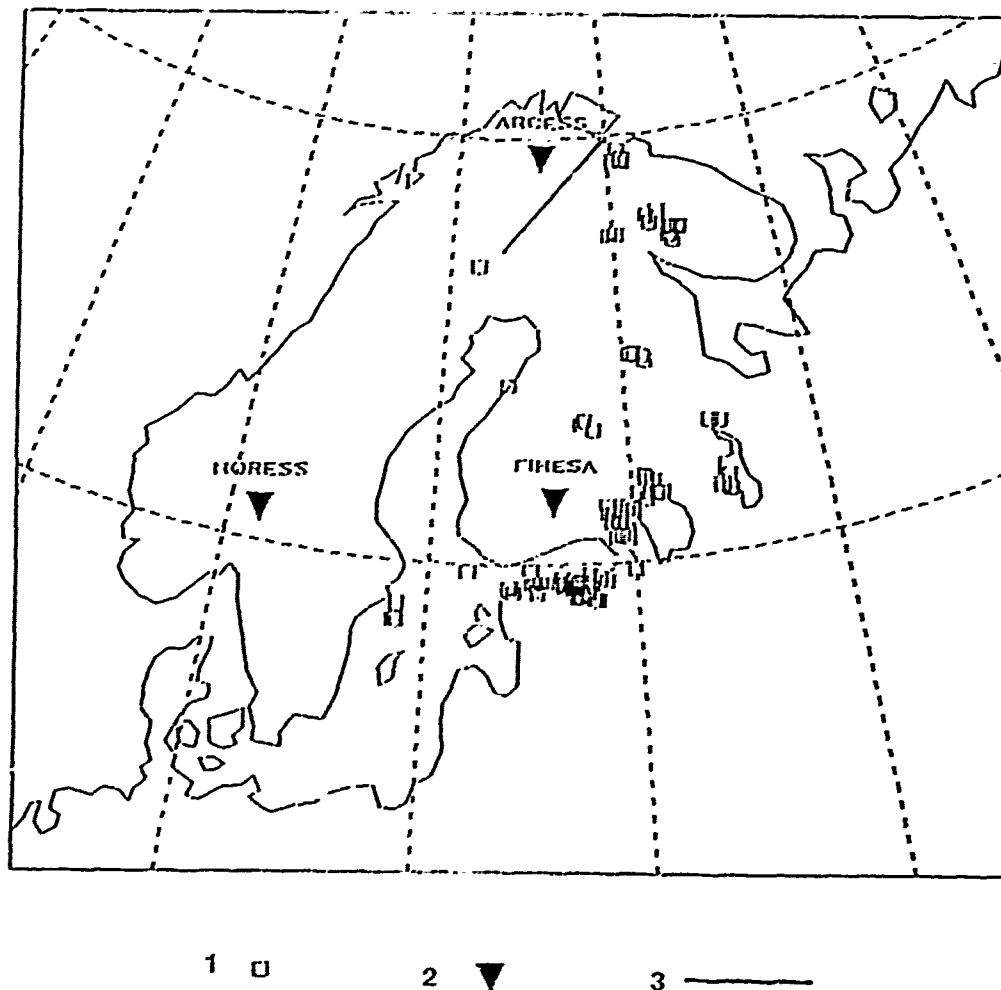


Figure 1. Location map of selected events for the comparison. 1 -- mine explosions listed in the IMS bulletin, 2 -- seismic arrays, 3 -- POLAR DSS profile.

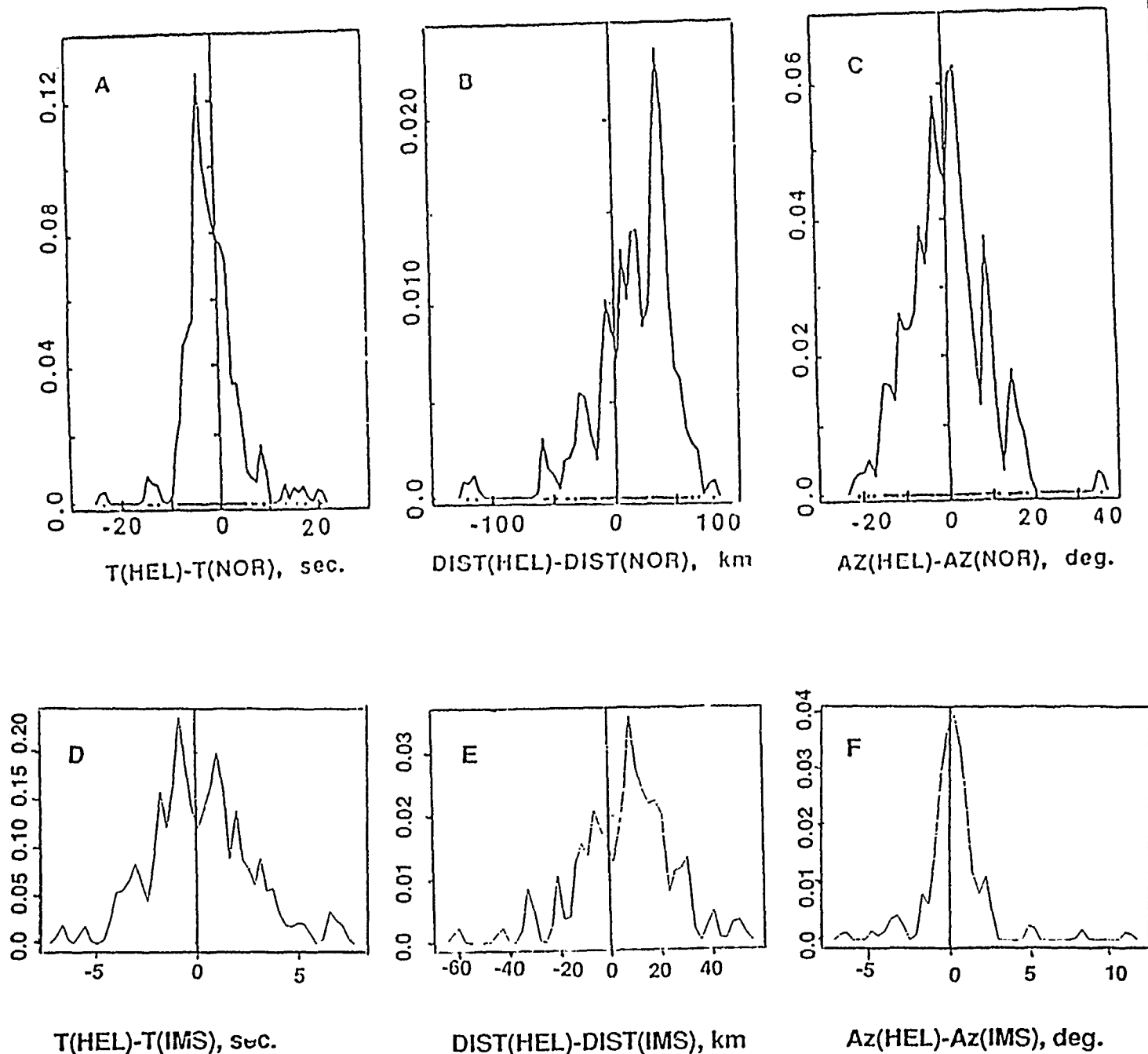


Figure 2. Probability density plots of differences between origin times (T), epicentral distances (DIST), and azimuths (AZ), respectively, from the Helsinki (HEL) and NORESS (NOR) bulletins, for 147 mine explosions detonated along the Oslo-Helsinki-Leningrad profile (A, B, and C) and from the HEL and IMS bulletins, for 103 mine explosions detonated along a profile from ARCESS to FINESA (D, E, and F). One can see that the probability density plots A, B, D, and E are non symmetric, while plots C and F are nearly symmetric about the vertical axis.

LIST OF EXPLOSIONS WITHIN THE EASTERN AREAS OF BALTIC SHIELD RECORDED BY ARCESS ARRAY

ACCORDING TO IMS AND HELSINKI BULLETINS (September - November 1989)

No. Orig	Date	IMS		bulletin		Origin time		Lat. deg.	Long. deg.	M	Dist. km	Az. deg.	Or-time		Discrepancy between Hel. and IMS bulletins (HEL) - (IMS)	
		No.D.Y	h: m: sec.	h: m: sec.	deg.	h: m: sec.	deg.						sec.	km	deg	Az.
1	107924	09.09.89	03:23:15.39	67.53	33.58	2.6	398.97	120.37	08:23:15.00	67.6	34.2	2.7	415.39	117.33	-1.39	16.42
2	107949	09.09.89	03:26:17.74	60.97	29.31	2.9	972.84	167.71	12:02:25.00	60.9	29.3	2.7	980.14	167.81	-1.74	7.30
3	107823	09.09.89	13:30:30.90	61.32	28.77	2.4	930.13	169.13	12:30:24.00	60.9	29.4	2.2	980.53	167.50	-6.80	50.84
4	107990	09.09.89	13:00:00.76	59.47	26.91	2.5	1125.22	176.22	13:00:02.00	59.5	26.5	2.0	1121.53	177.10	1.24	4.59
5	107997	09.09.89	13:00:00.76	59.47	26.91	2.5	398.97	120.37	13:00:02.00	61.6	34.0	-	408.46	117.52	-1.07	19.49
6	107957	09.09.89	13:00:00.76	59.47	26.91	2.5	1117.49	181.59	14:13:34.00	59.5	25.0	-	1129.43	155.94	-0.12	0.12
7	107936	09.09.89	13:00:00.76	59.47	26.91	2.5	1104.19	166.92	14:47:00.00	59.5	30.0	2.0	1129.43	155.94	-0.12	0.12
8	108561	09.10.89	13:00:00.76	67.63	29.94	2.7	276.46	136.10	13:00:00.00	67.6	30.5	-	297.16	134.51	-2.70	20.70
9	103556	09.10.89	13:00:00.76	67.63	29.94	2.5	284.88	136.10	13:00:00.00	68.1	30.5	-	349.54	113.66	-1.25	23.28
10	103520	10.02.89	13:25:01.53	68.03	32.28	2.2	321.44	118.35	12:25:58.00	68.1	30.5	2.2	349.54	113.66	-1.25	23.28
11	103539	10.02.89	13:25:01.53	68.03	32.28	2.2	1133.61	175.97	12:25:58.00	68.1	30.5	2.2	1121.53	177.10	2.17	12.08
12	104995	10.03.89	09:26:35.19	61.52	31.32	2.5	933.24	160.57	09:29:32.00	61.1	29.9	2.3	963.50	165.70	-3.19	30.26
13	105219	10.03.89	11:56:42.52	64.16	23.67	2.1	606.24	188.51	11:56:45.00	64.4	22.69	2.6	586.57	193.42	2.98	19.67
14	106770	10.04.89	11:27:41.64	61.58	30.33	2.3	915.30	169.04	12:29:19.00	60.9	29.4	2.2	924.53	163.57	-0.64	9.58
15	106779	10.04.89	12:29:23.26	61.14	28.64	2.3	950.38	169.04	12:29:19.00	60.9	29.4	2.2	924.53	163.57	-0.64	9.58
16	107234	10.04.89	16:19:26.27	59.86	24.86	2.3	1080.81	181.93	16:39:23.00	59.5	25.0	-	1120.8	181.47	-3.27	39.99
17	107854	10.05.89	10:54:09.83	59.35	24.06	2.1	1139.55	184.16	10:54:14.30	59.74	23.82	-	1096.64	184.99	4.47	42.91
18	107862	10.05.89	11:16:07.71	59.47	27.03	2.6	1126.75	175.58	11:16:07.00	59.3	27.2	2.6	1145.67	175.13	-0.71	18.92
19	107868	10.05.89	11:49:15.12	59.46	23.86	2.2	1127.92	184.78	14:48:28.00	59.5	26.5	2.3	1121.53	177.10	0.66	9.65
20	108213	10.05.89	14:48:27.34	59.59	26.47	2.5	1111.88	177.18	14:48:28.00	59.5	26.5	2.3	1121.53	177.10	0.66	9.65
21	111585	10.06.89	10:16:39.15	64.77	31.20	2.4	586.63	152.46	10:16:41.00	64.7	30.7	2.6	584.98	154.89	1.85	2.43
22	111787	10.06.89	11:12:39.70	59.43	27.13	2.7	1131.19	175.29	11:12:39.00	59.3	27.2	2.6	1145.67	175.13	-0.70	14.48
23	118708	10.11.89	07:49:36.46	59.81	21.86	2.6	1098.93	190.78	07:49:38.30	59.72	22.0	3.0	1108.35	190.31	1.84	9.42
24	119054	10.11.89	10:45:54.92	59.58	27.24	2.4	1115.17	174.93	10:45:51.00	59.3	27.2	2.4	1145.67	175.13	-0.32	30.50
25	119057	10.11.89	10:55:39.32	67.87	32.43	2.1	336.62	120.17	10:55:39.00	68.1	33.2	-	349.54	113.66	0.36	5.45
26	119078	10.11.89	14:09:24.34	59.01	18.58	2.5	1220.53	199.12	14:09:24.70	58.97	18.49	2.7	1225.98	199.32	-0.32	12.92
27	117198	10.12.89	11:36:51.78	61.44	30.77	2.4	935.93	162.43	11:36:53.00	61.5	30.4	2.8	924.88	163.57	1.22	11.05
28	123686	10.12.89	12:20:51.00	61.54	34.63	2.4	985.79	150.47	12:20:54.00	61.4	34.3	2.9	993.77	151.73	3.00	7.98
29	123721	10.13.89	11:41:30.79	67.68	33.56	2.8	388.02	118.46	11:41:29.00	67.6	34.0	2.9	408.46	117.92	-1.79	20.44
30	123728	10.13.89	12:00:25.89	64.83	30.50	2.5	568.23	155.31	12:00:24.00	64.7	30.7	2.8	584.98	154.89	-1.89	16.75
31	123746	10.13.89	12:54:06.95	67.41	33.73	2.1	412.51	121.29	12:54:08.00	67.6	34.0	2.1	408.46	117.92	1.05	-4.05
32	125224	10.14.89	12:01:59.73	68.10	32.93	2.2	339.81	114.61	12:01:58.00	68.1	33.2	-	349.54	113.66	-1.73	9.73
33	125589	10.16.89	10:21:15.18	59.29	27.28	2.6	1147.04	174.92	10:21:17.00	59.3	27.2	2.4	1145.67	175.13	1.82	-1.37

Table 1.

IMS bulletin										Helsinki bulletin										Discrepancy between Hel. and IMS bulletins (HEL) - (IMS)			
No.	Orid	Date	Origin time		Lat.	Long.	M	Dist.	Az.	Origin time		Lat.	Long.	M	Dist.	Az.	Or.time	Dist.	Az.				
			h: m: sec.	deg.						h: m: sec.	deg.									sec.	km	deg.	km
1	2	3	4	5	6	7	8	9		10	11	12	13	14	15	16	17	18					
34	125900	10.16.89	12:44:02.74	69.41	30.99	2.6	215.49	91.05		12:44:04.00	69.4	30.8	2.7	208.18	91.67	1.26	-7.31	0.62					
35	126850	10.17.89	11:10:33.05	69.63	30.68	2.5	202.28	84.60		11:10:38.00	69.6	29.9	2.2	171.71	85.52	4.95	-30.57	0.92					
36	126870	10.17.89	12:07:32.76	59.59	28.55	2.2	1120.04	171.13		12:07:31.00	59.4	28.5	-	1140.52	171.37	-1.76	20.48	0.24					
37	126865	10.17.89	14:55:04.12	59.55	26.78	2.6	1116.26	176.27		14:55:05.00	59.5	26.5	2.3	1121.53	177.10	0.88	5.27	0.83					
38	129545	10.18.89	12:08:26.46	69.39	30.40	2.9	192.80	92.62		12:08:26.00	69.4	30.8	2.7	208.18	91.67	-0.46	15.38	-0.95					
39	129551	10.18.89	14:11:31.19	63.08	34.43	2.2	822.87	146.77		14:11:33.50	62.8	34.4	2.4	850.95	147.76	2.31	28.08	0.99					
40	129607	10.19.89	12:53:00.03	59.49	27.14	2.7	1124.42	175.25		12:52:59.00	59.3	27.2	2.7	1145.67	175.13	-1.03	21.25	-0.12					
41	131862	10.20.89	06:41:23.94	67.66	34.18	2.8	410.60	116.48		06:41:24.00	67.6	34.2	3.0	415.39	117.23	0.06	4.79	0.75					
42	131898	10.20.89	11:58:29.00	63.21	27.58	2.0	712.27	171.55		11:58:27.00	63.1	27.7	-	725.40	171.18	-2.00	13.13	-0.37					
43	131911	10.20.89	13:25:32.58	59.41	25.22	2.4	1131.00	180.82		13:25:34.00	59.5	25.0	2.6	1145.67	175.13	2.55	-6.03	0.36					
44	133920	10.23.89	10:32:02.45	59.25	27.33	2.7	1151.70	174.77		10:32:05.00	59.3	27.2	2.2	1138.21	173.99	-0.90	9.19	0.59					
45	133920	10.23.89	10:38:34.70	59.47	27.78	2.6	1129.02	173.40		10:38:33.80	59.38	27.59	2.2	1158.28	174.03	1.02	12.46	0.05					
46	133523	10.23.89	11:35:28.98	59.31	27.60	2.4	1145.82	173.98		11:35:30.00	59.2	27.6	2.9	883.59	162.29	2.46	-11.69	1.4					
47	133590	10.23.89	13:28:47.54	61.85	31.12	2.4	895.28	160.65		13:28:50.00	61.9	30.6	2.4	1147.15	173.99	3.52	-15.97	0.85					
48	134640	10.24.89	10:29:48.48	59.17	27.92	2.6	1163.12	173.14		10:29:52.00	59.3	27.6	2.3	991.16	167.91	-0.65	17.64	0.25					
49	134667	10.24.89	13:27:30.65	60.96	29.33	2.4	973.53	167.66		13:27:30.00	60.8	29.3	2.3	1121.53	177.10	1.84	6.09	-0.09					
50	134678	10.24.89	15:10:35.16	59.55	26.47	2.5	1115.44	177.19		15:10:37.00	59.5	26.5	2.1	1121.53	177.10	1.84	6.09	-0.09					
51	135418	10.25.89	11:58:16.85	64.67	31.27	2.5	598.03	152.56		11:58:20.00	64.7	30.7	-	584.98	154.89	3.15	-13.05	2.33					
52	135514	10.26.89	10:13:57.86	61.19	29.97	2.5	954.38	165.38		10:13:59.00	61.1	29.9	2.7	963.50	165.70	1.14	9.12	0.32					
53	140711	10.26.89	12:34:52.97	59.52	25.12	2.3	1118.80	181.12		12:34:54.00	59.5	25.0	2.0	1139.95	171.65	-3.94	30.88	-0.38					
54	140713	10.26.89	12:59:05.94	59.67	28.22	2.3	1109.07	172.03		12:59:02.00	59.4	28.4	2.0	1012.44	168.41	3.03	-10.16	1.26					
55	140720	10.26.89	13:50:58.97	60.54	29.63	2.4	1022.60	167.15		13:51:02.00	60.6	29.2	2.5	950.45	159.90	1.3	18.56	0.08					
56	140725	10.26.89	14:38:21.70	61.56	31.54	2.4	931.89	159.82		14:38:23.00	61.4	31.6	2.5	993.77	151.73	6.64	-13.07	2.17					
57	140755	10.27.89	09:38:02.36	61.41	35.05	2.7	1006.84	149.56		09:38:09.00	61.4	34.3	2.7	993.77	151.73	-0.36	15.81	-0.81					
58	140759	10.27.89	11:32:57.36	64.81	30.43	2.4	569.17	155.70		11:32:57.00	64.7	30.7	2.8	584.98	154.89	1.81	-2.48	1.48					
59	140775	10.27.89	12:50:43.19	69.45	30.88	2.7	210.66	90.19		12:50:45.00	69.4	30.8	2.2	208.18	91.67	0.49	13.41	0.96					
60	140826	10.27.89	15:10:30.51	67.72	33.83	2.2	395.05	116.96		15:10:31.00	67.6	34.0	2.7	408.46	117.92	-0.22	4.34	1.69					
61	144002	10.29.89	05:19:31.22	67.71	34.08	2.5	404.12	116.23		05:19:31.00	67.6	34.0	2.3	991.16	167.91	-2.62	39.43	-0.47					
62	144111	10.30.89	12:26:26.66	58.64	18.52	2.3	1261.60	198.86		12:26:30.40	58.96	18.32	2.2	1229.29	199.76	3.74	-32.31	0.90					
63	144114	10.30.89	12:26:26.66	58.64	18.52	2.3	1261.60	198.86		12:26:30.40	58.96	18.32	2.2	1229.29	199.76	3.74	-32.31	0.90					
64	144120	10.30.89	13:05:52.21	59.57	26.26	2.2	1113.52	177.80		13:05:52.00	59.5	26.5	2.1	1121.53	177.10	-0.21	1.22	0.57					
65	144123	10.30.89	13:33:37.24	60.62	29.38	2.3	1011.22	167.84		13:33:36.00	60.6	29.2	2.3	1012.44	168.41	-1.24	1.22	0.57					
66	145133	10.31.89	13:36:42.13	59.55	26.56	2.7	1116.53	176.91		13:36:43.00	59.5	26.5	2.4	1121.53	177.10	0.87	5.00	-0.19					
67	147821	11.01.89	12:01:37.81	67.67	33.59	2.4	389.55	118.42		12:01:36.00	67.6	34.0	-	408.46	117.92	-1.81	18.91	-0.50					
68	147829	11.01.89	12:25:41.31	59.16	28.09	2.7	1164.83	172.67		12:25:45.00	59.2	27.6	2.6	1158.28	174.03	3.69	-6.55	1.36					
69	147845	11.01.89	13:02:59.13	60.93	28.98	2.6	974.71	168.81		13:02:57.00	60.7	29.0	2.6	999.86	168.04	-2.13	25.15	0.13					
70	147846	11.01.89	13:26:10.03	60.88	29.34	2.7	983.25	167.70		13:26:10.30	60.86	29.21	2.7	983.82	168.14	0.27	0.57	0.44					
71	147858	11.01.89	15:59:34.99	61.90	30.79	2.5	885.41	161.67		15:59:34.00	61.9	30.6	2.8	883.59	162.29	-0.99	-1.82	0.62					
72	149111	11.02.89	12:14:33.71	59.56	27.02	2.4	1116.49	175.56		12:14:30.00	59.3	27.2	2.5	1145.67	175.13	-3.71	29.18	-0.43					
73	152019	11.03.89	08:19:34.97	67.68	34.32	2.9	414.54	115.81		08:19:36.00	67.6	34.0	-	408.46	117.92	1.03	-6.08	2.11					
74	152109	11.04.89	10:05:21.28	64.78	30.44	2.7	572.83	155.74		10:05:19.00	64.7	30.7	2.9	584.98	154.89	-2.28	12.15	-0.85					
75	152931	11.04.89	11:02:02.19	61.19	29.98	2.3	954.75	165.33		11:02:04.00	61.1	30.2	2.5	966.49	164.75	1.81	11.74	-0.58					
76	152937	11.04.89	11:26:57.46	59.20	27.14	2.1	1156.83	175.34		11:27:00.00	59.3	27.2	2.2	1145.67	175.13	2.54	-11.16	-0.21					
77	152944	11.04.89	12:46:30.90	69.36	30.97	3.0	215.29	92.53		12:46:31.00	69.4	30.8	-	208.18	91.67	-0.10	-7.11	-0.86					
78	152996	11.05.89	11:05:54.39	59.45	27.11	2.2	1128.88	175.35		11:05:53.00	59.3	27.2	2.2	1145.67	175.13	-1.39	16.79	-0.22					
79	153033	11.06.89	11:59:14.43	63.09	28.24	2.3	729.81	169.05		11:59:15.00	63.1	27.7	2.8	725.40	171.18	0.57	-4.41	2.13					

Table 1. (continued)

IMS bulletin				Helsinki bulletin				Discrepancy between Hel. and IMS bulletins (HEL) - (IMS)									
No. Orid	Date	Origin time	Lat. Long.	M	Dist.	Az.	h: m: sec.	deg.	km	deg.	Az.	Or.time	Dist.	Az.			
	Mo.D.Y	h: m: sec.	deg.	deg.								sec.	km	deg			
1	2	3	4	5	6	7	8	9	10	11	12	13	14	15	16	17	18
80	160154	11.09.89	13:28:18.77	59.32	25.21	2.3	1141.16	180.85	13:28:22.00	59.5	25.0	-	1120.8	181.47	3.23	-20.36	0.62
81	161012	11.09.89	14:12:21.95	60.59	29.17	2.5	1013.18	168.52	14:12:19.00	60.8	29.5	2.0	992.84	167.29	-2.75	-20.33	-1.23
82	160944	11.10.89	10:42:14.17	59.43	27.27	2.4	1131.20	174.89	10:42:15.00	59.3	27.2	2.0	1145.67	175.13	0.3	14.47	0.24
83	161041	11.10.89	13:43:38.95	59.58	25.36	2.1	1111.53	180.44	13:43:41.00	59.5	25.0	-	1120.8	181.47	2.05	9.27	1.03
84	167870	11.13.89	13:54:01.46	61.76	35.05	2.4	971.32	148.70	13:54:08.00	61.4	31.6	2.5	950.46	159.90	6.54	-20.86	11.20
85	172081	11.14.89	12:00:33.60	61.17	30.06	2.3	957.96	165.11	12:00:28.00	61.5	30.4	2.1	924.88	163.57	-5.60	-33.08	-1.54
86	172095	11.14.89	14:47:22.23	59.48	26.50	2.8	1123.64	177.11	14:47:23.00	59.5	26.5	-	1121.53	177.10	0.77	-2.11	-0.01
87	172363	11.15.89	12:08:12.99	63.29	27.74	2.2	704.35	170.82	12:08:11.00	63.1	27.7	-	725.40	171.18	-1.99	21.05	0.36
88	190881	11.16.89	13:17:56.96	61.10	29.06	2.3	956.37	168.38	13:17:54.00	60.9	29.4	2.3	980.97	167.50	-2.96	24.60	-0.88
89	175305	11.16.89	14:55:49.83	59.53	27.14	2.2	1120.06	175.25	14:55:49.00	59.3	27.2	2.3	1145.67	175.13	-0.83	25.61	-0.12
90	177378	11.17.89	13:24:50.47	59.68	26.38	2.3	1101.45	177.44	13:24:51.00	59.5	26.5	2.2	1121.53	177.10	0.53	20.08	-0.34
91	177438	11.18.89	11:26:46.27	61.87	30.83	2.6	890.22	161.58	11:26:47.00	61.9	30.6	2.6	883.59	162.29	0.73	-6.63	0.71
92	178780	11.18.89	12:28:31.83	61.97	30.70	2.2	877.07	161.85	12:28:31.00	61.9	30.6	-	883.59	162.29	-0.83	6.52	0.44
93	178839	11.20.89	12:57:57.41	59.40	27.07	2.2	1134.46	175.47	12:57:57.00	59.3	27.2	-	1145.67	175.13	-0.41	11.21	-0.34
94	189277	11.21.89	11:03:29.73	58.62	18.66	2.4	1262.43	198.47	11:03:30.00	58.74	17.81	-	1260.06	200.82	0.27	-2.37	2.35
95	189367	11.21.89	13:05:42.98	61.27	29.78	2.3	943.45	165.88	13:05:42.00	61.9	30.6	2.8	883.59	162.29	-0.98	-59.86	-3.59
96	189332	11.22.89	10:17:52.95	67.97	32.92	2.4	347.23	116.63	10:17:52.00	68.1	33.2	2.7	349.54	113.66	-0.95	2.31	-2.97
97	189337	11.22.89	11:48:52.19	59.74	27.73	2.3	1099.19	173.44	11:48:49.00	59.3	27.6	2.0	1147.15	173.99	-3.19	47.96	0.55
98	186491	11.23.89	09:44:48.85	61.45	34.95	2.5	1000.61	149.75	09:44:56.00	61.4	34.3	2.5	993.77	151.73	7.15	-6.84	1.98
99	186520	11.23.89	12:49:19.69	63.01	34.96	2.3	841.43	145.31	12:49:23.70	62.84	34.53	2.3	849.61	147.22	4.01	8.18	1.91
100	189479	11.24.89	10:00:34.63	64.84	30.67	2.3	569.87	154.47	10:00:34.00	64.7	30.7	2.5	584.98	154.89	-0.63	15.11	0.42
101	189461	11.24.89	12:04:08.16	67.63	34.10	2.9	409.91	117.19	12:04:08.10	67.63	34.32	2.9	417.66	116.44	-0.06	7.75	-0.75
102	189469	11.24.89	16:02:09.78	66.95	21.66	2.3	329.64	210.69	16:02:10.00	67.1	20.6	2.6	339.08	218.99	0.22	9.44	8.30
103	189658	11.25.89	12:37:40.04	67.62	30.20	2.4	287.16	135.97	12:37:39.00	67.6	30.5	2.4	297.16	134.31	-1.04	10.00	-1.66

Table 1. (continued)

COMPARISON OF HELSINKI (HEL), IMS, AND NORESS (NOR) BULLETINS

Oslo-Helsinki-Leningrad profile

(147 events)

ARCESS-FINESA profile

(103 events)

	sec.	km	deg.	T(HEL)-T(NOR)	DIST(HEL)-DIST(NOR)	AZ(HEL)-AZ(NOR)	T(HEL)-T(IMS)	DIST(HEL)-DIST(IMS)	AZ(HEL)-AZ(IMS)
mean	-1.57	16.30	-0.29				0.16	5.91	0.25
median	-2.10	20.98	-0.26				0.06	9.19	0.20
mode	-3.21	37.50	2.20				-0.93	9.41	0.29
standard deviation	-5.41	-31.66	-9.64				-2.54	-19.49	-2.10
confidence level of mean									
5% level	-0.45	-2.61	-0.71				-0.25	-1.80	-0.21
95% level	-0.90	-5.22	-1.42				-0.50	-3.64	-0.42

T(HEL), T(NOR), and T(IMS) - origin time according to Helsinki, NORESS, and IMS bulletins ;
DIST(HEL), DIST(NOR), and D(IMS) - distance from NORESS and ARCESS arrays based on Helsinki, NORESS
and IMS bulletins;

AZ(HEL), AZ(NOR), AZ(IMS) - azimuth from R 555 and ARCESS arrays based on Helsinki, NORESS
and IMS bulletins.

Table 2.

We constructed ARCESS travel-time curves for P_n (Figure 3) and S_n (Figure 4) waves based on the both IMS and HEL bulletins. The ARCESS arrival times of these phases listed in the IMS bulletin were used to calculate the travel times. Figures 3 and 4 show that P_n and S_n waves predicted by the HEL bulletin arrive earlier compared with the IMS bulletin. Discrepancies between the travel-time curves are caused by differences in the origin times and event locations of the two bulletins. Approximately 1.0 s of difference is observed for distances less than 800 km, increasing to 1.5-2.0 s for larger distances. The statistics in Table 2 show that this is primarily due to event location effects rather than differences in origin times. At the 800-900 km distances, one can see an increase in P_n and S_n apparent velocities.

Note that the estimated standard deviations of P_n and S_n wave travel times based on the HEL bulletin are substantially larger than for the IMS bulletin (± 1.02 and ± 0.35 s for P_n ; ± 2.46 and ± 1.54 s for S_n for the HEL and IMS bulletins, respectively). This is expected as the ARCESS arrival time used in the plot to calculate the travel time curves is an integral part of the IMS solution but not used in the HEL solution. For a truly unbiased comparison, independent data must be utilized.

To estimate the quality of the P_n wave travel-time curves based on the HEL and IMS bulletins we compared the travel time curves in Figure 3 with observations from the 440 km long POLAR deep seismic sounding (DSS) profile located approximately 100 km southeast of the ARCESS array (Luosto et al., 1989). Detailed reversed and overlapping seismic refraction investigations of the earth crust and uppermost mantle were carried out along the profile up to distances of more than 400 km from the shot points. Figure 5 shows an example of P-wave record sections for a shot point located in the southern part of the DSS profile. Travel-time and distance picks from this profile are shown as pluses in Figure 3. A comparison of the P_n travel-time curves on Figure 3 and travel-times of the P_n waves recorded on the POLAR profile shows that the P_n travel-time curve based on the IMS bulletin provides a better fit for observations on the POLAR profile. As a result, we conclude that the IMS bulletin is more accurate than the HEL bulletin in the vicinity of the POLAR profile.

The proximity of the HEL network to the events studied in this report would make it's locations normally preferred over the NORESS and ARCESS seismic array locations. Consequently, it is worth discussing the previous conclusion in more detail. As was mentioned above, the analyzed events were mainly located beyond the boundaries of the region covered by the Helsinki network (Figure 1). This fact, combined with an inaccurate velocity model leads to systematic mislocation. In addition, a majority of the events listed in the HEL bulletin have "manual locations", indicating that they were associated with a known mine based on pattern recognition by analysts. Satellite images of mine locations in Fennoscandia show that mines can be as large as 20 km across, and in some areas of the northwestern

Pn TRAVEL-TIMES BASED ON DSS DATA, IMS AND HELSINKI BULLETINS

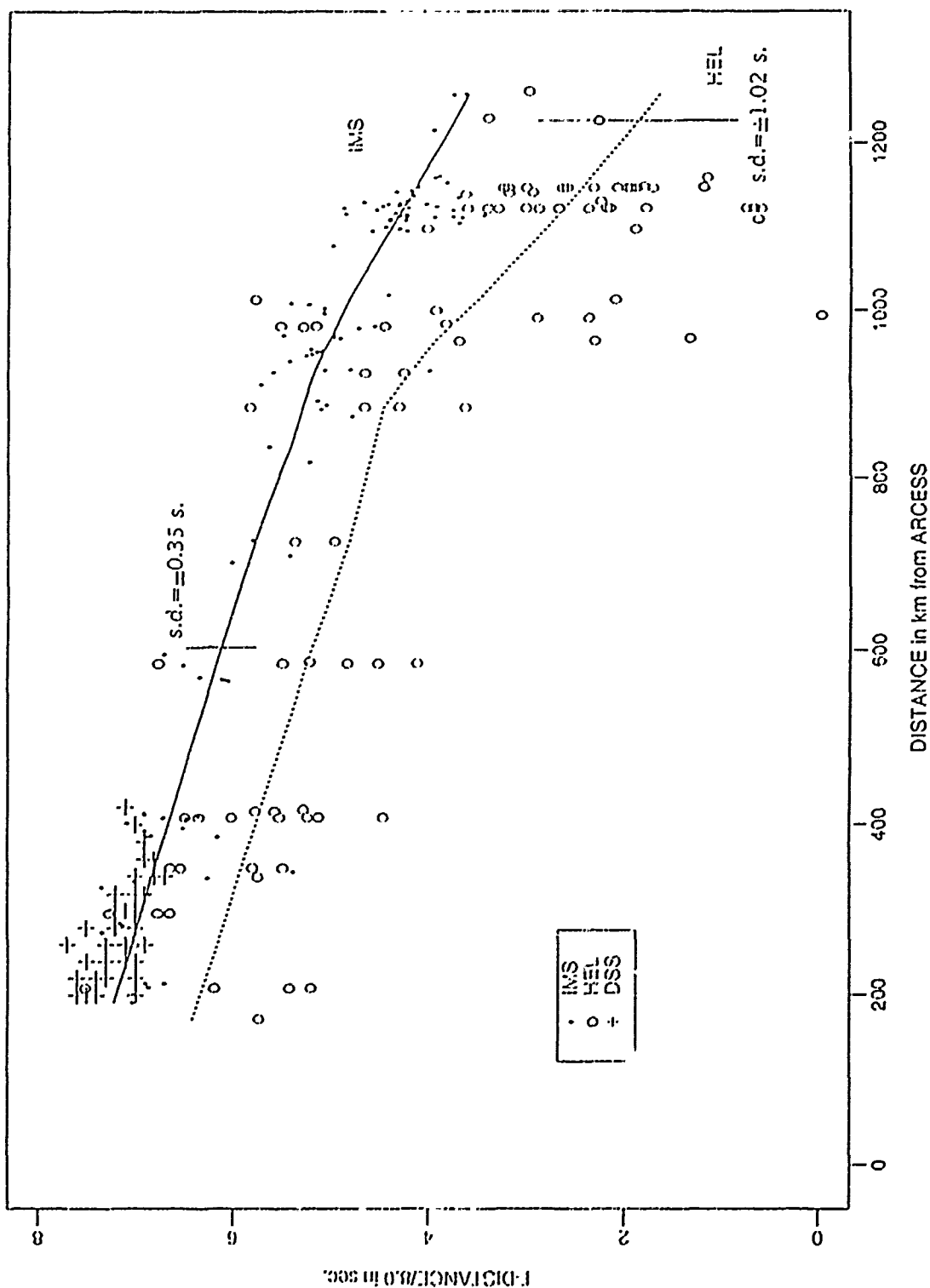


Figure 3. Pn travel-times for selected events based on POLAR DSS profile data (pulses), IMS (dots), and HEL (circles) bulletins. One can see bias between the travel-time curves based on the IMS and HEL bulletins. Independent DSS observations are a better fit to IMS data.

Sn TRAVEL-TIME CURVES BASED ON IMS AND HELSINKI BULLETINS

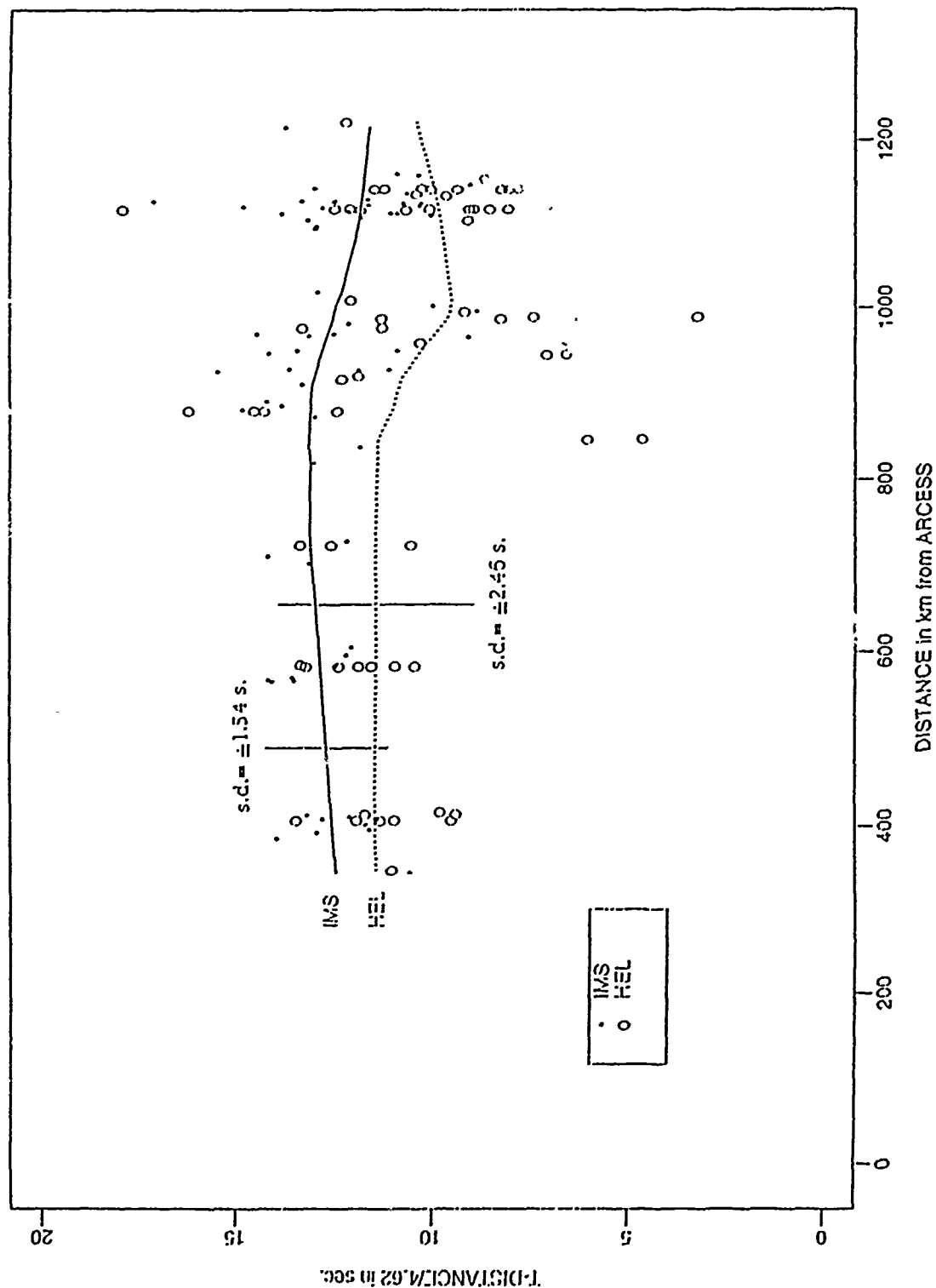


Figure 4. Sn travel-times for the ARCESS-FINESA profile based on IMS and HEL bulletins. One can see the bias between the travel-time curves based on the IMS and HEL bulletins.

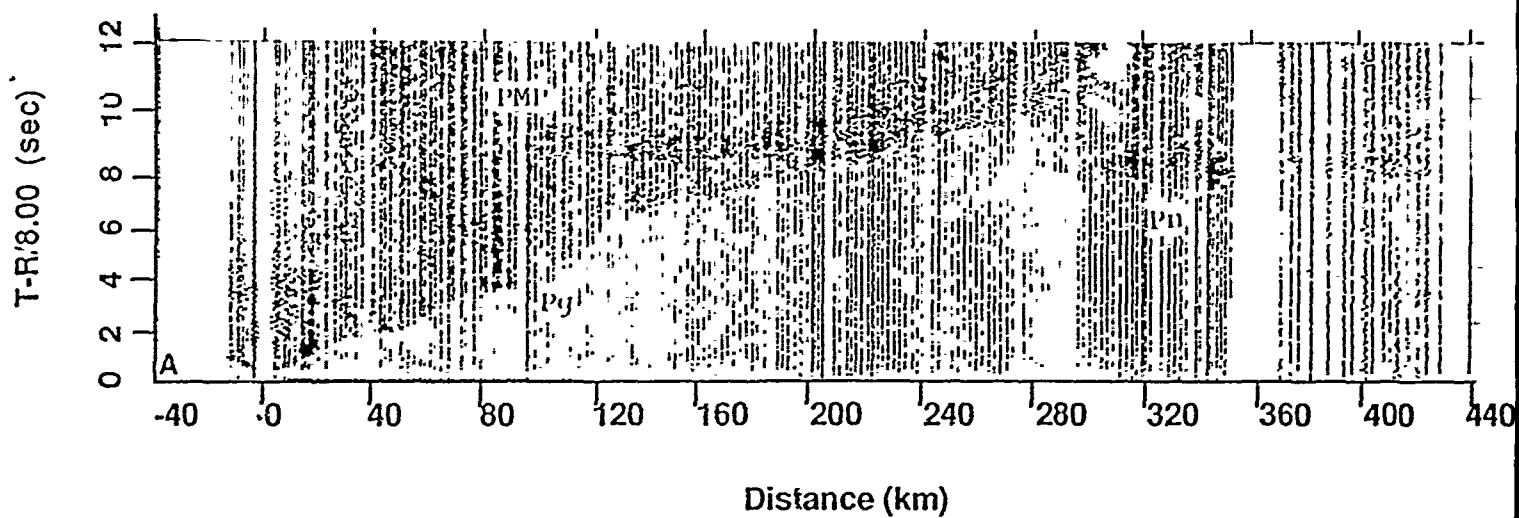


Figure 5. POLAR DSS profile. Trace-normalized P-wave record section for shot-point A (southern part of the profile). Adapted from Luosto et al. (1989).

regions of the USSR they are distributed very densely (see *Figure 2* in Bratt et al., 1990). Consequently, it is not an easy problem to locate these mine explosions accurately, even for skilled analysts. It is especially difficult for events which occur beyond the region covered by the HEL network. These circumstances may eliminate the advantages of the HEL network over the IMS.

We stress that our preliminary conclusion about the advantages of the IMS locations over the HEL network locations is valid only for events located beyond the boundaries of the region covered by the HEL network. It would be wise to repeat the analysis for two groups of events, occurring within and beyond the boundaries of the region covered by the Helsinki network. Additionally, it would be extremely helpful for understanding IMS capability to compare both bulletins with parameters of precisely located events.

Vladislav Ryaboy

REFERENCES

- Bache, T. C., Bratt S. V., Wang, J., Fung, R. M., Kobryn, C., and Given, J. W., "The Intelligent Monitoring System," *Bull. Seism. Soc. Am. (in press)*, p. 18, 1990.
- Bratt, S. V., Swanger, H. J., Stead, R. J., Ryall, F., and Bache, T. C., "Initial results from the Intelligent Monitoring System," *Bull. Seism. Soc. Am. (in press)*, p. 29, 1990.
- Luosto, U., Fjorvick E. R., Lund C.-E., and Working Group, "The crustal structure along the PO₁ profile from seismic refraction investigations," *Tectonophysics*, vol. 162, p. 51-85, 1989.
- Ryaboy, V., "Upper mantle structure along a profile from Oslo (NORESS) to Helsinki to Leningrad, based on explosion seismology," in *Technical report for the period 1 October 1987 - 30 September 1989*, pp. 2.1-2.38, Center for Seismic Studies, Arlington, VA, 1990.

3.1 ANALYSIS OF 3-COMPONENT DATA FROM IRIS STATIONS IN THE USSR

ABSTRACT

This paper presents results of backazimuth, incidence angle, and phase identification studies based on the three-component polarization of seismic signals recorded at the IRIS stations within the USSR. A data set was built from the analysis of 3-component (3-C) recordings from seismic stations at Arti (ARU), Garm (GAR), Kislovodsk (KIV), and Obninsk (OBN) for the month of March 1989. Approximately 260 events were studied. At stations ARU, KIV, and OBN teleseisms dominated the recordings. Station GAR, however, recorded a larger set of events which included a significant number of local and regional events.

Except for station OBN, all of the IRIS stations are located near major geologic structural boundaries that are characterized by significant lateral variation in the deep velocity structure. The effect of these boundaries is to cause systematic deviations in estimates of backazimuth and angle of incidence. At station GAR, both of these measurements were influenced by the structure.

Polarization characteristics of seismic phases were studied individually for each station. At stations OBN and KIV, the initial teleseismic *P*-wave was characterized, for the most part, by prograde elliptical motion. At ARU and GAR the motion was rectilinear. Regional *S* phases from Hindu-Kush earthquakes recorded at GAR were dominated by transverse horizontally polarized motion (*SH*). At KIV and ARU *Lg* motion was predominantly in a near-horizontal plane.

A phase identification study was performed using discriminant analysis based on polarization parameters and frequency content. Two discriminants, linear combinations of polarization and frequency measurements, were able to separate arrival data into one of three groups of phases: teleseismic *P*, regional *P*, and regional *S*. At GAR, the first discriminant is correlated with polarization and separates arrivals with *P*-wave characteristics from arrivals with *S*-wave characteristics. The second discriminant accentuates the differences in the frequency content of the arrivals and provides a good separation between regional and teleseismic phases.

Backazimuth estimates were made for local, regional, and teleseismic events at GAR; and for teleseismic events at ARU, KIV, and OBN. The unique structural environment of each station required that custom processing parameters be developed for each station. The assumed particle motion (rectilinear or elliptical) used in the polarization computation, the window length, and the frequency band (characteristic for each station) were determinant factors. Backazimuth estimates within $\pm 25^\circ$ of the theoretical value were obtained for about 70% of the events at most of the stations. At GAR, systematic backazimuth errors caused by large lateral velocity discontinuities degraded the results. Corrections could be made to reduce these errors.

3.1.1 Introduction

Accuracy of event location is one of the main problems in seismology. Several reliable methods have been developed for determining the location, origin-time, and depth of events using arrival time data from a network of seismic stations (Eaton, 1969; Lee and Lahr, 1972; Klein, 1984; Lienert *et al.*, 1986). Methods have also been developed for locating events using single 3-C station data (Magotra *et al.*, 1987; Ruud *et al.*, 1988). The locations determined using these methods are not as reliable as the network solutions but the backazimuth and distance information contained in 3-C data is now being incorporated into network solutions. A study involving a sparse network of 3-C stations was described by Thurber *et al.* (1989) in which an accurate location was provided for events recorded at two or more stations. Backazimuth information from small aperture arrays is also being used effectively for event location in Scandinavia (Bratt and Bache, 1988).

Polarization analysis is the main source of information from 3-C data (Jurkevics, 1988, Christoffersson *et al.*, 1988) and has been used effectively for event location, phase identification, and velocity structure studies. At the beginning of the century one of the first upper-mantle velocity sections was constructed for Northern Eurasia on slowness estimates inferred from incidence angle measurements at a single 3-C station (Golitsyn, 1960). Phase identification based on polarization has been studied as a method of identifying converted P - S waves at teleseismic distances (Pomerantseva and Mozzhenko, 1977). A method for automated phase identification based on multivariate analysis of signal characteristics (Cooley and Lohnes, 1971) was applied to the short period seismic arrays NORESS and ARCESS in Norway by Suteau-Henson (1991). In this paper, the methods used by Suteau-Henson to identify phases are extended in two ways. First, teleseismic P arrivals are included, so that discrimination is obtained between three groups: teleseismic P , regional P , and regional S . And second, the dominant frequency is used as a predictor along with polarization.

Walck and Chael (1990) pointed out the importance of parameters such as frequency band and window length in the process of backazimuth estimation. A strong site dependency was also recognized in their polarization results. These observations demonstrate the importance of determining the polarization characteristics for each station individually. Applying generic polarization processing schemes to data from different stations may lead to unsatisfactory results.

3.1.2 Receiver Structure

This section summarizes published soviet work on crust and upper-mantle velocity structure in the regions containing the four IRIS seismic stations (Table 1) (IRIS, 1989), and presents average structural models for use in analyzing data from the stations. Three stations are located in the European part of the USSR: one near

Obninsk (OBN), the second in Arti (ARU), and the third near Kislovodsk (KIV). Stations OBN and ARU are situated in the center (Moscow syncline) and east (Cis-Urals foredeep) of the Precambrian East-European platform, respectively, station KIV is on the Paleozoic Scythian platform at its border with the Greater Caucasus. A fourth station is located in Central Asia not far from Garm (GAR) in the Southern Tien-Shan Mountains at their junction with the Pamir ranges. Station GAR is located near an important geological boundary which follows the Surkhob river. North of the river the rocks of the southern Tien-Shan are crystalline, Paleozoic in age, and highly metamorphised. To the south, in the Peter the First range, the rocks are sedimentary, highly deformed (folded and faulted), and Mesozoic to Cenozoic in age. Seismic velocities are about ten percent slower in the upper crust of the Peter the First range than in the Tien-Shan (Rautian *et al.*, 1978, Popandopulo, 1990). *Figure 1* shows the locations of the IRIS stations and the deep seismic soundings (DSS) profiles used to infer the velocity structures presented in this study.

Table 1. IRIS SEISMIC STATIONS in the USSR				
No.	Location	Latitude (deg.)	Longitude (deg.)	Elevation (m)
1.	Arti (Cis-Urals foredeep)	56.40N	58.60E	250
2.	Garm (South Tien-Shan)	39.00N	70.32E	1300
3.	Kislovodsk (Cis-Caucasus foredeep)	43.95N	42.68E	1206
4.	Obninsk (Moscow syncline)	55.10N	36.60E	130

To date, the most reliable information about the earth crust and upper mantle structure is produced from DSS profiles. Sources for these long range reflection and refraction profiles are usually nuclear or large chemical explosions. Reversed and overlapping profiles recorded with a dense receiver array provide precise structural control that is unavailable to earthquake studies.

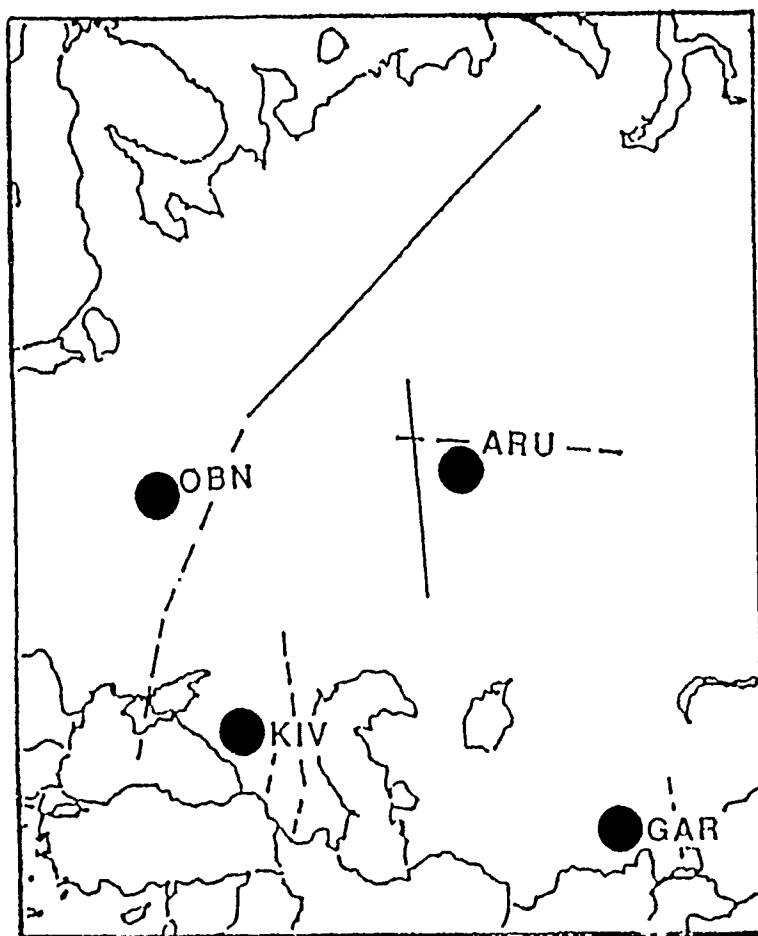


Figure 1. Locations of the IRIS stations and deep seismic sounding (DSS) profiles used for this study. DSS profiles of the earth crust and upper mantle based on peaceful nuclear explosions are shown as solid lines. Dashed lines are DSS profiles based on chemical explosions.

Deep seismic studies in North Eurasia indicate significant lateral and vertical heterogeneities in the structure of the crust and upper-mantle. These are manifested in travel-time anomalies, amplitudes, and frequency content. In crossing from one geological structure to another, changes typically occur in both the velocities of seismic waves and in the character of their distribution with depth. For this reason, we have limited our extrapolation of results to just those geological units in which the IRIS stations are located.

Average *P*-wave velocity sections have been constructed based on DSS results for the areas containing the four IRIS stations (*Figure 2, Table 2*). Tectonically active regions such as the southern Tien-Shan (GAR) are generally distinguished from the East-European (OBN and ARU) and Scythian (KIV) platforms by the presence of thick low-velocity layers in the upper-mantle. Similar layers of reduced velocity also exist in the upper mantle beneath platforms, but they are usually thinner and not as pronounced.

Table 2. PARAMETERS OF THE EARTH CRUST AND UPPER MANTLE VELOCITY MODELS FOR IRIS STATIONS IN THE USSR BASED ON EXPLOSION SEISMOLOGY DATA				
Parameter	OBN	ARU	KIV	GAR
1. Earth crust thickness (km)	45	43	45	70
2. Mean velocity of the earth (km/s) crust (km/s)	6.3	6.3	5.7	6.5
3. Low-velocity layers in the earth crust, range of depths (km/s)	-	25-35	15-20	10-21
4. Low-velocity layers in the earth crust, layer velocity (km/s)	-	6.5-6.7	5.6-5.7	5.8-6.0
5. Pn wave velocity (km/s)	8.2	8.3	8.3	8.1
6. Low-velocity layer in the upper mantle, range of depths (km)	60-90	70-100	-	110-210
7. Low-velocity layer in the upper mantle, layer velocity (km/s)	8.1	8.2	-	8.15

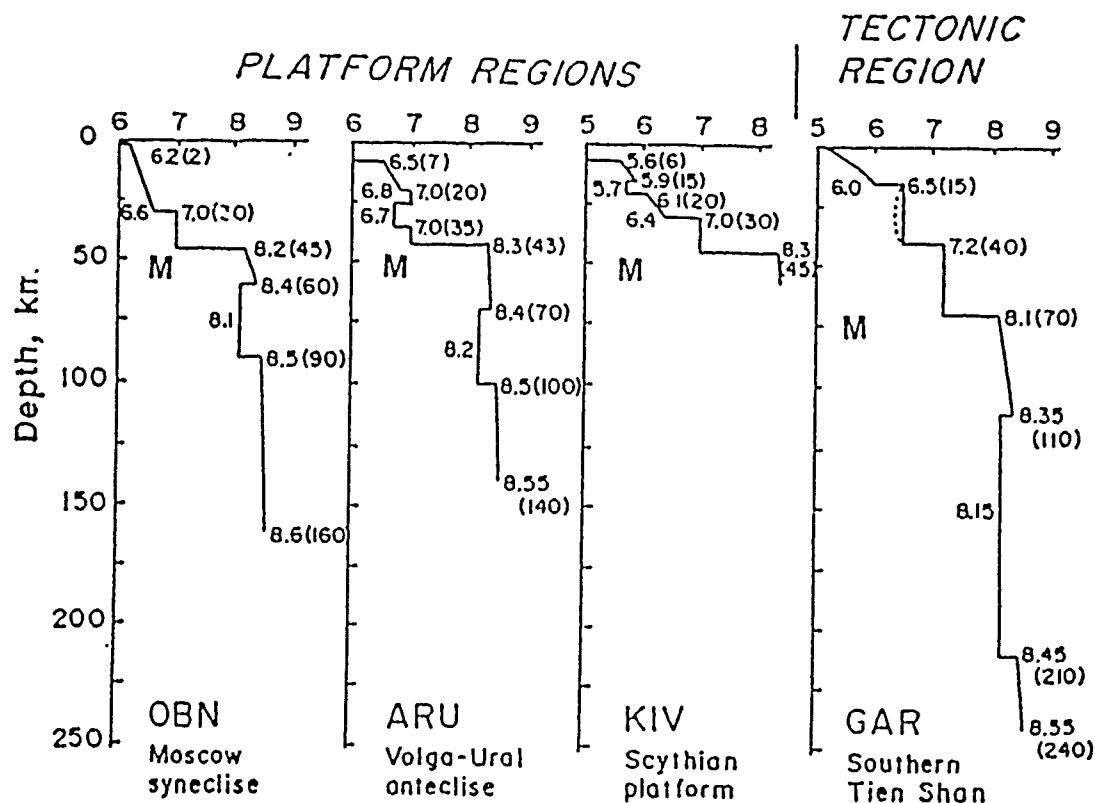


Figure 2. Seismic velocity-depth curves of the earth crust and upper mantle near the IRIS stations. The curves are based on published data obtained from studies of major geological units of Northern Eurasia. OBN (Moscow syncline), ARU (eastern Russian plate and Cis Urals foredeep), KIV (southern Scythian platform, Cis-Caucasus foredeep), GAR (southern Tien-Shan). Solid lines -- explosion seismology data, dashed lines -- earthquake seismology data, M -- Moho. An extensive list of references was given in (Ryaboy, 1989, 1990).

3.1.3 Seismicity

Data for this study were recorded during the month of March in 1989 and include more than 1,000 individual events from local to teleseismic distances. About 260 of these were studied in detail.

Nearly 150 teleseisms were reported in the National Earthquake Information Center (NEIC) bulletin for this month. *Figure 3* shows that most of the teleseisms with distances larger than 40° were located near Japan and the Philippines. Only one was reported along the Mid-Atlantic ridge. The events that were recorded between distances of 20 and 40° were mainly located in the USSR, a few were located in China, and some occurred along the Mediterranean ridge.

At station GAR, 871 local and regional events were recorded during this month. Very few of them were recorded at the other Soviet stations which implies that the magnitudes of these events were very small. The GAR area has been described as one of the most seismically active in the Soviet Union (Leith and Simpson, 1986). Eneva and Hamburger (1989) showed that the majority of the seismicity around GAR (in the Gissar-Kokshal area) is due to microearthquakes occurring at shallow depths. Intermediate focus earthquakes occur to the southeast in the Hindu-Kush (Chatelain *et al.*, 1980).

Although station ARU detected most of the teleseismic events that were reported during this period, only 85 of them were selected for analysis. The local and regional events recorded at ARU were located within a distance range of 2 to 10°. Most of the seismic activity in this area is related to mining blasts (Leith, 1990). A weekly distribution of the local and regional seismicity around ARU showed intense activity Monday through Friday when the mines were in operation. Among the 25 regional events located, 19 of them exhibited an *Rg* phase which is indicative of a very shallow source. By comparison, only 9 events out of more than 800 had an identifiable *Rg* at station GAR.

Most of the events recorded at stations KIV and OBN were from teleseismic distances. Besides having noise problems, OBN is located in a relatively aseismic area and only six local events were recorded during the month. The small number of events recorded at ARU, KIV and OBN prevented a thorough study of local and regional events.

The noise characteristics of the IRIS stations in the USSR have been described by Given (1990). Of the four studied, GAR had the lowest noise level. Its useful frequency band was between 1 and 5 Hz. KIV did not have excessive background noise, but some external effects, possibly wind or cultural noise, introduced a strong regular noise lasting a few minutes at spaced intervals during the day. This noise could be eliminated on the vertical component by using a bandpass filter from 1.0 to 3.0 Hz, but remained on the horizontal components at the same

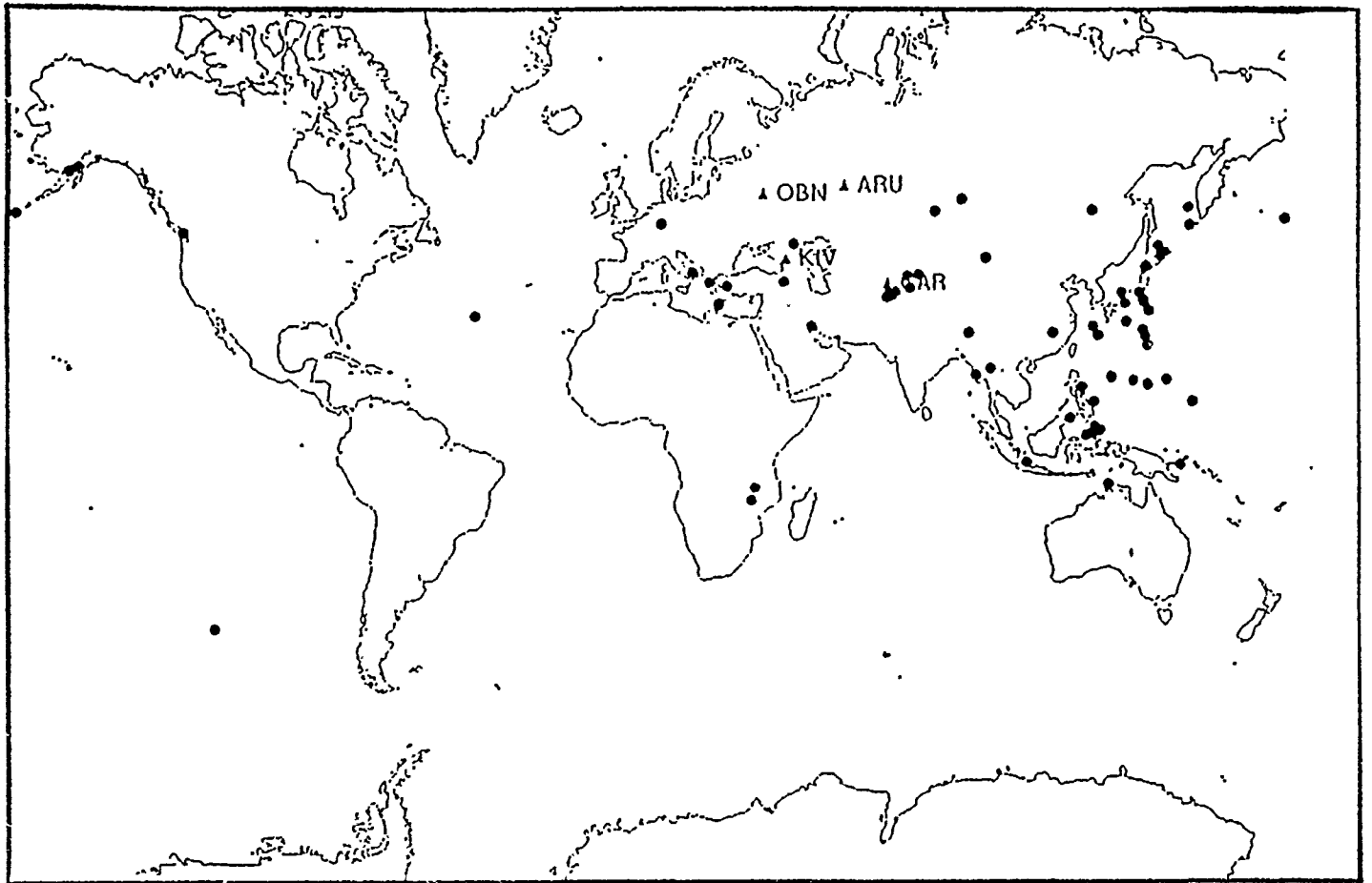


Figure 3. Locations of the teleseismic events recorded at the IRIS stations. Some events close to one station are at teleseismic distances from the other stations.

frequencies. ARU was contaminated by many noise bursts which were difficult to eliminate because they were in the same frequency band as the signal. OBN also had regular background noise in the same frequency band as the signal.

Source locations and magnitudes for the teleseisms and large regional events were obtained from event catalogs. The small local and regional events were not reported for most of the stations, but at GAR a local event catalog was used to verify the locations of the recorded events.

3.1.4 Waveform Polarization

For single station 3-C data, polarization methods are the only means for locating seismic events and are very useful for identifying phases. Continuous IRIS data (20 samples/second) were processed with an automatic detection program that also computed polarization parameters for each detection (Bache et al., 1990). The polarization measurements were based on an eigensystem decomposition of the wavefield developed by Jurkevics (1988). Data surrounding detections were prefiltered in a set of frequency bands selected on the basis of their signal-to-noise ratio (hereafter referred to as "3-C SNR"). Polarization analysis was performed in small, overlapping time windows for each of the frequency bands and the results averaged. Those polarization parameters particularly useful for characterizing local and regional phases were: rectilinearity (*rect*), planarity (*plan*), ratio of horizontal to vertical power (H/V), incidence angle of the long axis of the polarization ellipsoid (*inc1*), incidence angle of the short axis (*inc3*) and frequency characterizing the band used in the analysis. The signal-to-noise ratio also provided important information about the signal quality. These and other polarization attributes were fully described in Suteau-Henson (1991).

Polarization attributes from automated processing were studied for "regional S" as a group (note that, although reliably identified, *Sn* and *Rg* arrivals were not numerous enough to be included in the analysis). The automated processing did not always provide reliable measurements for *P*-type phases, as demonstrated by comparing backazimuth estimates with those from bulletin locations (see the section on backazimuth estimation). Thresholds of 3-C SNR or rectilinearity could be used to reduce the scatter in the estimates and the number of outliers. Complete analysis of *P*-wave polarization awaits optimization of the procedure for automated processing.

GAR

The largest concentration of local and regional events was around Garm. For each event from the Hindu-Kush area, only one large *S*-type phase was detected (hereafter referred to as "*S*"). This phase may be a direct *S*, although modeling experiments indicate that it could also be a combination of phases that have

bounced once in the crust (Helmberger *et al.*, 1990).

We studied a total of 643 *Lg* and *S* phases that were detected and associated to seismic events. Only 11 of those were from events with distances larger than 5°. Fifty-two percent were from events located at distances between 2.25° and 2.75° (*Figure 4, left*). Azimuth estimates of their dominant rectilinear motion form a bimodal distribution with peaks around 90° and 270° (*Figure 4, middle*). This is consistent with dominant transverse (*SH*) motion and a backazimuth of about $180^\circ \pm 30^\circ$ (with a 180° ambiguity). Therefore, although it may include some mislocated events, this set was interpreted as a cluster of intermediate-focus earthquakes from the Hindu-Kush seismic zone.

This interpretation was confirmed by investigating backazimuth estimates from *P*-type arrivals. Only events located between 2.25° and 2.75° distance were considered. Scatter in the estimated backazimuths and the number of outliers was reduced by limiting the study to arrivals with rectilinearity higher than 0.8. The resulting distribution (*Figure 4, right*) agreed with that obtained for *S* (median of 174°). This confirmed that most of these events were probably located in the Hindu-Kush seismic area.

Local and near-regional *Lg* and *S* at GAR have very characteristic polarization, as indicated by the distributions of polarization attributes for the 643 arrivals studied (*Table 3* gives their median and standard deviation). A very high ratio of horizontal to vertical power (*H/V*) and small short-axis incidence (*inc3*) indicate dominant motion in a near-horizontal plane. The statistics for the cluster near 2.5° are also given in *Table 3*. The distributions are similar to those for the entire data set, except that the plane of dominant motion is even more horizontal. For events in that distance range, 354 *P* arrivals were characterized by high rectilinearity (0.82) and low incidence angles (median of 23°) (*Table 3*).

The anomalously low (for *Pn* waves) incidence angles of *P* arrivals for events occurring in the Hindu-Kush area can be explained by laterally heterogeneous structure. A subset of 157 arrivals with backazimuths between 130° and 210° and rectilinearity greater than 0.8 was used to study the low incidence angles. This backazimuth range was selected based on our observations (*Figure 4*) and on seismicity studies (Chatelain *et al.*, 1980). The *inc1* distribution of the resulting set had a median of 20° and a standard deviation of 6°. The apparent incidence angle was converted to "true" incidence angle using standard formulas (Bullen, 1959). This, in turn, was converted to slowness using a subsurface velocity of 5.0 km/s for the Peter the First Range immediately south of GAR (Khamrabaev and Zunnunov, 1984, Popandopulo, 1990). For a given distance (2.5°) and slowness, Herrin tables were used to estimate source depth as a first order approximation.

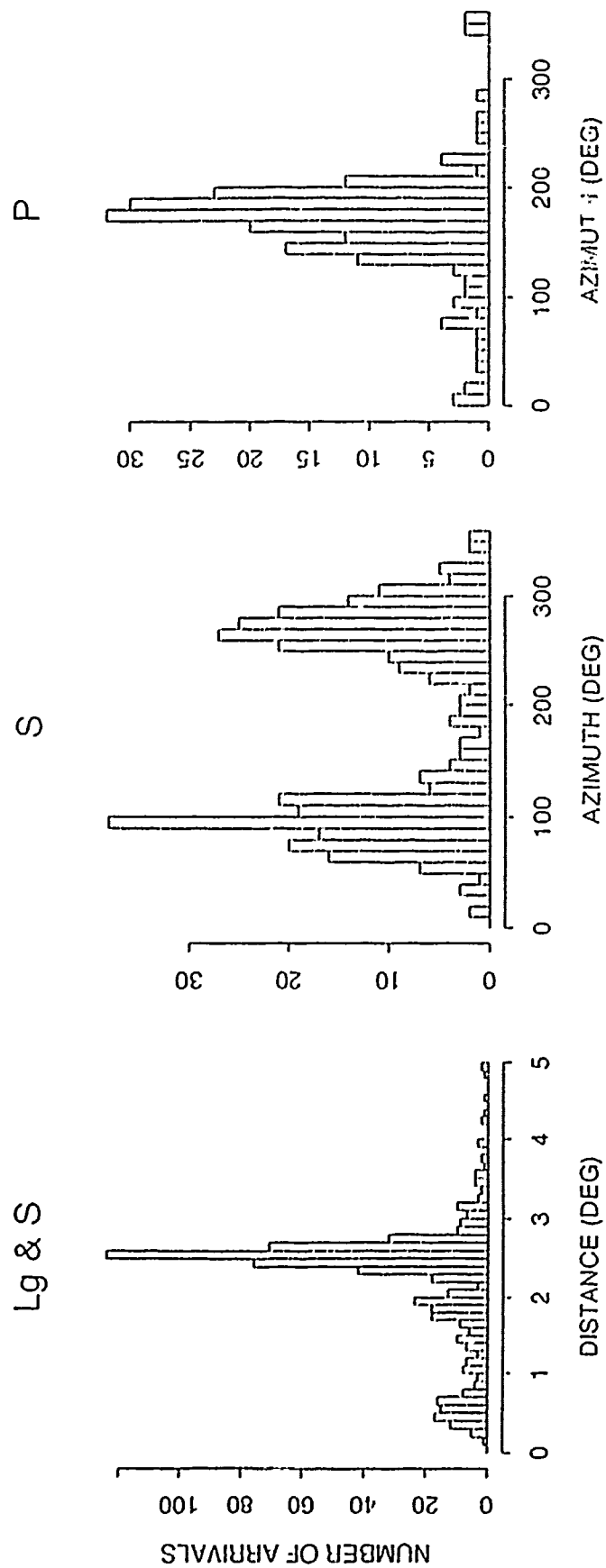


Figure 4. *Left:* Histograms of epicentral distance for local and near-regional events with detected *Lg* and "*S*" arrivals at GAR. A sharp peak is observed at about 2.5°. *Middle:* Histograms of azimuth of principal linear motion for presumed "*S*" arrivals, with distance of about 2.5°. The distribution is consistent with transverse (*SH*) motion propagating from the South. *Right:* Histograms of backazimuth from *P*-type arrivals (with rectilinearity > 0.8) for events at about 2.5° distance. Backazimuths from the South are consistent with the "*S*" azimuths, and correspond to locations within the Hindu-Kush seismic zone.

<p align="center">Table 3. Polarization of Local/Regional Phases at GAR</p>							
Attribute	Symbol	<i>Lg</i> & <i>S</i>		<i>S</i> †		<i>P</i> †	
		Median	S.D.	Median	S.D.	Median	S.D.
Rectilinearity	<i>rect</i>	0.63	0.12	0.66	0.11	0.82	0.12
Planarity	<i>plan</i>	0.42	0.19	0.43	0.19	0.22	0.18
Horizontal/Vertical††	<i>H/V</i>	3.3	2.2	4.0	2.7	0.30	0.26
Incidence Angle	<i>incl</i>	82°	15°	84°	15°	23°	18°
Short-Axis Incidence	<i>inc3</i>	18°	19°	14°	19°	79°	13°

† From presumed Hindu-Kush earthquakes

† † Logarithmic distribution

For observed incidence angles ranging from 17-23°, the derived range in source depth is 420-590 km. This contrasts with the results of Chatelain *et al.* (1980) who found a concentration of hypocenters around two shallower depth ranges: 70-170 m and 180-300 km based on local network studies. This discrepancy can be explained by lateral heterogeneity along the path in the upper part of the earth's crust. A few kilometers south of GAR, a sharp boundary separates the southern Tien-Shan to the north from the Peter the First Range to the south (Rautian *et al.*, 1978). According to seismological and geological data, this boundary is almost vertical in the uppermost crust and its slope decreases with depth (Hamburger *et al.*, 1990; Leith, 1985).

The velocity of the southern Tien-Shan beneath GAR is approximately 5.5 km/s, but it is 5.0 km/s under the Peter The First range just south of GAR (Zverev and Kosminskaya, 1980; Khamrabaev and Zunnunov, 1984; Hamburger *et al.*, 1991, Popandopulo, 1990). Seismic waves from events located to the south must cross this boundary and their paths are deflected accordingly. Assuming for simplicity that this boundary is vertical in the upper crust, simple calculations show that an observed incidence angle of 20° corresponds to a "true" incidence angle of 17.5° for events north of the boundary and 30° for events located south of the boundary (Figure 5). Converting the "true" incidence angles of the events south of the boundary into slowness, new estimates of depth were obtained. The 17-23° range of observed incidence angles corresponds to depths of 200-250 km. This is in agreement with the depths estimated by Chatelain *et al.* (1980).

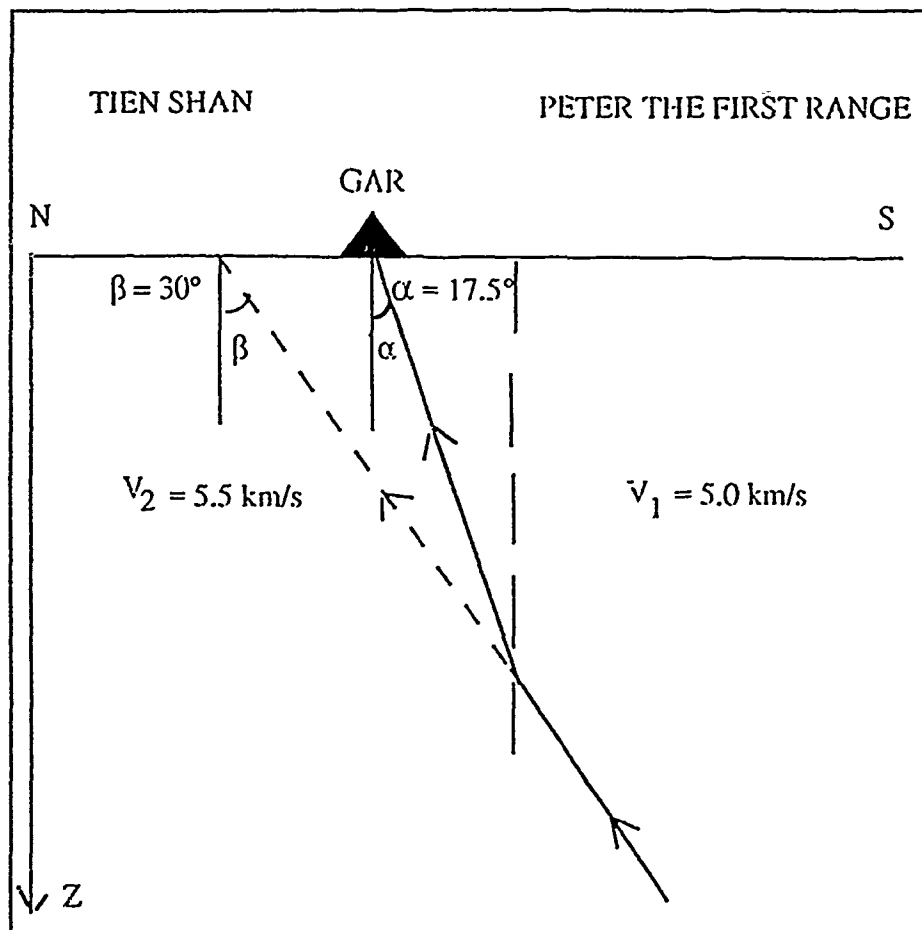


Figure 5. Schematic north-south cross-section of the upper crust under station GAR. Ray paths from intermediate focus earthquakes in the Hindu-Kush, south of the station, are probably deflected due to the *P*-wave velocity contrast in the upper crust between the Peter The First Range and the Tien Shan. This simple model predicts "true" incidence angles (α) under Garm about 13° lower than those expected for a laterally homogeneous structure (β).

The effect of a laterally heterogeneous structure on observed incidence angles at GAR is further illustrated by shallow local events. Network locations were available from a local catalog for a set of 89 such events. A subset of 77 local *P* arrivals was selected for which the difference between the backazimuth from polarization and that derived from the catalog location was less than 40°. The epicentral distances of the selected events were less than 1.5°, and their depths were less than 44 km according to the catalog. They were characterized by a fairly uniform azimuthal coverage. However, a distribution of incidence angles showed two peaks: one around 30° and the other around 55°. No correlation was found between *incl* and distance or depth. In contrast, we observed an interesting correlation between incidence angle and backazimuth from the catalog (*Figure 6, left*). For backazimuths of 0-90°, *incl* was high (50-65°). It was low (20-40°) between 90° and 270° and high again from 270° through 360°.

Figure 6 (right) shows *incl* as a function of backazimuth determined from polarization methods for local and regional *P* arrivals with rectilinearity greater than 0.8. In spite of larger scatter and some outliers, a similar trend was observed. The very low values of *incl* around 180° correspond to the Hindu-Kush events discussed above. This trend is explained by differences in velocity structure north (0-90° and 270-360°) and south (90-270°) of GAR. North of GAR, plausible values of *incl* were found for local *P_g*, while south of GAR, the observed values were anomalously low. This is consistent with our observations for the Hindu-Kush events.

ARU, KIV, and OBN

As seen earlier, local and regional seismicity was lower at ARU than at GAR. Levels of seismicity at KIV and OBN were even lower, limiting the extent of our study. In addition to the low level of seismicity, seismic noise played an important role in determining the polarization characteristics at these stations. More scatter was observed in the distributions of polarization attributes for the stations with high noise levels, KIV and OBN. Some interesting results were obtained, however, at each of these stations.

Table 4 shows that *L_g* was characterized by dominant particle motion in a near-horizontal plane at each of the stations. This was particularly true at ARU where the ratio of horizontal-to-vertical power was nearly double that at the other stations based on a sample of 84 arrivals. Non-isotropic noise observed at KIV may explain the near-horizontal polarization of the 36 *L_g* arrivals studied at this station.

Teleseismic *P*-waves provided the most polarization information at these stations. For ARU, the motion of the first teleseismic *P* arrival was observed to be rectilinear. At KIV and OBN, however, the particle motion of the first arrival changed from rectilinear to prograde elliptical after one second.

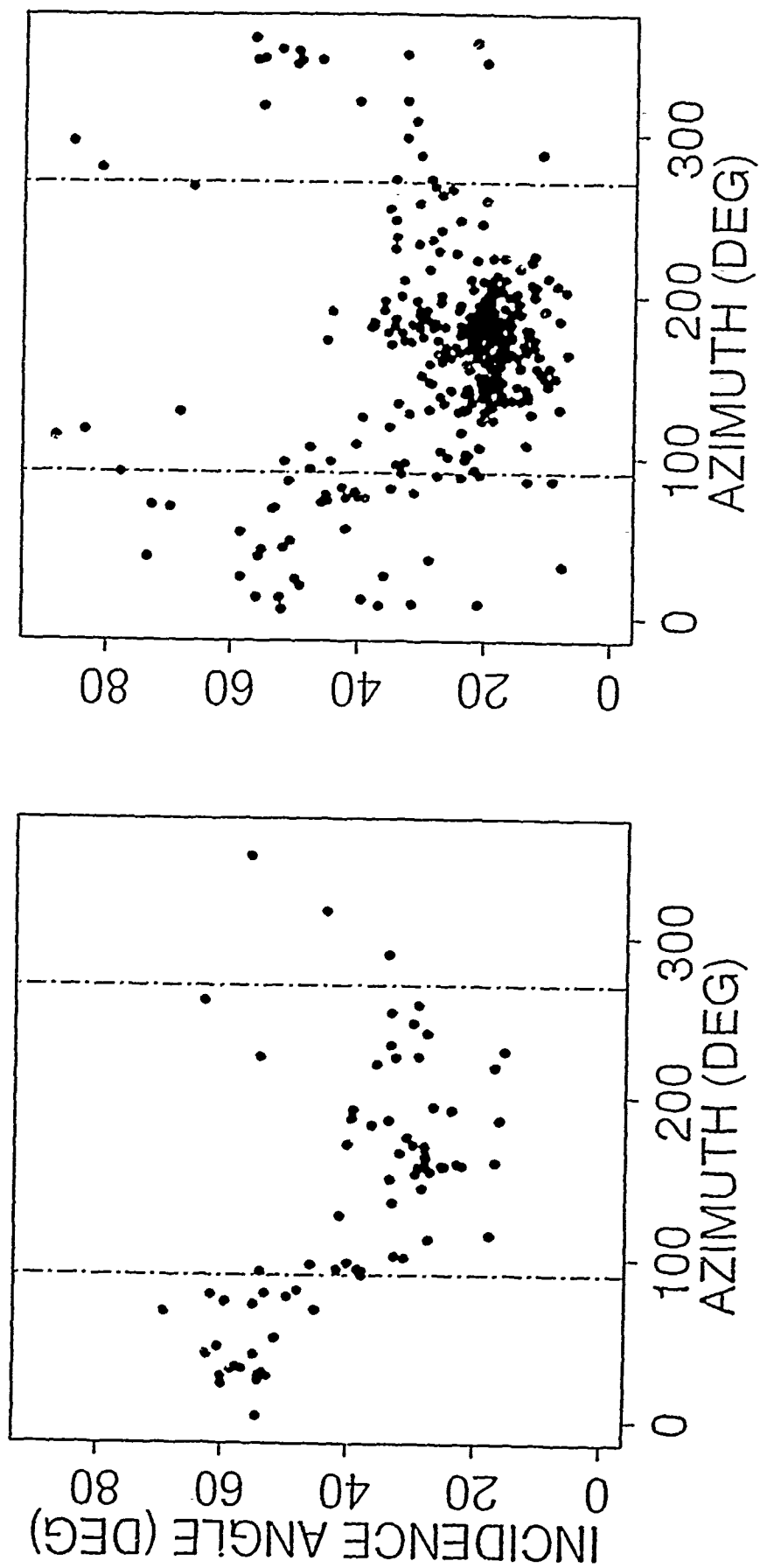


Figure 6. Incidence angle is plotted as a function of event backazimuth for two sets of P arrivals at GAR: *left*, local P_g selected from Garm catalog; *right*, local and regional P -type phases (with rectilinearity > 0.8), from the March 1989 database of this study. Decreased incidence angles are observed south of GAR (between the dashed lines).

Table 4. Medians of <i>Lg</i> Polarization Attributes			
Attribute	GAR†	ARU	KIV
Rectilinearity	0.63	0.68	0.66
Planarity	0.42	0.62	0.52
Horizontal/Vertical	3.3	6.4	3.2
Incidence Angle	82°	86°	82°
Short-Axis Incidence	18°	11°	18°

† "S" arrivals are included at this station

3.1.5 Phase Identification

Before an event can be located using single station 3-C data, the arriving phases must be identified. If reliable methods of phase discrimination can be found that are based on signal characteristics, then these measurements can be used to determine the phase type automatically. This section describes a discriminant analysis method applied to automated phase identification.

All measurements of polarization and frequency used in this analysis were determined automatically. A large scatter was present in the polarization estimates of *P*-type arrivals. Better results are expected when the parameters for automated signal processing are optimized. However, the performance obtained with the data currently available demonstrates the capabilities of this method for initial phase identification at GAR, ARU, and KIV.

Two groups of signal features were used as predictors of phase type. Features associated with the 3-C SNR of the waveforms and polarization features. The first group makes use of the filtered channel with the highest 3-C SNR (*chan*=1 for horizontal, 2 for vertical) and the dominant frequency of this channel (*freq*). The second consists of a set of signal parameters obtained from polarization analysis, similar to that used in the section on polarization. center frequency (*freq2*) of the wide band used in polarization analysis, rectilinearity (*rect*), planarity (*plan*), horizontal-to-vertical power ratio (*H/V*) measured at the time of maximum 3-C amplitude, horizontal-to-vertical power ratio (*H/V2*) measured at the time of maximum rectilinearity, long-axis incidence angle (*inc1*), and short-axis incidence angle (*inc3*).

Discriminant analyses and classification procedures were first applied to a training set, then replicated on a testing set. Principal Component Analysis was performed prior to Discriminant Analysis to reduce the number of variables. In the following, results will be presented for the case where only the first three principal components are used. The discriminant performance was obtained by averaging the results for the training and testing sets.

GAR

At this station 1729 arrivals were analyzed: 108 teleseismic *P*, 767 regional *P*, and 854 regional *S*. Two discriminants were empirically obtained that best separate the three groups. The discriminant plane they form is plotted in *Figure 7*. Each discriminant is a linear combination of the measurements, properly normalized and standardized (Suteau-Henson, 1991). The first discriminant, D_1 , is weighted heavily towards the polarization measurements:

$$D_1 = -0.32 \text{ chan} - 0.03 \text{ freq} + 0.10 \text{ freq2} - 0.30 \text{ rect} + 0.02 \text{ plan} \\ + 0.38 \text{ H/V} + 0.38 \text{ H/V2} - 0.34 \text{ inc3} + 0.35 \text{ inc1}$$

The discriminant value is low for arrivals that are detected on the vertical component, and have high rectilinearity, low *H/V*, large *inc3* (principal motion in near vertical plane), and small incidence angle. Thus, D_1 is low for teleseismic *P* and high for regional *S*. The second discriminant, D_2 , is correlated with frequency.

$$D_2 = 0.03 \text{ chan} + 0.70 \text{ freq} + 0.65 \text{ freq2} - 0.03 \text{ rect} - 0.09 \text{ plan} \\ + 0.00 \text{ H/V} - 0.03 \text{ H/V2} + 0.03 \text{ inc3} - 0.03 \text{ inc1}$$

The discriminant value is low for teleseismic *P* and high for regional *P*. Clearly, the inclusion of frequency greatly facilitates discrimination between regional and teleseismic phases.

The discriminant performance is summarized in *Table 5* which gives the percentage of correctly identified arrivals (using the analyst's identification as reference). It is highest for regional *S* (93%) and lowest for regional *P* (81%). The performance significantly improved, however, for regional *P* with 3-C SNR > 5 (90%).

GAR

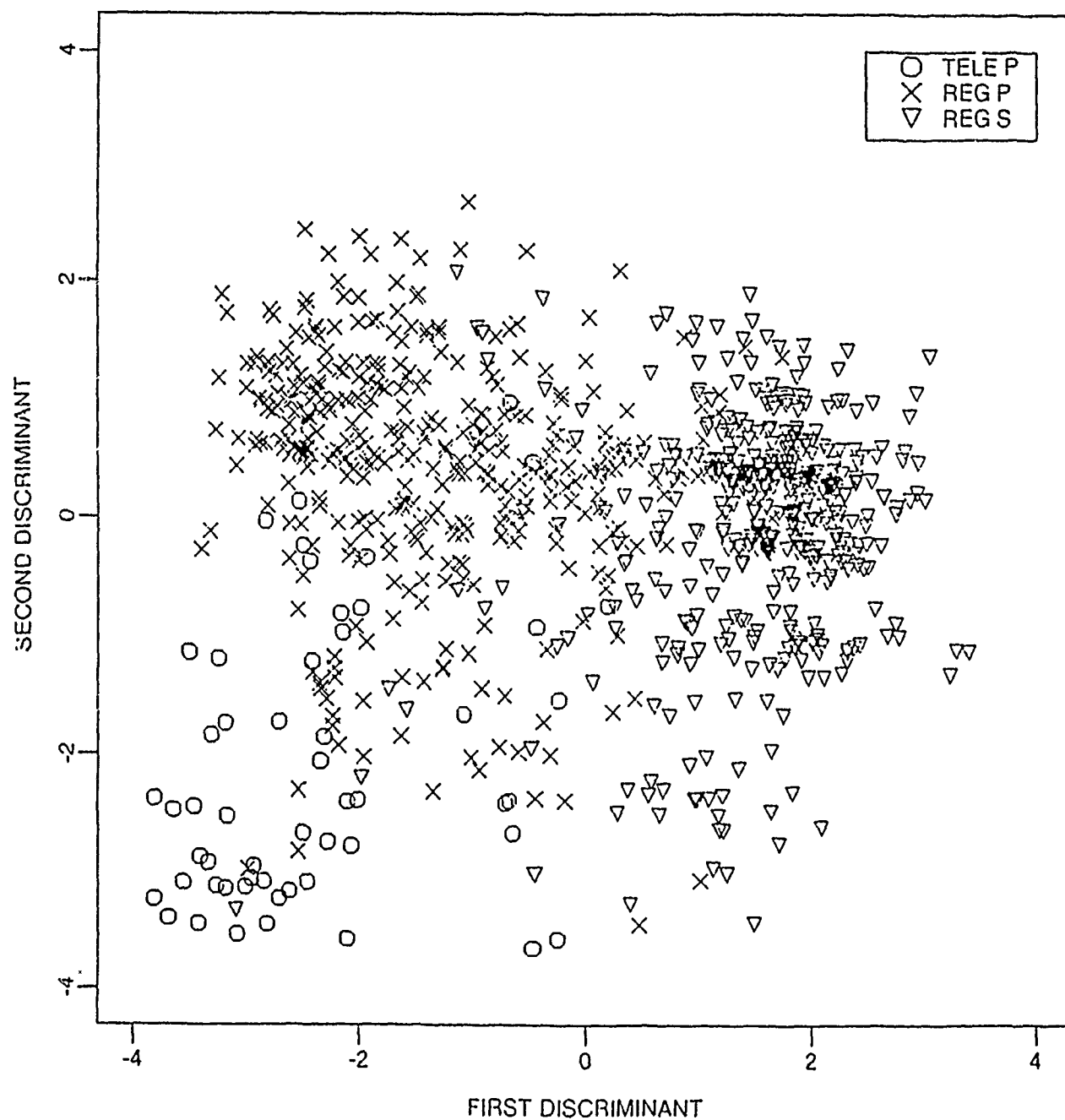


Figure 7. Discriminant plane showing the first and second discriminants separating three phase groups at GAR: teleseismic *P*, regional *P*, and regional *S*. The 865 arrivals in the training set used to derive the discriminants are shown.

Table 5. Performance of Phase Identification			
Phase Group	GAR†	ARU	KIV
Teleseismic <i>P</i>	83% (88%)	78%	84%
Regional <i>P</i>	81% (90%)	67%	71%
Regional <i>S</i>	93% (97%)	83%	78%

† Numbers in parentheses correspond to arrivals with 3-C SNR > 5

ARU

A similar discriminant analysis was performed at ARU, and the results are shown in *Figure 8 (left)*. The data set was much smaller than at GAR (231 arrivals). Therefore, several training and testing sets were used and the results averaged to stabilize the analysis. The correlation between the two discriminants and the measurements (frequency and polarization) was similar to that at GAR, although not as pronounced.

The discriminant performance is given in *Table 5*. The relative performance for the three phase groups is slightly lower than that obtained for GAR. The 14% difference for regional *P* discrimination reflects the large scatter in polarization estimates from automated processing for this phase group.

KIV

Discriminant analysis at KIV is illustrated in *Figure 8 (right)*. An adequate separation between the three phase groups was obtained. However, only 132 arrivals were available for analysis. Therefore, no testing set was available to replicate the analysis performed on the training set and the results must be considered as preliminary.

The performances of the discriminants are given in *Table 5*. Overall, the results are comparable to those at ARU. The best performance was obtained for the teleseismic *P* group, which, for most arrivals, was well separated from the other phase groups (*Figure 8, right*).

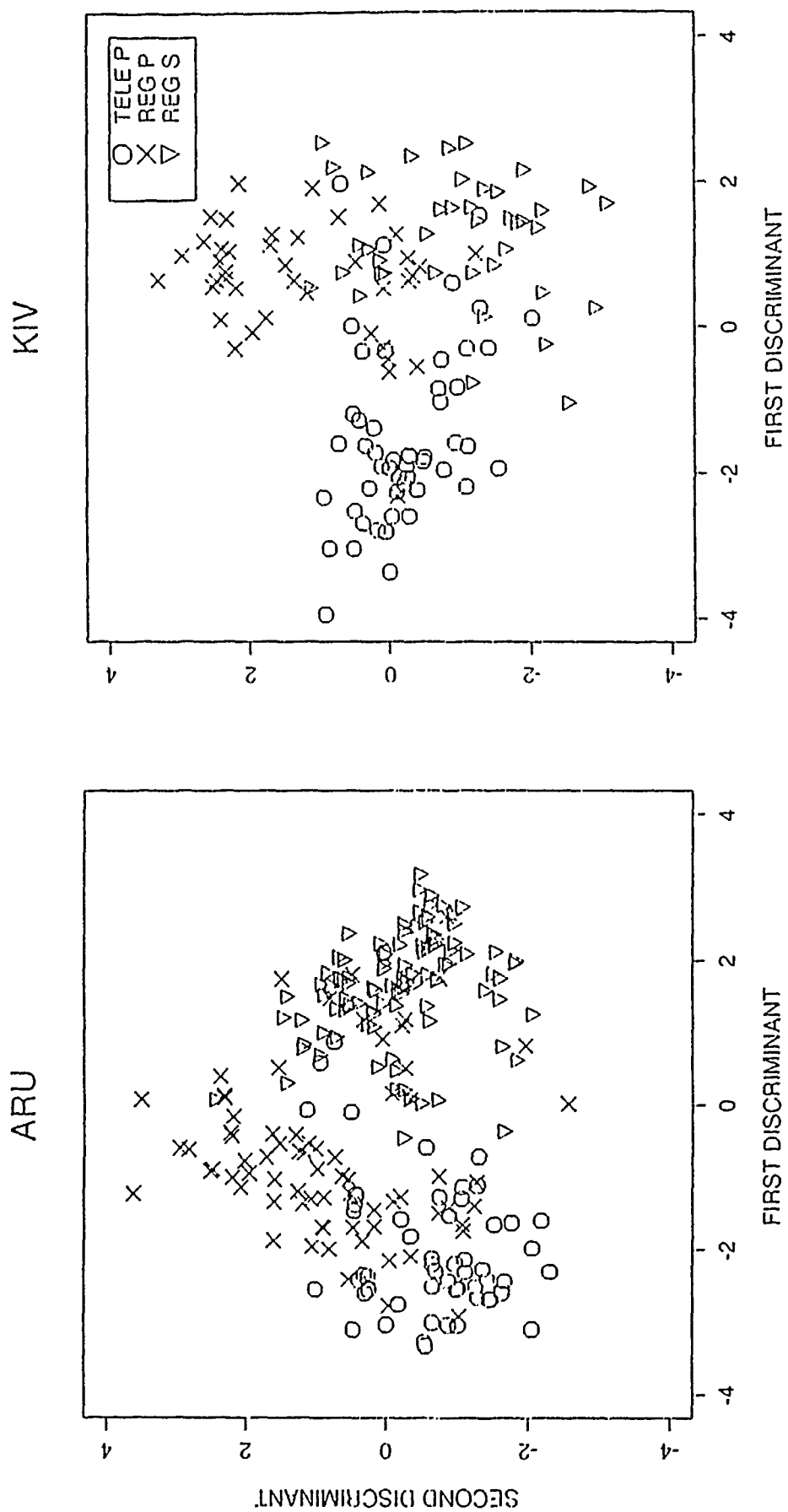


Figure 8. The discriminant plane is plotted at ARU to the left and KIV to the right (see Figure 7). The entire data set is shown for both ARU (231 arrivals) and KIV (132 arrivals).

3.1.6 Backazimuth Estimation

Event location is primarily a determination of backazimuth and distance. In this section we focus on the problem of backazimuth estimation using data from a single 3-C station. An important aspect of this study was to determine the true backazimuths to each of the events. By using only the events reported in the NEIC bulletin or other reference sources, we were able to establish a "ground truth" for the backazimuths.

The same methodology was applied at the four stations for all of the waveforms. First, an optimal frequency band was determined for each station. Data could then be band-passed filtered and processed in a routine manner to determine the polarization attributes. Five different polarization attributes were systematically determined for overlapping windows of data: incidence angle, rectilinear backazimuth, planarity, planar backazimuth from horizontal components, and maximum-to-minimum horizontal amplitude ratio (h_{max}/h_{min}).

Processing parameters determine when and how often the polarization attributes are computed. Varying these parameters allows us to customize the estimation of backazimuth for each station and each type of event (local, regional and teleseismic). The most important processing parameters are: the frequency band of high 3-C SNR, the start time of the process (with respect to the arrival time), the signal length (length of signal to be processed), the window length, and the overlap between consecutive windows. For rectilinear *P*-waves (GAR and ARU), the best backazimuths were obtained at the time of maximum rectilinearity. *P*-to-*S* converted waves exhibiting prograde elliptical motion (OBN and KIV) gave the best backazimuths at the time of maximum 3-C amplitude.

3.1.7 Teleseismic events at GAR

One-hundred forty-eight teleseismic events were studied at GAR. Most of these events occurred to the east of the station on the western edge of the Pacific rim. The distances from these events to GAR were well scattered over the teleseismic range (*Figure 3*).

Although individual events produced reliable results in many different frequency bands, the best overall results were obtained using a narrow frequency band, from 1.0 to 2.0 Hz, and a signal length of 3 s starting at the arrival time. The addition of the frequency bands below 1.0 Hz degraded the 3-C SNR.

In *Figure 9*, backazimuth residuals are plotted as a function of predicted backazimuth for the teleseisms recorded at GAR. The predicted values were computed using locations and origin-times reported in the NEIC bulletin. Events with a 3-C SNR > 3 are denoted with circles. The backazimuth residuals are within $\pm 25^\circ$ of the predicted backazimuths for 55% of the events. Using only events with a 3-C SNR >

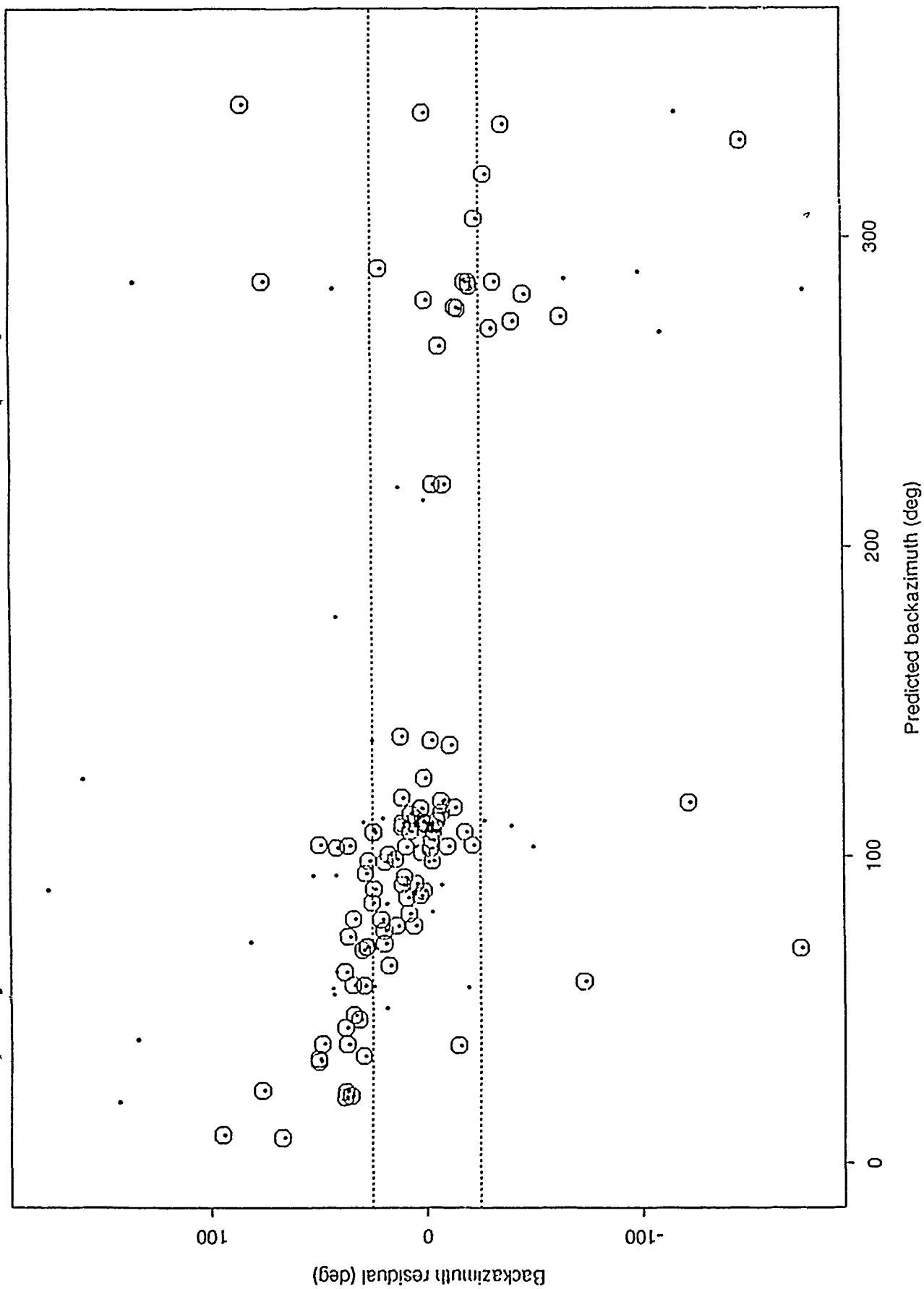


Figure 9. Predicted backazimuth vs. backazimuth residual for 148 teleseisms at GAR. Events with a 3-C SNR greater than 3. Between 10 and 150° the backazimuth residuals decrease from about 100° to 0°. From 270 and 350° backazimuth residuals are mostly negative.

3, however, the percentage increases to 61%. A trend is observed in the backazimuth residuals between 10 and 150°. Large positive residuals of about 100° around a predicted backazimuth of 10° decrease gradually to 0° at a predicted backazimuth of 100°. Little data were available between 140° and 270° and for events coming from the northwest (270°-350°) the data are widely scattered but tend to have negative backazimuth residuals.

3.1.8 Regional events at GAR

Among the many regional events recorded at Garm, only 27 were reported in the NEIC bulletin. *Figure 10* shows that most were located to the southwest but a few were to the north and east of GAR.

For regional events a signal window length of 1.0 s was found to give the best results. Different frequency bands were also tested, but the results were not improved, so the band from 1.0 to 2.0 Hz was retained. In *Figure 11*, backazimuth residuals are plotted vs. predicted backazimuth. Eighty-nine percent of the events had an observed backazimuth within 25° of the predicted backazimuth for this set of events. These results are better than for the teleseisms, but this may be due to larger 3-C SNRs. None of these events have 3-C SNR lower than 5.0.

3.1.9 Local events at GAR

"Ground truth" for the local events was obtained from a local catalog which reported 229 events for March 1989 (the last day was missing). We located more than 400 events for the same time span using data from station GAR but only 89 of these events were reported in the local catalog. There are two reasons for this discrepancy: either the detector used in our processing did not trigger at all for some events reported in the catalog, or the phase identification based on the GAR data differed from that predicted by the catalog (inconsistent data).

In *Figure 12*, the events from the Garm catalog are plotted by distance and local magnitude (dots). The 89 events used in the backazimuth estimation study are shown as solid triangles (consistent data). Inconsistent data are shown as open triangles. The set of 89 events had a large azimuthal coverage and a large range of 3-C SNR. As expected, the lower magnitude limit of the consistent data increases with range and many of the events that were either not detected or had inconsistent data lie below this limit.

Different parameters were tested to optimize the backazimuth estimation process. A 1.0 s window length was found to be optimal (1.5 s for the teleseisms) with a 50% overlap (75% for the teleseisms). The processing start time was set to 1.0 s before the first arrival and the signal length used in the process was set to 3.0 s. The signal was filtered between 1.0 and 2.0 Hz. Additional frequency bands were used with both lower and higher frequencies. In both cases, the results were

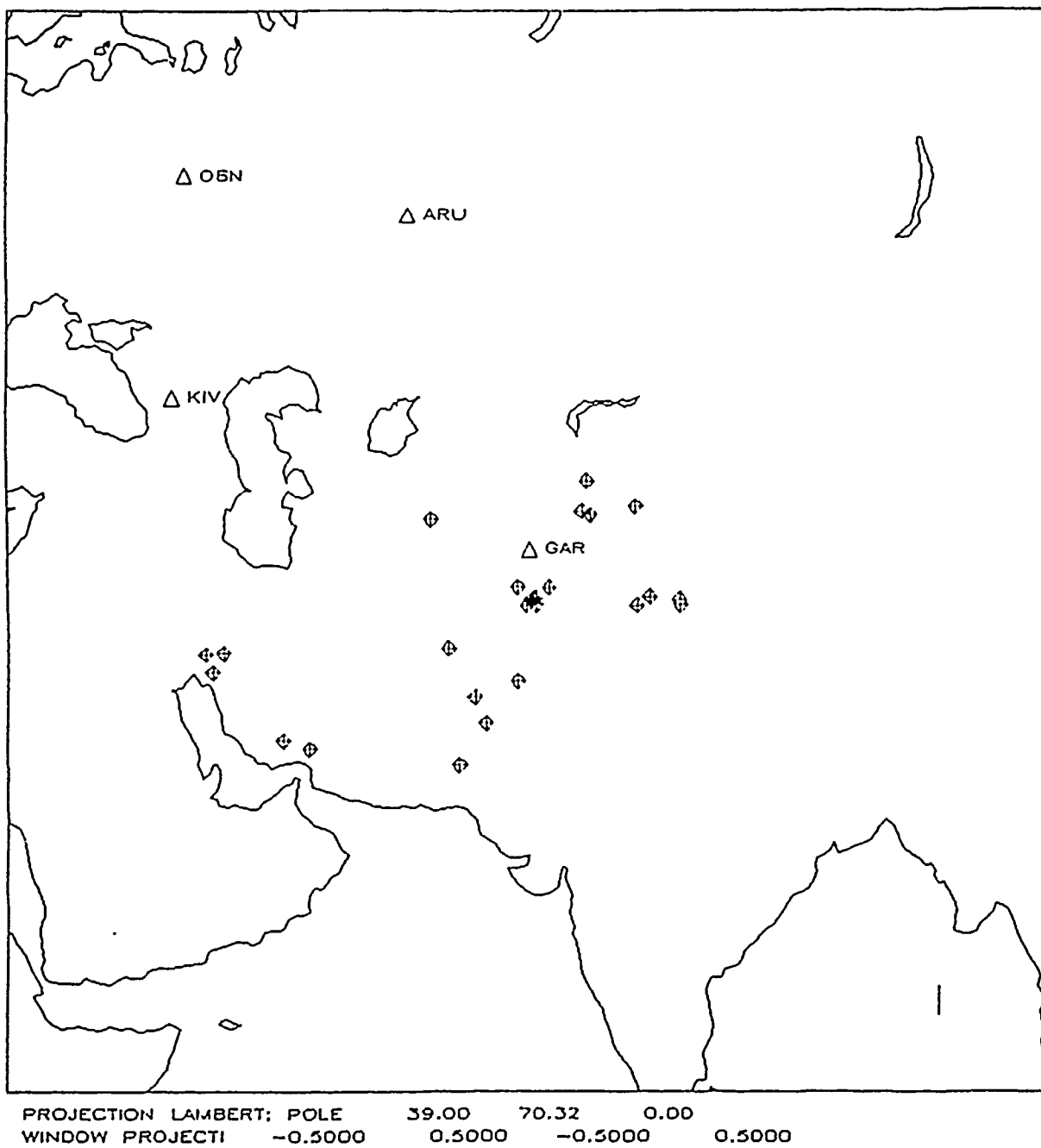


Figure 10. Locations of 27 regional events recorded at GAR.

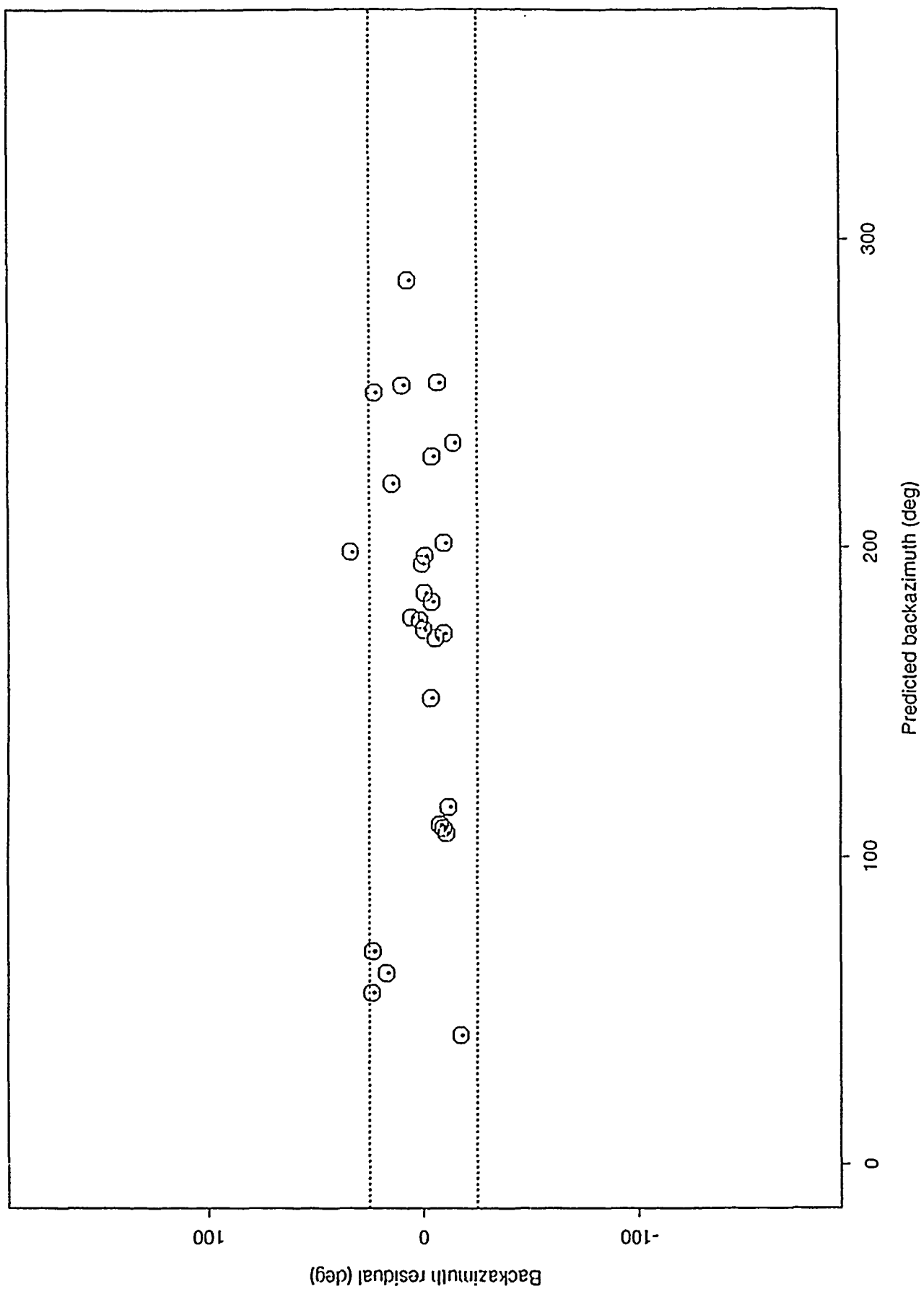


Figure 11. Predicted backazimuth vs. backazimuth residual for 27 regional events recorded at GAR. For 25 events (89%), an accurate backazimuth estimate is obtained. The results are better than for the teleseisms, but this may be due to larger signal-to-noise ratios (all of the events have a 3-C SNR > 3).

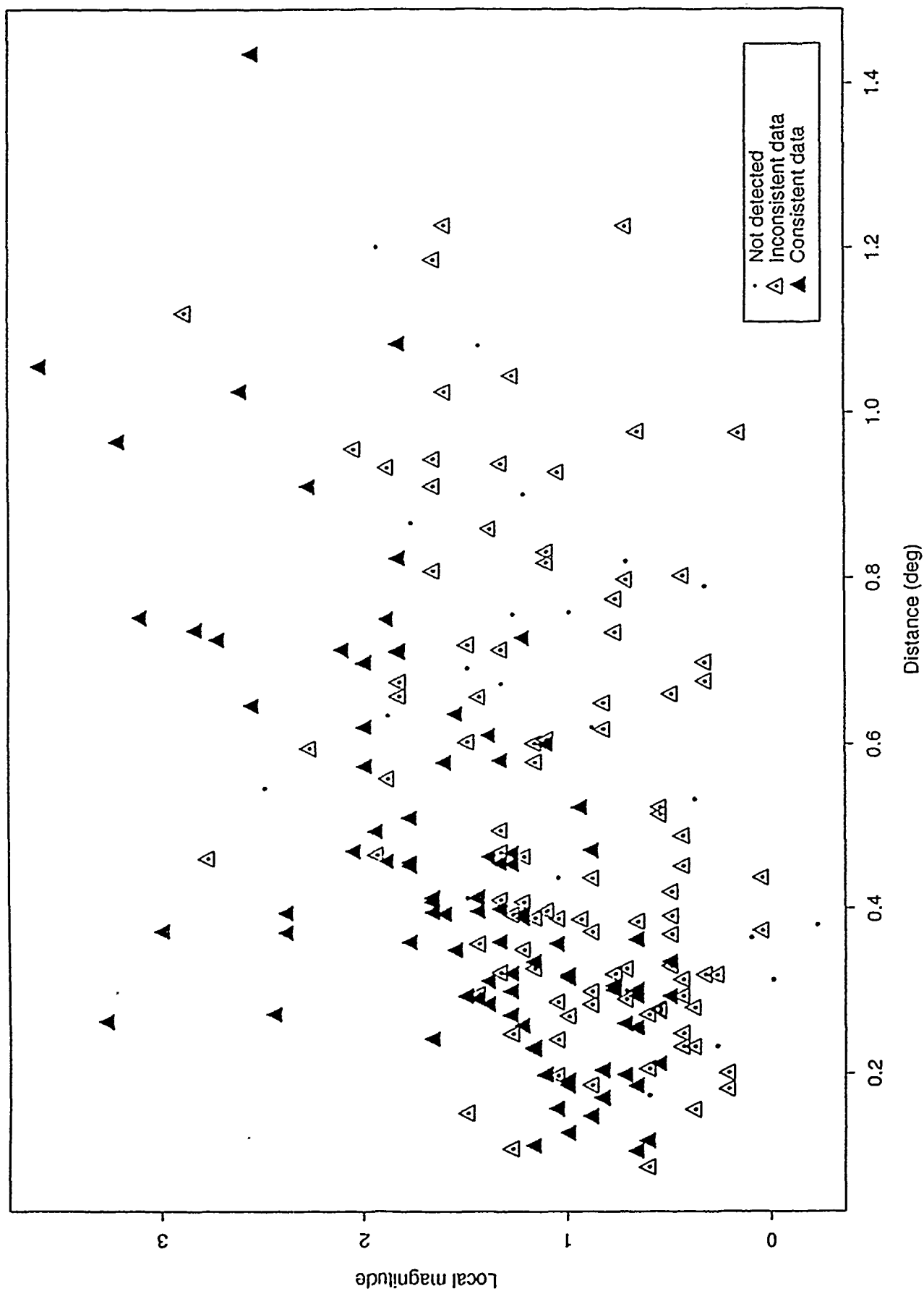


Figure 12. Local magnitude as a function of distance from GAR for events reported in a local catalog. The arrival times and phase identifications derived from station GAR data were consistent with the catalog for 89 of these events (solid triangles). Events for which the phase identification from GAR data differed from that predicted by the catalog are shown as open triangles with dots. Events reported in the catalog but not detected at station GAR are shown as dots.

slightly degraded.

In *Figure 13*, backazimuth residuals are shown as a function of predicted backazimuth. Events with 3-C SNR > 3 are circled. Seventy-nine percent of the events give a computed backazimuth within 25° of the reference value; 87% of those with 3-C SNR > 3 have a residual within the 25° bounds. This plot does not show any particular clustering of events characteristic of an active seismic area. Nearly all of the events with large backazimuth residuals had predicted backazimuths between 0 and 50°. Note that the large deviations are similar to those observed for the teleseismic data (*Figure 10*).

Figures 9 and 13 show the importance of local structure on the polarization characteristics of arrivals. Both local and teleseismic data show a distinct trend of positive backazimuth residuals between 0 and 50°. Regional data was too sparse in this backazimuth range to contribute one way or the other to this observation. We suggest that some structural feature or features near GAR deflects or modifies the signal in the range of backazimuths between 0 and 50°. We have shown above that the polarization characteristics of seismic arrivals are unique to each station for each phase. This observation shows that polarization can also be a function of azimuth.

The processing parameters used to estimate backazimuth for local, regional, and teleseismic data are, for the most part, unique. Surprisingly, the frequency band remained the same for each category at GAR. Usually, the frequency content of seismic phases is indicative of distance. This may still be the case (see the section on phase identification), but the useful band for backazimuth estimation at GAR is constant and equal to 1.0 to 2.0 Hz.

3.1.10 Teleseismic events at ARU

Eighty-five teleseisms, mainly from Japan and the Philippines (*Figure 3*), were studied at station ARU during March 1989.

Despite the location of ARU, on the structural border between the East-European platform and the Ural mountains, the information derived from the teleseisms recorded at this station was accurate regardless of the 3-C SNR. The optimum backazimuths were obtained by taking a signal length of 5.0 s starting 0.5 s before the first arrival and a 1.5 s window length with a 50% overlap. A weighted frequency band average of the results from 0.5 to 2.0 Hz provided the best results.

As shown in *Figure 14*, the backazimuth residuals are small. The observed backazimuth is within $\pm 25^\circ$ of the predicted backazimuth for 68% of the events. This percentage rises to 78% for the arrivals with 3-C SNR > 3 and 90% with 3-C SNR > 4. However, the number of events in the sample set decreases significantly as the 3-C SNR threshold rises. There are 85 events represented in the complete

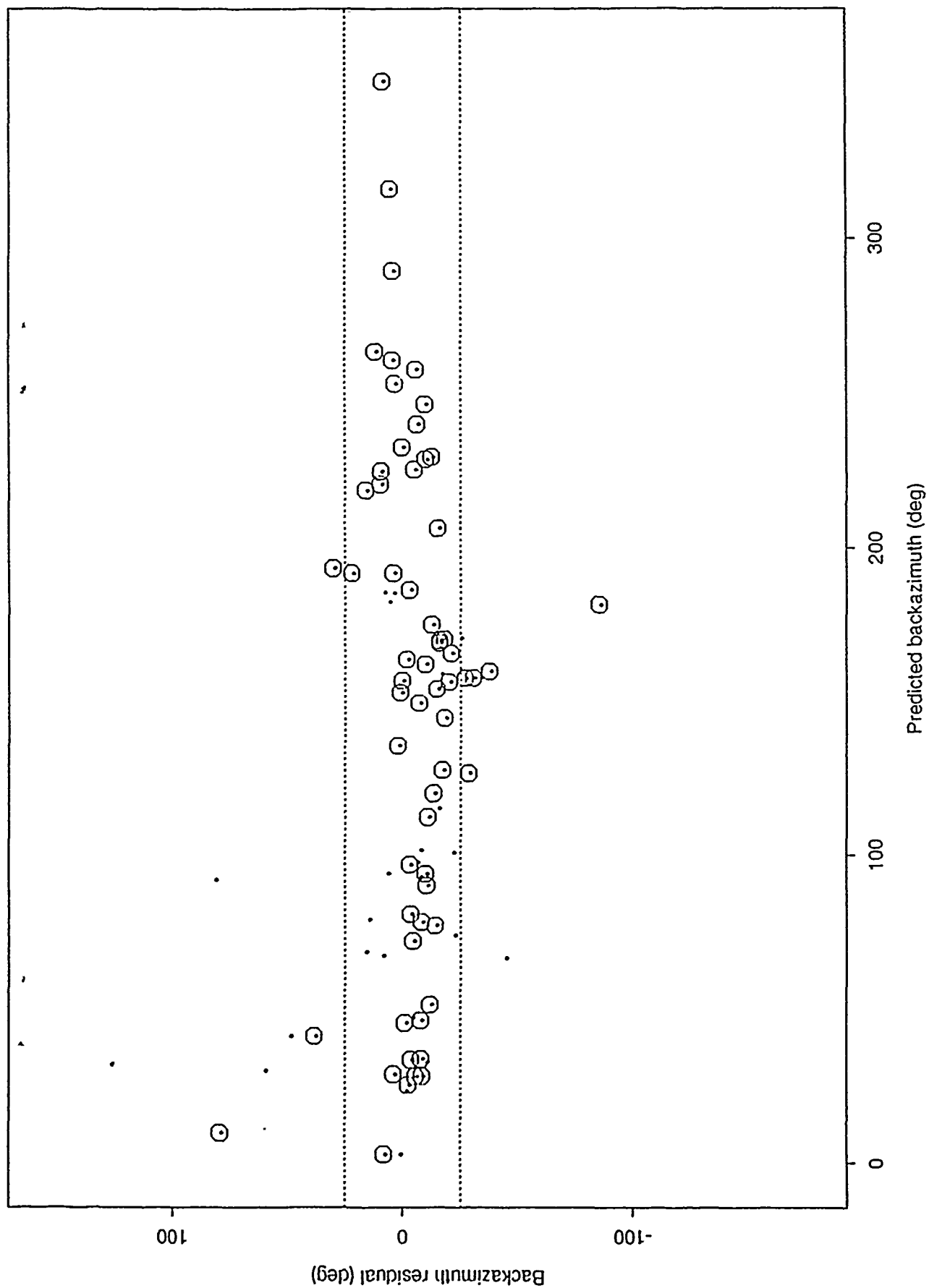


Figure 13. Predicted backazimuth vs. backazimuth residual for 89 local events at G.A.R. The largest backazimuth residuals occur for events between 0 and 100°. Data with 3-C SNR > 3 are circled.

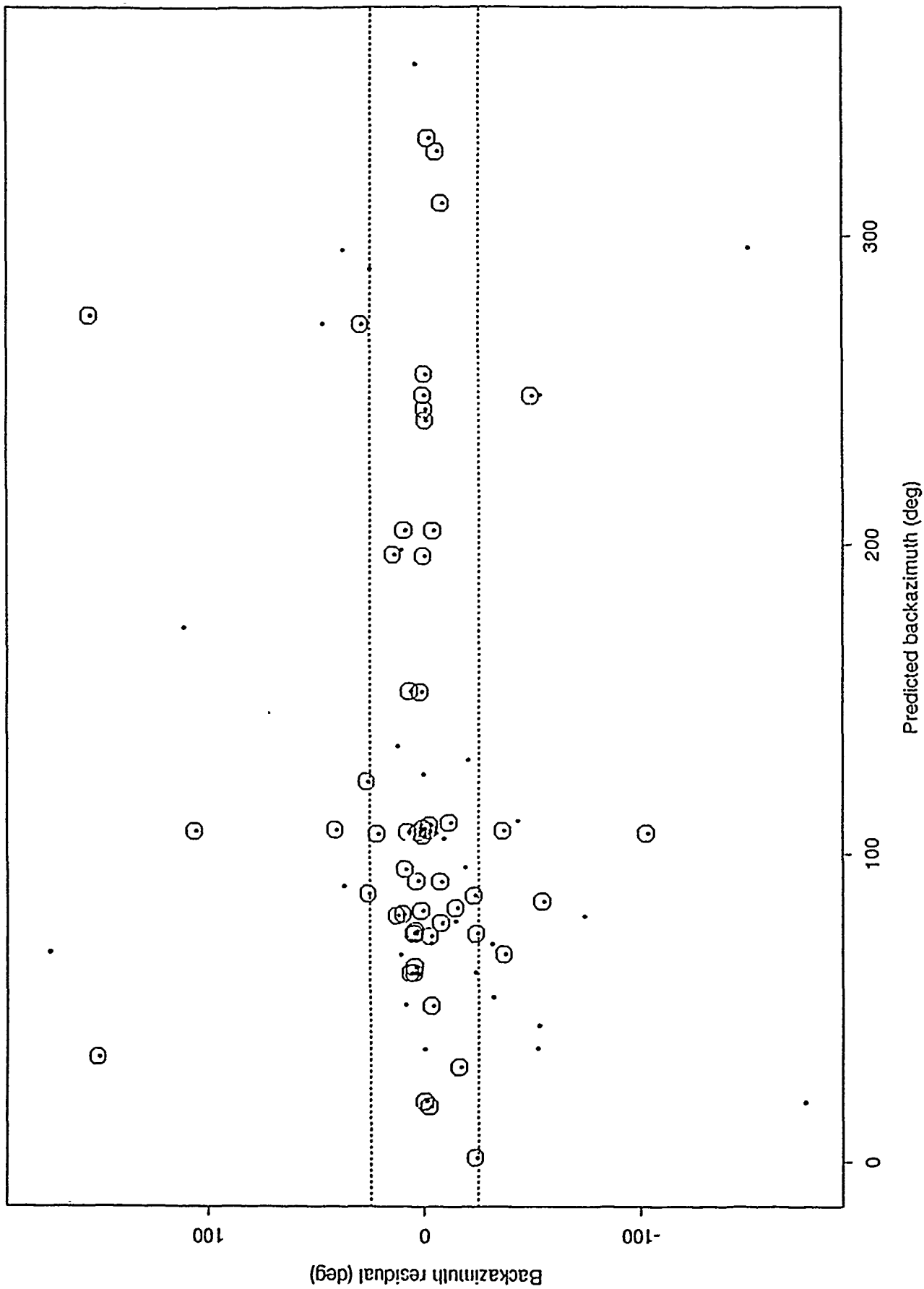


Figure 14. Predicted backazimuths vs. backazimuth residuals for 85 teleseisms recorded at ARU. Even in the presence of noise, polarization results are stable. The observed backazimuth is within $\pm 25^\circ$ of the predicted backazimuth for 68% of the events. This percentage rises to 78% for the arrivals with 3-C SNR > 3 (circled measurements).

sample set, 55 with 3-C SNR > 3, and only 39 with 3-C SNR > 4.

3.1.11 Teleseismic events at KIV

At KIV, the particle motion of first arrivals is not rectilinear. In *Figure 15* we plot typical particle motions for the first few seconds of the initial *P* arrivals at stations KIV and ARU. The ARU data shows strong rectilinearity during the few seconds of the first arrival, but at KIV the motion changes drastically less than one second after the first arrival, becoming a prograde elliptical motion. A careful study of the elliptical wave polarization shows that it is possible to determine the correct backazimuth for almost all teleseisms using the prograde elliptical phase.

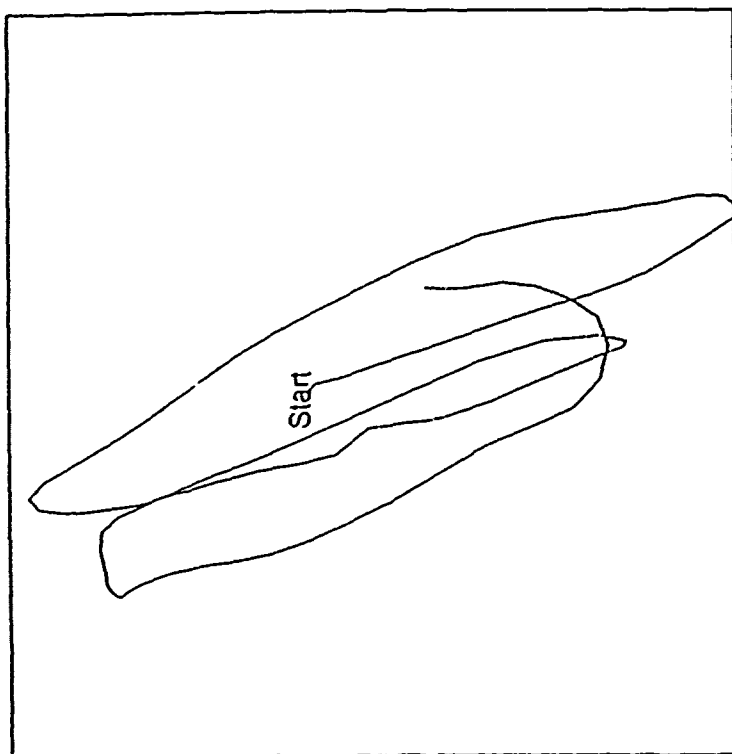
The selected frequency band for analysis was from 0.5 Hz to 2.0 Hz with the results being computed from a weighted average of the two octave bands within this interval. The optimal length for the signal was 3.0 s starting 0.5 s before the first arrival. A window length of 1.5 s with a 75% overlap was used. The backazimuth value was averaged over three windows.

The results were strongly influenced by the length of signal processed as the backazimuth was computed at the point of maximum 3-C amplitude. For many signals, the maximum 3-C amplitude occurred between 10 and 20 s after the first arrival and the resulting backazimuth would be incorrect. A shorter length of signal processed reduced the errors and provided more accurate results. The use of the maximum of planarity or the maximum of h_{max}/h_{min} ratio to determine the best backazimuth estimate did not improve the results. Assuming elliptical motion, backazimuth estimates within $\pm 25^\circ$ of the predicted value were obtained for 73% of the 24 arrivals. Half of the arrivals had a 3-C SNR > 3, and accurate backazimuth estimates were obtained for 85% of them.

Backazimuth residuals were computed and plotted with respect to the predicted backazimuth in *Figure 16*. Except for four events, the plot shows a small discrepancy between predicted and observed values based on the prograde elliptical wave.

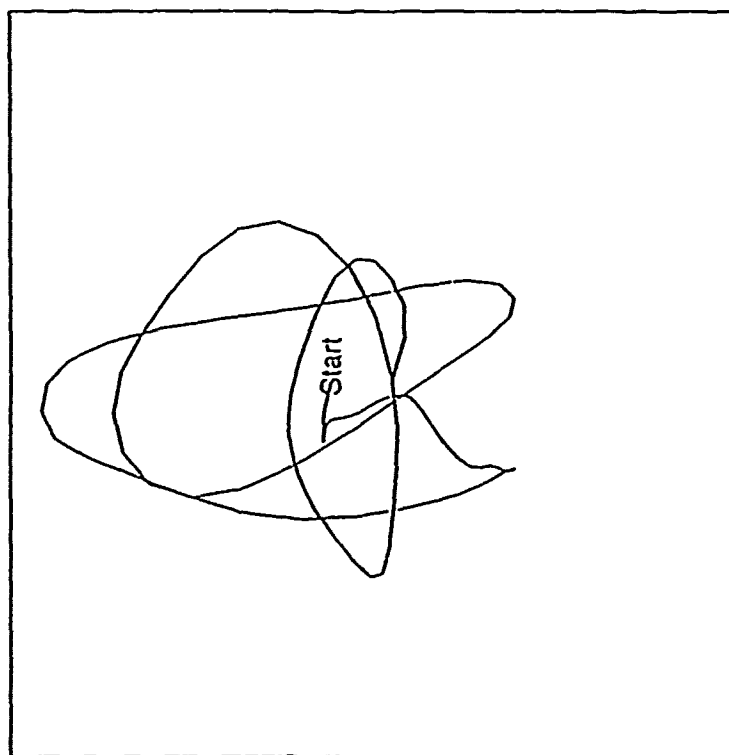
3.1.12 Teleseismic events at OBN

Teleseismic *P*-waves at OBN are similar to those recorded at KIV. A prograde elliptically polarized wave is present in the *P* coda which affected the determination of the backazimuth from the initial *P*. The results from three different frequency bands: 0.5 Hz to 1.0 Hz, 0.75 Hz to 1.50 Hz, and 1.0 Hz to 2.0 Hz were combined in a weighted average to get the final best estimate. The length of signal processed in the computation was set to 7.0 s, starting 0.5 s before the first arrival (somewhat longer than for KIV). We also used a longer window, 2.0 s, with an overlap of 50%. The other parameters were the same. Based on elliptical motion, the correct backazimuth was determined for 17 out of the 23 teleseisms recorded at



Radial component

(b)



Radial component

(a)

Figure 15. a) Typical particle motion of teleseismic *P*-waves at KIV during the first 1.5s. The particle motion shows a drastic change in polarization from rectilinear to prograde elliptical motion within 1 second of the first arrival. b) Typical particle motion of teleseismic *P*-waves at ARU during the first 1.5s. As expected, the particle motion is rectilinear.

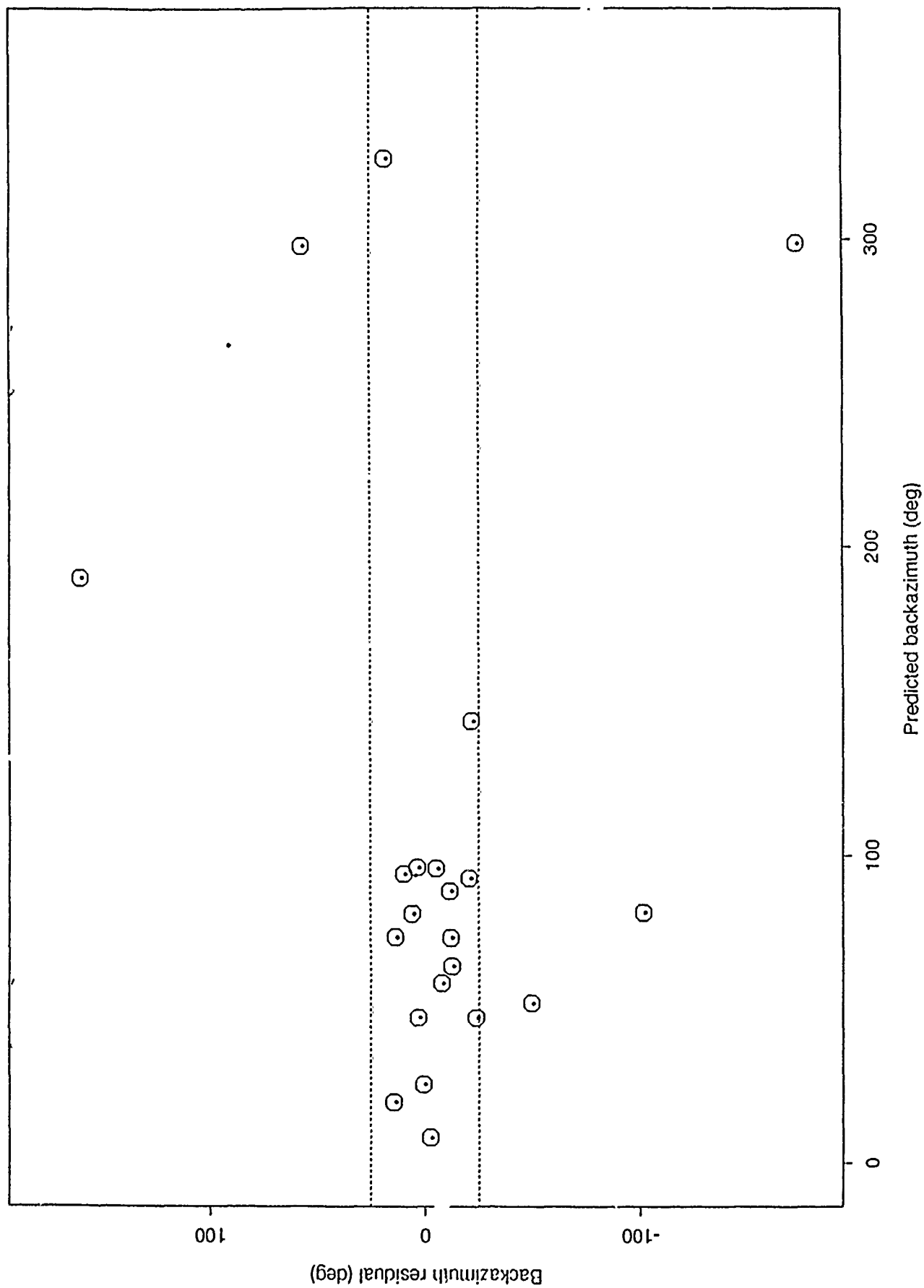


Figure 16. Backazimuth deviation for 24 teleseisms recorded at KIV. Assuming elliptical motion, accurate backazimuth estimates are obtained for 73% of the 24 *P* arrivals. 85% of the arrivals with 3-C SNR > 3 (circled measurements) have residuals less than 25°.

OBN during March 1989.

Figure 17 shows the deviation between the predicted backazimuth and the backazimuth residuals for the teleseisms studied. Seventy-two percent of them had good backazimuth estimates. The effect of noise was strong. When only the arrivals with 3-C SNR > 3 were included, 89% had good estimates. For some events, it was not possible to determine an accurate backazimuth even when the data had a large 3-C SNR. Many of these events were located to the southwest between 200° and 300° and all had computed backazimuths 180° from the predicted values. This implies that the motion of the elliptical arrival for these events was retrograde rather than prograde.

3.1.13 Travel Time Residuals

The structure surrounding the IRIS stations in the USSR has been shown above to have a tremendous effect on the polarization of the signals recorded at each of the IRIS stations studied in this paper. In addition to affecting the polarization, the structure has a recognizable effect on the travel times of phases recorded at these stations. Below we show the results of computing the difference between the observed and the theoretical Jeffreys-Bullen travel-times (travel-time residual) for teleseisms based on the NEIC network bulletin origin times and event locations. Teleseisms were chosen for this study for two reasons. First, the ray paths of teleseismic *P*-waves are nearly vertical near the receiver which makes it possible to easily predict the travel-time residuals based on the models presented in this paper, and second, the origin time and event locations are more accurate for the relatively large teleseismic events than for the local and regional events.

For each station, the mean travel-time residual was compared to the value predicted using travel-times based on Jeffreys-Bullen tables with the local velocity model substituted in the crust and upper mantle (*Figure 2, Table 2*). By averaging the residual over several events, the effect of location errors, origin time errors, and source structural differences are minimized.

At station GAR the residuals ranged from -2 s to 3 s (time positive for late arrivals) but most of them were between -1 s and 1 s. The mean value of the observed residual was 0.39 s. The theoretical travel-time computed from the Tien-Shan model gives a residual value of 0.5 s, very close to the observed value.

The time residual computation at ARU shows that all of the events except one arrived early with respect to the predicted time. This implies that the Jeffreys-Bullen travel-time model is too slow with respect to the velocity around Arti. The observed average value of the teleseismic travel-time residuals was -0.44 s, with most events having negative time residuals. The theoretical value of the travel-time residual calculated using a local crust and upper-mantle velocity structure for this station was -0.8 s. Our model overcompensates for the effect of the velocity model

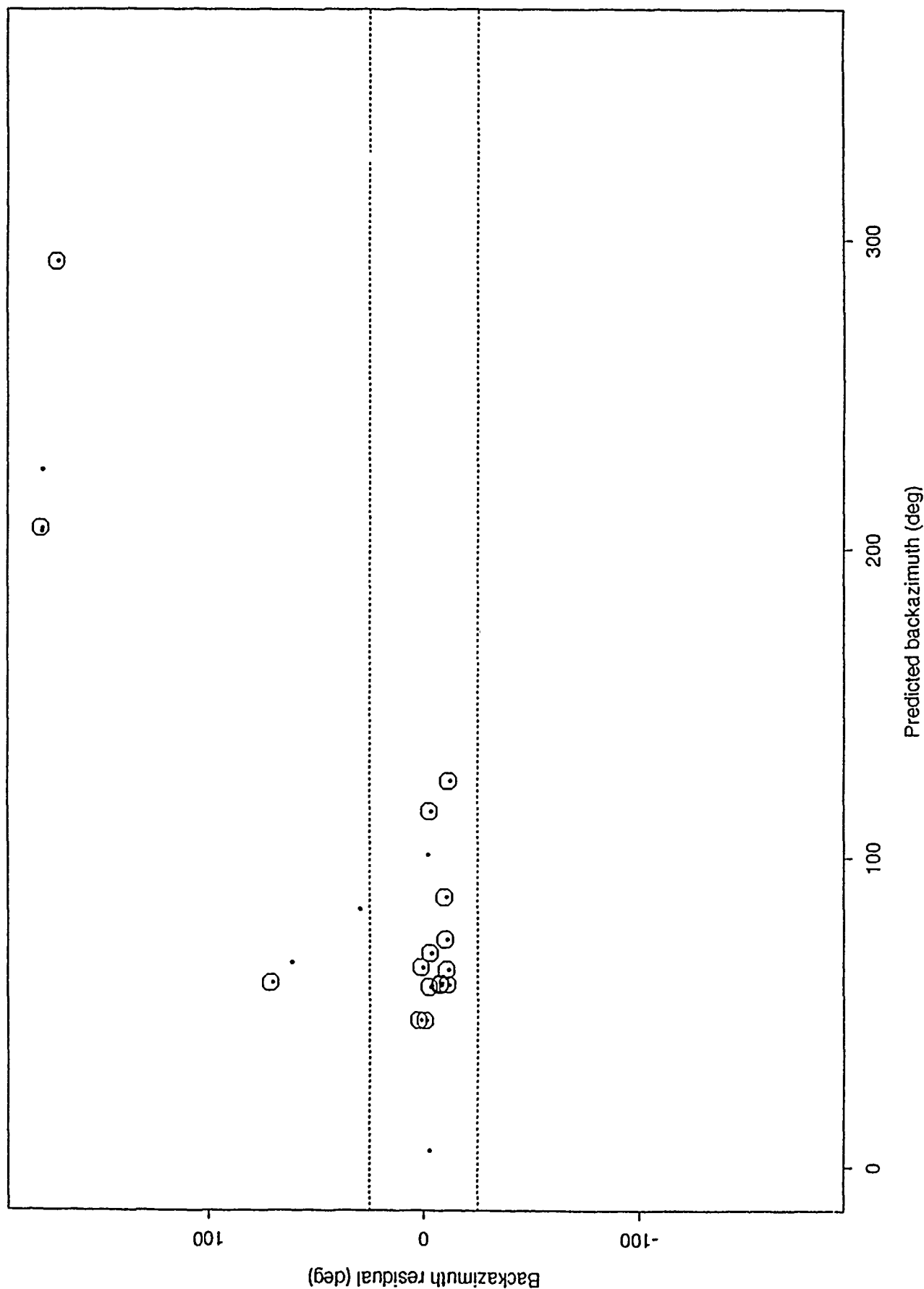


Figure 17. Backazimuth deviation for 23 teleseisms recorded at OBN. Assuming prograde elliptical motion, a good backazimuth estimate is obtained for 72% of the *P* arrivals. The effect of noise is strong: when only the arrivals with 3-C SNR > 3 are included, 89% have good estimates. For the events with theoretical backazimuths between 180° and 340°, the observed backazimuth is in error by 180°.

at ARU.

The residual travel-times at KIV were positive in most cases with a mean value of 0.72 s. The Jeffreys-Bullen velocity model is too fast for this station. No velocity section for the upper-mantle was available; therefore, no theoretical value could be computed. However, the crustal velocities are much lower than in the Jeffreys-Bullen model, and positive travel-time residuals were expected.

Travel-time residuals at OBN were the most consistent of all stations studied. Most were negative (early arrivals) and the mean was -0.48 s. The theoretical value calculated using the crust and upper mantle structure for OBN given in *Figure 2* and *Table 2* was -0.5 s, a nearly identical match.

3.1.14 Discussion and Conclusions

The velocity-depth profiles for stations ARU, GAR, KIV and OBN (*Figure 2* and *Table 2*) are useful for processing and interpreting seismic signals. These models accurately predict the average travel time residuals at these stations. The polarization characteristics of the recorded waveforms, however, indicate that lateral inhomogeneities influence the behavior of the particle motion. All of the IRIS stations except OBN are located near structural boundaries of major geological provinces of Northern Eurasia.

The influence of lateral velocity heterogeneities on the results is clearly shown at GAR. The boundary between the Tien-Shan area and the Turanian platform constitutes a large scale lateral inhomogeneity (thousands of kilometers) which affects teleseismic waveforms approaching GAR from the north. Velocity profiles show the crust thickening from 40 km northeast of GAR (Turanian platform) to more than 60 km below GAR (Tien-Shan area) along with a significant change in the upper-mantle velocity structure. The crust begins to thicken below the Turanian platform and reaches a thickness of 60 km below GAR about 300 km to the south. This thickening does not follow a regular slope but rather is a zone of irregular crustal thickness beginning abruptly at the boundary between the Turanian platform and the Tien-Shan area. A very thick and pronounced low velocity layer was observed in the upper mantle beneath the Tien-Shan. A similar layer probably does not exist beneath the Turanian platform. The large scatter in the backazimuth estimates determined from teleseismic *P*-waves from events located to the northwest and the systematic positive backazimuth residual of teleseismic and local events located to the northeast may be explained by this structure.

Sharp variations in the slope of the boundary affect the backazimuths measured from teleseismic data, even for events with a good 3-C SNR. In addition, low incidence angles for local and regional events southeast of the same station highlight the existence of a boundary between the Tien-Shan area and the Peter the First Range on a smaller scale (hundreds of kilometers). A thorough study of these

lateral inhomogeneities should provide valuable information for the construction of multi-dimensional models which will aid in the analysis and interpretation of seismic data.

The polarization characteristics of seismic phases recorded at the IRIS stations have shown a strong site dependence related to structural inhomogeneities. The elliptical motion observed in the first seconds of the recorded signal for teleseismic events at KIV and OBN is probably due to a conversion of *P*- to *S*- wave energy at the sharp lower boundary of the upper sedimentary layer. These observations fit with the model for KIV (Figure 2) which has an upper sedimentary layer with a thickness of 6 km. With a shear velocity of 2 km/s, the delay between the first *P* and the converted *S*-wave should be at least 1.3 s for this model. We observe a delay of about one second between the initial rectilinear impulse and the start of elliptical motion at these stations. By studying the receiver function at OBN, Gurrrola *et al.* (1990) have shown that reverberations seen in the first 4 s of the initial arrival are caused by a low velocity surface layer. In addition, the relatively low velocity of the sedimentary layer (3.6 km/s at KIV, 3.5 km/s at OBN) at both stations causes nearly vertically incident *P* arrivals and, consequently, low SNRs on the horizontal components. These small *P*-wave amplitudes recorded on the horizontal components degrade backazimuth estimates.

Polarization characteristics are also useful for phase identification. Multivariate discriminant analysis was successfully applied to identify teleseismic *P*, regional *P*, and regional *S* phases at GAR, ARU and KIV. Polarization parameters and frequency were used as predictors of phase type. Our preliminary results show that the three phase types are easily distinguished at GAR (80-90% success, increasing to 90-100% for arrivals with 3-C SNR > 5). The performance was somewhat lower at ARU and KIV (70-80% success) where smaller data sets were available.

Accurate backazimuths can be estimated at 3-C stations if the polarization of the arrivals is first characterized through careful studies. The usual assumption that *P*-waves are rectilinearly polarized is not always true and can lead to inaccurate results. This assumption may have contributed to the conclusion drawn by Walck and Chael (1990) that eigenvalue decomposition polarization methods are not always adequate for backazimuth estimation. A careful examination of the polarization characteristics at each of the stations has allowed us to make backazimuth estimates to within $\pm 25^\circ$ for most events using this method. The stability of the measurements is especially critical when these methods are considered for use in automatic processing. Backazimuth estimates are not only a function of the polarization characteristics of the seismic phase being considered at a given station but also of the true azimuth of approach.

3.1.15 Acknowledgments

The manual phase identifications for this project were made by Flori Ryall. John Coyne, Steve Bratt, and the IMS group at the Center for Seismic Studies provided helpful assistance with software and database routines. The local event catalog for the Garm region was provided by Mike Hamburger and his Soviet colleagues. This work was supported by the Air Force Geophysics Laboratory, under contract F19628-89-C-0203.

Florence Riviere-Barbier
Anne Suteau-Henson
Vladislav Z. Ryaboy
Jerry A. Carter

REFERENCES

- Bache, T. C., S. R. Bratt, J. Wang, R. M. Fung, C. Kobryn, and J. W. Given (1990). The Intelligent Monitoring System, *Bull. Seism. Soc. Am.*, **80**, 1833-1851.
- Bratt, S.R., and T. C. Bache (1988). Locating events with a sparse network of regional arrays, *Bull. Seism. Soc. Am.* **78**, 780-798.
- Bullen, K. E. (1959). *An Introduction to the Theory of Seismology*, Cambridge University Press, London, England, 126-128.
- Chatelain, J. L., S. W. Roecker, D. Hatzfeld, and P. Molnar (1980). Microearthquake seismicity and fault plane solutions in the Hindu-Kush region and their tectonic implications, *Jour. Geophys. Res.* **85**, B3, 1365-1387.
- Christoffersson, A., E. S. Husebye, and S. F. Ingate (1988). Wavefield decomposition using ML-probabilities in modeling single-site 3-component records, *Jour. Geophys. Res.*, **93**, 197-213.
- Cooley, W. W. and P. R. Lohnes (1971). *Multivariate Data Analysis*, John Wiley & Sons, Inc., 364 pp.
- Eaton, J. P. (1969). *HYPOLAYR, a computer program for determining hypocenters of local earthquakes in an earth consisting of uniform flat layers over a half space*, U. S. Geol. Surv. Open-File Rept., 155pp.
- Eneva M. and M. W. Hamburger (1989). Spatial and Temporal Patterns of Earthquake Distribution in Soviet Central Asia: Application of Pair Analysis Statistics. *Bull. Seism. Soc. Am.* **79**, 4, 1457-1476.
- Given, H. K., (1990). Variations In Broadband Seismic Noise at IRIS/IDA Stations in the USSR with Implications for Event Detection. *Bull. Seism. Soc. Am.*, **80**, 2072-2088.
- Golitsyn, B. B., (1960). Selected works (in Russian). *Seismology, USSR Academy of Science*. 2,490.
- Gurrola, H., J.B. Minster, T. Owens (1990). Receiver Responses at IRIS/IDA Stations in the USSR. *Proceedings of the 12th Annual DARPA/GL Seismic Research Symposium (18 - 20 September 1990)*, GL-TR-90-0212, 266-272. ADA226635
- Hamburger, M. W., Swanson II W. A., and Popandopulo G. A. (1990). Velocity Structure and Seismicity of the Garm Region, Soviet Central Asia. submitted to *Geophysical Journal International*.
- Helmberger, D., L. Zhao, and D. Dreger (1990). Broad-band Modeling of Regional Seismograms, *Proceedings of the 12th Annual DARPA/GL Seismic Research Symposium (18 - 20 September 1990)*, GL-TR-90-0212, 273-280. ADA226635
- IRIS, (1989). Some data sets of the IDA/IRIS data collection center.

- Jurkevics, A., (1988). Polarization Analysis of Three-Component Array Data. *Bull. Seism. Soc. Am.* **78**, 1725-1743.
- Khamrabaev, I. Kh. and F. Kh. Zunnunov (Editors) (1984). The Earth's crust and the upper-mantle of the Pamirs, Himalayas and Southern Tien-Shan. Nauka (Science) Publisher House (in Russian), 160.
- Klein, F. W. (1984). *User's guide to HYPERINVERSE, a program for Vax and PC350 computers to solve for earthquake locations*, U. S. Geol. Surv. Open-File Rept., 53pp.
- Lee, W. H. K. and J. C. Lahr (1972). *HYPO71: A computer program for determining hypocenter and magnitude and first motion pattern of local earthquakes*, U. S. Geol. Surv. Open-File Rept., 53pp.
- Leith, W. (1990). *Geology, Crustal Structure and Mining Activity in the Vicinity of ARU*, U. S. Geol. Surv. Internal Rept..
- Leith, W. and D. W. Simpson (1986). Seismic Domains Within the Gissar-Kokshal Seismic Zone, Soviet Central Asia. *Journ. Geoph. Res.* **91**, B1, 689-699.
- Leith, W. (1985). A mid-Mesozoic extension across Central Asia? *Nature*, **313**, 567-570.
- Lienert, B. R., E. Berg, and L. N. Frazer (1986). Hypocenter: an earthquake location method using centered, scaled, and adaptively damped least squares, *Bull. Seism. Soc. Am.* **76**, 771-783.
- Magotra, N., N. Ahmed, and E.P. Chael (1987). Seismic event detection and source location using single-station (three-component) data. *Bull. Seism. Soc. Am.* **77**, 958-971.
- Pomerantseva, I. V., and A. N. Mozzhenko (1977). Seismic Investigations with the "Zemlya" Apparatus. Moscow, Nedra.
- Popandopulo, G. A. (1990). Construction of three-dimensional velocity models based on small earthquakes observations (in Russian). In book. "Seismic regime geophysical observations". Ed. A. Ya. Sidorin. Moscow, Institute of Physics of the Earth of the USSR Academy of Sciences, 104-125.
- Rautian, T. G., V. I. Khalturin, V. G. Martynov and P. Molnar (1978). Preliminary Analysis of the Spectral Content of P and S waves from Local Earthquakes in the Garm, Tadjikistan Region. *Bull. Seism. Soc. Am.* **68**, 4, 949-971.
- Ruud, B. O., E. S. Husebye, S. F. Ingate and A. Christoffersson (1988). Event location at any distance using seismic data from a single, three component station. *Bull. Seism. Soc. Am.* **78**, 308-325.
- Ryaboy, V. Z. (1989). Upper mantle structure studies by explosion seismology in the USSR. *DELPHIC associates*, 154.

- Ryaboy, V. Z.,(1990). Crust-upper Mantle Structure beneath IRIS Stations in the USSR. *Technical Report* in press. Center for Seismic Studies.
- Suteau-Henson, A. (1991). Three-Component Analysis of Regional Phases at NORESS and ARCESS: Polarization and Phase Identification, submitted to *Bull. Seism. Soc. Am.*.
- Thurber, C., H. Given and J. Berger (1989). Regional Seismic Event Location with a Sparse Network: Application to Eastern Kazakhstan, USSR. *Bull. Seism. Soc. Am.* **12**, 17,767-17,780.
- Walck, C. M. and E. P. Chael (1990). Optimal Back-azimuth Estimation for Three-Component Recordings of Regional Seismic Events, submitted to *Bull. Seism. Soc. Am.*.
- Zverev, S. M. and I. P. Kosminskaya (Editors) (1980). Seismic models of the lithosphere for the major geostructures on the territory of the USSR (in Russian). Nauka (Science) Publisher House, 184.

4.1 PRELIMINARY RESULTS OF Lg-YIELD STUDIES FROM ANALYSIS OF SOVIET SEISMIC DATA

4.1.1 Introduction

A seismic data set, unique to the field of seismic verification, has recently been collected. It includes a large number of recordings at in-country stations from Soviet underground nuclear explosions, many with announced yields. More than 1,100 such recordings, which are copies of analog photographic records, are currently in the process of being transformed into computer readable form.

Most of the data are from explosions during the early years, of underground explosion testing, from 1965 through 1972. However, data from more recent explosions, like the JVE explosion on Sep 14, 1988, are also included in the data set.

In this note we present some preliminary results from analysis of about 100 recordings at 9 Soviet stations from 32 explosions, mainly at the Semipalatinsk test range, but also at Novaya Zemlya. This analysis is part of an effort to establish an optimized relationship between amplitude measures of Lg waves and explosion yield.

4.1.2 Data

Relevant information on the explosions analyzed here including time, location, and, when available, yield and other source characteristics (from Vergino, 1989), are listed in Table 1. Yields for historical explosions, recently released by Soviet sources (Vergino, 1989), have allegedly been determined primarily by hydrodynamic methods and only in one or two instances have radio-chemical techniques been employed. The map in *Figure 1* shows those source-to-station paths for which recordings are available.

Explosions

The distribution of the 26 explosions at the Semipalatinsk test range on the three sub-regions, Degelen (10), Murzhik (or Koynstan, 6), and Balapan (or Shagan river area, 10) is shown in *Figure 2*. The explosion epicenters cover an area with a maximum dimension of about 100 km.

Point estimates of yields, from 2 to 165 kt, are available for 19 of these explosions (Cf. Table 1). Two of the explosions, on Dec 10, 1972, were set off only 10 seconds apart, one at Balapan and the other at Degelen, and will therefore have interfering Lg waves. The yield of the smaller of the two explosions (at Degelen)

TABLE 1.
SOURCE PARAMETERS FOR EXPLOSIONS

Date			Time	Latitude	Longitude	Depth	Yield	Region	Rock	Empl.
-	-	-	-	(N)	(E)	(m)	(kt)	-	Type	-
1965	nov	21	04:58:00.0	49.81919	78.06358	278	29	D	Gr	A
1966	feb	13	04:58:00.1	49.80894	78.12100	297	125	D	QP	A
1966	mar	20	05:50:00.3	49.76164	78.02389	294	100	D	QP	A
1966	may	07	03:58:00.2	49.74286	78.10497	274	4	D	QP	A
1967	sep	22	05:03:59.0	49.95964	77.69106	229	10	M	Al	H
1968	sep	29	03:43:00.0	49.81197	78.12194	290	60	D	QP	A
1969	dec	28	03:47:00.2	49.93733	77.71422	388	46	M	Al	H
1969	jul	23	02:47:00.2	49.81564	78.12961	175	16	D	QP	A
1969	nov	30	03:32:59.7	49.92428	78.95575	472	125	B	Co	H
1971	apr	25	03:32:59.9	49.76853	78.03392	296	90	D	Gr	A
1971	jun	06	04:02:59.7	49.97542	77.66028	299	16	M	Al	H
1971	oct	09	06:02:59.7	49.97789	77.64144	237	12	M	Al	H
1971	oct	21	06:02:59.7	49.97381	77.59733	324	23	M	Sa	H
1972	aug	16	03:16:59.8	49.76547	78.05883	139	8	D	Gr	A
1972	dec	10	04:27:00.0	49.81939	78.05822	264		D	Gr	A
1972	dec	10	04:27:10.0	50.02700	78.99556	478	140	B	TS	H
1972	feb	10	05:03:00.0	50.02428	78.87808	295	16	B	Al	H
1972	mar	28	04:22:00.1	49.73306	78.07569	124	6	D	QP	A
1972	nov	02	01:27:00.2	49.92697	78.81725	521	165	B	Al	H
1972	sep	02	08:56:59.9	49.95942	77.64089	185	2	M	Sa	H
*1976	sep	29	02:59:57.4	73.40000	54.81000			NZ		
*1977	sep	1	02:59:57.5	73.37000	54.58000			NZ		
*1978	aug	10	07:59:57.7	73.33000	54.79000			NZ		
*1979	aug	04	03:56:57.3	49.86000	78.94000			B		
*1979	dec	23	04:56:57.6	49.93000	78.80000			B		
*1979	oct	18	07:09:58.3	73.33000	54.80000			NZ		
*1979	oct	28	03:16:57.6	49.96000	79.07000			B		
*1979	sep	24	03:29:58.3	73.36000	54.70000			NZ		
*1981	oct	18	03:57:02.7	49.88000	78.89000			B		
*1984	may	26	03:13:12.5	49.93000	79.03000			B		
*1988	dec	04	05:19:53.6	73.49000	54.18000			NZ		
*1988	sep	14	03:59:57.4	49.83300	78.80800			B		

Origin time and epicenter data for explosions marked with asterisks have been obtained from the ISC annual bulletins. For the other explosions, the data are in accordance with a compilation by Vergino (1989) of descriptions of nuclear explosions published by Soviet seismologists (Bocharov *et al.*, 1989).

Region: B-Balapan, D-Degelen, M-Murzhik (Konystan), NZ-Novaya Zemlya.

Rock. Gr-Granite, QP-Quartz Porphyrite, Al-Aleurolite (Siltstone), Co-Conglomerate, TS-Tuffaceous Sandstone, Sa-Sandstone

Empl. - Emplacement: A-Adit, H-Hole.

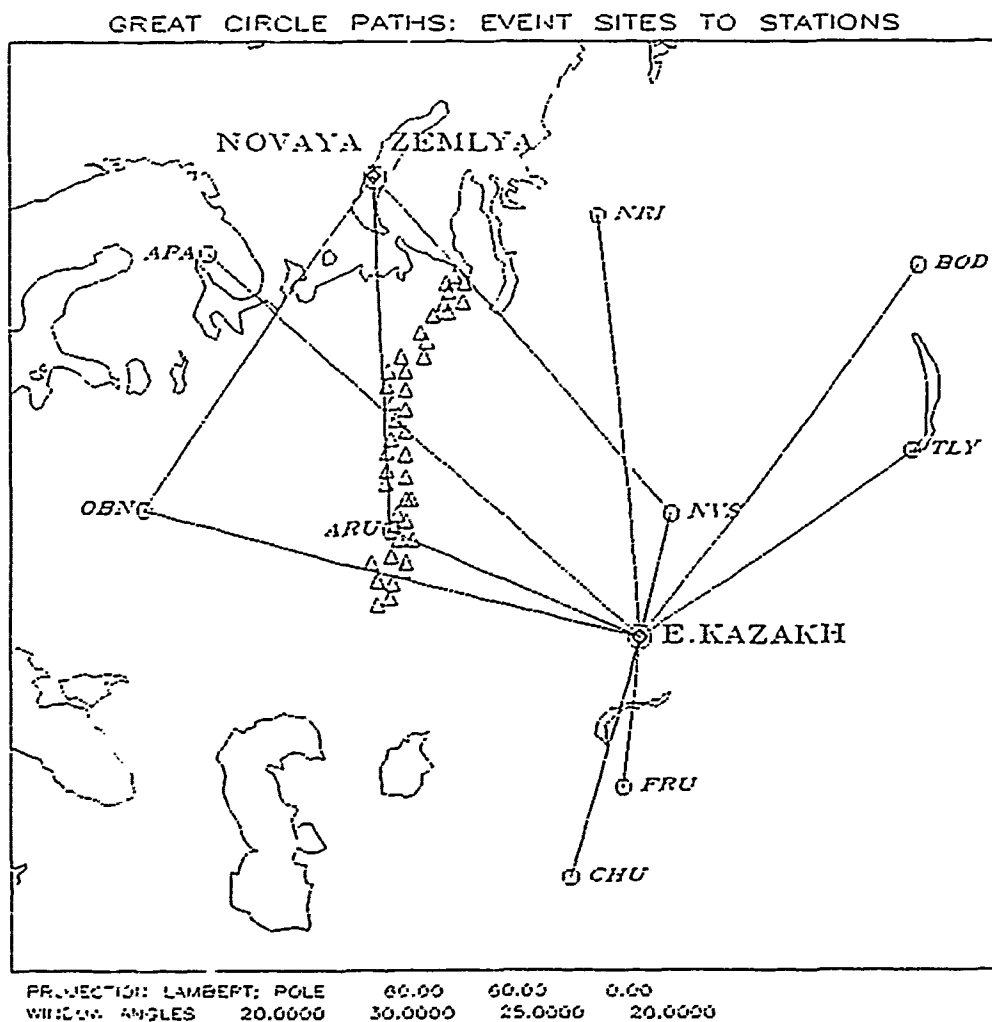


Figure 1. Source to station paths for which data are available. The numbers for each path indicate the number of recordings available for that path. The Ural mountain range is outline by triangles.

EPICENTERS OF E. KAZAKH EVENTS

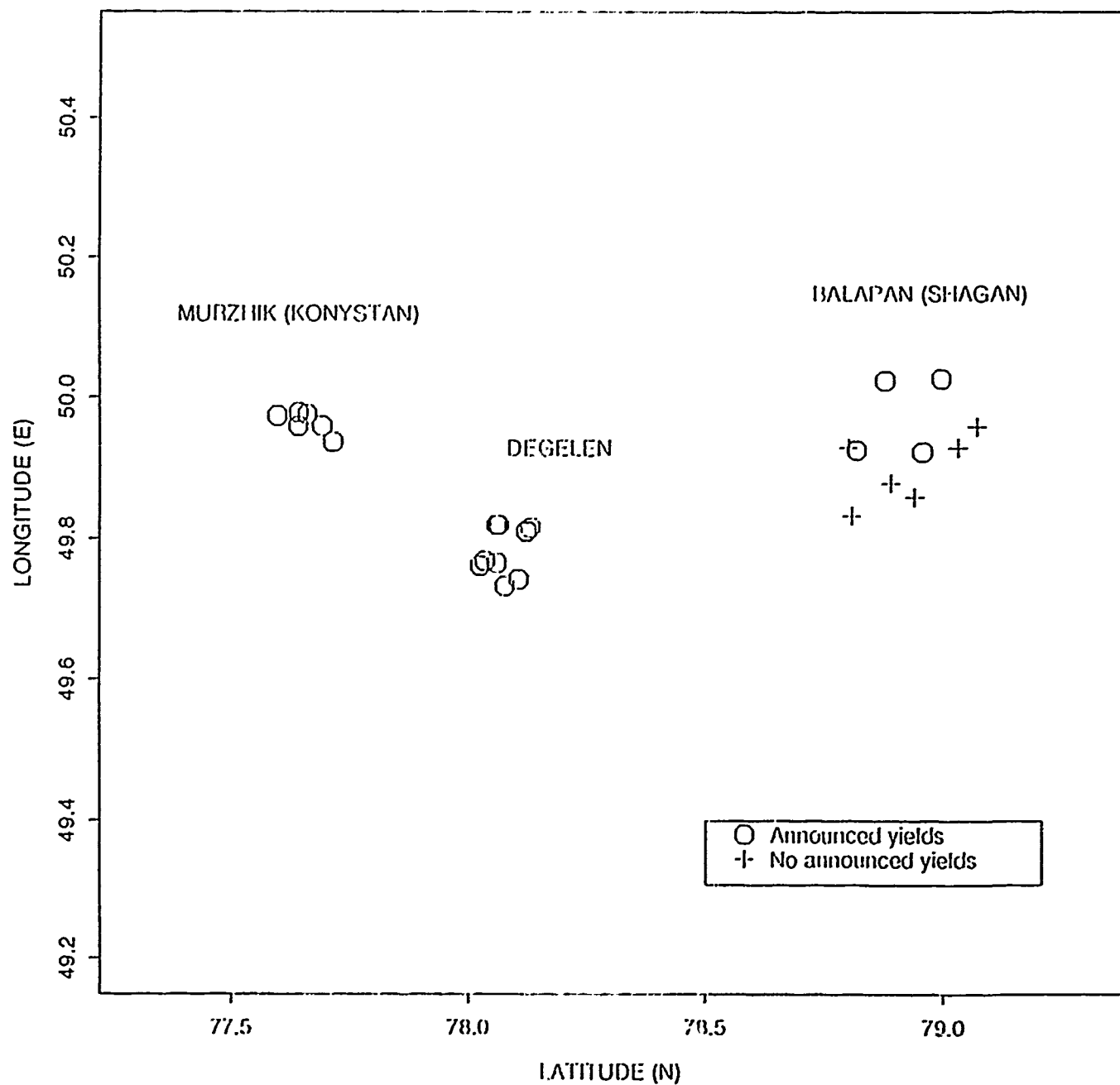


Figure 2. Relative location of explosions at the Semipalatinsk test range.

has not been announced, but has been constrained to the interval 20-150 kt (Vergino, 1989).

In *Figure 3* the shot depth, h , is plotted against the explosion yield, W , for the explosions listed in Table 1. Jih *et al.* (1990) found that the shot depths for Murzhik and Balapan explosions follow approximately the relation. $h = 146 \cdot W^{\frac{1}{4}}$ and the data in *Figure 3* are in reasonable agreement with this relation. That is to say, the depth is proportional to the quartic root of the yield rather than to the cubic root, mostly used for explosions at the Nevada Test Site. However, for Degelen explosions, usually adit shots, the depth scaling with yield appears to be different. For example, the data in *Figure 3* show that 6 of the Degelen explosions with yields from 4 to 125 kt have almost the same shot depth, around 270-290 m, regardless of yield.

No information on yield or other detailed source characteristics has been released for the Novaya Zemlya explosions. They are all located along the Matochkin Shar, the narrow strait that separates the northern and the southern islands of Novaya Zemlya.

Stations

The relative locations of the seismological stations are shown on the map in *Figure 1*. The paths between source sites and stations range in distance between 5 (Semipalatinsk - NRI) and 26 (Semipalatinsk - APA) degrees. We have made no distinction between the regions, Murzhik, Degelen and Balapan, of the Semipalatinsk Test Range.

Typical recordings for each of the 12 paths as a function of epicentral distance are shown in the seismogram section of *Figure 4*. Clear Lg phases can be seen for all paths except for the two paths from Novaya Zemlya to the stations NVS and OBN. The absence of clear Lg phases could be due to blockage by large sediment thickness variations in the Barents and Kara Seas (Baumgart, 1990). The comparatively large Lg waves at TLY from explosions at the Semipalatinsk test range could just be an effect of *high* attenuation of P and S waves and *low* attenuation of L_g along the path to Lake Bajkal.

The number adjacent to each path in *Figure 1* represents the number of Lg recordings with acceptable data quality that were used in this study. Table 2 shows the stations for which data are available for each explosion. Recordings with poor quality are also indicated.

The recordings, vertical component only, have been obtained mostly with a standard CKM 3 instrument. However, the parameter settings, like period and

TABLE 2.

EXPLOSION			DATA AVAILABILITY								
			STATION								
-	-	-	APA	ARU	BOD	CHU	FRU	NRI	NVS	OBV	TLV
1965	nov	21					1		1		
1966	feb	13								1	
1966	mar	20								1	
1966	mar	20								(1)	
1966	may	7				1			1	1	
1967	sep	22								1	
1967	sep	29						1	(1)	1	
1969	jul	23			1				(1)	1	
1969	nov	30			1				(1)	1	
1969	dec	28			1					1	
1971	apr	25		1	1			1	(1)	1	
1971	jun	6					(1)	1	(1)	1	
1971	oct	9		1				1	(1)	1	
1971	oct	21						1	1	1	
1972	feb	10		1	1				(1)	1	
1972	mar	28		1	1	1		1	1	1	
1972	aug	16		1	1				1	1	
1972	sep	2		1			1	1	1	1	
1972	nov	2		1	1				(1)	1	
1972	dec	10		1	1					1	
1976	sep	29								1	
1977	sep									1	
1978	aug	10		1					1	1	
1979	aug	4		1				1		1	
1979	sep	24		1					1		
1979	oct	18		1							
1979	oct	28			1			1		1	
1979	dec	23			1			1		1	
1981	oct	18		1	1			1		1	
1984	may	26	1	(1)	(1)	1		1		1	1
1988	sep	14	1	1				1	(1)	1	1
1988	dec	4							1		

For explosion/station combinations indicated with 1 1g data is available; in cases with numbers within parentheses the 1g data is incomplete.

EXPLOSION YIELD AND SHOT DEPTH

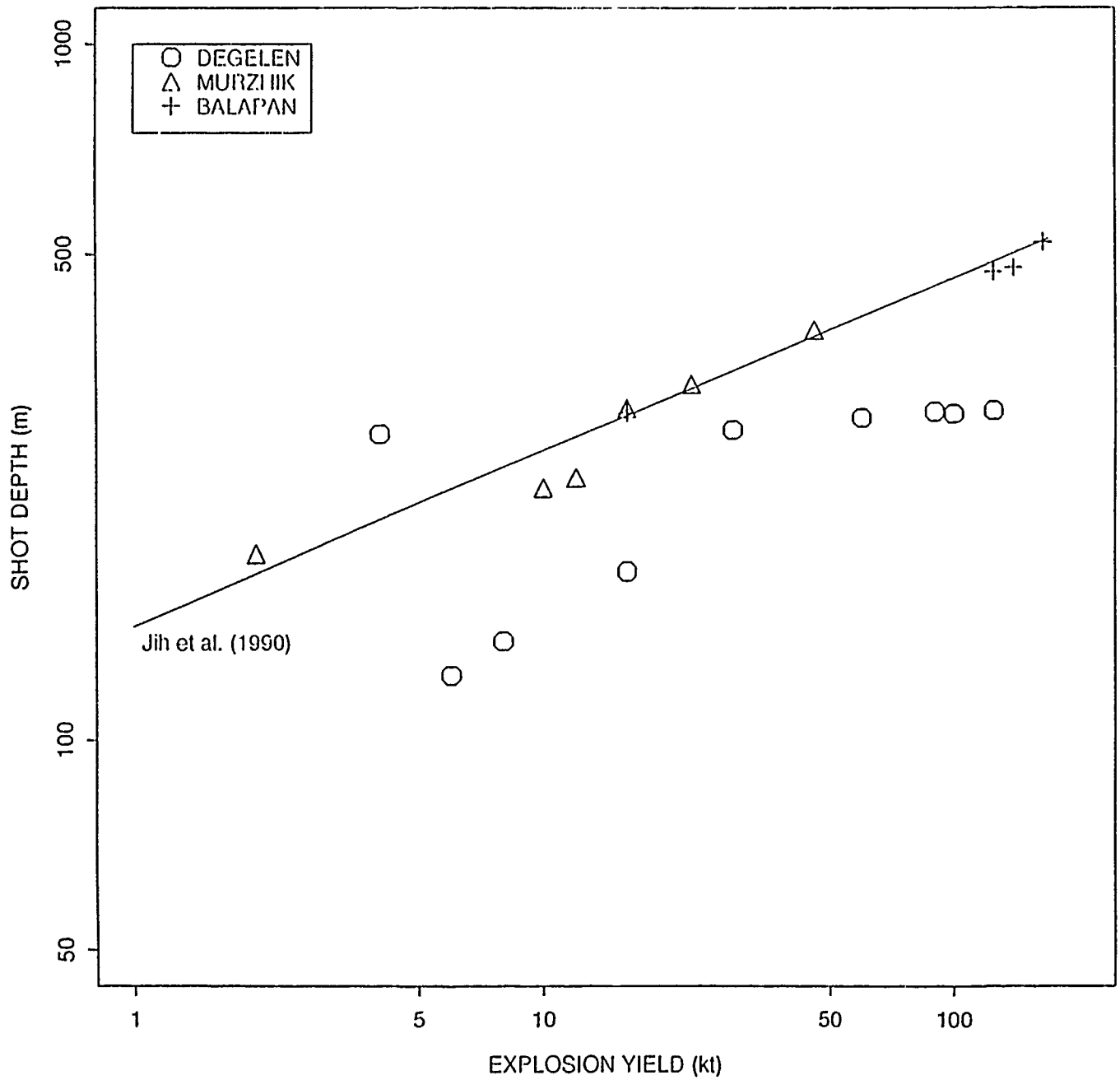


Figure 3. Explosion depth, h , as a function of explosion yield, W . The curve, $h=150 \cdot W^{\frac{1}{3}}$, has been suggested by Jih *et al.* (1990).

AMPLITUDE RESPONSE CURVES

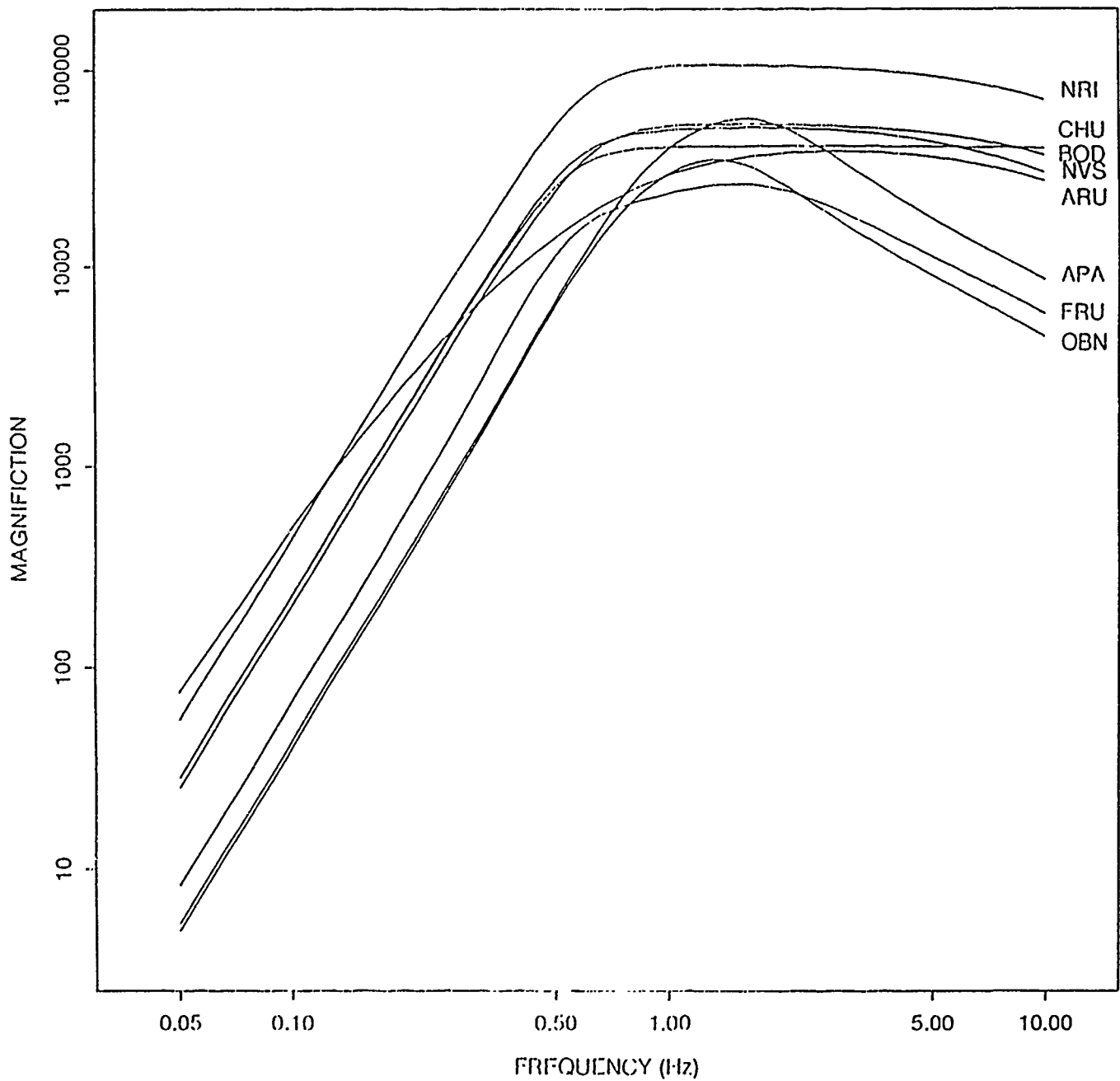


Figure 4. Seismogram section with a typical record for each path plotted as a function of epicentral distance. The records are aligned on the arrival time of the initial P wave. The relative travel time curves for *S*-waves (Jeffreys-Bullen) and a group velocity of 3.5 km/s are drawn for comparison.

damping of seismometers and galvanometers, vary among the stations, so that the instrument response also differ somewhat from one station to another. *Figure 5* shows typical response curves for the stations derived from values of periods and dampings and other instrument parameters published in annual calibration summaries. The response curves change over long time periods and *Figure 6* illustrates the variation showing that the standard deviation of the instrument magnification for annual calibrations usually stays below 5 per cent.

Information on instrument response is also available for the individual records in many instances, but is given only as the maximum magnification and the period range in which the magnification is 90% or larger of the maximum magnification.

Data Quality

The procedure used to digitize the analog recordings have been described by Chiburis *et al.* (1980) and Kemerait *et al.* (1981). Hand digitized data is limited with regard to missing data segments, timing, dynamic range, and frequency band. Here we compare the hand digitized recordings at the station in Arti (ARU) to the digital data from the IRIS station at Arti for the JVE explosion (*Figure 7*). Both the Soviet CKM-3 and the IRIS instruments are installed in vaults of the same tunnel system. As can be seen from *Figure 8*, the amplitude responses are somewhat different for the two instruments, with the IRIS response peaked around 5 Hz and with the CKM-3 instrument having a fairly constant magnification above 1 Hz. The noise spectra in *Figure 8* shows that the IRIS instrument appears, perhaps somewhat surprisingly, to have the highest noise level at frequencies just above 1 Hz, the high noise of the IRIS recording is also obvious from the traces in *Figure 7*. Sharp peaks, at 4 and 5 Hz, of the IRIS noise spectrum indicate that the high level might partly be caused by instrumental or system noise. The two amplitude spectra of the P wave, corrected for noise and instrument response, look fairly similar, the ratio is fairly constant in a band from about 0.6 to about 2 Hz. The two Lg spectra have similar general shapes although the ratio varies considerably, about an order of magnitude, in the band from about 0.4 to 1.0 Hz.

Figure 9 compares the P and Lg waves in more detail. In addition to the original records of the two instruments, a hand digitized trace with a response equivalent to an IRIS instrument response is also included in this comparison. There are apparent shifts between signatures of the Lg wave train along the trace. The first significant amplitude, about 5 s after the beginning of the trace in the figure, appears *delayed* in the hand digitized data relative to the IRIS trace, whereas the two significant amplitudes around 50 s after the beginning appear to be *ahead* on the hand digitized records. The reason for this discrepancy is not known at this point in time.

VARIATION IN MAGNIFICATION

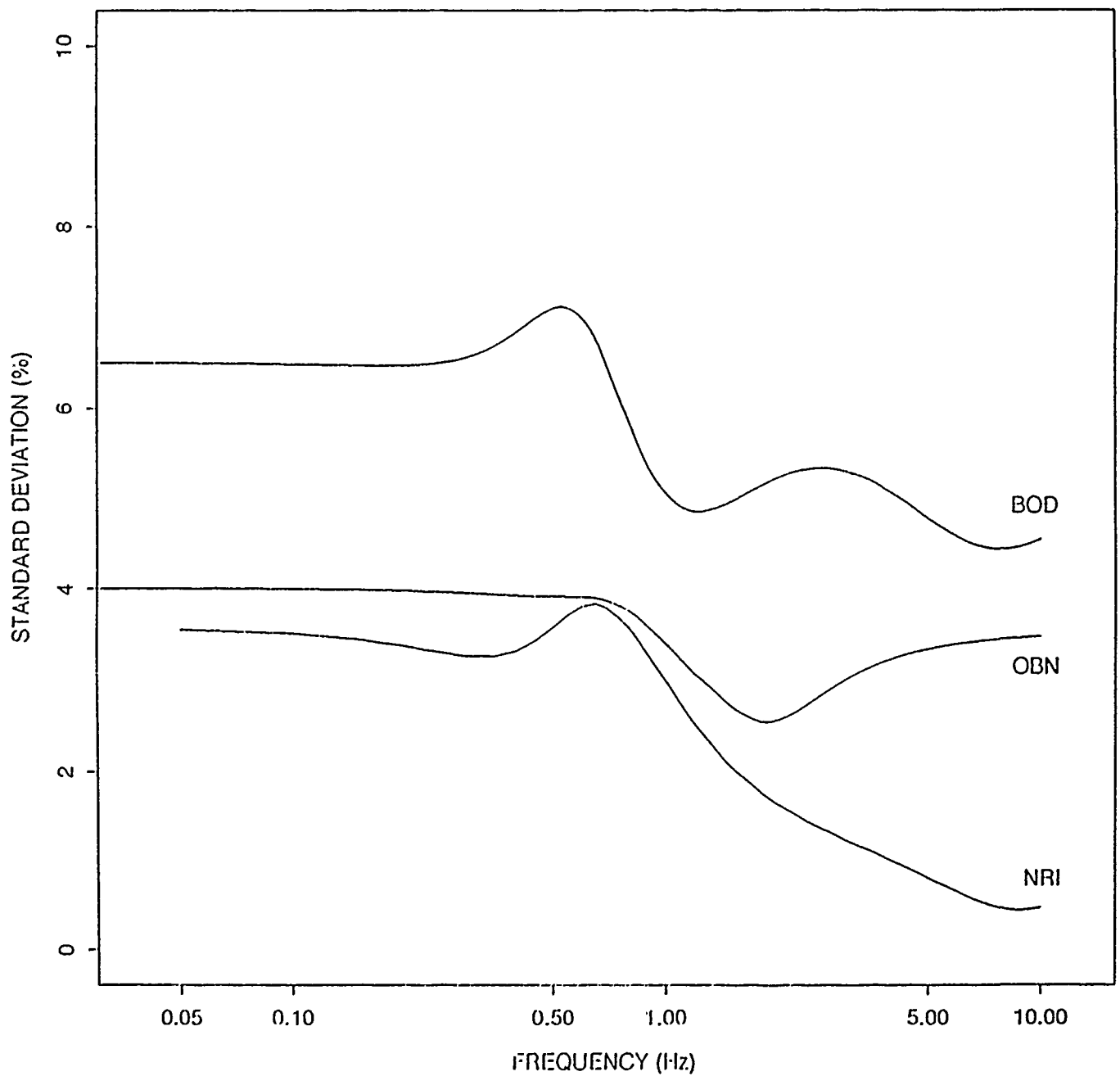


Figure 5. Typical amplitude response curves for the instruments at the stations.

TYPICAL SHORT PERIOD RECORDS

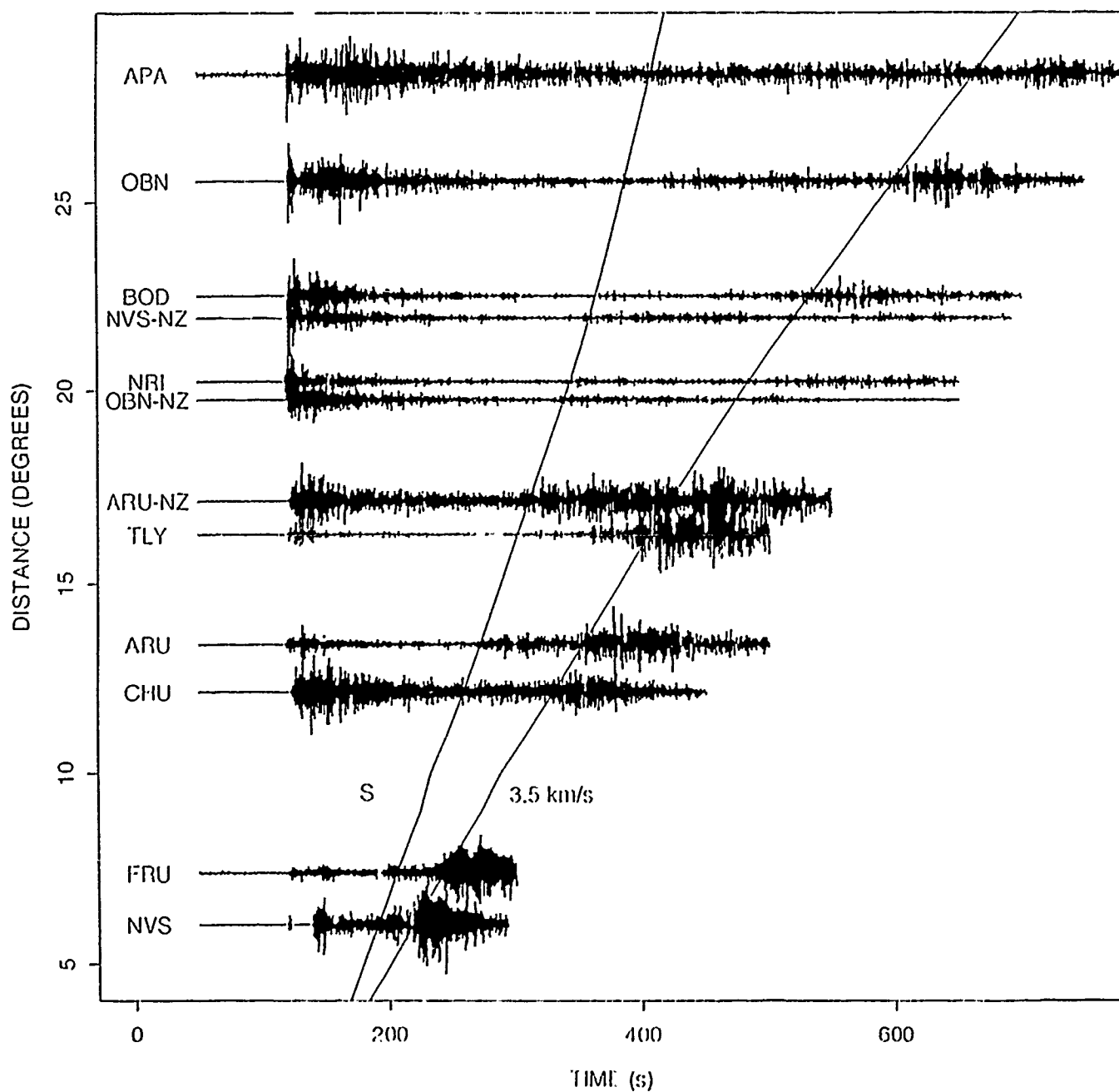


Figure 6. Standard deviation (in per cent) of the instrument magnifications for stations BOD, NRI, and OBN for similar response curves in the period 1965-1988.

COMPARISON OF HAND DIGITIZED AND DIGITAL IRIS RECORDS

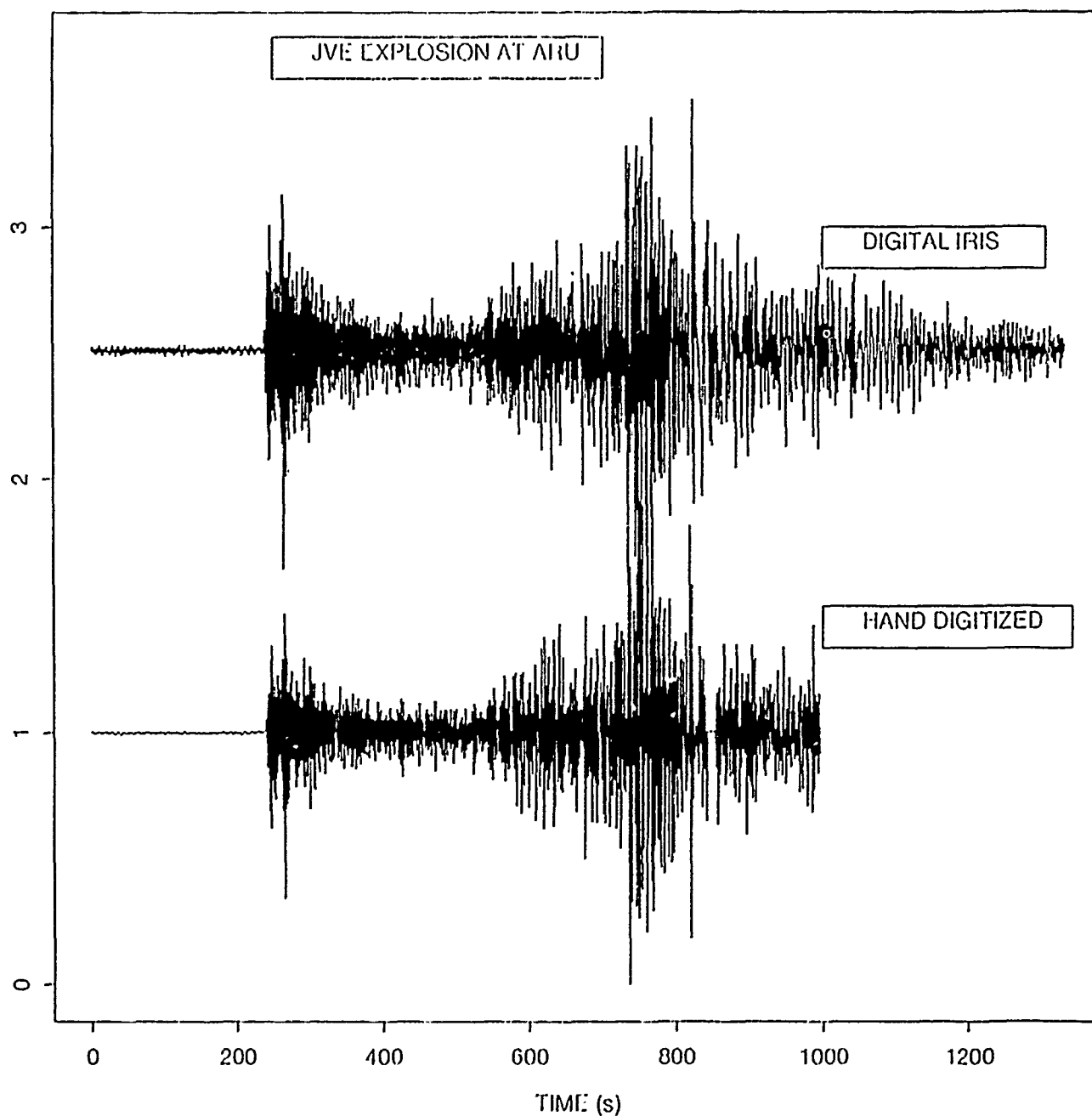
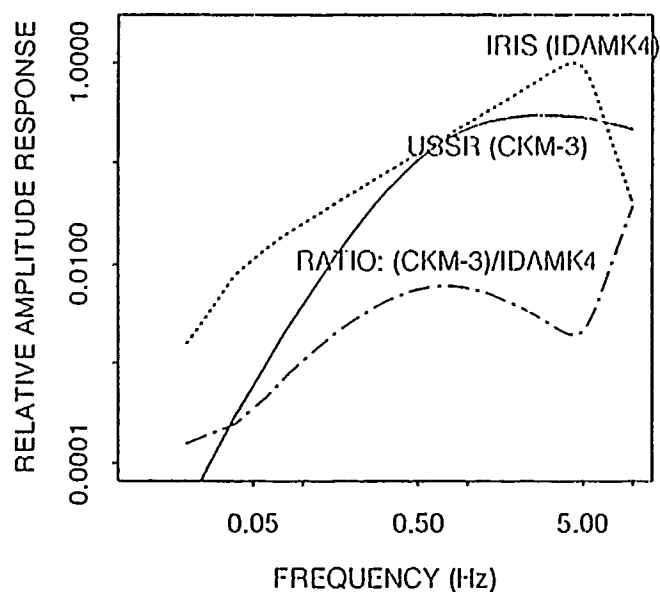
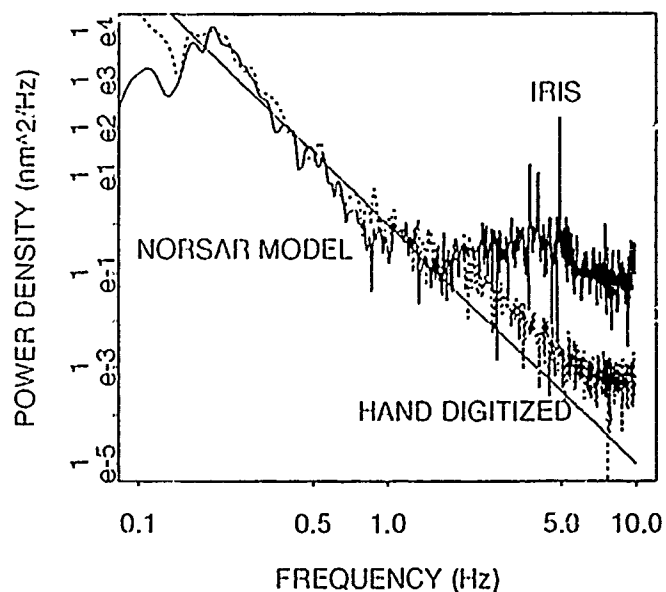


Figure 7. Vertical component recordings of JVI explosion on Sep 14, 1988, at IRIS stations and U.S.S.R station at Arti (ARU).

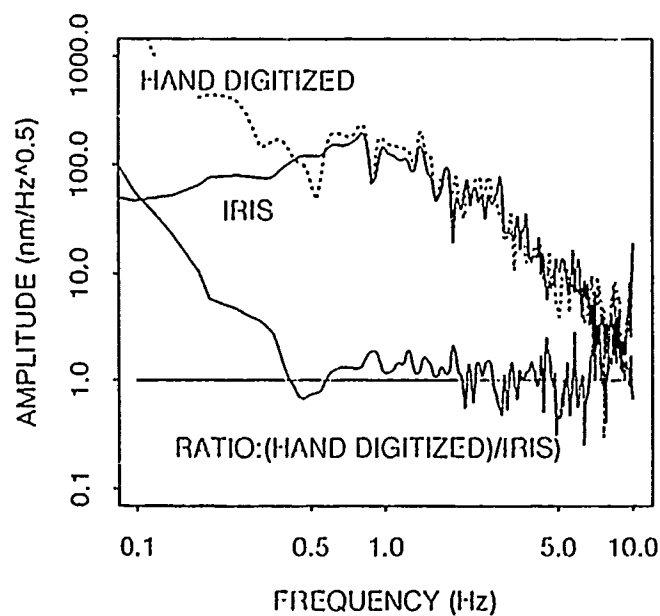
INSTRUMENTS



NOISE SPECTRA



P-WAVE SPECTRA



Lg-WAVE SPECTRA

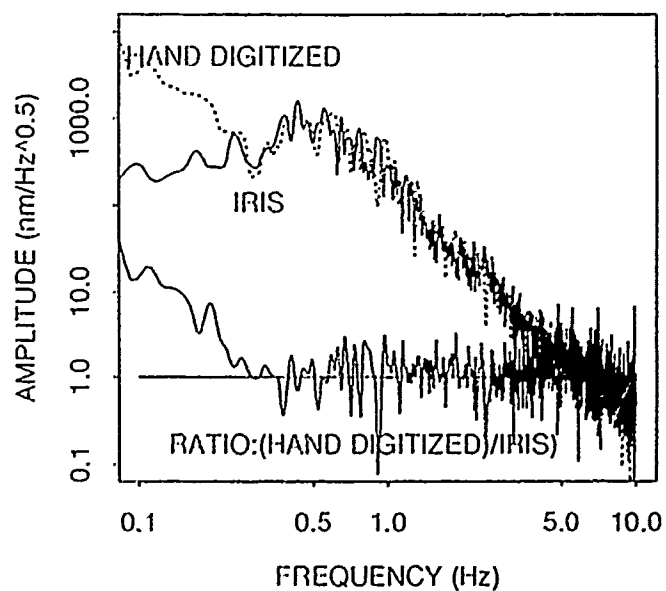
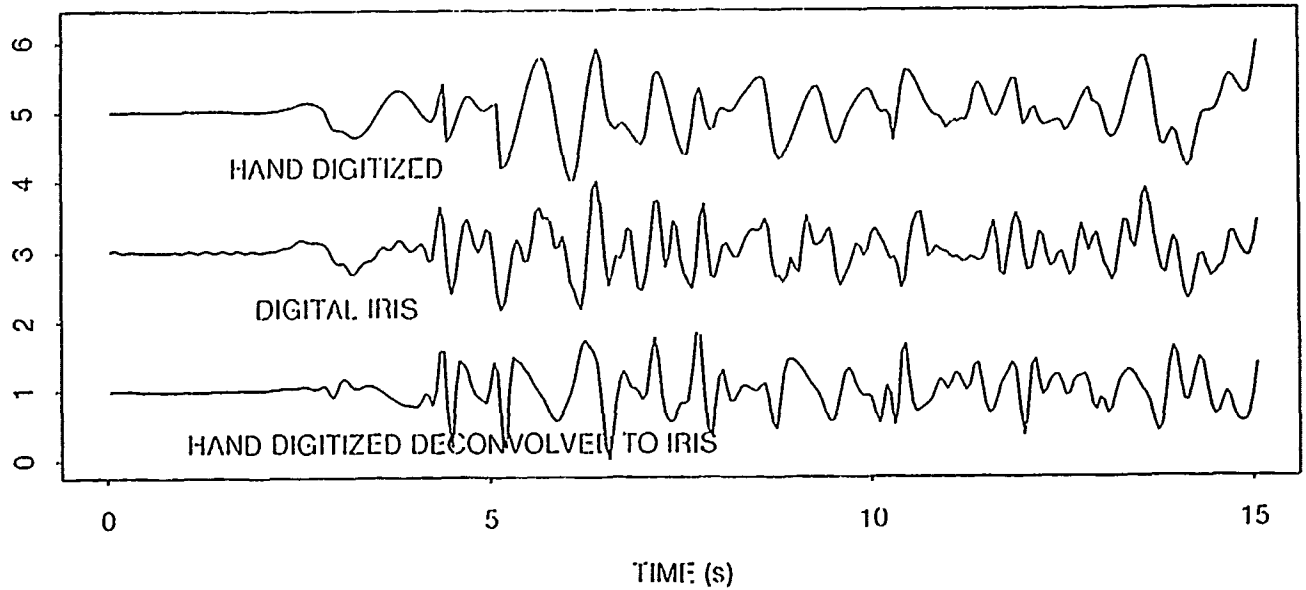


Figure 8. Comparison of instrument responses, noise, P-wave, and Lg spectra for the JVE explosion recorded by IRIS (IDAMK4) and Soviet CKM instrument at station ARU.

P at ARU for JVE Explosion



Lg at ARU for JVE Explosion

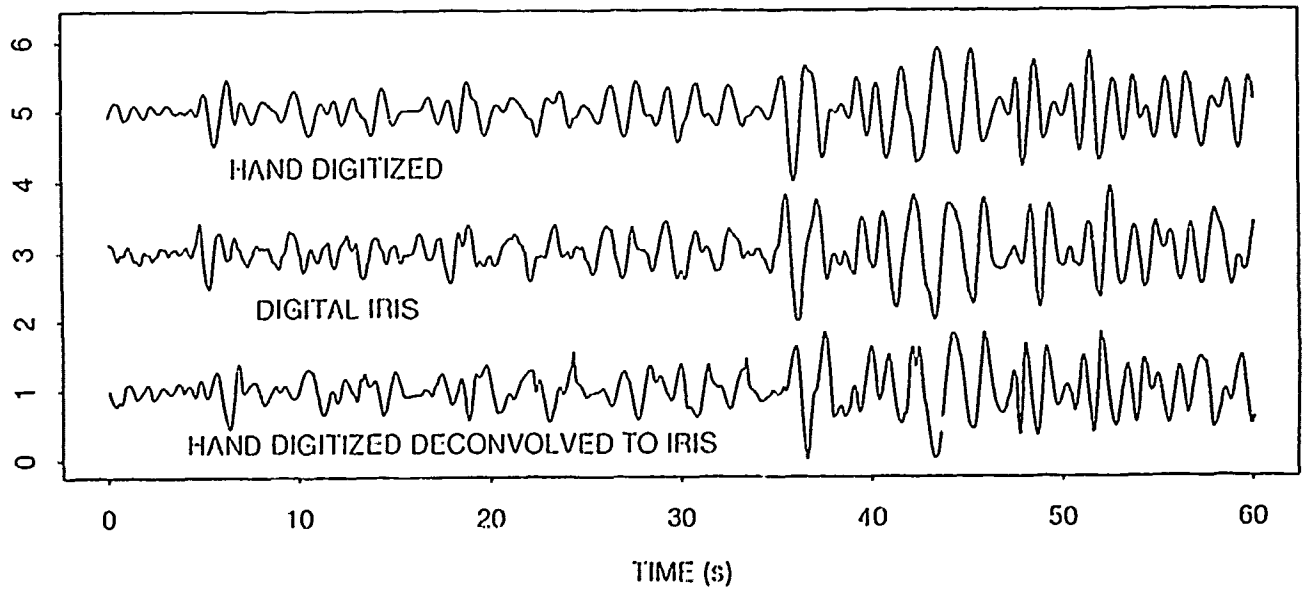


Figure 9. Panels with P waves and Lg-waves recorded by IRIS and Soviet instruments at ARU from the JVE. The Soviet hand digitized recording has also been deconvolved with its instrument response and convolved with that of the IRIS instrument (bottom trace in the panels).

4.1.3 Lg Waves

Figures 10a-e show recordings of Lg waves for the stations ARU, BOD, NRI, NVS, and OBN from explosions at the Semipalatinsk test range. The time windows vary somewhat depending on available data but usually cover velocities from 3.0 - 4.0 km/s. For each station the wave segments are grouped according to subregion, Degelen, Konystan, and Balapan, and within each region the traces are plotted according to the yield of the associated explosion.

The median of the group velocity for the maximum amplitude of the Lg wave is low for most paths (e.g., 3.37 and 3.39 km/s for ARU and OBN). The shape of the Lg wave train varies significantly from explosion to explosion for a given station. The record at OBN for the Degelen explosion on Feb 13, 1966 (1966044) in Figure 10e is strikingly different from the other recordings since it was obtained with a broadband CDK instrument. All the other OBN recordings were obtained with the standard short period CKM-3 instrument. There are only a few pairs which show a high degree of similarity, like 1971115 and 1972229 at ARU and 1966079 and 1971115 at OBN and 1988258 and 1981291 at OBN in Figures 10a and e. The spectra of the Lg wave is usually sharply peaked (for example, around 0.5, 0.6 and 0.8 Hz for recordings at OBN, ARU, and NVS respectively).

The signal-to-noise ratio peaks for Lg waves at ARU and OBN in rather narrow frequency bands (0.7-1.4 and 0.4-1.0 Hz respectively) and velocity windows (3.20-3.55 km/s).

4.1.4 RMS Lg Magnitudes

Some tentative results of analysis of RMS Lg magnitudes, originally defined by Ringdal (1983) and later applied to various data sets (e.g. Hansen *et al.*, 1990), are summarized in Figures 11 and 12. Parameter settings used in the calculations were somewhat different from those used by Ringdal and co-workers. For example, the maximum RMS value of the Lg phase was calculated for a sliding window limited to 90 s rather than the 120 s used by Ringdal (1983), because of limitations in available data. Furthermore, the calculations were based on traces bandpass filtered between 0.4-1.2 Hz, since the filter 0.6-2.0 Hz used by Ringdal did not give sufficient signal-to-noise ratio for weak events. The noise RMS value used to subtract from the Lg RMS value was also based on a time window of 110 s rather than 30 s. Calculations of noise RMS values as a function of window length for the data here showed that stable values, with little variation, usually were obtained for window lengths larger than 60 s. It should, however, be noted that the Lg RMS value corrected for noise is quite insensitive to the parameter settings. Experiments with a variety of window length and filter settings showed only small differences, hardly statistically significant from the results in Figures 11 and 12.

Lg at ARU from E.Kazakh events

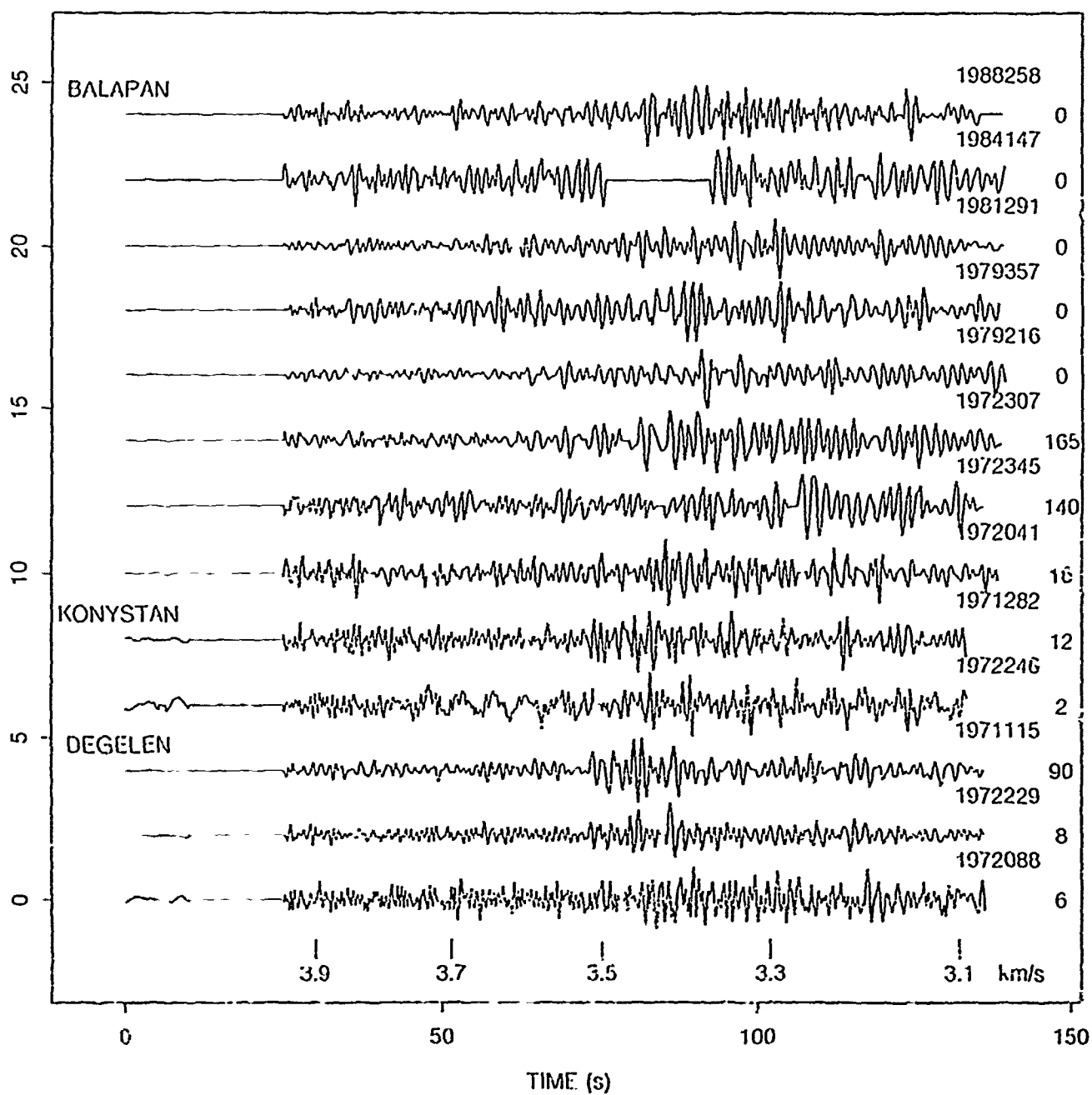


Figure 10 a-e. Lg waves at U.S.S.R stations ARU, BOD, NRI, NVS, and OBN from explosions at the Semipalatinsk test range.

Lg at BOD from E.Kazakh events

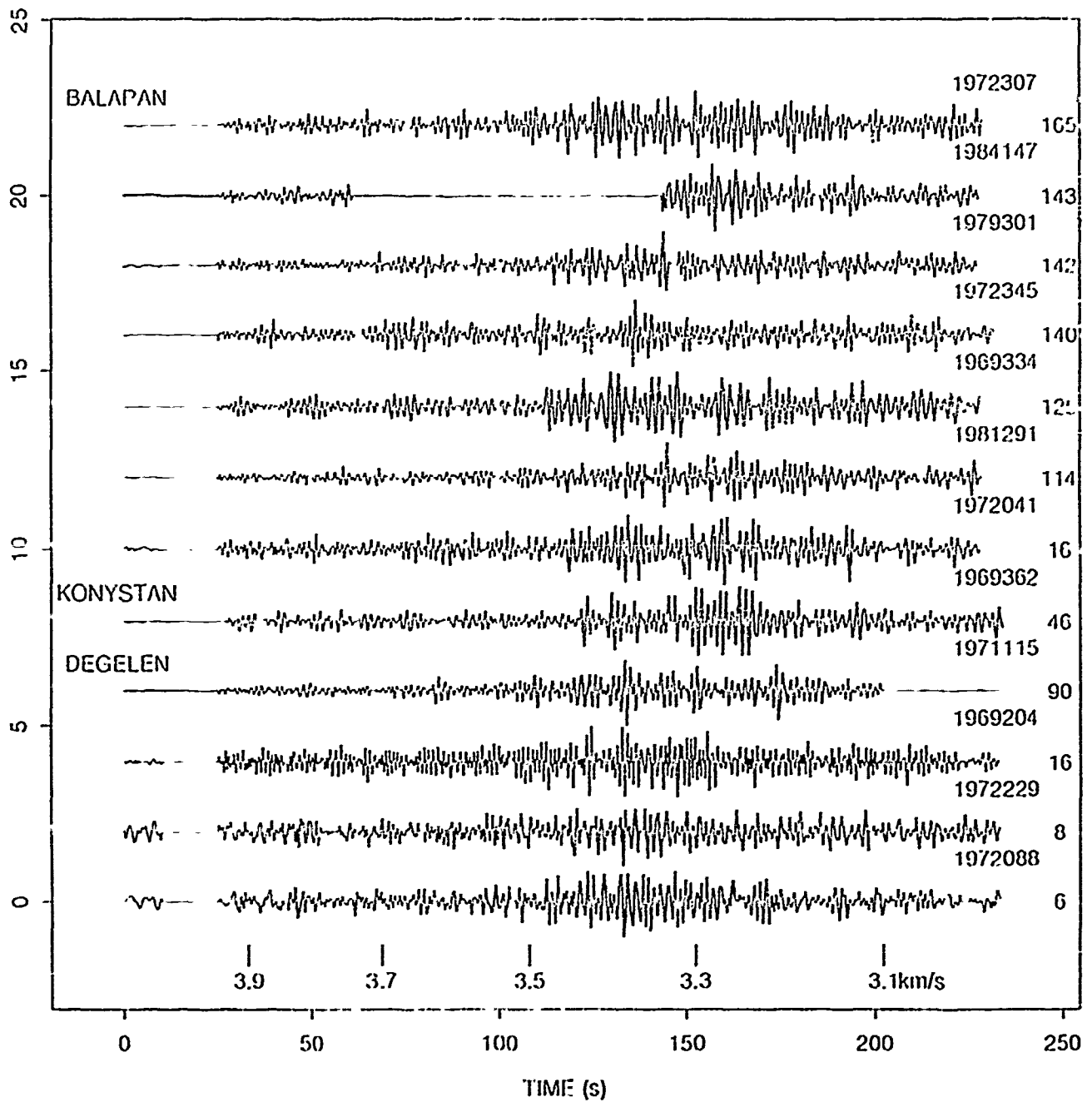


Figure 10b

Lg at NRI from E.Kazakh events

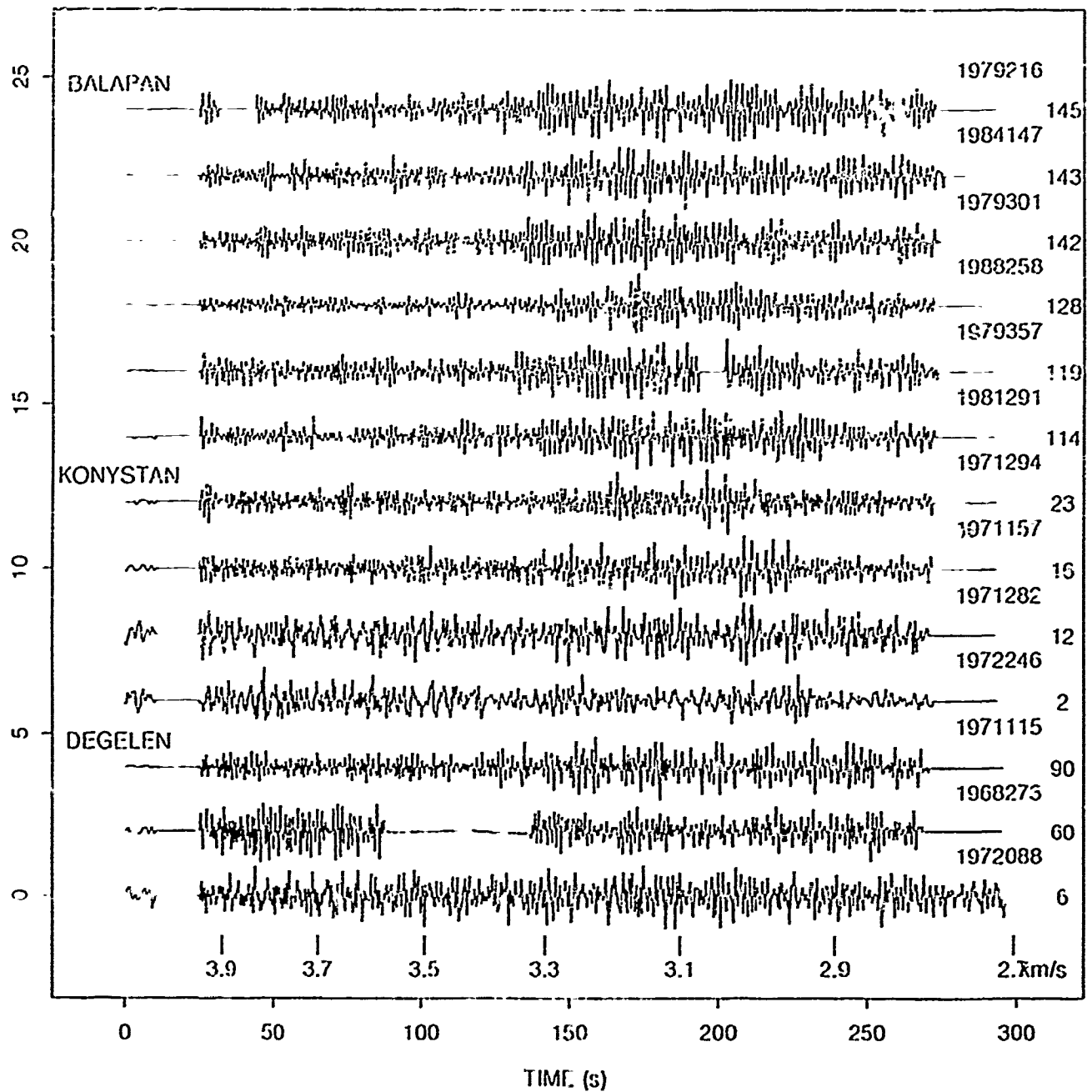


Figure 10c

Lg at NVS from E.Kazakh events

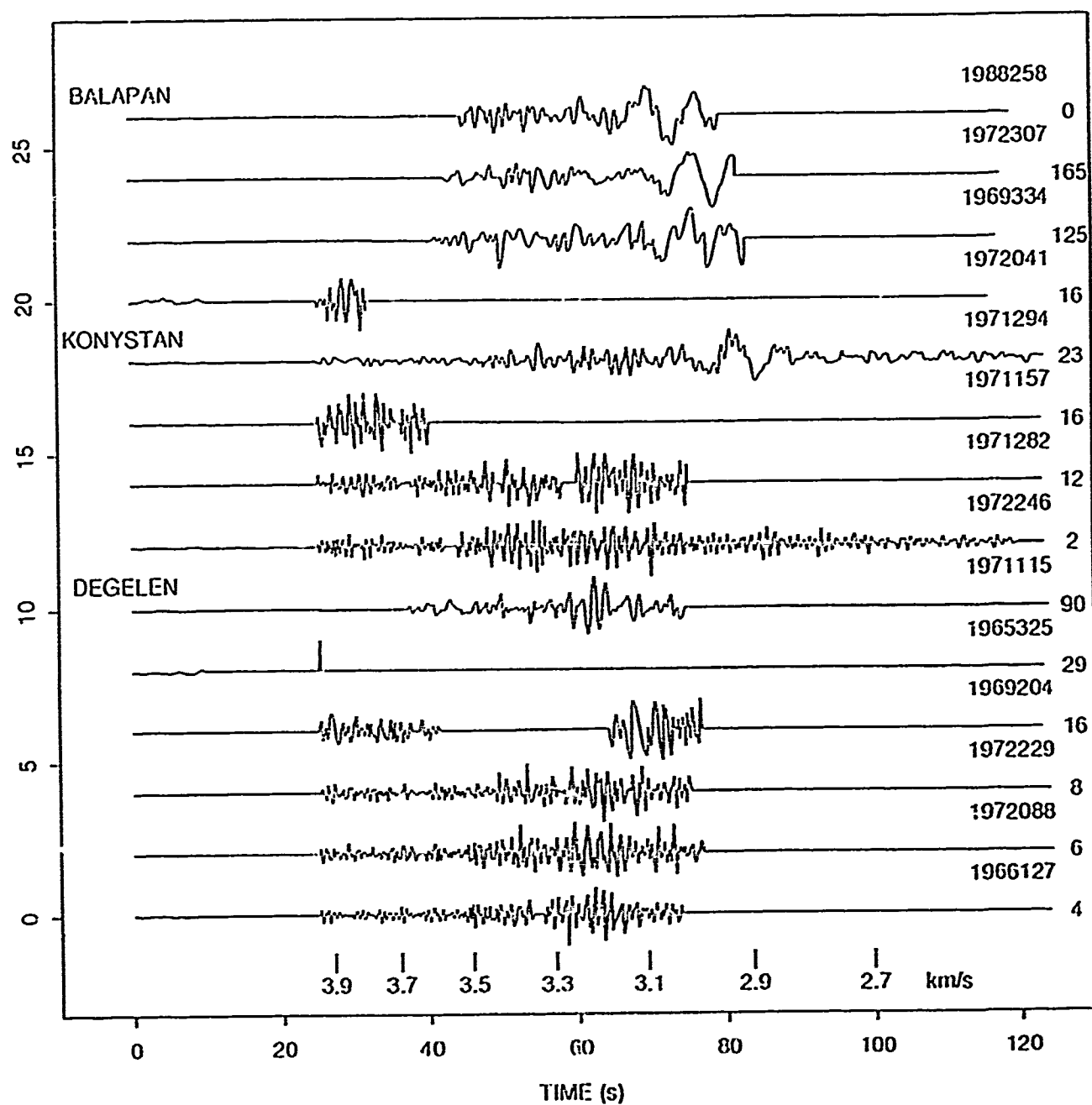


Figure 10d

Lg at OBN from E.Kazakh events

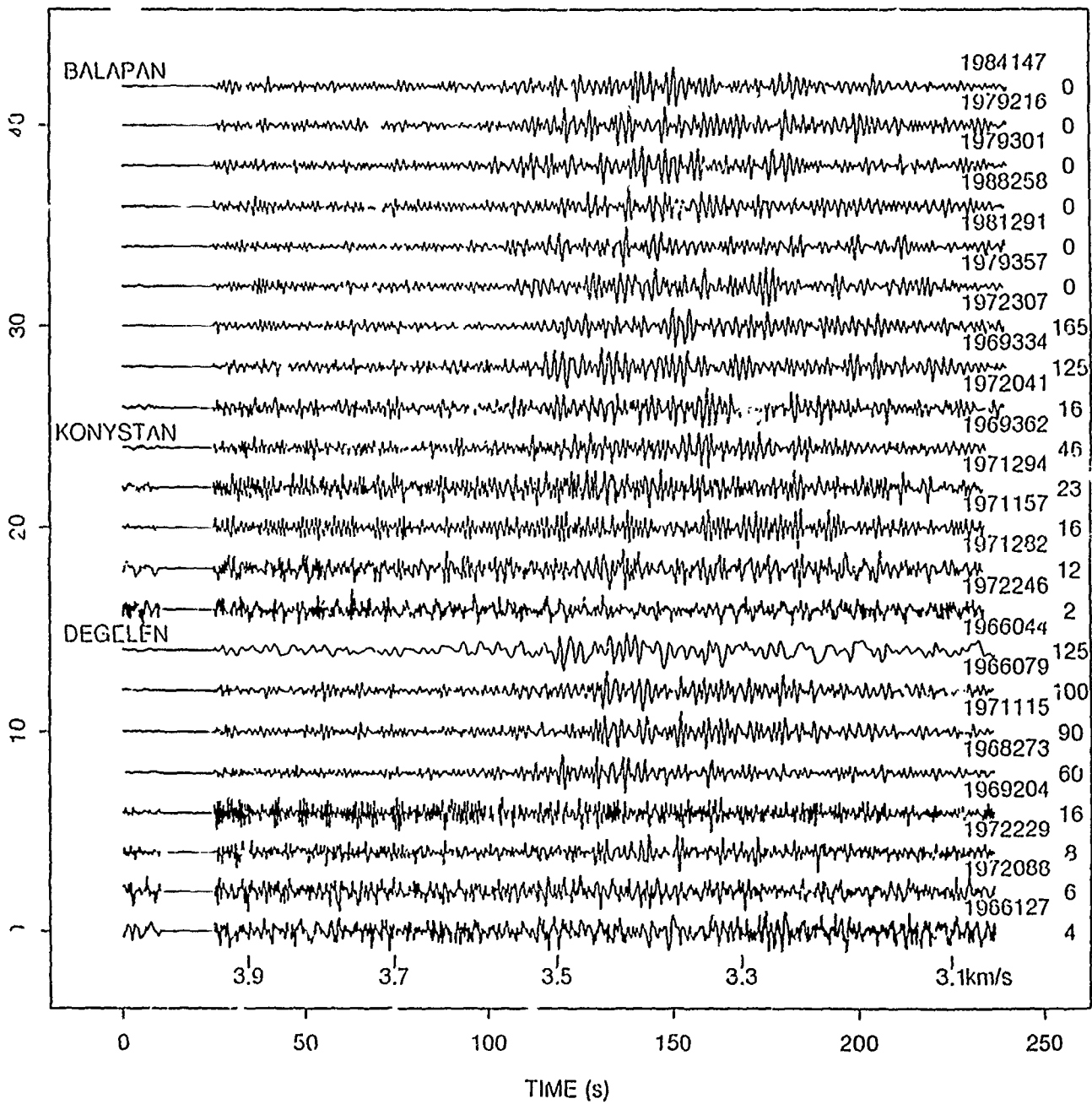


Figure 10c

COMPARISON OF LOG(RMS Lg): 0.4-1.2 Hz, 90s, NO INSTRUMENT CORRECTIONS

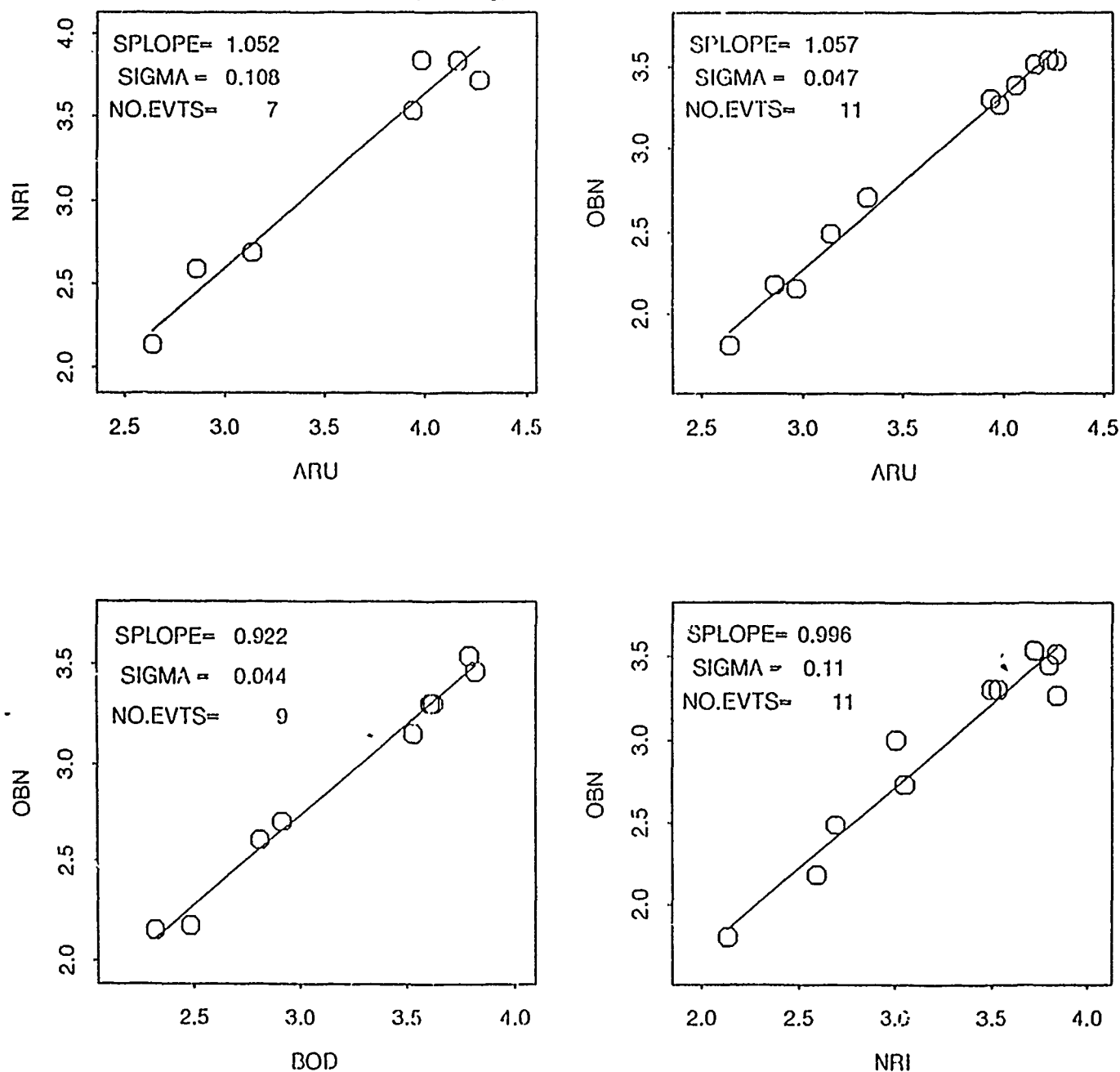


Figure 11. Comparison of Lg RMS magnitudes for common events at stations ARU, BOD, NRI, and OBN.

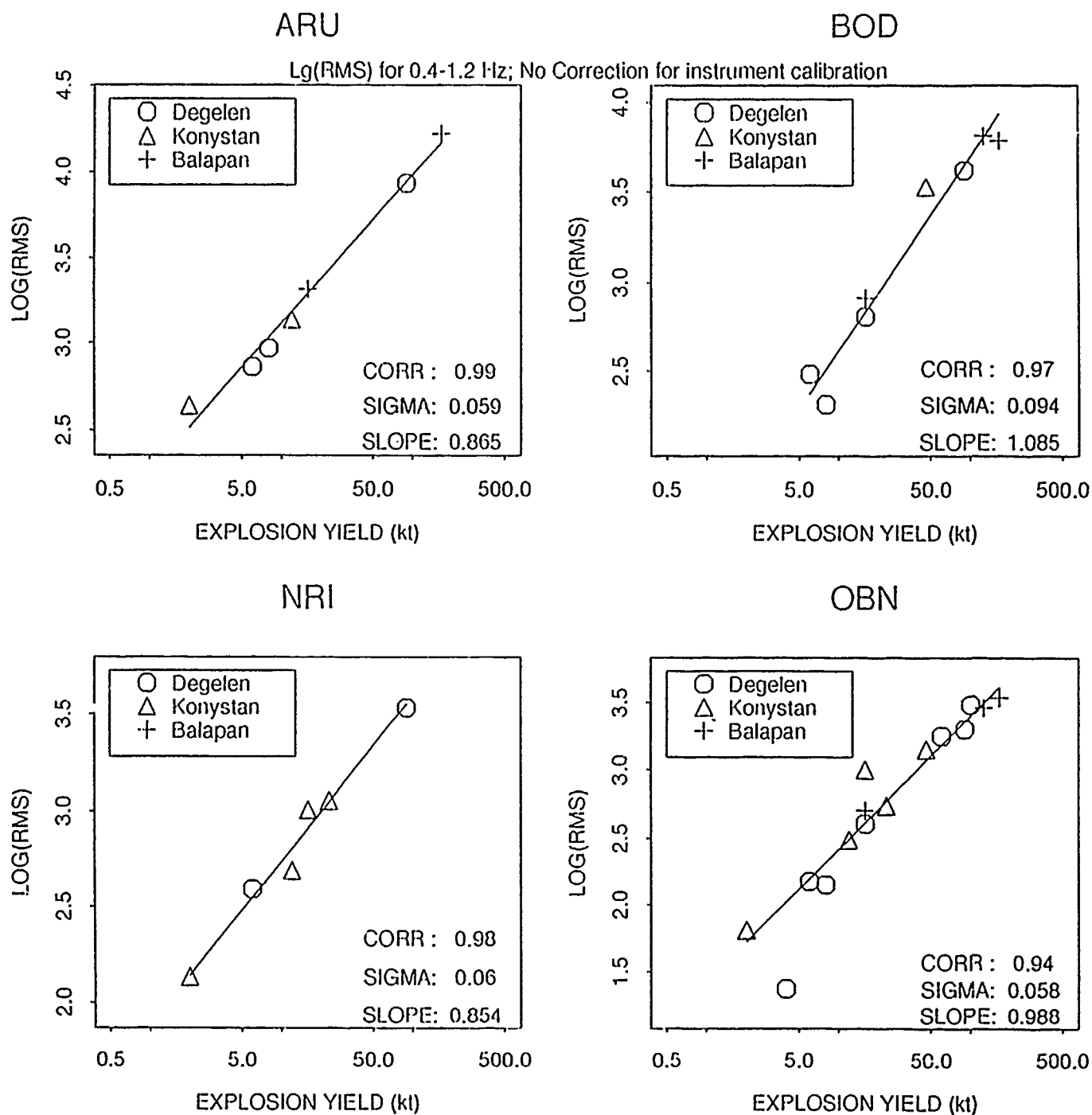


Figure 12. Comparison of Lg RMS magnitudes and yields of explosions at the Semipalatinsk test range at stations ARU, BOD, NRI, and OBN.

Figure 11 compares log RMS values of events common to station pairs ARU-NRI, ARU-OBN, BOD-OBN, NRI-OBN. Because of the small number of events, no distinction is made in the scatter diagrams between subregions of the Semipalatinsk test range. The slope of a linear relation, estimated on the assumption of equal and independent errors of the two RMS values, is also indicated in the diagrams (Ericsson, 1971). The standard deviation of the error terms, also given in the diagrams, varies between 0.044 to 0.11. The smaller value is comparable to those of obtained by Hansen *et al.* (1990).

In Figure 12 the RMS values are compared with the explosion yields released by Soviet sources and compiled by Vergino (1989). Again estimates of slope and standard deviations in the diagrams were obtained on the assumption of equal error in RMS value and the logarithm of the explosion yield. Apart from two outlying data points for the OBN data, there is a fairly close correlation between the data sets. Values of standard deviation, 0.059-0.09, are comparable to those of standard deviations for RMS values between stations. Data for the two outlying data points were omitted for the estimation of slope and sigma values.

One of the outlying data points for OBN is from a Degelen event, 1966 (4 kt), and the other is from a Konystan explosion (16 kt). We note that the 4 kt explosion is over buried compared to the scaled depth relation with yield by Jih *et al.* (1990) shown in Figure 3. It has been suggested that the generation of Lg waves from over buried explosions in hard rock should be reduced (McLaughlin *et al.*, 1990). Before any far reaching conclusions can be drawn on this point, it should be noted that the RMS *noise* level for this event is unusually low, which suggests that the anomalous value for this event could simply be caused by improper calibration correction. It should be noted that the RMS data in Figures 11 and 12 were not corrected for possible differences in instrument responses, but calculated on the assumption that the recordings for a given station were obtained with instruments of the same characteristics. A detailed analysis of available instrument calibrations is necessary to determine whether calibration corrections should be applied to the RMS values in Figures 11 and 12. Rigorous conclusions on the stability of RMS values and estimates of standard deviations of announced explosion yields will have to await the results of this calibration analysis.

Hans Israelsson

References

- Baumgardt, D.R. (1990), Causes of Lg Amplitude Variations and Scattering in the Eurasian Continental Crust. in Proceedings of the Twelfth Annual DARPA/GL Seismic Research Symposium. (Eds J. Lewkowics and J McPhetres), GL-TR-90-0212 Geophysics Laboratory, Hanscom AFB, MA **ADA226635**
- Chiburis, E.F., R.O. Ahner, E.J. Reinhart (1980), Procedures for Digitizing Seismograms ENSCO Technical Report DCS-STR-80-53
- Ericsson, U.E. (1971) Maximum likelihood linear fitting when both variables have normal and correlated error. Report C4474-A1, Research Institute of National Defense, Stockholm, Sweden.
- Hansen, R.A., F. Ringdal, and P.G. Richards (1990), The stability of RMS Lg measurements, and their potential for accurate estimation of the yields of Soviet underground nuclear explosions. Bull. Seism. Soc. Am., Special Issue (in press).
- Jih, R.S. (1990) Geotech's Magnitude-Yield Study During 1989-1990. in Proceedings of the Twelfth Annual DARPA/GL Seismic Research Symposium. (Eds J. Lewkowics and J McPhetres), GL-TR-90-0212 Geophysics Laboratory, Hanscom AFB, MA **ADA226635**
- Kemerait, R. C., G. Kraft, J. S. Mott, and E. Dohner (1981), A study of the hand-digitizing process for digitizing short period seismic data. ENSCO Technical Report DCS-SDR-81-57
- McLaughlin, K., J. Stevens, T. Barker and H. Shkoller (1990), Non-Linear and Linear Hypotheses for the Excitation of Lg by Contained Explosions in High Velocity Media. in Proceedings of the Twelfth Annual DARPA/GL Seismic Research Symposium. (Eds J. Lewkowics and J McPhetres), GL-TR-90-0212 Geophysics Laboratory, Hanscom AFB, MA **ADA226635**
- Ringdal, F. (1983), Magnitudes from P coda and Lg using NORSAR data, in NORSAR Semiannual Technical Summary, 1 Oct 82- 31 Mar 83, NORSAR Sci. Rep. No. 2-82/83, NTNF/NORSAR, Kjeller, Norway.
- Vergino, E.S. (1989) Soviet test yields. EOS, Trans. A.G.U. Nov 28.

5.1 MULTIPLE EVENT WAVEFORM SIMULATIONS

Executive Summary

Simulated recordings of multiple Balapan test site explosions were constructed by summing recordings of individual explosions. Six multiple explosion cases were considered in which an initial explosion was followed by a larger second shot. Delays between shots were between 0.0 and 2.0 seconds inclusive. Initial data consisted of recordings for four shots, with estimated yields of 125, 72, 35 and 20 kt. Data were scaled appropriately to yields of 5 kt, 20 kt, 35 kt, 40 kt, 45 kt, and 125 kt. Yield was determined using a network m_b from recordings at ARCESS (distance 31.8° from Balapan) and four CDSN stations. Yield was also computed using RMS Lg amplitudes recorded at station Arti (distance 13.8°).

- At delays of 2.0 seconds or greater, the P-waveforms of the individual shots comprising a two shot sequence can be easily recognized if the second shot has a yield comparable to or larger than the first shot. The yields of the two shots can be determined fairly accurately if they both have yields above 35 kt.
- For a 0.5 second delay, m_b yields are usually within 20 percent of the yield of the larger shot.
- In all cases, the RMS Lg amplitude of the multiple explosion was equal to the square root of the sum of the squares of the RMS Lg amplitudes of the individual explosions.
- For delays in the 0.1-0.5 second range, constructive and destructive interference of P-waveforms can alter the m_b of a shot sequence significantly for narrow-band data. However, different delays between shots give seismic yield minima at different frequencies, and it appears that for any delay in the 0.1-0.5 second range there is some frequency band that will always give a seismic yield at least equal to the yield of the largest explosion in the series.
- The methods used in this paper cannot distinguish between the yields of individual shots in a sequence when the shots have delays less than 0.1 second and are located close to one another in space. The summed yield of the sequence is determined, but *not* the yields of the individual shots.

5.1.1 Introduction

This study was designed to test our ability to monitor the yield of underground nuclear explosions under the Protocol to the Treaty between the United States of America and the Union of Soviet Socialist Republics on the Limitation of Underground Nuclear Weapon Tests.

With the current configuration of small aperture arrays (NORESS, ARCESS, FINESA, and GERESS) our ability to monitor a single explosion at or above the 35 kt level is excellent. This study examines multiple shot scenarios by simulating multiple shot data using existing explosion data. Several cases are considered in which an explosion of one yield is followed by an explosion of the same or larger yield at time intervals ranging from 0.0 to 2.0 seconds. The six cases considered are

- Case 1: A 35 kt shot followed by a 40 kt shot
- Case 2: A 35 kt shot followed by a 125 kt shot
- Case 3: A 5 kt shot followed by a 35 kt shot
- Case 4: A 5 kt shot followed by a 125 kt shot
- Case 5: A 20 kt shot followed by a 45 kt shot
- Case 6: A 35 kt shot followed by a 35 kt shot

Both regional Lg measurements and teleseismic P-wave magnitudes were studied.

5.1.2 Data

The data for this study are all from Balapan explosions as recorded at the Soviet IRIS station ARU (Arti) for regional Lg waves and at the ARCESS array, the NORESS array, and China Digital Seismic Network (CDSN) stations BJI, KMI, LZH, and HIA for teleseismic P-waves. *Figure 1* shows the locations of Balapan, ARU, ARCESS, NORESS, and the CDSN stations used. The list of explosions is given in *Table 1*.

Table 1 Balapan Explosions					
Date	Time	Lat	Long	$Y(m_b)$	$Y(Lg)$
Sept 14, 1988	04:00:00.0	49.87	78.82	125	125
Nov 12, 1988	03:30:07.2	50.64	79.15	18	26
Feb 12, 1989	04:15:10.6	50.67	78.31	71	72
Jul 08, 1989	03:47:01.9	50.66	78.51	35	35

The true yields of these explosions are classified. Thus, yields were estimated using both an m_b -yield relationship and an Lg-yield relationship derived for this study. m_b 's were calculated as a network average of the m_b 's from ARCESS and the four CDSN stations. High frequency data from the high frequency central element of the NORESS array were used in a study of short time delays between shots. Variations in m_b from station to station due to source, station, and path effects are typical and a network average is considered to be a superior estimate. Our network average m_b was used to derive a magnitude-yield curve by assuming a yield of 125 kt for the September 14 JVE shot and 35 kt for the July 8 shot. This gives the m_b yields in *Table 1*.

Recent research by Hansen *et al.* [1989, 1990] has shown that the RMS Lg measurement is quite stable over large distance ranges and azimuths for events from Balapan. Our Lg analysis followed that of Hansen *et al.* [1990]. Data were band pass filtered between 0.6 and 3.0 Hz (4 pole zero-phase Butterworth filter) and measured for RMS amplitude in a 120 second sliding window across the Lg arrival. The maximum of the RMS value in the Lg window (between 3.2 and 3.6 km/sec group

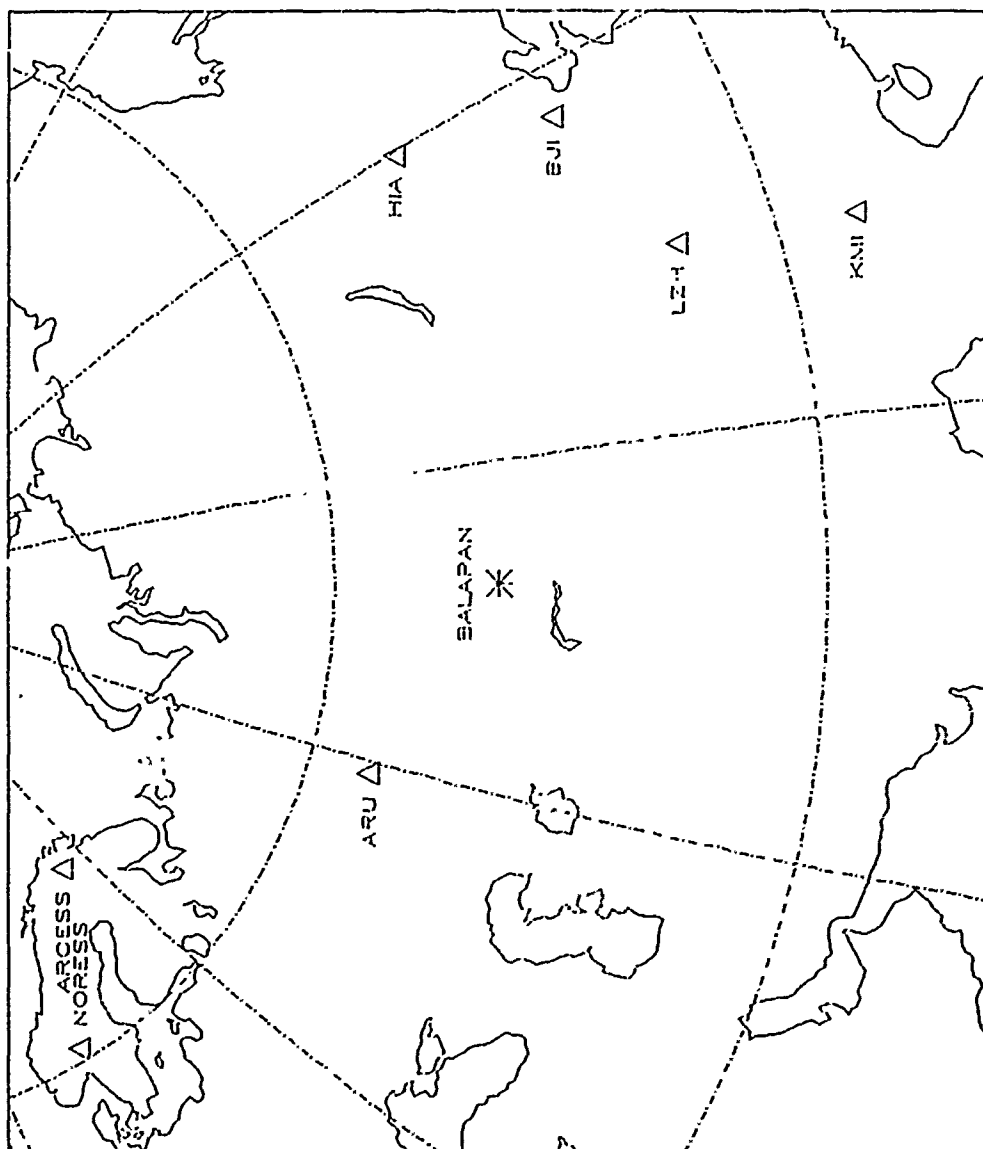


Figure 1. Location of Balapan test site, the Soviet station ARU, the ARCESS and NORESS arrays, and some stations of the Chinese Digital Seismic Network (CDSN).

velocity) was used as our Lg measurement. As with the m_b data, the Lg data were tied to yield by assuming a yield of 125 kt for the JVE shot and 35 kt for the July 8 shot. The yields so derived for the four events are given in the Y(Lg) column of Table 1.

It is important to note that the yields given in Table 1 are not "true" yields for the data being used. Because this is a comparative study in which the yields of two shot sequences are compared to the yields of individual shots, the "true" yields are not as important as the relative sizes of the events.

5.1.3 Analysis Procedure

To achieve the desired yields for this study the data from the shots listed in Table 1 had to be scaled appropriately. In cases where the yield was close to the desired yield no scaling was used. Scale factors for each of the shots are given in Table 2 and scaled data from ARU are shown in Figure 2 as a demonstration of the relative amplitudes of the scaled data. The scaled yield for each shot is also given in Table 2. In each of the six shot sequence cases, data from two different shots were used in the simulations as it is more difficult to separate two different wavetrains than it is to separate two identical ones.

Table 2 Scale Factors			
Date	m_b Scale Factor	Lg Scale Factor	Yield
Sept 14, 1988	1.00	1.00	125
Nov 12, 1988	0.33	0.18	5
Feb 12, 1989	0.67	-	45
Feb 12, 1989	0.61	0.54	40
Feb 12, 1989	0.54	-	35
Jul 08, 1989	1.00	1.00	35
Jul 08, 1989	0.62	-	20

Spectral differences between large and small shots were not considered when scaling the data. Data from shots close to the desired yields were used in an effort to minimize the effects of spectral differences.

An effort was made to measure m_b consistently. However, multiple shot data require some degree of freedom in analysis. For most cases, the amplitudes and phases were measured at the initial P arrival. In cases where a second shot could be clearly identified, the m_b was measured for both explosions. Except for the high frequency cases described below, all data were filtered between 0.5 and 2.0 Hz prior to determining m_b .

ARU Regional Data

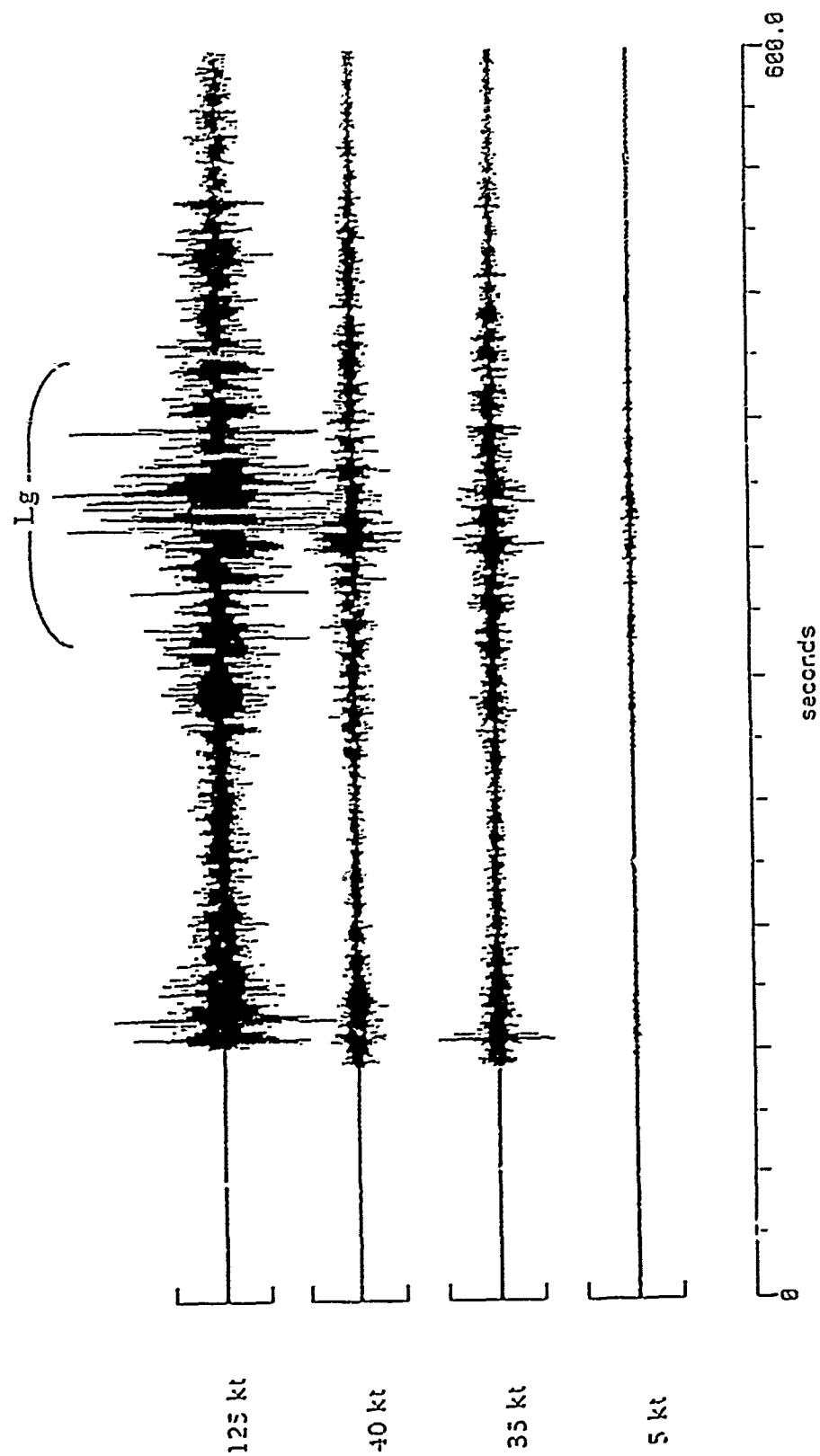


Figure 2. Regional Data Recorded at ARU.

5.1.4 Regional Lg Results

Figures 3 through 6 show the filtered ARU data used for the Lg study. Each figure corresponds to one of the first four cases and includes the scaled data from the individual shots and the simulated data for time delays of 0.5 and 2.0 seconds.

The results of the case study are given in Table 3. For each of the first four cases we list the yields at both of the delay times obtained in the Lg window, the yield of the larger of the two shots, and a "theoretical yield" for the two shot sequence. The "theoretical yield" is the yield produced by taking the square root of the sum of the squares of the individual shot measurements.

Table 3 Lg Yield at ARU				
	0.5 sec delay Yield (kt)	2.0 sec delay Yield (kt)	Theoretical Yield (kt)	Yield of Larger Shot
Case 1 (35-40)	52	46	53	40
Case 2 (35-125)	128	129	130	125
Case 3 (5-35)	35	35	35	35
Case 4 (5-125)	125	126	125	125

As Table 3 shows, the Lg yield of a multiple shot sequence can be predicted from the yields of the individual shots. Lg measurements of multiple shot sequences at this distance (13.8°) and at these delays (0.5 and 2 seconds) are scaled by the square root of the sum of the squares of the Lg measurements of the individual shots.

5.1.5 Teleseismic P Results

The results of our analysis for teleseismic P-waves are given in Table 4. The yields derived for delays of 0.5 and 2.0 seconds in cases 1, 2, 5 and 6 are listed along with the yields determined for the two individual shots. The analyst was able to easily identify multiple shots with 2.0 second delays in each of the cases and two yields were subsequently determined. At 0.5 second delay, our simple analysis interpreted the data as being from a single event. Data for each of the cases as recorded at the ARCESS array are shown in Figures 7 through 10. As can be seen in the figures, the 0.5 second delays are the most interesting as the initial P-waves from the two shots interfere with each other.

ARU Regional Data

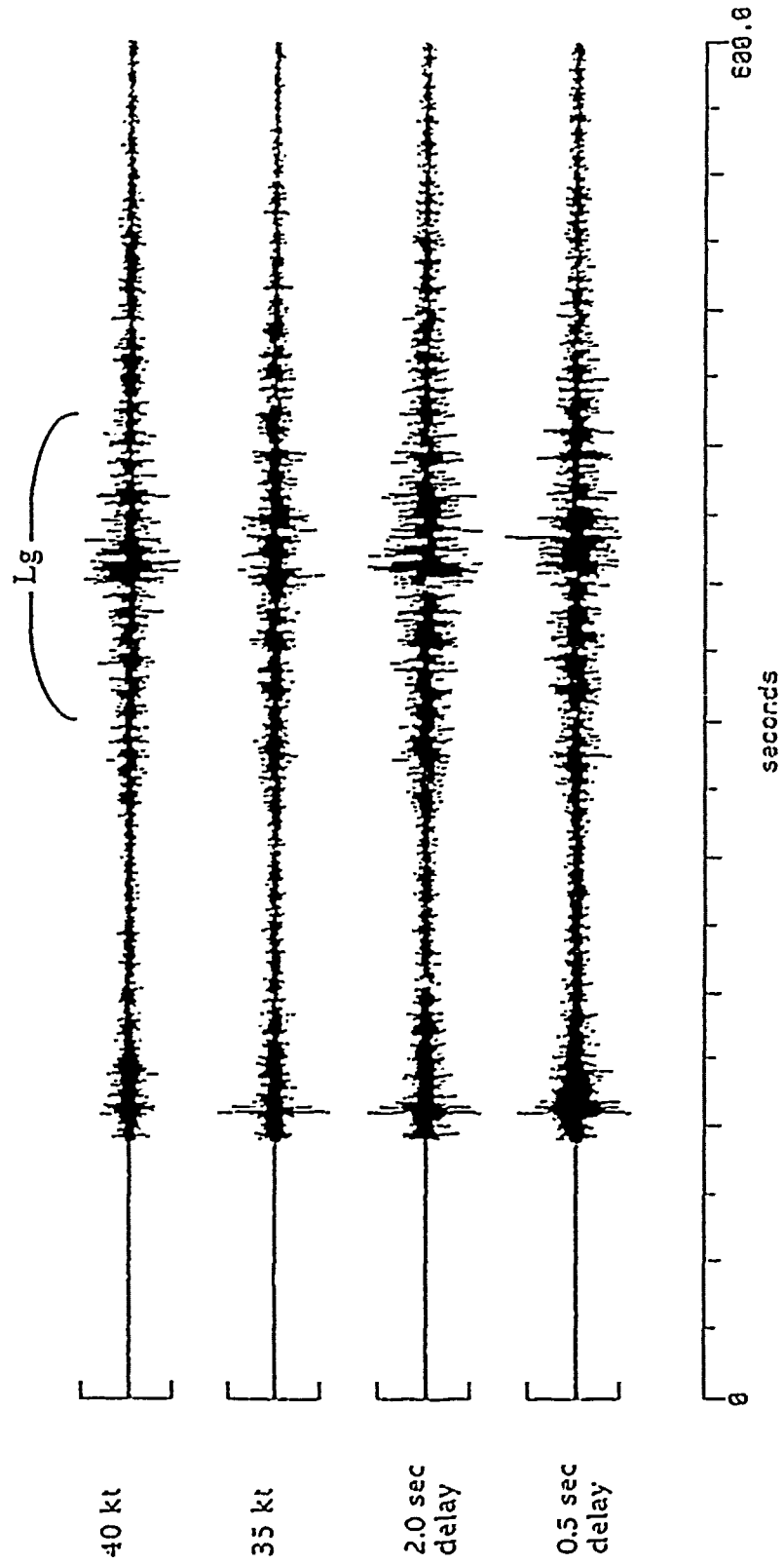


Figure 3. Case 1: A 35 kt shot followed by a 40 kt shot.

ARU Regional Data

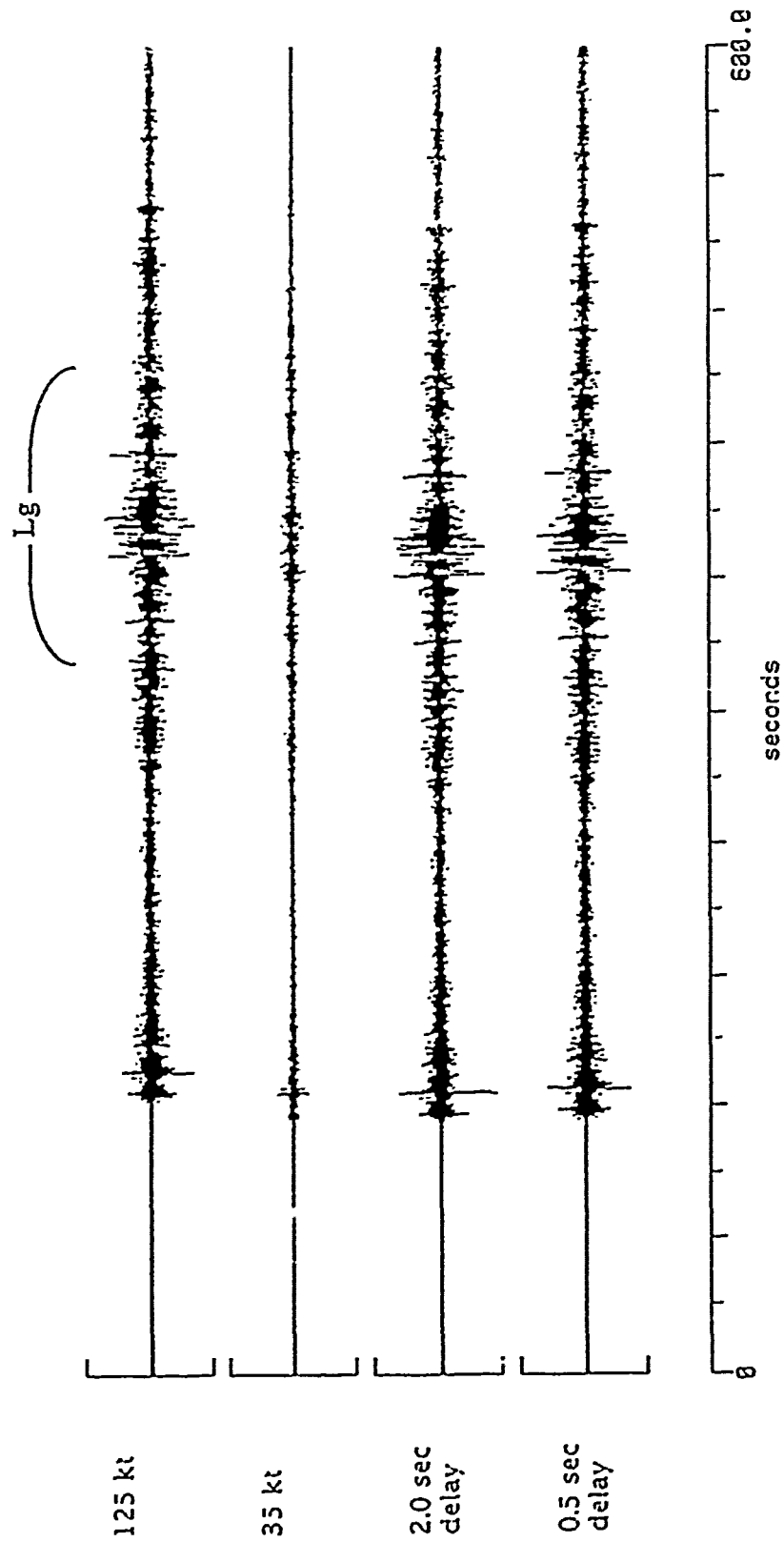


Figure 4. Case 2: A 35 kt shot followed by a 125 kt shot.

ARU Regional Data

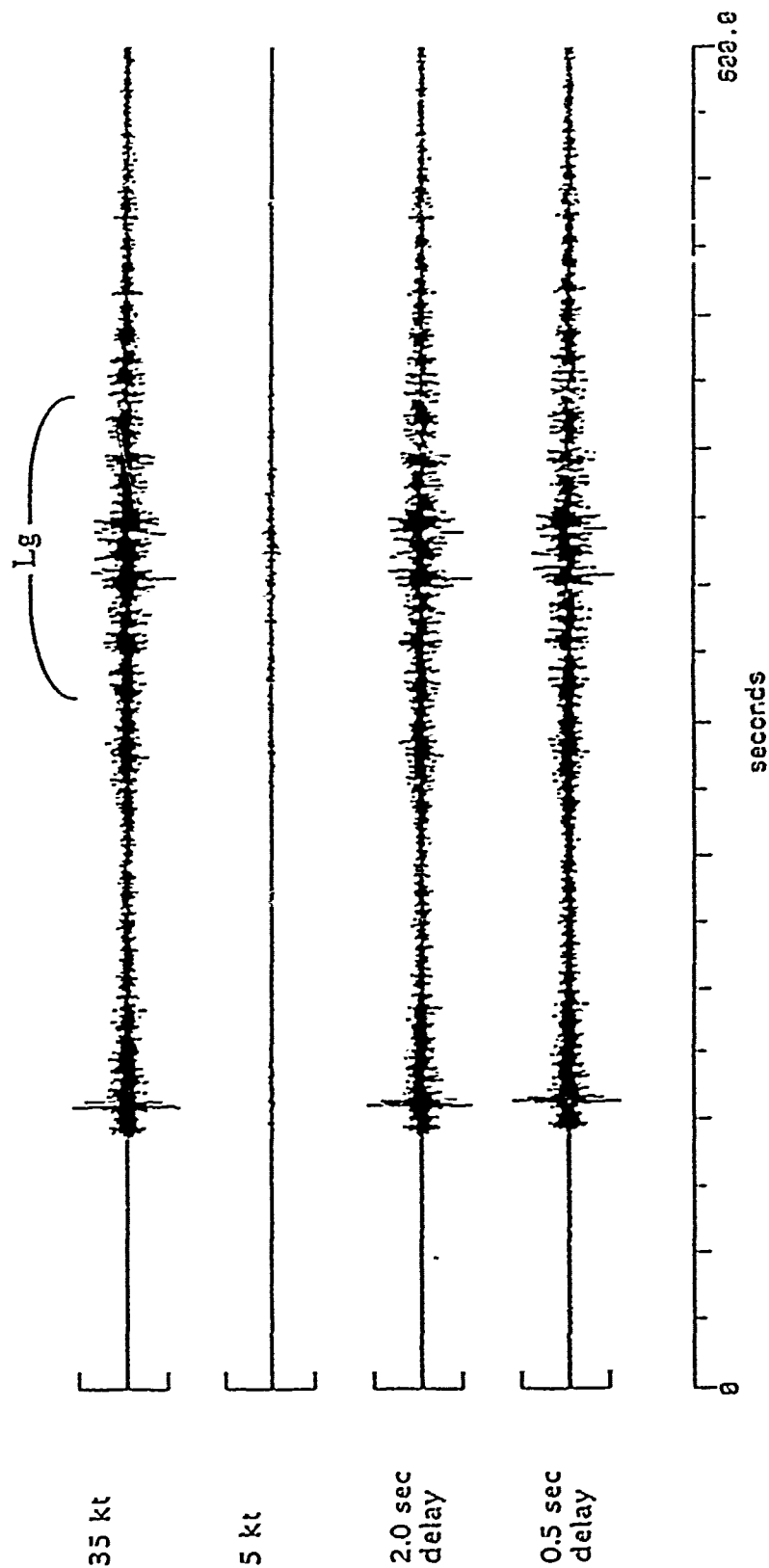


Figure 5. Case 3: A 5 kt shot followed by a 35 kt shot.

ARU Regional Data

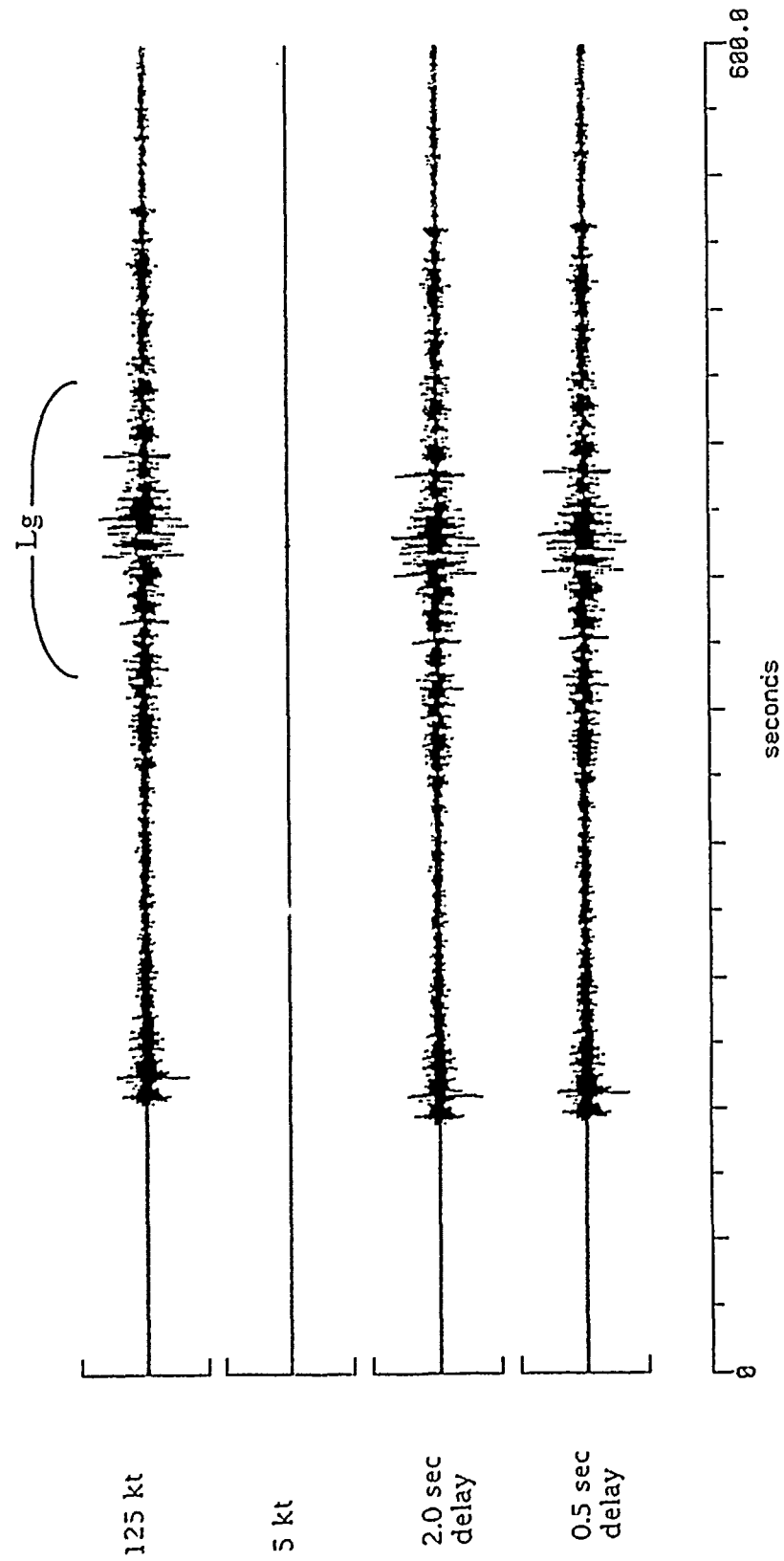


Figure 6. Case 4: A 5 kt shot followed by a 125 kt shot.

ARCESS Teleseismic Data

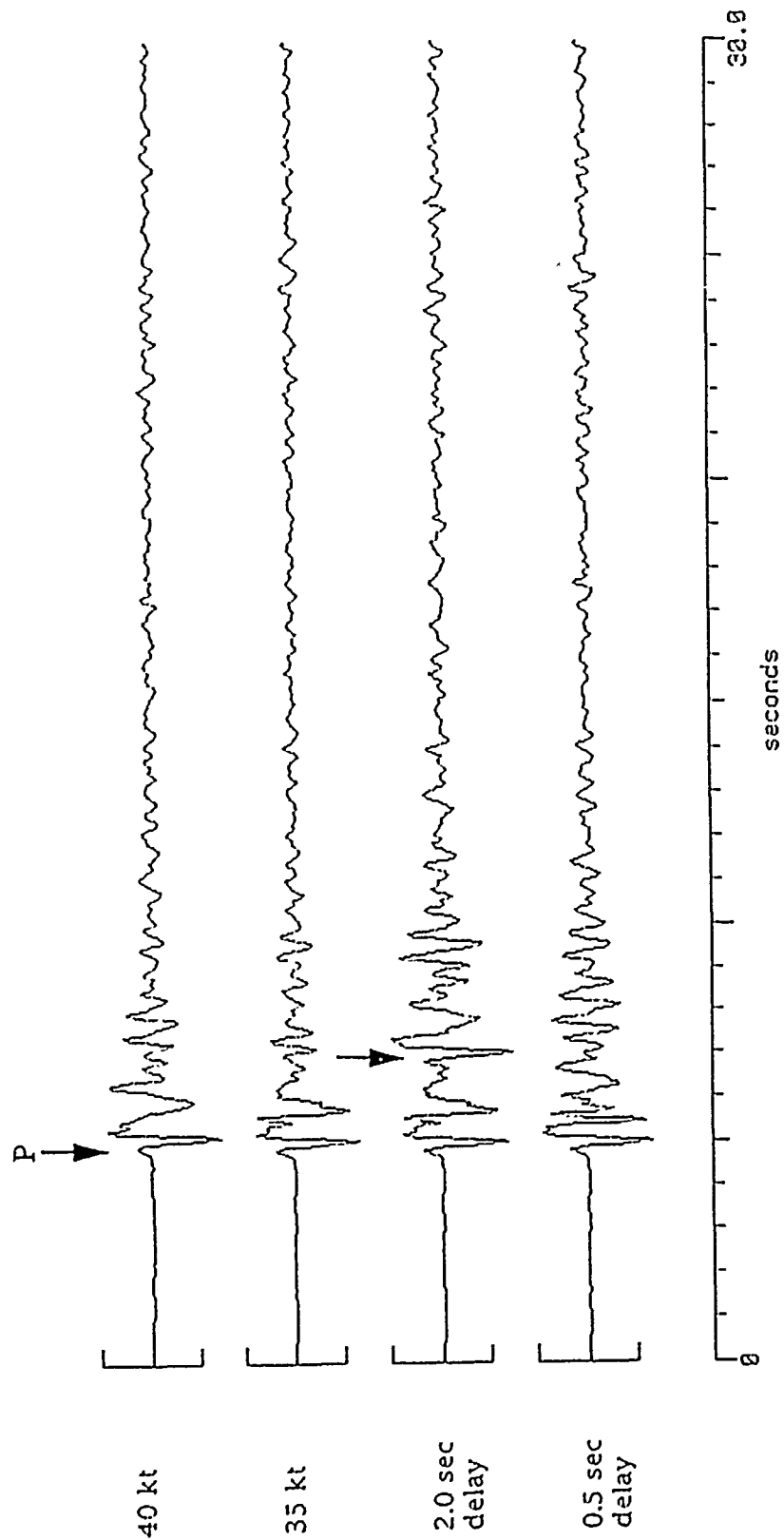


Figure 7. Case 1: A 35 kt shot followed by a 40 kt shot.

ARCESS Teleseismic Data

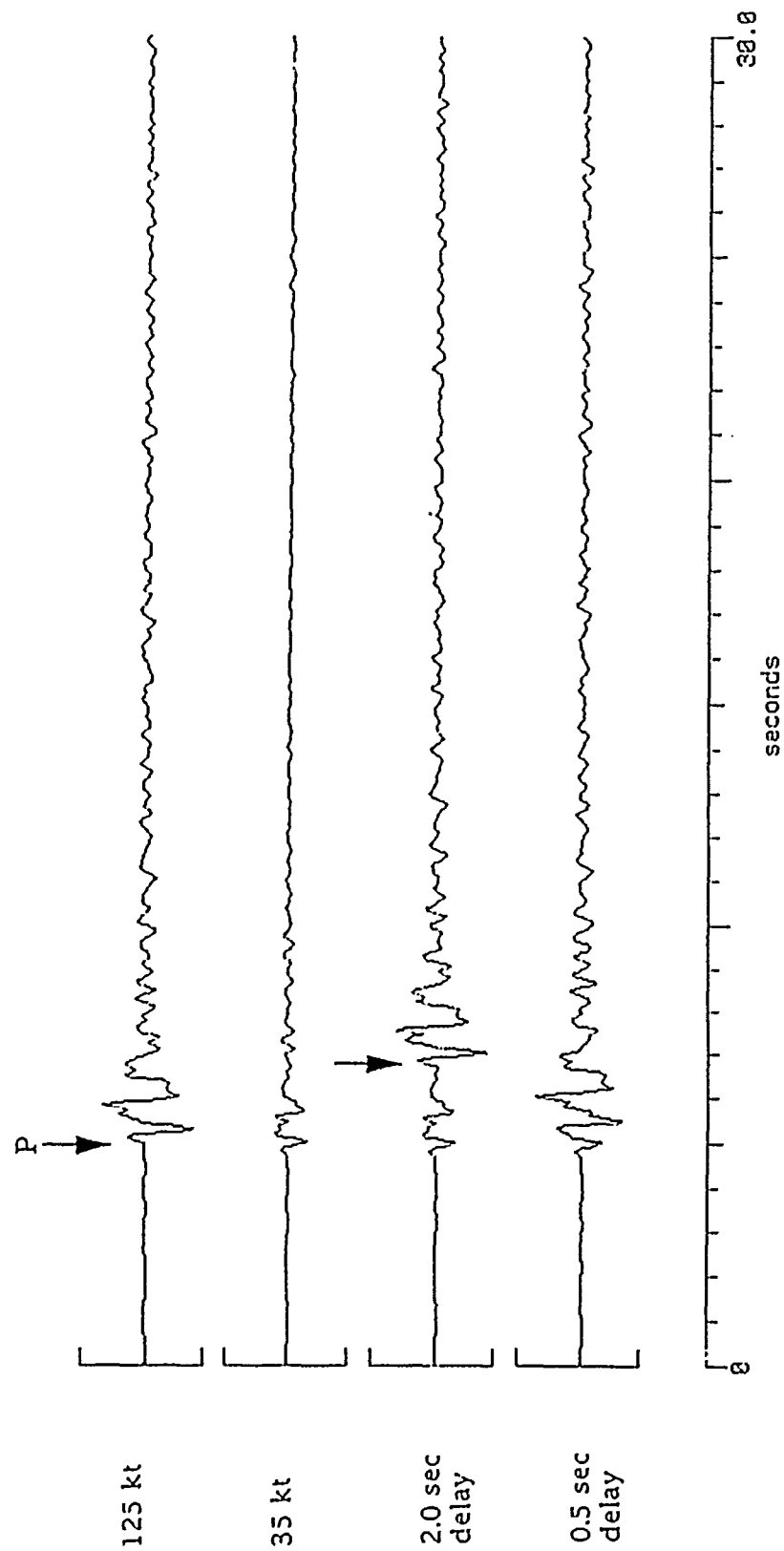


Figure 8. Case 2: A 35 kt shot followed by a 125 kt shot.

ARCESS Teleseismic Data

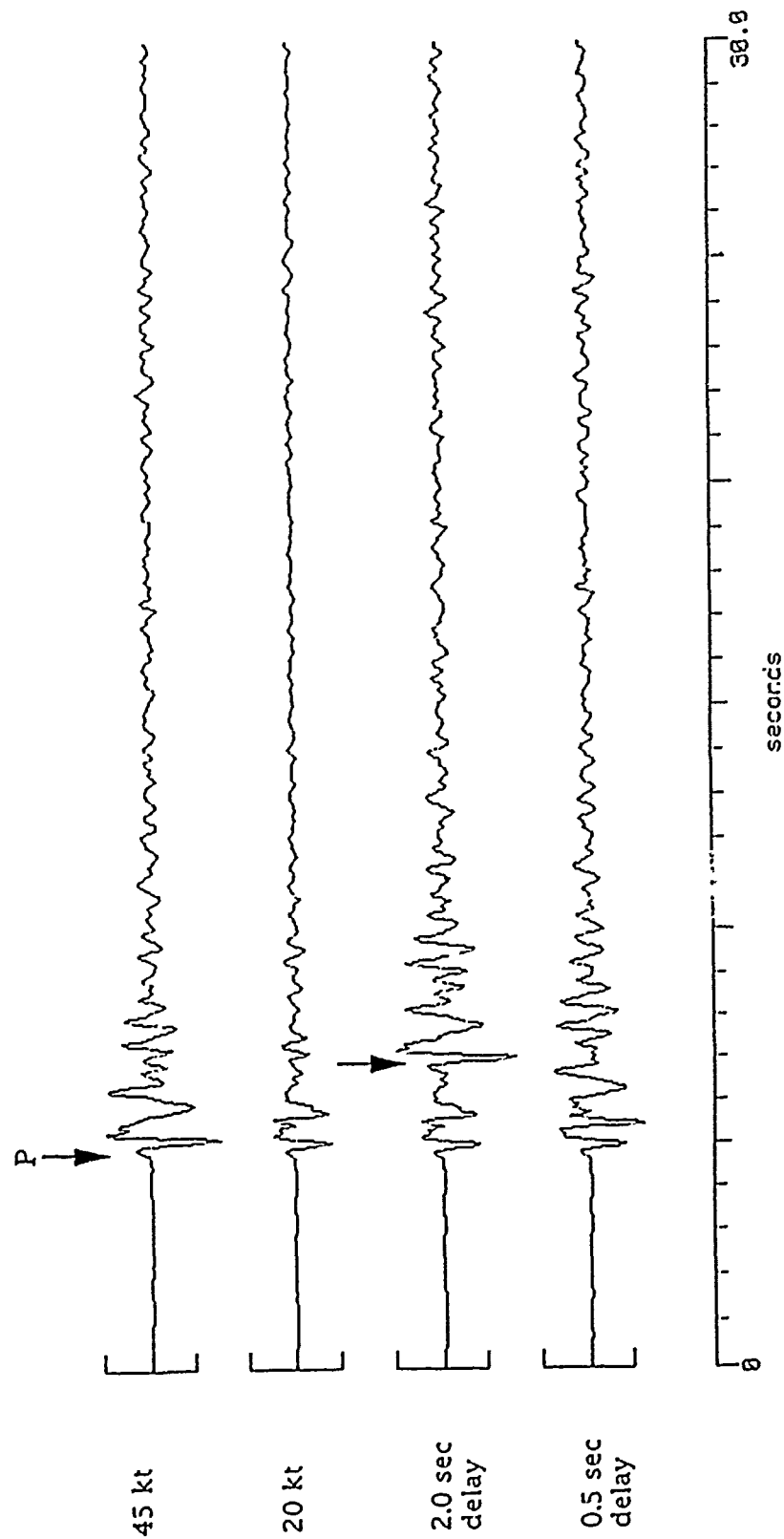


Figure 9. Case 5: A 20 kt shot followed by a 45 kt shot.

ARCESS Teleseismic Data

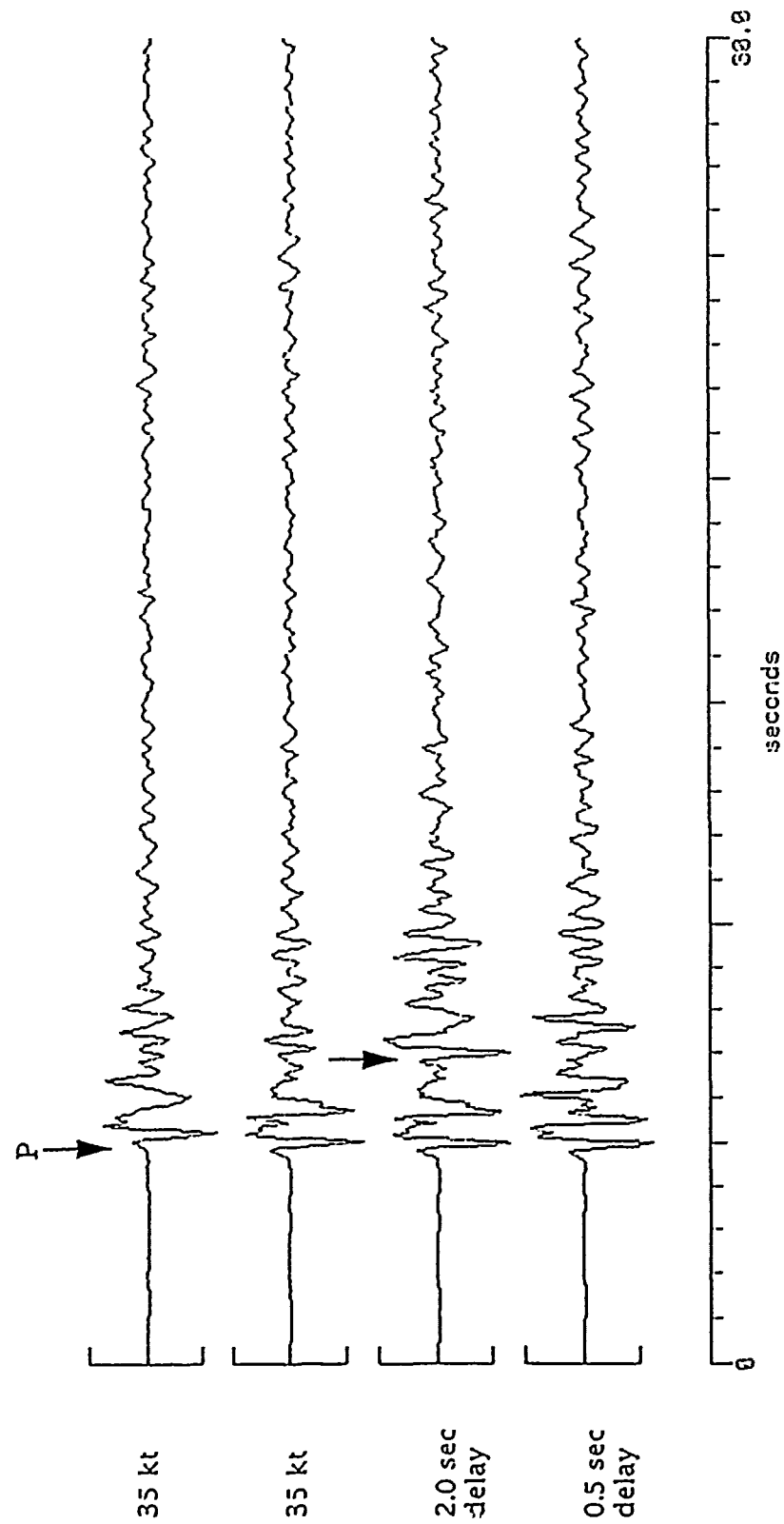


Figure 10. Case 6: A 35 kt shot followed by a 35 kt shot.

Table 4 Teleseismic m_b Yield			
	0.5 sec Yield (kt)	2.0 sec Yield (kt)	Yields of the Individual Shots
Case 1 (35-40)	44	33-49	35-40
Case 2 (35-125)	99	31-126	35-125
Case 5 (20-45)	36	27-49	24-42
Case 6 (35-35)	35	31-43	35-40

At 2.0 seconds delay both of the events were easily identified and the magnitudes of each were determined fairly accurately. For 0.5 second delay between shots, this simple analysis showed that the data may be interpreted as being from a single shot and that the resulting yield may not be similar to the yield of the largest shot. In all cases, however, the yield determined at 0.5 second delays was within 20% of the yield of the larger shot.

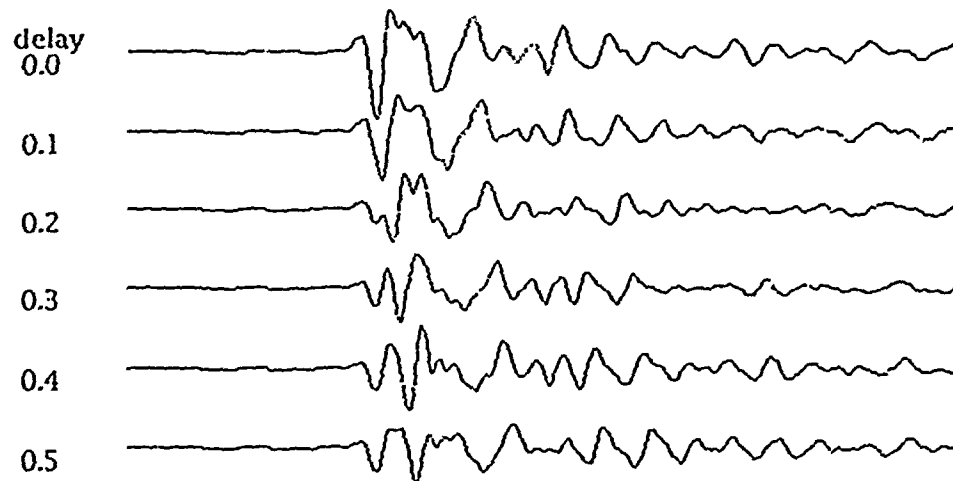
5.1.6 Short Delay Results

The results of the teleseismic P-wave study suggested that further research was warranted into the effects of small time delays between shots. The effects of shot delays from 0.0 to 0.5 seconds at 0.1 second intervals were examined for cases 5 and 6 at the ARCESS array. The data for this study are shown in *Figure 11*. As the delay increases from 0.0 seconds to 0.5 seconds, the amplitude of the P-waves decreases and the frequency fluctuates. Both amplitude and frequency are used to make m_b measurements, so m_b will change from trace to trace. The results are shown in *Figure 12* as plots of normalized apparent yield vs. delay between shots. Apparent yield is normalized to the yield determined for the 0.0 second delay. The normalized yields for the theoretical yield values of the individual shots are also shown in the figures. The analyst measured m_b using two different methods, m_b measured in the first full cycle of the initial P-wave and m_b measured from the maximum amplitude in the first five seconds of P-wave. The results of each method are shown in *Figure 12*. As expected, the yield at 0.0 seconds is the largest. At 0.2 seconds delay the P-waves interfere destructively and the apparent yield determined is at a minimum. As the delay increases, there is no interference in the initial P-wave arrivals and the measured yield using the initial P method is that of the first (smaller) shot. The m_b measured as the maximum value in the first five seconds of P-wave continues to oscillate, approaching the larger yield as the interference of the P wavetrain dies out at larger and larger delays.

These results indicate that for certain shot delays, the yield determined from teleseismic P-waves using these methods may be significantly underestimated. If this is the case, then obvious schemes for violating the Protocol emerge. One example would be to detonate a device with a yield greater than 35 kt 0.2 seconds after a

ARCESS array data

Case 5: 20 kt shot followed by a 45 kt shot



Case 6: 35 kt shot followed by a 35 kt shot

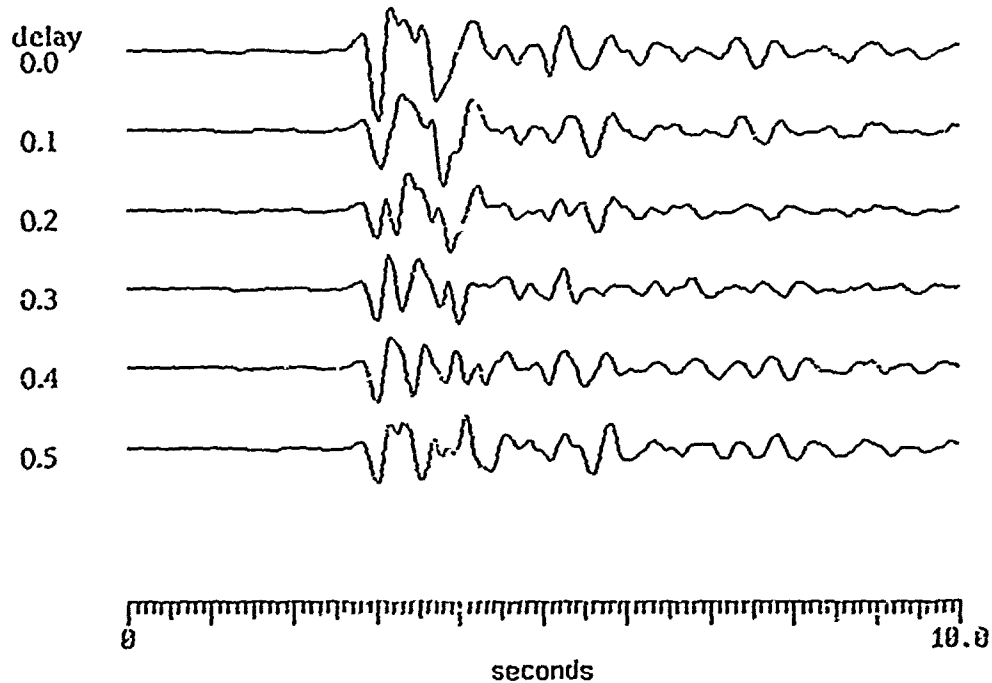
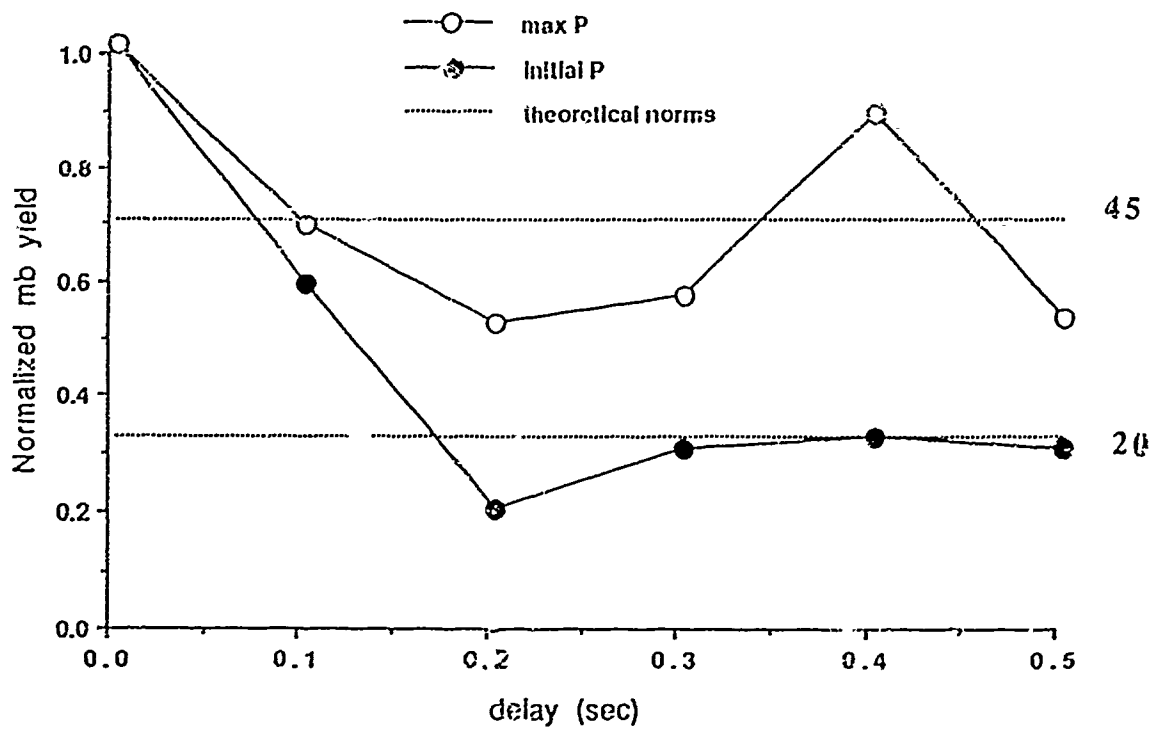


Figure 11. ARCESS unfiltered data for cases 5 and 6 at delays between 0.0 and 0.5 seconds inclusive.

ARCESS array data - Case 5



ARCESS array data - Case 6

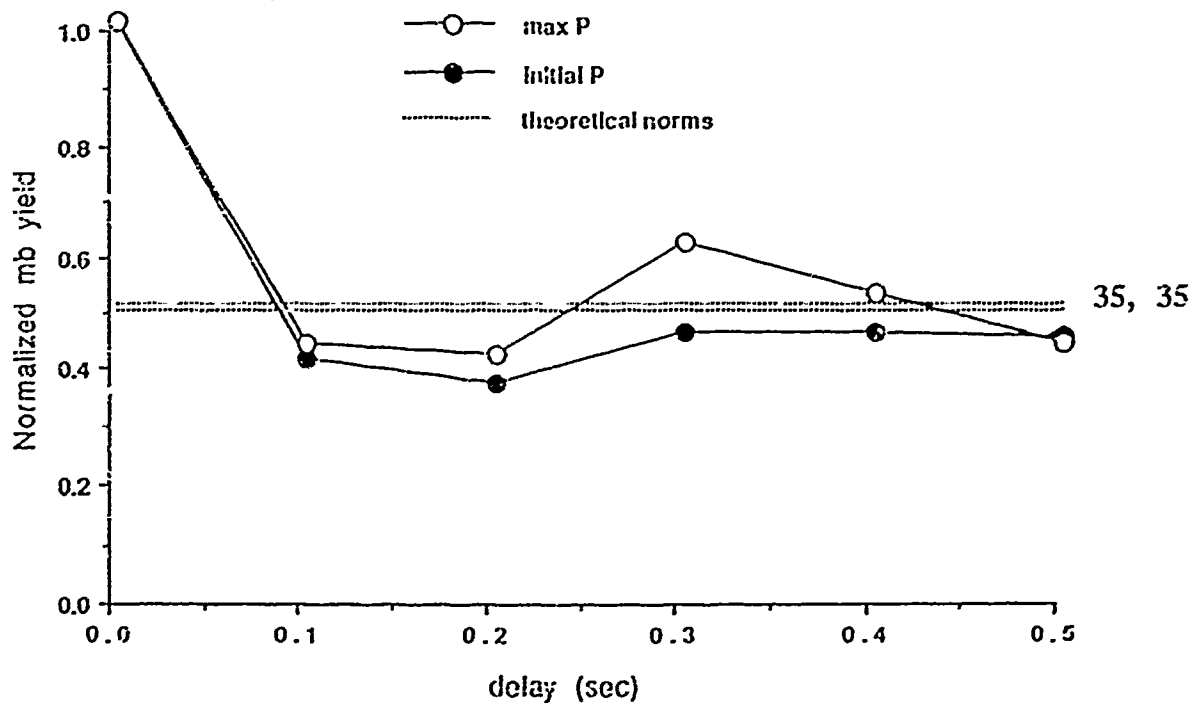


Figure 12. Normalized yield versus delay time for cases 5 and 6 at ARCESS. Yields are normalized to the sum of the yields of the individual shots.

device with significantly smaller yield. Lg yield from such a pair of explosions could not be differentiated seismically from the yield of two smaller (presumably less than 35 kt) devices and the m_b yield, as we have determined it above, would be smaller than the yield of the smaller shot for m_b measured from the initial P-wave, and between the two yields for m_b based on maximum amplitude. The evader could claim that both devices had yields smaller than 35 kt and were therefore not subject to verification procedures (including the 2 second minimum delay between shots).

To counter such a possibility, we examined the use of high frequency data. At higher frequencies, the minimum in the yield-delay curve should occur at a smaller delay than that shown above for the ARCESS data.

5.1.7 High Frequency Short Delay Results

Data for this study came from the high frequency element of the NORESS seismic array in Norway. Up to this point, the data used have had a maximum useful frequency of about 5 Hz and were sampled at 40 samples/second. The high frequency element at NORESS is sampled at 125 Hz and is useful for signal frequencies up to 30 Hz. Data from this instrument allow a more complete study of our ability to distinguish between single and multiple explosions. Unfortunately, data from the four shots analyzed in the preceding section were not available and two 1987 explosions were selected as replacements. The two new events are listed in Table 5.

Table 5 Balapan Explosions			
Date	Time	Lat	Long
Apr 17, 1987	01:03:04.8	49.89	78.69
Jun 20, 1987	00:53:04.8	49.91	78.74

The yields of these shots are not known but their worldwide network average m_b 's are similar to the m_b of the Balapan JVE explosion. To compare the results of this high frequency study to the previous one we have assumed that the yields of the two shots are 35 kt. This is obviously a gross underestimation. The frequency content of the data will not be the same as data from smaller shots and the signal-to-noise ratio will be artificially large. Narrow band filtering at high frequencies where the m_b measurements are made reduces some of the discrepancy.

Data for this study are shown in Figure 13 and the results (case 5) are plotted in Figures 14 and 15. The data were analyzed in four different frequency bands: unfiltered, 0-1 Hz, 2-6 Hz, and 4-8 Hz. As was done for the ARCESS data, yields were normalized to the yield at zero delay in each of the frequency bands. Figure

NORESS High Frequency Data

Case 5: 20 kt shot followed by a 45 kt shot

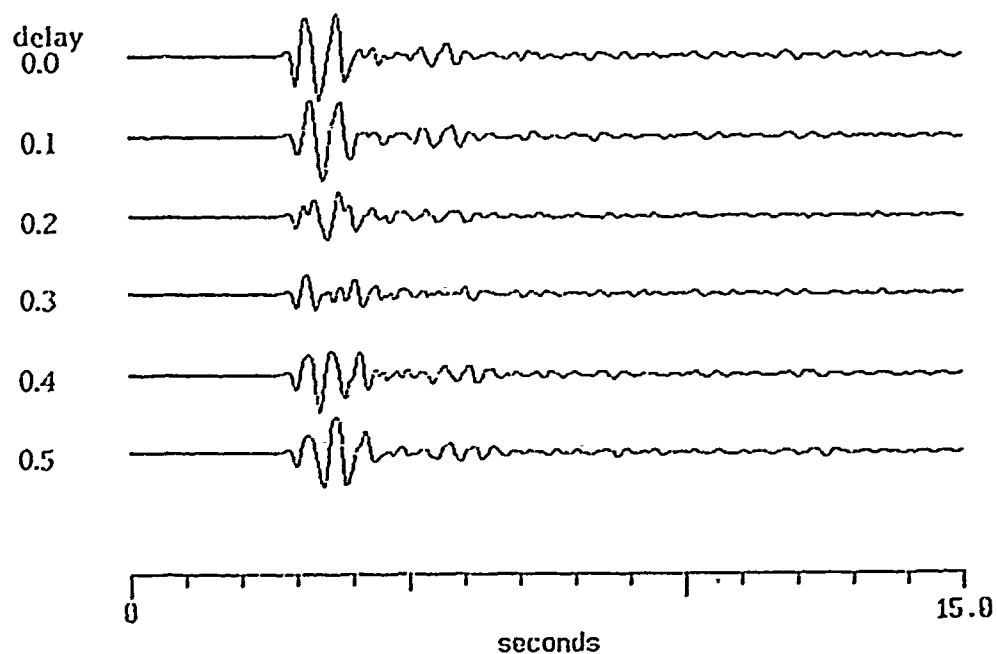


Figure 13. NORESS unfiltered high frequency data for case 5 at delays between 0.0 and 0.5 seconds inclusive.

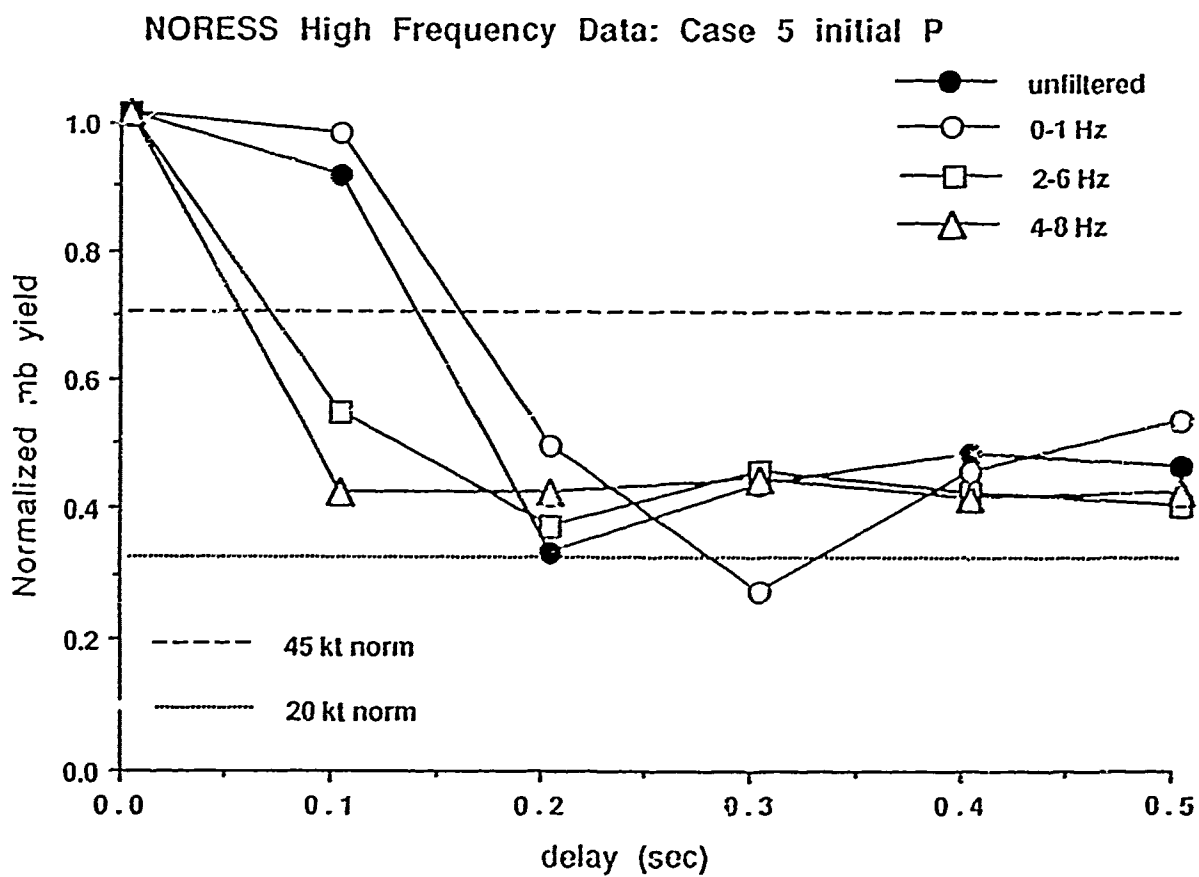


Figure 14. Normalized yield versus delay time for case 5 for NORESS high frequency data. Four frequency bands are shown. As frequency increases, the minimum in the yield curve decreases in delay time. mb measured in the first cycle of the P-wave.

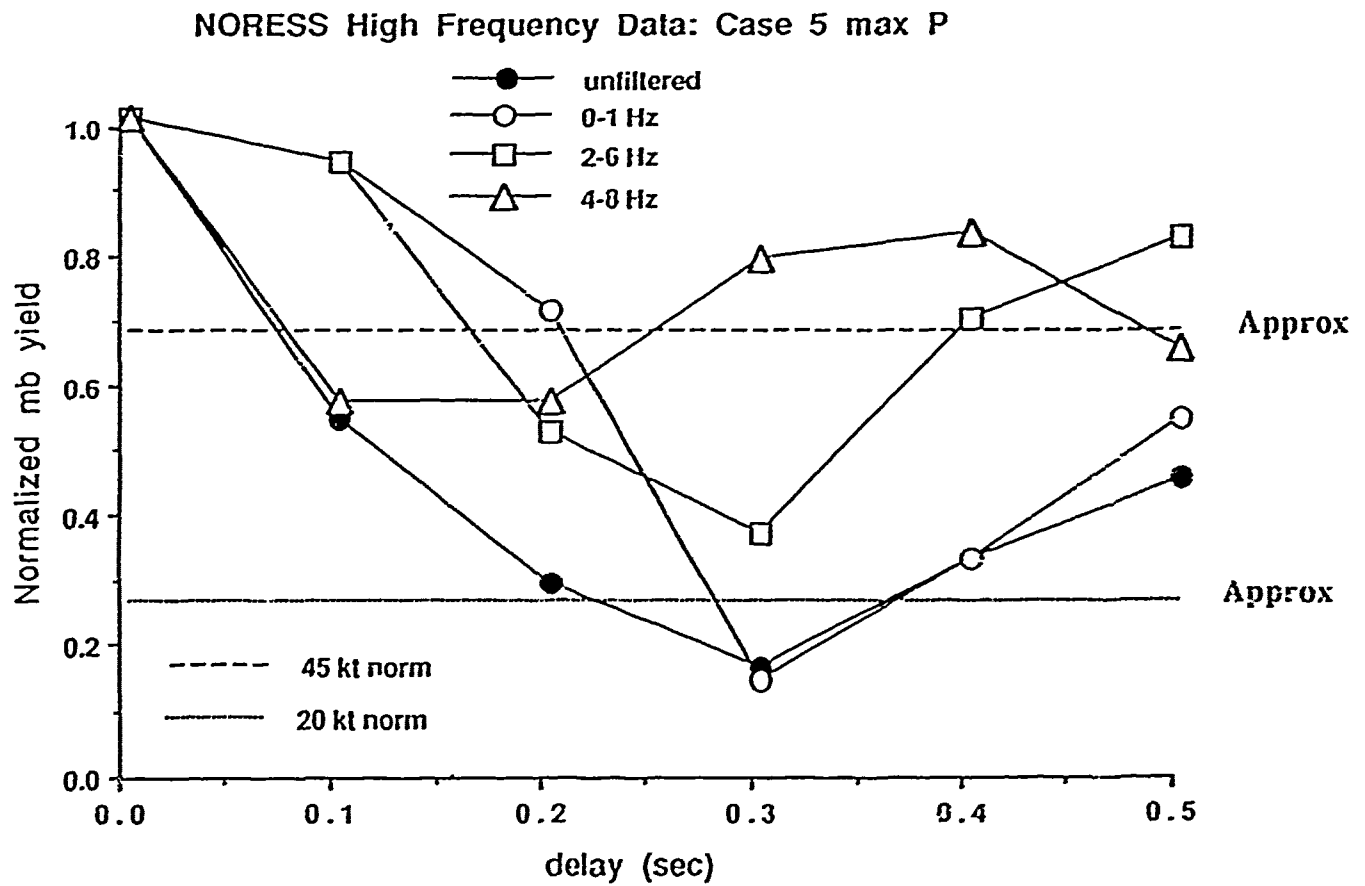


Figure 15. Normalized yield versus delay time for case 5 for NORESS high frequency data. Four frequency bands are shown. mb measured at the maximum amplitude in the 5 seconds following the first arrival.

14 displays the results for a 20 kt shot followed by a 45 kt shot (case 5) using the initial few cycles of P to compute m_b , and Figure 15 shows results for the same case for m_b based on the largest amplitude in the 5 second P-wave window. In Figure 14 the *unfiltered* data give the same results as before for the initial P-wave m_b -- the yield minimum occurs at 0.2 seconds delay. However, for the 0-1 Hz band the minimum occurs at 0.3 seconds, for the 2-6 Hz band it occurs at 0.2 seconds, and for the 4-8 Hz band no distinctive minimum is seen. Quite different results are observed when m_b is computed from the maximum of the P-wave window. Minima for the unfiltered, 0-1 Hz, and 2-6 Hz curves occur at 0.3 seconds delay while the minimum for the 4-8 Hz data is between 0.1 and 0.2 seconds delay. Curves for the different delays have different shapes, and from this preliminary analysis it appears that one of the frequency bands will always give a yield at least equal to the yield of the largest shot. The minimum for each curve, as well as the predicted range of the minimum based on the interference patterns of perfect sinusoids, are given in Table 6.

Table 6 Minima of Yield-Delay Curves for High Frequency Data			
Frequency Band	Measured Delay (sec)		Predicted Delay (sec)
	Initial P	Max. P	
unfiltered	0.2	0.3	-
0-1	0.3	0.3	≥ 0.5
2-6	0.2	0.3	0.08 - 0.25
4-8	-	0.1	0.06 - 0.13

The results given in Table 6 are consistent with our prediction that the minimum in the yield-delay curve occurs at shorter time delays for higher frequency bands. By using data that spans a large frequency range, and by measuring m_b in several bands, it may be possible to deter an attempt to violate the Protocol by detonating an explosion greater than the 35-kt threshold at some delay designed to reduce the seismic yield of the combined explosions by destructive interference. Delays less than 0.1 second would always give yields close to the value of the sum of the individual shots.

Jerry A. Carter
John M. Coyne
Hans Israelsson

References

Hansen, Roger A., F. Ringdal, P.G. Richards (1989), "Analysis of IRIS data for Soviet nuclear explosions," *NORSAR Semiannual Technical Summary, 1 October 1988 - 31 March 1989*, Vol. 2-88/89, pp. 124-140.

Hansen, Roger A., F. Ringdal, and P.G. Richards (1990), "The Stability of RMS Lg Measurements, and Their Potential for Accurate Estimation of the Yields of Soviet Underground Nuclear Explosions," *AFGL Technical Report*, Vol. GL-TR-90-0061, p. 31. **ADA222186**

CONTRACTORS (United States)

Prof. Thomas Ahrens
Seismological Lab, 252-21
Division of Geological & Planetary Sciences
California Institute of Technology
Pasadena, CA 91125

Prof. Charles B. Archambeau
CIRES
University of Colorado
Boulder, CO 80309

Dr. Thomas C. Bache, Jr.
Science Applications Int'l Corp.
10260 Campus Point Drive
San Diego, CA 92121 (2 copies)

Prof. Muawia Barazangi
Institute for the Study of the Continent
Cornell University
Ithaca, NY 14853

Dr. Jeff Barker
Department of Geological Sciences
State University of New York
at Binghamton
Vestal, NY 13901

Dr. Douglas R. Baumgardt
ENSCO, Inc
5400 Port Royal Road
Springfield, VA 22151-2388

Prof. Jonathan Berger
IGPP, A-025
Scripps Institution of Oceanography
University of California, San Diego
La Jolla, CA 92093

Dr. Gilbert A. Bollinger
Department of Geological Sciences
Virginia Polytechnical Institute
21044 Derring Hall
Blacksburg, VA 24061

Dr. Lawrence J. Burdick
Woodward-Clyde Consultants
566 El Dorado Street
Pasadena, CA 91109-3245

Dr. Jerry Carter
Center for Seismic Studies
1300 North 17th St., Suite 1450
Arlington, VA 22209-2308

Prof. Vernon F. Cormier
Department of Geology & Geophysics
U-45, Room 207
The University of Connecticut
Storrs, CT 06268

Professor Anton W. Dainty
Earth Resources Laboratory
Massachusetts Institute of Technology
42 Carleton Street
Cambridge, MA 02142

Prof. Steven Day
Department of Geological Sciences
San Diego State University
San Diego, CA 92182

Dr. Zoltan A. Der
ENSCO, Inc.
5400 Port Royal Road
Springfield, VA 22151-2388

Prof. Lewis M. Duncan
Dept. of Physics & Astronautics
Clemson University
Clemson, SC 29634-1901

Prof. John Ferguson
Center for Lithospheric Studies
The University of Texas at Dallas
P.O. Box 830688
Richardson, TX 75083-0688

Dr. Mark D. Fisk
Mission Research Corporation
735 State Street
P. O. Drawer 719
Santa Barbara, CA 93102

Prof. Stanley Flatte
Applied Sciences Building
University of California
Santa Cruz, CA 95064

Dr. Alexander Florence
SRI International
333 Ravenswood Avenue
Menlo Park, CA 94025-3493

Dr. Clifford Frohlich
Institute of Geophysics
8701 North Mopac
Austin, TX 78759

Dr. Holy K. Given
IGPP, A-025
Scripps Institute of Oceanography
University of California, San Diego
La Jolla, CA 92093

Prof. Henry L. Gray
Vice Provost and Dean
Department of Statistical Sciences
Southern Methodist University
Dallas, TX 75275

Dr. Indra Gupta
Teledyne Geotech
314 Montgomery Street
Alexandria, VA 22314

Prof. David G. Harkrider
Seismological Laboratory
Division of Geological & Planetary Sciences
California Institute of Technology
Pasadena, CA 91125

Prof. Danny Harvey
CIRES
University of Colorado
Boulder, CO 80309

Prof. Donald V. Helmberger
Seismological Laboratory
Division of Geological & Planetary Sciences
California Institute of Technology
Pasadena, CA 91125

Prof. Eugene Herrin
Institute for the Study of Earth and Man
Geophysical Laboratory
Southern Methodist University
Dallas, TX 75275

Prof. Bryan Isacks
Cornell University
Department of Geological Sciences
SNEE Hall
Ithaca, NY 14850

Dr. Rong-Song Jih
Teledyne Geotech
314 Montgomery Street
Alexandria, VA 22314

Prof. Lane R. Johnson
Seismographic Station
University of California
Berkeley, CA 94720

Dr. Richard LaCoss
MIT-Lincoln Laboratory
M-200B
P. O. Box 73
Lexington, MA 02173-0073 (3 copies)

Prof Fred K. Lamb
University of Illinois at Urbana-Champaign
Department of Physics
1110 West Green Street
Urbana, IL 61801

Prof. Charles A. Langston
Geosciences Department
403 Deike Building
The Pennsylvania State University
University Park, PA 16802

Prof. Thorne Lay
Institute of Tectonics
Earth Science Board
University of California, Santa Cruz
Santa Cruz, CA 95064

Prof. Arthur Lerner-Lam
Lamont-Doherty Geological Observatory
of Columbia University
Palisades, NY 10964

Dr. Christopher Lynnes
Teledyne Geotech
314 Montgomery Street
Alexandria, VA 22314

Prof. Peter Malin
Department of Geology
Old Chemistry Bldg.
Duke University
Durham, NC 27706

Dr. Randolph Martin, III
New England Research, Inc.
76 Olcott Drive
White River Junction, VT 05001

Prof. Thomas V. McEvilly
Seismographic Station
University of California
Berkeley, CA 94720

Dr. Keith L. McLaughlin
S-CUBED
A Division of Maxwell Laboratory
P.O. Box 1620
La Jolla, CA 92038-1620

Prof. William Menke
Lamont-Doherty Geological Observatory
of Columbia University
Palisades, NY 10964

Stephen Miller
SRI International
333 Ravenswood Avenue
Box AF 116
Menlo Park, CA 94025-3493

Prof. Bernard Minster
IGPP, A-025
Scripps Institute of Oceanography
University of California, San Diego
La Jolla, CA 92093

Prof. Brian J. Mitchell
Department of Earth & Atmospheric Sciences
St. Louis University
St. Louis, MO 63156

Mr. Jack Murphy
S-CUBED, A Division of Maxwell Laboratory
11800 Sunrise Valley Drive
Suite 1212
Reston, VA 22091 (2 copies)

Prof. John A. Orcutt
IGPP, A-025
Scripps Institute of Oceanography
University of California, San Diego
La Jolla, CA 92093

Prof. Keith Priestley
University of Cambridge
Bullard Labs, Dept. of Earth Sciences
Madingley Rise, Madingley Rd.
Cambridge CB3 0EZ, ENGLAND

Dr. Jay J. Pulli
Radix Systems, Inc.
2 Taft Court, Suite 203
Rockville, MD 20850

Prof. Paul G. Richards
Lamont Doherty Geological Observatory
of Columbia University
Palisades, NY 10964

Dr. Wilmer Rivers
Teledyne Geotech
314 Montgomery Street
Alexandria, VA 22314

Prof. Charles G. Sammis
Center for Earth Sciences
University of Southern California
University Park
Los Angeles, CA 90089-0741

Prof. Christopher H. Scholz
Lamont-Doherty Geological Observatory
of Columbia University
Palisades, NY 10964

Thomas J. Sereno, Jr.
Science Application Int'l Corp.
10260 Campus Point Drive
San Diego, CA 92121

Prof. David G. Simpson
Lamont-Doherty Geological Observatory
of Columbia University
Palisades, NY 10964

Dr. Jeffrey Stevens
S-CUBED
A Division of Maxwell Laboratory
P.O. Box 1620
La Jolla, CA 92038-1620

Prof. Brian Stump
Institute for the Study of Earth & Man
Geophysical Laboratory
Southern Methodist University
Dallas, TX 75275

Prof. Jeremiah Sullivan
University of Illinois at Urbana-Champaign
Department of Physics
1110 West Green Street
Urbana, IL 61801

Prof. Clifford Thurber
University of Wisconsin-Madison
Department of Geology & Geophysics
1215 West Dayton Street
Madison, WI 53706

Prof. M. Nafi Toksoz
Earth Resources Lab
Massachusetts Institute of Technology
42 Carleton Street
Cambridge, MA 02142

Prof. John E. Vidale
University of California at Santa Cruz
Seismological Laboratory
Santa Cruz, CA 95064

Prof. Terry C. Wallace
Department of Geosciences
Building #77
University of Arizona
Tucson, AZ 85721

Dr. William Wortman
Mission Research Corporation
8560 Cinderbed Rd.
Suite # 700
Newington, VA 22122

Prof. Francis T. Wu
Department of Geological Sciences
State University of New York
at Binghamton
Vestal, NY 13901

OTHERS (United States)

Dr. Monem Abdel-Gawad
Rockwell International Science Center
1049 Camino Dos Rios
Thousand Oaks, CA 91360

Michael Browne
Teledyne Geotech
3401 Shiloh Road
Garland, TX 75041

Prof. Keiiti Aki
Center for Earth Sciences
University of Southern California
University Park
Los Angeles, CA 90089-0741

Mr. Roy Burger
1221 Serry Road
Schenectady, NY 12309

Prof. Shelton S. Alexander
Geosciences Department
403 Deike Building
The Pennsylvania State University
University Park, PA 16802

Dr. Robert Burrige
Schlumberger-Doll Research Center
Old Quarry Road
Ridgefield, CT 06877

Dr. Kenneth Anderson
BBNSTC
Mail Stop 14/1B
Cambridge, MA 02238

Dr. W. Winston Chan
Teledyne Geotech
314 Montgomery Street
Alexandria, VA 22314-1581

Dr. Ralph Archuleta
Department of Geological Sciences
University of California at Santa Barbara
Santa Barbara, CA 93102

Dr. Theodore Cherry
Science Horizons, Inc.
710 Encinitas Blvd., Suite 200
Encinitas, CA 92024 (2 copies)

Dr. Susan Beck
Department of Geosciences
Bldg. # 77
University of Arizona
Tucson, AZ 85721

Prof. Jon F. Claerbout
Department of Geophysics
Stanford University
Stanford, CA 94305

Dr. T.J. Bennett
S-CUBED
A Division of Maxwell Laboratory
11800 Sunrise Valley Drive, Suite 1212
Reston, VA 22091

Prof. Robert W. Clayton
Seismological Laboratory
Division of Geological & Planetary Sciences
California Institute of Technology
Pasadena, CA 91125

Mr. William J. Best
907 Westwood Drive
Vienna, VA 22180

Prof. A. Dahlen
Geological and Geophysical Sciences
Princeton University
Princeton, NJ 08544-0636

Dr. N. Biswas
Geophysical Institute
University of Alaska
Fairbanks, AK 99701

Mr. Charles Doll
Earth Resources Laboratory
Massachusetts Institute of Technology
42 Carleton St.
Cambridge, MA 02142

Dr. Stephen Bratt
Center for Seismic Studies
1300 North 17th Street
Suite 1450
Arlington, VA 22209

Prof. Adam Dziewonski
Hoffman Laboratory, Harvard Univ.
Dept. of Earth Atmos. & Planetary Sciences
20 Oxford St
Cambridge, MA 02138

Prof. John Ebel
Department of Geology & Geophysics
Boston College
Chestnut Hill, MA 02167

Eric Fielding
SNEE Hall
INSTOC
Cornell University
Ithaca, NY 14853

Dr. John Foley
Phillips Laboratory/LWH
Hanscom AFB, MA 01731-5000

Prof. Donald Forsyth
Department of Geological Sciences
Brown University
Providence, RI 02912

Dr. Anthony Gangi
Texas A&M University
Department of Geophysics
College Station, TX 77843

Dr. Freeman Gilbert
IGPP, A-025
Scripps Institute of Oceanography
University of California
La Jolla, CA 92093

Mr. Edward Giller
Pacific Sierra Research Corp.
1401 Wilson Boulevard
Arlington, VA 22209

Dr. Jeffrey W. Given
SAIC
10260 Campus Point Drive
San Diego, CA 92121

Prof. Stephen Grand
University of Texas at Austin
Department of Geological Sciences
Austin, TX 78713-7909

Prof. Roy Greenfield
Geosciences Department
403 Deike Building
The Pennsylvania State University
University Park, PA 16802

Dan N. Hagedorn
Battelle
Pacific Northwest Laboratories
Battelle Boulevard
Richland, WA 99352

Dr. James Hannon
Lawrence Livermore National Laboratory
P.O. Box 808
Livermore, CA 94550

Prof. Robert B. Herrmann
Dept. of Earth & Atmospheric Sciences
St. Louis University
St. Louis, MO 63156

Ms. Heidi Houston
Seismological Laboratory
University of California
Santa Cruz, CA 95064

Kevin Hutchenson
Department of Earth Sciences
St. Louis University
3507 Laclede
St. Louis, MO 63103

Dr. Hans Israelsson
Center for Seismic Studies
1300 N. 17th Street, Suite 1450
Arlington, VA 22209-2308

Prof. Thomas H. Jordan
Department of Earth, Atmospheric
and Planetary Sciences
Massachusetts Institute of Technology
Cambridge, MA 02139

Prof. Alan Kafka
Department of Geology & Geophysics
Boston College
Chestnut Hill, MA 02167

Robert C. Kernerait
ENSCO, Inc.
445 Pineda Court
Melbourne, FL 32940

William Kikendall
Teledyne Geotech
3401 Shiloh Road
Garland, TX 75041

Prof. Leon Knopoff
University of California
Institute of Geophysics & Planetary Physics
Los Angeles, CA 90024

Prof. Jack Oliver
Department of Geology
Cornell University
Ithaca, NY 14850

Prof. John Kuo
Aldridge Laboratory of Applied Geophysics
Columbia University
6-2 Mudd Bldg.
New York, NY 10027

Dr. Kenneth Olsen
P. O. Box 1273
Linwood, WA 98046-1273

Prof. L. Timothy Long
School of Geophysical Sciences
Georgia Institute of Technology
Atlanta, GA 30332

Prof. Jeffrey Park
Department of Geology and Geophysics
Kline Geology Laboratory
P. O. Box 6666
New Haven, CT 06511-8130

Dr. Gary McCartor
Department of Physics
Southern Methodist University
Dallas, TX 75275

Howard J. Patton
Lawrence Livermore National Laboratory
L-205
P. O. Box 808
Livermore, CA 94550

Prof. Art McGarr
Mail Stop 977
Geological Survey
345 Middlefield Rd.
Menlo Park, CA 94025

Prof. Robert Phinney
Geological & Geophysical Sciences
Princeton University
Princeton, NJ 08544-0636

Dr. George Mellman
Sierra Geophysics
11255 Kirkland Way
Kirkland, WA 98033

Dr. Paul Pomeroy
Rondout Associates
P.O. Box 224
Stone Ridge, NY 12484

Prof. John Nabelek
College of Oceanography
Oregon State University
Corvallis, OR 97331

Dr. Norton Rimer
S-CUBED
A Division of Maxwell Laboratory
P.O. Box 1620
La Jolla, CA 92038-1620

Prof. Geza Nagy
University of California, San Diego
Department of Ames, M.S. B-010
La Jolla, CA 92093

Prof. Larry J. Ruff
Department of Geological Sciences
1006 C.C. Little Building
University of Michigan
Ann Arbor, MI 48109-1063

Dr. Keith K. Nakanishi
Lawrence Livermore National Laboratory
L-205
P. O. Box 808
Livermore, CA 94550

Dr. Richard Sailor
TASC Inc.
55 Walkers Brook Drive
Reading, MA 01867

Prof. Amos Nur
Department of Geophysics
Stanford University
Stanford, CA 94305

Dr. Susan Schwartz
Institute of Tectonics
1156 High St.
Santa Cruz, CA 95064

John Sherwin
Teledyne Geotech
3401 Shiloh Road
Garland, TX 75041

Dr. Matthew Sibol
Virginia Tech
Seismological Observatory
4044 Derring Hall
Blacksburg, VA 24061-0420

Dr. Albert Smith
Lawrence Livermore National Laboratory
L-205
P. O. Box 808
Livermore, CA 94550

Prof. Robert Smith
Department of Geophysics
University of Utah
1400 East 2nd South
Salt Lake City, UT 84112

Dr. Stewart W. Smith
Geophysics AK-50
University of Washington
Seattle, WA 98195

Donald L. Springer
Lawrence Livermore National Laboratory
L-205
P. O. Box 808
Livermore, CA 94550

Dr. George Sutton
Roncut Associates
P.O. Box 224
Stone Ridge, NY 12484

Prof. L. Sykes
Lamont-Doherty Geological Observatory
of Columbia University
Palisades, NY 10964

Prof. Pradeep Talwani
Department of Geological Sciences
University of South Carolina
Columbia, SC 29208

Dr. David Taylor
ENSCO, Inc.
445 Pineda Court
Melbourne, FL 32940

Dr. Steven R. Taylor
Lawrence Livermore National Laboratory
L-205
P. O. Box 808
Livermore, CA 94550

Professor Ta-Liang Teng
Center for Earth Sciences
University of Southern California
University Park
Los Angeles, CA 90089-0741

Dr. Gregory van der Vink
IRIS, Inc.
1616 North Fort Myer Drive
Suite 1440
Arlington, VA 22209

Professor Daniel Walker
University of Hawaii
Institute of Geophysics
Honolulu, HI 96822

William R. Walter
Seismological Laboratory
University of Nevada
Reno, NV 89557

Dr. Raymond Willeman
Phillips Laboratory/LWH
Hanscom AFB, MA 01731-5000

Dr. Gregory Wojcik
Weidinger Associates
4410 El Camino Real
Suite 110
Los Altos, CA 94022

Dr. Lorraine Wolf
Phillips Laboratory/LWH
Hanscom AFB, MA 01731-5000

Dr. Gregory B. Young
ENSCO, Inc.
5400 Port Royal Road
Springfield, VA 22151-2388

Dr. Eileen Vergino
Lawrence Livermore National Laboratory
L-205
P. O. Box 808
Livermore, CA 94550

J. J. Zucca
Lawrence Livermore National Laboratory
P. O. Box 808
Livermore, CA 94550

GOVERNMENT

Dr. Ralph Alcwine III
DARPA/NMRO
1400 Wilson Boulevard
Arlington, VA 22209-2308

Mr. James C. Battis
Phillips Laboratory/LWH
Hanscom AFB, MA 01731-5000

Harley Benz
U.S. Geological Survey, MS-977
345 Middlefield Rd.
Menlo Park, CA 94025

Dr. Robert Blandford
AFTAC/TT
Center for Seismic Studies
1300 North 17th St. Suite 1450
Arlington, VA 22209-2308

Eric Chael
Division 9241
Sandia Laboratory
Albuquerque, NM 87185

Dr. John J. Cipar
Phillips Laboratory/LWH
Hanscom AFB, MA 01731-5000

Cecil Davis
Group P-15, Mail Stop D406
P.O. Box 1663
Los Alamos National Laboratory
Los Alamos, NM 87544

Mr. Jeff Duncan
Office of Congressman Markey
2133 Rayburn House Bldg.
Washington, DC 20515

Dr. Jack Eyemden
USGS - Earthquake Studies
345 Middlefield Road
Menlo Park, CA 94025

Art Frankel
USGS
922 National Center
Reston, VA 22092

Dr. Dale Glover
DIA/DT-1B
Washington, DC 20301

Dr. T. Hanks
USGS
Nat'l Earthquake Research Center
345 Middlefield Road
Menlo Park, CA 94025

Dr. Roger Hansen
AFTAC/TT
Patrick AFB, FL 32925

Paul Johnson
ESS-4, Mail Stop J979
Los Alamos National Laboratory
Los Alamos, NM 87545

Janet Johnston
Phillips Laboratory/LWH
Hanscom AFB, MA 01731-5000

Dr. Katharine Kadinsky-Cade
Phillips Laboratory/LWH
Hanscom AFB, MA 01731-5000

Ms. Ann Kerr
IGPP, A-025
Scripps Institute of Oceanography
University of California, San Diego
La Jolla, CA 92093

Dr. Max Koontz
US Dept of Energy/DP 5
Forrestal Building
1000 Independence Avenue
Washington, DC 20585

Dr. W.H.K. Lee
Office of Earthquakes, Volcanoes,
& Engineering
345 Middlefield Road
Menlo Park, CA 94025

Dr. William Leith
U.S. Geological Survey
Mail Stop 928
Reston, VA 22092

Dr. Richard Lewis
Director, Earthquake Engineering & Geophysics
U.S. Army Corps of Engineers
Box 631
Vicksburg, MS 39180

James F. Lewkowicz
Phillips Laboratory/LWH
Hanscom AFB, MA 01731-5000

Mr. Alfred Lieberman
ACDA/VI-OA'State Department Bldg
Room 5726
320 - 21st Street, NW
Washington, DC 20451

Stephen Mangino
Phillips Laboratory/LWH
Hanscom AFB, MA 01731-5000

Dr. Robert Masse
Box 25046, Mail Stop 967
Denver Federal Center
Denver, CO 80225

Art McGarr
U.S. Geological Survey, MS-977
345 Middlefield Road
Menlo Park, CA 94025

Richard Morrow
ACDA/VI, Room 5741
320 21st Street N.W
Washington, DC 20451

Dr. Carl Newton
Los Alamos National Laboratory
P.O. Box 1663
Mail Stop C335, Group ESS-3
Los Alamos, NM 87545

Dr. Bao Nguyen
AFTAC/TTR
Patrick AFB, FL 32925

Dr. Kenneth H. Olsen
Los Alamos Scientific Laboratory
P. O. Box 1663
Mail Stop D-406
Los Alamos, NM 87545

Mr. Chris Paine
Office of Senator Kennedy
SR 315
United States Senate
Washington, DC 20510

Colonel Jerry J. Perrizo
AFOSR/NP, Building 410
Bolling AFB
Washington, DC 20332-6448

Dr. Frank F. Pilotte
HQ AFTAC/TT
Patrick AFB, FL 32925-6001

Katie Poley
CIA-ACIS/TMC
Room 4X16NHB
Washington, DC 20505

Mr. Jack Rachlin
U.S. Geological Survey
Geology, Rm 3 C136
Mail Stop 928 National Center
Reston, VA 22092

Dr. Robert Reinke
WL/NTESG
Kirtland AFB, NM 87117-6008

Dr. Byron Ristvet
HQ DNA, Nevada Operations Office
Attn: NVCG
P.O. Box 98539
Las Vegas, NV 89193

Dr. George Rothe
HQ AFTAC/TTR
Patrick AFB, FL 32925-6001

Dr. Alan S. Ryall, Jr.
DARPA/NMRO
1400 Wilson Boulevard
Arlington, VA 22209-2308

Dr. Michael Shore
Defense Nuclear Agency/SPSS
6801 Telegraph Road
Alexandria, VA 22310

Mr. Charles L. Taylor
Phillips Laboratory/LWH
Hanscom AFB, MA 01731-5000

Phillips Laboratory
Attn: XO
Hanscom AFB, MA 01731-5000

Dr. Larry Turnbull
CIA-OSWR/NED
Washington, DC 20505

Phillips Laboratory
Attn: LW
Hanscom AFB, MA 01731-5000

Dr. Thomas Weaver
Los Alamos National Laboratory
P.O. Box 1663, Mail Stop C335
Los Alamos, NM 87545

DARPA/PM
1400 Wilson Boulevard
Arlington, VA 22209

Phillips Laboratory
Research Library
ATTN: SULL
Hanscom AFB, MA 01731-5000

Defense Technical Information Center
Cameron Station
Alexandria, VA 22314 (2 copies)

Phillips Laboratory
ATTN: SUL
Kirtland AFB, NM 87117-6008 (2 copies)

Defense Intelligence Agency
Directorate for Scientific & Technical Intelligence
Attn: DT1B
Washington, DC 20340-6158

Secretary of the Air Force
(SAFRD)
Washington, DC 20330

AFTAC/CA
(STINFO)
Patrick AFB, FL 32925-6001

Office of the Secretary Defense
DDR & E
Washington, DC 20330

TACTEC
Battelle Memorial Institute
505 King Avenue
Columbus, OH 43201 (Final Report Only)

HQ DNA
Attn: Technical Library
Washington, DC 20305

DARPA/RMO/RETRIEVAL
1400 Wilson Boulevard
Arlington, VA 22209

DARPA/RMO/Security Office
1400 Wilson Boulevard
Arlington, VA 22209

CONTRACTORS (Foreign)

Dr. Ramon Cabre, S.J.
Observatorio San Calixto
Casilla 5939
La Paz, Bolivia

Prof. Hans-Peter Harjes
Institute for Geophysik
Ruhr University/Bochum
P.O. Box 102148
4630 Bochum 1, FRG

Prof. Eystein Husebye
NTNF/NORSAR
P.O. Box 51
N-2007 Kjeller, NORWAY

Prof. Brian L.N. Kennett
Research School of Earth Sciences
Institute of Advanced Studies
G.P.O. Box 4
Canberra 2601, AUSTRALIA

Dr. Bernard Massinon
Societe Radiomana
27 rue Claude Bernard
75005 Paris, FRANCE (2 Copies)

Dr. Pierre Mecheler
Societe Radiomana
27 rue Claude Bernard
75005 Paris, FRANCE

Dr. Svein Mykkeltveit
NTNF/NORSAR
P.O. Box 51
N-2007 Kjeller, NORWAY (3 copies)

FOREIGN (Others)

Dr. Peter Basham
Earth Physics Branch
Geological Survey of Canada
1 Observatory Crescent
Ottawa, Ontario, CANADA K1A 0Y3

Dr. Eduard Berg
Institute of Geophysics
University of Hawaii
Honolulu, HI 96822

Dr. Michel Bouchon
I.R.I.G.M.-B.P. 68
38402 St. Martin D'Heres
Cedex, FRANCE

Dr. Hilmar Bungum
NTNF/NORSAR
P.O. Box 51
N-2007 Kjeller, NORWAY

Dr. Michel Campillo
Observatoire de Grenoble
I.R.I.G.M.-B.P. 53
38041 Grenoble, FRANCE

Dr. Kin Yip Chun
Geophysics Division
Physics Department
University of Toronto
Ontario, CANADA M5S 1A7

Dr. Alan Douglas
Ministry of Defense
Blacknest, Brimpton
Reading RG7-4RS, UNITED KINGDOM

Dr. Manfred Henger
Federal Institute for Geosciences & Nat'l Res.
Postfach 510153
D-3000 Hanover 51, FRG

Ms. Eva Johannisson
Senior Research Officer
National Defense Research Inst.
P.O. Box 27322
S-102 54 Stockholm, SWEDEN

Dr. Fekadu Kebede
Geophysical Observatory, Science Faculty
Addis Ababa University
P. O. Box 1176
Addis Ababa, ETHIOPIA

Dr. Tormod Kvaerna
NTNF/NORSAR
P.O. Box 51
N-2007 Kjeller, NORWAY

Dr. Peter Marshall
Procurement Executive
Ministry of Defense
Blacknest, Brimpton
Reading FG7-4RS, UNITED KINGDOM

Prof. Ari Ben-Menahem
Department of Applied Mathematics
Weizman Institute of Science
Rehovot, ISRAEL 951729

Dr. Robert North
Geophysics Division
Geological Survey of Canada
1 Observatory Crescent
Ottawa, Ontario, CANADA K1A 0Y3

Dr. Frode Ringdal
NTNF/NORSAR
P.O. Box 51
N-2007 Kjeller, NORWAY

Dr. Jorg Schlittenhardt
Federal Institute for Geosciences & Nat'l Res.
Postfach 510153
D-3000 Hannover 51, FEDERAL REPUBLIC OF
GERMANY

Universita Degli Studi Di Trieste
Facolta Di Ingegneria
Istituto Di Miniere E. Geofisica Applicata, Trieste,
ITALY

Dr. John Woodhouse
Oxford University
Dept of Earth Sciences
Parks Road
Oxford OX13PR, ENGLAND